Modelling Headland Sandbank Processes

Thesis submitted in accordance with the requirements of University College London for the degree of Doctor in Philosophy

by

Oliver P. Jones

January 2007

ProQuest LLC
789 East Eisenhower Parkway
P.O. Box 1346
Ann Arbor, MI 48106-1346

Declaration

I, Oliver P. Jones, confirm that the work presented in this thesis is my own. Where information has been derived from other sources, I confirm that this has been indicated in the thesis.

Acknowledgements

There are so many individuals whose contribution to my learning experience I would like to acknowledge. It seems like I have been writing this page in my mind for the last three years. I am indebted to you all and hope I can do some justice to you here.

Firstly, I would like to thank University College London and to the EPSRC for entrusting me with a PhD scholarship. I hope that my hard work has fulfilled the obligation that the privilege bestows.

I would like to thank my principal supervisor, Richard Simons of UCL, for giving me the latitude to explore my own ideas in this study. My three years at UCL would not have been anywhere near as enriching without it. Thank you also for the many highly discursive - but always constructive - discussions that we have had over the years. I hope that just a little bit of your wisdom has rubbed off on to me.

A special thank you also to John Harris of ABPmer. Giving me the opportunity to spend time in industry has, I hope, helped to make a more relevant end product. Your support and friendship have also been greatly appreciated.

Special thanks also to Henrik Kofoed-Hansen of DHI Group, who first took an interest in my work at Littoral 2004 in Aberdeen. Your work-ethic and methodical approach are qualities I attempt to imitate. Thanks also for providing an opportunity to spend time at DHI Denmark. Being surrounding by so much knowledge was as humbling as it was educational. There are a number of other people who I would also like to thank for making my time in Denmark the experience that it was. Thanks to Ole Pedersen, for your input to my learning and also for your hospitality in DK. My housemates in Hørsholme, Martin, Henrietta and Lorenzo, thanks for your friendship and I look forward to many more weeks together. Thanks also to Ole Sørenson for the time you afforded me and for showing me how much I have yet to learn. Jesper Grooss, thank you for your hospitality and for explicating the mathematics of unstructured grids. Thanks to Hakeem Johnson for finding the time to entertain my ideas and for many useful discussions. Thanks also to Ann Skou for your generous help and comments.

I would also like to thank John Jones of UCL. Thanks for your unwavering enthusiasm and continuous flow of ideas. It has been fun working with you. I am also grateful to other colleagues at UCL, especially Amah Bahra and Tristan Robinson who were great colleagues and friends. Thanks to Adrian Wright for making me feel so welcome at ABPmer and I look forward to many more road trips together.

I am also in debt to those involved in the refereeing of various papers that came out of this work. Specifically, Tim Chesher of HR Wallingford, Prof. Jim Kirby of the University of Delaware, Dr. Jebbe J. van der Werf of the University of Twente, Prof. David Huntley of the University of Plymouth, Prof. Chris Flemming of Halcrow Group and others who remain anonymous. All of your valuable comments and suggestions have immensely helped to improve the quality of this work and they are much appreciated. Thanks also to Dr. Rich Signell of the U.S. Geological Survey, Dr. Garret Duffy of the Canadian Geological Survey, Prof. Rolf Deigaard of DHI group and Dr. Jacob Jensen also of DHI group for many useful comments and suggestions.

Finally I would like to thank my parents whom deserve the most gratitude. It is because of their relentless encouragement that I ever arrived at UCL in October of 2003 and to whom I dedicate this work.

Oliver Jones

December 2006

Abstract

This thesis describes an investigation into near-shore headland-associated sandbanks that used process-based modelling techniques. The modelling experiments involved tidal, wave, sediment transport and morphological modules. The motivation came from a need to understand the dynamics of near-shore headland sandbanks which are valuable resources of raw material, ecology and coastal protection.

An idealised model of a coastal headland was first used in which the physical system was simplified in order to quantify the influence of individual variables on sandbank initiation and growth. This approach provided a number of useful insights into headland sandbank dynamics. Firstly, the relative impact of the Coriolis force was shown to be minor in comparison with parameters including the seabed slope, headland geometry and tidal forcing. It was shown that a causal relationship between sandbank initiation and headland eddies does not exist. For certain headland geometries, however, the model suggested that the eddies become important in the long term maintenance of the associated headland sandbanks.

The initiation and potential growth mechanisms of a real near-shore sandbank in the central Bristol Channel have also been investigated. The results confirmed many of the ideas obtained from the idealised investigation and provided a number of new insights into the complex physical system in which the bank exists. The presence of a wave-induced mechanism was detected, capable of replenishing sandy material in the large coastal embayments and supplying the headland sandbanks of the central Bristol Channel. The work also suggested that the sandbank itself was initiated, and its position controlled, by large gradients in the tidal currents produced by the headland. Its further maintenance and development was shown to be the result of a self-sustaining feedback mechanism, detected in the surrounding flow field.

Table of Contents

Table of Figures

List of Tables

List of Symbols

a	radius of shore-normal ellipse
A	wave action density
A_0	directional action spectrum
b_e	radius of shore-parallel ellipse – ebb side
b_f	radius of shore-parallel ellipse – flood side
c	wave celerity
C_D	frictional coefficient
c_s	user specified constant in the computation of horizontal eddy viscosity
c_{dis}	proportional factor on the white capping dissipation source function
CFL	Courant-Friedrichs-Levy number
$c_{0\ x,y,\theta}^{\bullet}$	propagation speed through the spatial and spectral domains of m_0
$c_{0\ x,y,\theta}^{\bullet\bullet}$	propagation speed through the spatial and spectral domains of m_1
d	grain size
d_m	model grain size
d_p	prototype grain size
d_{50}	median grain size
D	still water depth
D_c	vorticity diffusion
D_f	wave and current dissipation due to bottom friction
D_x	horizontal x-component of momentum diffusion
D_y	horizontal y-component of momentum diffusion
$D*$	dimensionless grain size
E	wave energy density
f	planetary vorticity (Coriolis)

fq	frequency of wave observations
F_u	horizontal Reynolds stresses in the x-direction
F_v	horizontal Reynolds stresses in the y-direction
FVT	frictional vorticity transport
F_x	depth-averaged wave-induced forcing in the horizontal x-direction
F_y	depth-averaged wave-induced forcing in the horizontal y-direction
g	gravity
h	characteristic length scale
H	total water depth
H_m	model water depth (mean)
H_p	prototype water depth (mean)
H_{rms}	root mean square of wave height
H_s	significant wave height
H_θ	representative wave height
J	Jacobian operator
$\cdot\mathbf{k}$	the vertical unit vector
$\mathbf{k}\cdot$	wave number vector
k	wave number
K_N	bed roughness
K_R	ripple-related roughness
l	characteristic length scale
M_ξ	contribution to the momentum equation from external sources
M_η	contribution to the momentum equation from external sources
m_0	zeroth moment of wave action
m_1	first moment of wave action
n	porosity
N	non-linear advective term

p	pressure
p_a	atmospheric pressure
Q	sediment transport rate
Q_x	x-component of the sediment transport rate
Q_y	y-component of the sediment transport rate
s	ratio of grain and water densities
S	radiation stress tensor
S_c	magnitude of the discharge due to point sources
$\bar{S}$	shearing intensity
S_{ij}	deformation rate
S_T	sediment transport updating interval
S_{xx}	radiation stress tensor in the direction of wave propagation
S_{yy}	radiation stress tensor in the long-shore direction
S_{yy}	radiation stress tensor in the transverse wave direction
t	time
T	unsteady source function
T_{pk}	peak wave period
T_{xx}	x-component of lateral stress
T_{xy}	x-y-component of lateral stress
T_{yy}	y-component of lateral stress
T_z	zero crossing period
T_0	parameterized source function of for m_0
T_1	parameterized source function of for m_1
u	horizontal x-component of depth-averaged velocity
u'	horizontal x-component of turbulent velocity
$\tilde{u}$	horizontal x-component of velocity due to the mean flow and Stokes drift
$\bar{u}^E$	Eulerian velocity vector

u_f	friction velocity
$\bar{u}_h$	2-D horizontal vector representing depth-averaged horizontal velocity
$\bar{u}^L$	Generalized Lagrangian Mean (GLM) velocity vector
u_s	x-component of velocity by which water is discharged into an ambient water body
$\bar{u}^S$	Stokes drift vector
u_0	velocity at top of boundary layer
$u*$	shear velocity
U	horizontal x-component of transport velocity
U_{fc}	friction velocity due to the mean current
U_{f0}	friction velocity for the mean current profile in the wave boundary layer
U^{no}	Ursell number
v	horizontal y-component of depth-averaged velocity
v'	horizontal y-component of turbulent velocity
$\bar{v}_h$	2-D horizontal vector representing depth-averaged horizontal velocity
v_s	y-component of velocity by which water is discharged into an ambient water body
$\tilde{v}$	horizontal y-component of velocity due to the mean flow and Stokes drift
V	horizontal y-component of transport velocity
V_A	ambient current velocity
V_m	model velocity
V_p	model velocity
w	vertical velocity component
w_s	settling velocity
w_δ	additional vertical velocity just outside of the wave boundary layer
x	horizontal Cartesian co-ordinate
y	horizontal Cartesian co-ordinate
z_b	non-dimensional boundary layer thickness

z	vertical co-ordinate
z^n	bed level at the present time-step
z^{n+1}	bed level at the next time-step
α_b	proportional factor on the wave breaking source function
α_1	Smagorinsky coefficient
γ	angle between waves and current
γ_b	wave height to water depth ratio
δ	thickness of the boundary layer
δ_u	mean boundary layer thickness
δ_w	coefficient controlling the rate of dissipation in the energy/action spectrum
Δx_n	grid spacing
ζ	sea surface elevation above still water depth
θ	spectral wave direction
κ	von Karman's constant
λ	wavelength
Π	transport vorticity
ρ	density
ρ_d	grain density
ρ_0	reference density
τ_{ij}	internal fluid shear stress
τ_{str}	contribution to bottom bed shear stress from wave streaming effect
$\overline{\tau_{wc}}$	mean bed shear stress in response to wave and current motion
ϕ	dimensionless ratio
υ	kinematic viscosity of water
υ_{bl}	boundary layer eddy viscosity
υ_H	horizontal turbulent viscosity
υ_t	vertical turbulent viscosity

φ	geographical latitude
ψ	coordinate in (x, y)-space normal to the spectral wave direction
ω	wave angular frequency
ω_0	mean wave frequency
Ω	angular rate of revolution of the earth
ϖ	fluid vorticity
ϑ	rate of deformation
Θ	angle between the instantaneous bed shear stress and the mean current direction

1. Introduction

1.1 General Problem Definition and Objective

Predicting sandbank behaviour is important both in coastal and offshore engineering. Within the coastal region, sandbanks help to maintain beach levels and prevent cliff erosion through the exchange of material with the beach and foreshore. They also provide natural protection from storms, helping to refract and dissipate wave energy. In shallow water, sandbanks lower current speeds through increased bed friction. This can provide important nursery and feeding grounds for fish. Shallow sandbanks can also be potentially hazardous to navigation and the dynamic nature of some features is of particular concern. Recently, wind farm developments have exploited some of the more stable banks where installation in relatively shallow water favours both initial construction and maintenance costs. Some sandbanks are mined for high quality marine aggregates.

Sandbanks are thus valuable natural resources that are under pressure from various stakeholders with conflicting interests. Understanding their response to anthropogenic pressures and natural processes is extremely important.

In spite of the importance of sandbanks in coastal science, their behaviour is often poorly understood and methods of prediction are mainly theoretical or qualitative. This is due, primarily, to the complexity of the environments in which they exist and the range of spatial and temporal scales over which they develop.

An example of a large and dynamic sandbank is the Nash Sands in the central Bristol Channel, U.K (see Figure 1.1). The bank exists in a near-shore position close to a prominent coastal headland and is subject to both high tidal and wave energy. It forms an important barrier from wave attack, an important fishing ground and has been extensively mined for its high quality aggregate over the last three decades. The lack in understanding of the bank's dynamic nature and its interaction with local hydrodynamics and sediment transport processes has provided the motivation behind the present study. The overall aim is to predict and understand the initiation and growth of near-shore sandbanks using process-based modelling techniques.

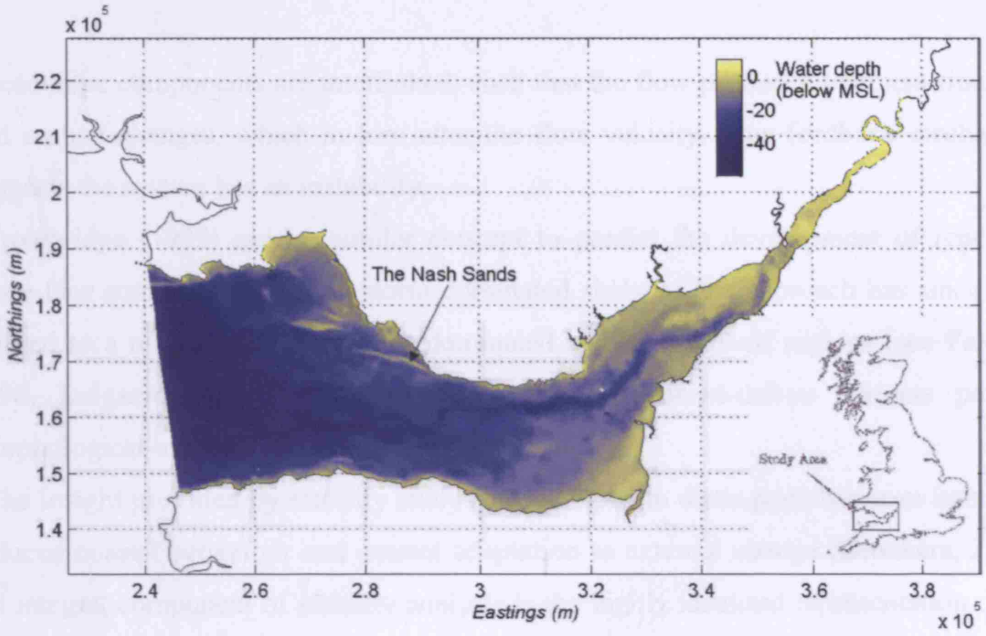

Figure 1.1. The Nash Sands in the central Bristol Channel, South West, U.K.

1.2 Methods of Predicting Sandbank Initiation and Behaviour

Much work was dedicated to the understanding of sandbanks during the late 70's and 80's when there was a drive to improve the long-term stability of oil and gas pipelines in the North Sea. The pipelines passed through fields of large elongated sandy ridges whose positions and shapes appeared to follow repeating patterns or 'harmonic' spatial arrangements.

1.2.1 Initial Development of Sandbanks by Linear Instability

Huthnance (1980) first described the initial growth and subsequent persistence of these features using a technique called 'linear stability analysis'. The approach used an idealised representation of the sea-bed to provide basic insight to the processes which initiate sandbank growth and migration rates. It is based on considering the following components:

i) hydrodynamics of the flow in the presence of the emerging bank;

ii) sediment transport related to the flow;

iii) evolution of the seabed where sediment transport converges.

These three components are interlinked, such that the flow produces sediment transport and seabed changes, which in turn alter the flow velocity. This feedback mechanism suggests the system has an instability.

Trowbridge (1995) used a similar concept to predict the development of repeating shore-face connected ridges on storm-dominated shelves. The approach has since been applied to a number of other storm dominated continental shelf regions (see Falques, 1998, Deigaard et al, 1999) in which wave and wind-driven currents provide morphological instabilities that trigger growth.

The insight provided by stability analysis has helped to distinguish between internally induced coastal behaviour and coastal adaptation to external change (Dronkers, 2005). An integral component of stability analysis is the highly idealised representation of the real coastal system which helps to isolate clear cause-effect relationships and provides transferable analogies for similar coastlines. For isolated sandbank features that are not repeating, such as those found around coastal headlands, stability analysis is not applicable. More qualitative approaches have been used to explain their initiation and growth. The concept of using an 'idealised' approach to understand the growth of headland sandbanks is highly desirable though, and is pursued further in the present work.

1.2.2 Process-based Modelling of Sandbank Initiation

Historically, morphological prediction of coastline development has used either *behaviour-oriented* models, governed by relationships that are data driven, or *probability-based* models that use simple descriptions of the physical processes to drive multiple simulations and provide an envelope of 'potential' morphological change (see Southgate, 1995). *Probability-based* models require a large number of long-term simulations to be conducted quickly and, therefore, are typically applied to processes that can be adequately described by simple equations. Examples include the N-line contour model of Perlin and Dean (1983), in which the cross-shore sediment transport that governs the beach shape is based on an equilibrium profile argument and the resulting sediment transport if the profile is out of equilibrium. For sandbank morphodynamics, these types of model are difficult to apply because the processes that

govern the morphodynamics cannot be defined by simplified deterministic equations. *Behaviour-oriented* models are a better alternative because they are based on rules derived from site-specific data. The model does not need to have a relationship with the underlying physical processes as it is phenomenological. For large complex coastal systems such as tidal basins, behaviour-type models have been used to describe the morphological evolution in terms of an equilibrium state (O'Connor et al., 1990). For sandbank morphodynamics, a number of studies have been conducted using empirical orthogonal functions (EOF) which can loosely be classed as a behaviour-oriented approach. Wijnber and Terwindt (1995), as well as Reeve et al (2001) applied EOF to a series of historical bathymetric surveys of nearshore sandbank systems in the eastern Dutch and U.K. coasts, respectively. They were able to identify cyclical trends in the evolution of the sandbanks which could be used to indicate future morphological change. The main drawback of the approach is that the rules are based on historical trends and may not be indicative of future changes.

Physical modelling is another option that is helpful in understanding sandbank growth and maintenance. The process of setting up a physical model involves firstly, scaling down of the prototype (or feature of interest) geometrically by multiplying all the dimensions by a given fraction. The difficult part is determining the real-scale values from the model results due partly to restrictions in the size of the laboratory and partly to *scaling effects*. These occur when some of the forces in the model become exaggerated (or reduced) compared to values in the prototype. For example, in morphodynamics, gravitational effects, which in the real world are an important limiting factor on the vertical height of bed features, may be much less important than the cohesiveness or porosity. To counter scaling effects, it is possible to distort some of the dimensions. For example, including a vertical length scale of 1/10 and a horizontal length scale of 1/100 may ensure that the frictional effects of the bed do not dominate the model flows. In the present study, the spatial scale of the given problem is such that it would require an extremely large laboratory to adequately replicate the physical processes in model form. Some simple experiments involving idealised geometries in a narrow flume are described in Chapter 2, but limitations on resources and associated

scaling effects have led to the majority of this project being conducted using numerical approaches.

In the last decade, the sophistication of hydrodynamic and sediment transport process-based modelling has increased in line with computational power, bringing about the development of morphodynamic modelling.

Process-based modelling systems vary in function and applicability but all share common features. Model input is information that describes the physical system. Model output is future predictions of that same system based on physical laws that are programmed into the model algorithms (see Figure 1.2 below).

Spatial information that describes the physical system is converted or 'schematized' into an 'equivalent physical system'. This involves interpolating bathymetric and topographic information onto a grid. Physical laws that describe fluid or particle motion are then expressed in discrete form (discretization) and solved on the grid using a numerical method. The choice of method is usually dictated by its suitability to a given problem.

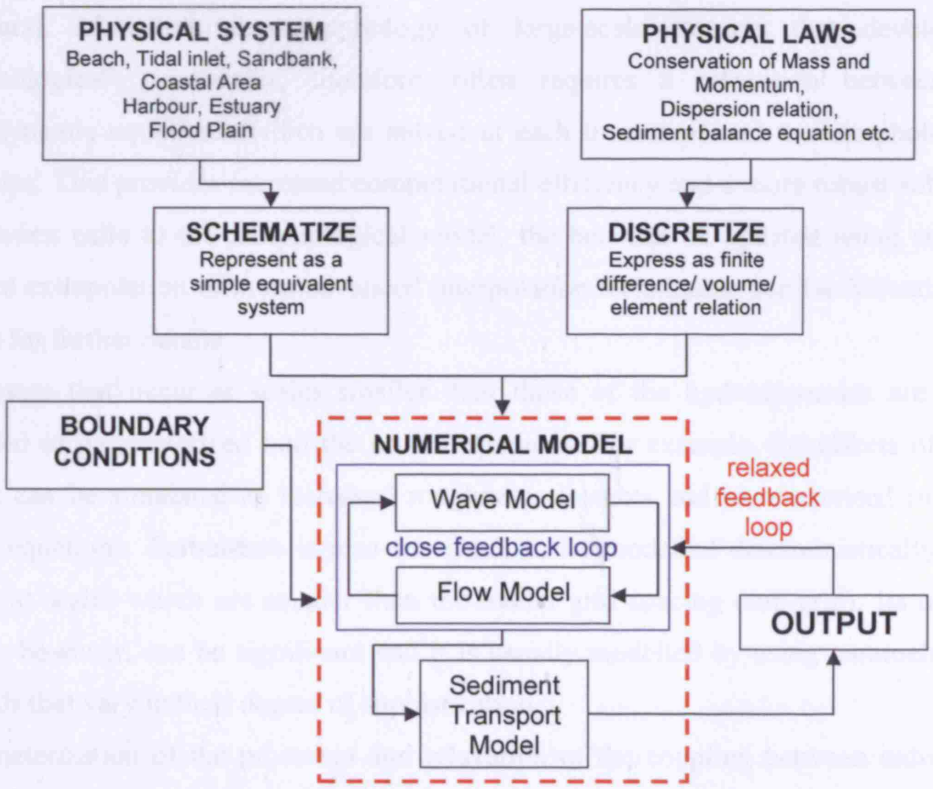

Figure 1.2 Principles of process-based morphodynamic modelling models

There are a number of problems involved in attempting to reproduce nature using a numerical model. These include approximations of the physics of the natural system and approximations involved in converting the continuum equations into a discrete set of equations which can be solved by a computer. For models based on finite differences (*FD*), this conversion involves a Taylor series expansion of all the terms in the partial differential equations. This leads to an infinite number of discrete terms of which the majority are then discarded leaving usually only first and second order approximations to the original set of equations. A low order of accuracy (i.e. first order) introduces numerical diffusion. This has the advantage of damping numerical instabilities but provides only a primitive description of the physics.

A large part of the physical understanding that underpins process-based modelling concerns processes with 'hydrodynamical' time-scales (i.e. hours to days) and which are many orders of magnitude smaller than the morphological scales of interest (i.e. months to years). Modelling the morphology of large-scale features that develop at 'morphological' time-scales, therefore, often requires a relaxation between the hydrodynamic equations (which are solved at each time-step) and the morphological equations. This provides increased computational efficiency and a more robust solution. In between calls to the morphological model, the bed can be updated using straight forward extrapolation or more advanced interpolation techniques. See De Vriend et al. (1993) for further details.

Processes that occur at scales smaller than those of the hydrodynamics are often excluded or parameterized into the model equations. For example, the effects of sand ripples can be simulated as increased roughness elements and parameterised into the model equations. Turbulence is also too small to be modelled deterministically as it occurs at scales which are smaller than the model grid spacing (sub-grid). Its overall impact, however, can be significant and it is usually modelled by using parameterized methods that vary in their degree of sophistication.

Parameterization of the processes and relaxation of the coupling between individual models is based on *a priori* assumptions about the sensitivity of a typical coastal system to processes that occur over a variety of scales. Therefore, they are site specific, which

suggests that a model should be applied always with an appreciation of the likely interaction between the 'reduced' and the 'resolved' processes. The model should thus be compatible with the real physics of the problem but will still need to be calibrated and verified at the site to be studied. If its limitations are appreciated then applying it in a diagnostic sense, in order to assess a given hypothesis, has much more validity. The model can then be regarded as another 'tool' that will help to prove or disprove a theory. Such an approach has been carefully followed throughout the present study.

Process-based models typically consist of a number of separate modules representing tide-, wave- and wind-induced currents as well as wave propagation, sediment transport and morphology. These are coupled together to provide a dynamic link and feedback between the different processes. In coastal engineering, coastal profile (2-DV) and coastal area (2-DH/3D) models are the most commonly employed process-based methods. Coastal profile models describe only the cross shore components of sediment transport, assuming uniformity in the long-shore direction. The models describe surf zone hydrodynamics in some detail, including processes such as undertow and wave asymmetry as well contributions from long-shore wave and tidally induced currents. See Roelvink and Brøker (1993) for an overview. Application of these models to sandbank dynamics is difficult due to the non-uniform nature of the hydrodynamics and sediment transport on and around sandbanks.

2-DH coastal models depend on depth-averaged estimates of current and sediment distributions which are often based on assumptions regarding vertical flow velocity and concentration profiles. This raises doubt about their applicability to modelling processes that include 3-D effects. For the purposes of sandbank modelling, 2-DH models ignore vertical variations in the pressure gradient and thus may be excluding processes that are significant to the maintenance of the features. 3-D coastal area models include vertical variation in the current field and might be more suited to modelling sandbank dynamics. However, a recent study on the morphodynamics of shoreface nourishments in a barred nearshore zone (Grunnet, 2004), demonstrated that for these features, the predictions from a 3-D process-based model were very similar to those of a 2-DH model of the same system. This may have important significance to this study because the spatial extent of nearshore bars is comparable to that of many sandbanks.

However, the processes that dominate the morphodynamics are different: sandbank morphology is driven principally by tidal currents, while bar systems are dominated by surf zone processes that include wave-decay and return flows. The application of both 2-DH and 3-D coastal area models to sandbank dynamics will be tested in this study.

A number of other studies into sandbank dynamics and morphology have included both 2-DH and 3-D coastal models. Most notably the CSTAB project (O'Connor, 1996), used 2-DH and 3-D approaches to determine residual current patterns and sediment transport around large offshore sandbanks in the southern North Sea. Other notable examples include the work of Damgaard and Chesher (1997) which used a coupled hydrodynamic and sediment transport model, including morphological feedback to the flow. These studies demonstrated the advantages of process-based approaches in the prediction of sandbank behaviour. They were able to capture the spatial gradients in the horizontal current fields which dominate the processes of growth and maintenance. These studies also outline some of the limits of the approach, the latter study citing numerical problems with the bed updating scheme which, over longer timescales, led to unrealistic predictions (see Damgaard and Chesher, 1997, for further details).

The application of coastal process-based models over longer time-scales (years to decades) is also questionable for other reasons. The neglect of sub-grid processes, (including bed ripple effects) and the parameterisation of others (including turbulence) may lead to significant error accumulation. The residual effect of these processes have potentially important contributions to the sandbank evolution. The omission of long term trends in the forcing conditions and also the stochastic nature of storms, suggests that the final deterministic prediction will only provide one solution to what could be a whole array of potential outcomes. These limitations, however, should not discount the potential usefulness of process-based modelling in understanding sandbank morphodynamics. Providing the limitations and basic assumptions of the underlying model equations are understood and a thorough calibration and validation exercise has been performed, the models can provide useful insights into the underlying physical processes from which the longer-term morphodynamic processes can be inferred. In

addition, these models can also be applied in diagnostic mode, to isolate and evaluate the impact of different sets of processes and mechanisms (Grunnet, 2004).

Further motivation for using process-based modelling in this study is that one of the original aims of the project was to investigate the applicability of these types of tool to the simulation of sandbank dynamics. Through industrial contacts the study was given access to the commercial coastal modelling package Delft-3D. At the time of the study, however, the version of the model available did not include the coupled effects of waves and tidal currents. For the simulations requiring wave and current induced processes, the study made use of another modelling system, DHI's MIKE-21/3 FM.

1.3 Headland Sandbank Initiation and Growth

Sandbank formation is initiated in areas where there is both a zone of sediment convergence and a plentiful supply of material (Dyer and Huntley, 1999). Isolated sandbank features occur commonly around coastlines in which an acute change of direction occurs or where a headland feature is present. They are, therefore, often described as 'headland-associated' or 'banner-type' banks (see Dyer and Huntley, 1999) and can form on one or both sides of a coastal headland in water depths of between 10 and 30 metres. Some headland banks present significant hazards to shipping and exposure of the bank crest at low water is not uncommon.

Pingree (1978) suggested a link between headland sandbanks and the tidal eddies that form in their wakes. He suggested that residual tidal eddies are responsible for 'tidal stirring' (see Figure 1.3), a phenomenon which produces strongly convergent flow near the bed and gives rise to local centres of sediment deposition and sandbank development. Pingree & Maddock, (1979), further speculated that the Coriolis force acts either to augment or to reduce the 'tidal stirring' effect and hence explains the disparity between sandbank sizes around headlands (in particular the banks either side of Portland Bill, U.K.).

Bastos et al. (2003) suggested that the Portland Bill sandbanks are not sustained by tidal eddies but by the frictional torque that they introduce to the tidal flow. This supported the modelling of Signell and Harris (2000) which predicted eddy positions that were not commensurate with sand bank growth around either side of an idealised

coastal headland. The work did not, though, rule out the action of the Coriolis force on sandbanks of this scale. This is taken up as part of the present work.

Headlands are unusual coastal features in the sense that tidal currents actually increase as the flow moves towards the headland due to continuity effects, despite increasing shallowness and bed friction (see Robinson, 1983). Vorticity is produced in the region close to the headland, referred to as the 'headland boundary layer' (see Signell and Geyer, 1991 and Duffy, 2006). The vorticity is generated by frictional and topographical effects as well as by the spatial gradient in the current velocity from the headland obstruction. The resulting band of vorticity may be advected downstream (flow and length scales permitting, see Duffy, 2006) and flow separation and eddy formation in the downstream wake may then occur. Headland dynamics are, therefore, controlled by the strength of the local current field relative to the seabed topography and curvature of the headland and this has important implications for sediment transport and bank building. The effects of seabed slope and headland geometry are also investigated in the present work.

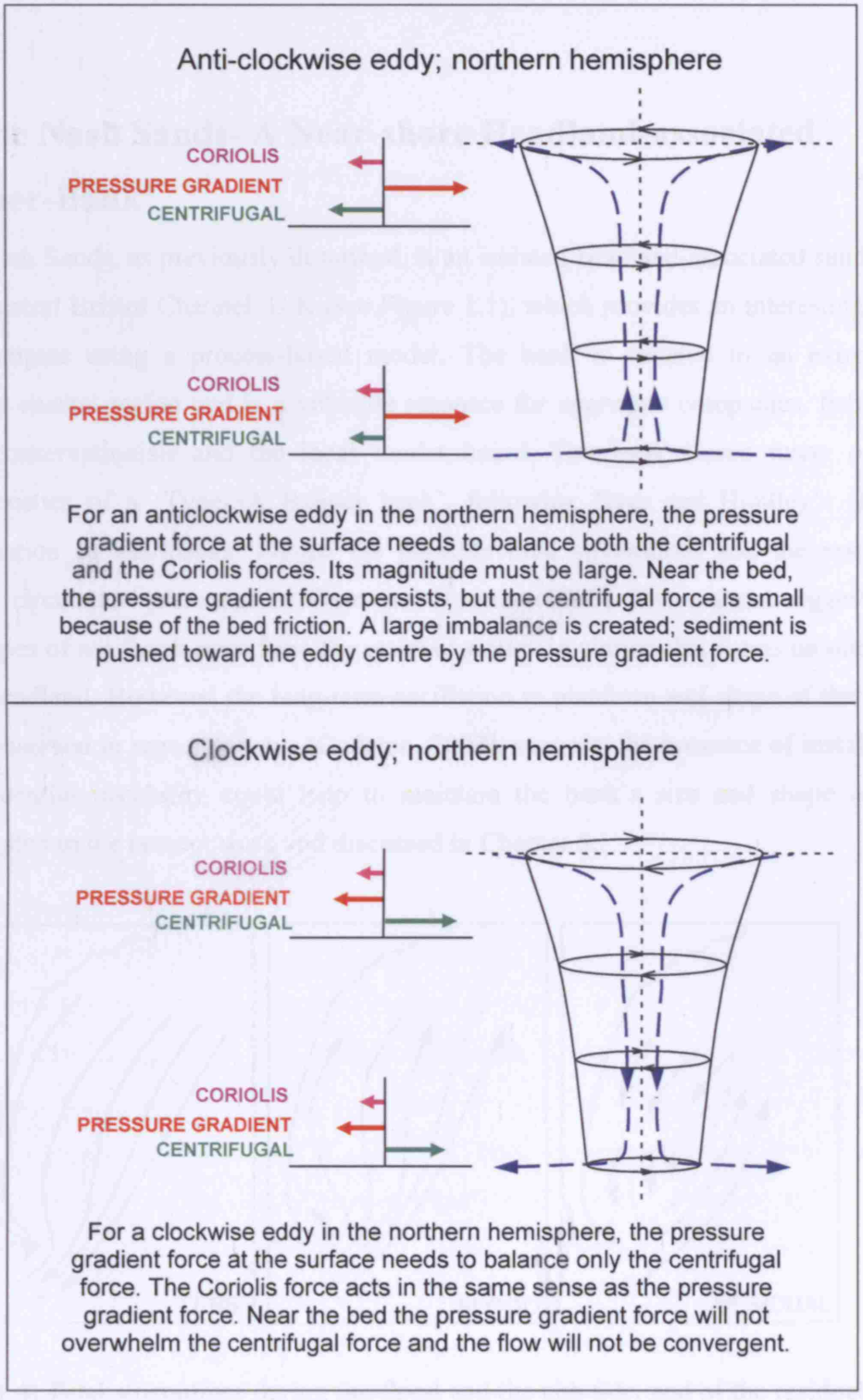

Figure 1.3 The 'tidal stirring' mechanism as suggested by Pingree (1978).

1.4 The Nash Sands- A Near-shore Headland-associated 'Banner-Bank'

The Nash Sands, as previously described, is an isolated headland-associated sandbank in the central Bristol Channel, U.K (see Figure 1.1). which provides an interesting case to investigate using a process-based model. The bank is situated in an extremely complex coastal region and is a valuable resource for aggregate companies, fisheries, beach conservationists and the local tourist board. The bank shows many of the characteristics of a 'Type-3A Banner bank', following Dyer and Huntley's (1999) classification of sandbanks. Figure 1.4 presents tidal streamlines and the resulting residual circulation presented by Dyer and Huntley (1999). The authors suggest that these types of sandbank arise from the residual water circulation that forms on one side of the headland. However, the long-term oscillation in planform and shape of the Nash Sands observed in repeat surveys (Cudemo, 2003), suggests the presence of instability. This potential instability could help to maintain the bank's size and shape and is investigated in the present work and discussed in Chapter 5.

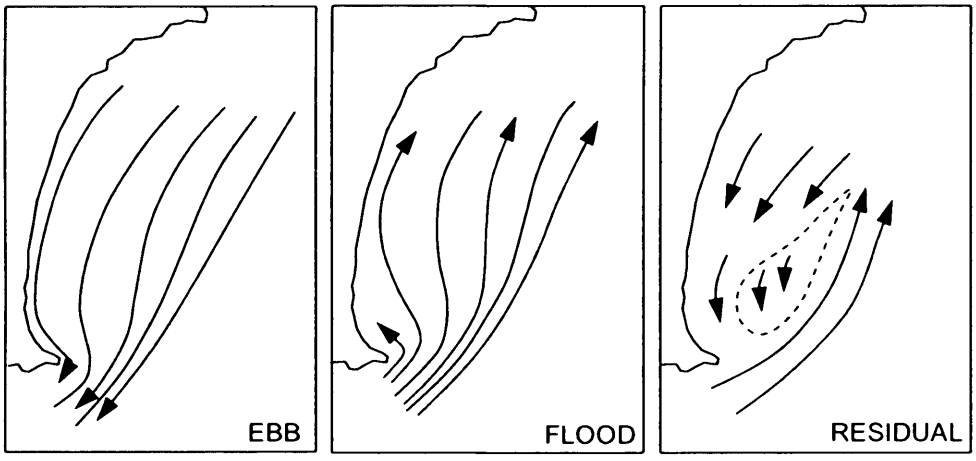

Figure 1.4. Tidal streamlines during the flood and the ebb tide, and of the residual around a type 3A 'banner bank'. Redrawn from Dyer and Huntley (1999). Sandbank position is indicated by the dashed line.

One important question, related to the bank's sustainability in its present environment, is that of whether the bank forms part of an 'open' or 'closed' system (see Thompson et al., 2003). A 'closed' system implies that there is no exchange of sediment between the sandbank and the surrounding seabed and foreshore. For an 'open' system to exist, however, the bank needs to have a link with larger, regional sediment transport pathways.

Interpretations of the bank as being either 'open' or 'closed' have important repercussions both on the sustainability of the bank as an aggregate deposit and that of the surrounding beach levels. It has been argued that the bank is part of a 'closed' system in which wave action disperses sediment from the bank crest and tidal action builds it back up again (Evans, 2006). This concept is based on calculations of volume change over the past decade, which show a gradual decline in the bank's overall volume in line with the total volume of material dredged. Further, the regional tidal transport is strongly ebb-dominated suggesting that the sand rich sediments on the bank can not be easily replenished by tidal action because of a lack of non-cohesive sediment upstream.

If present wisdom accepts that local tidal currents are capable of accumulating sediment dispersed by wave action, then it follows that the bank has a predisposition to collect sediment and, hence, *must* interact with the surrounding seabed sediments. It cannot, therefore, be a purely 'closed' or relict feature.

It has also been suggested by a number of authors, including Collins & Ferentinos, (1989) and McClaren et al., (1993), that despite the ebb-dominance of the regional tidal currents, a mechanism exists that is capable of bringing marine-derived sediment into the coastal fringes of the central Bristol Channel. The basis of this hypothesis was inferred from observational data, which lacked both temporal and spatial detail. Demonstrating the presence of such a mechanism is crucial in this study: the estuary is ebb dominated and the upper estuary is mostly devoid of the sandy material found on the bank deposit. If the potential for accumulating sandy material on the bank does exist, it follows that a sufficient source of marine-derived sediment is required. This study employs a process-based modelling approach to demonstrate the dominant mechanism.

The dynamics of the Nash Sands are studied using a refined model of the local area. Model output is compared with geological, sedimentological and bed-form interpretations of the sandbank and the surrounding seabed. The influence of 'headland-associated' sandbank building processes are considered by studying, first, the possible bank initiation by sediment convergence around the headland and, second, the potential for the feature to grow by the action of tidal eddies and secondary circulations. The frictional effects of the sandbank on the tidal currents are also investigated to help identify the presence of a hydrodynamic mechanism for maintaining the shape and volume of the sandbank.

1.5 Research Objectives and Thesis Outline

The principal aim of this thesis is to improve the understanding of near-shore headland-associated sandbanks. As has been mentioned previously, the motivation comes from a need to understand the processes on a 'banner' bank in the Bristol Channel, U.K. To achieve the central aim, the following research objectives and questions have been formulated:

Objective 1. *Identify the principal factors that control the initiation of near-shore sandbanks around coastal headlands.*

- How do headland associated tidal eddies affect sandbank initiation and growth?
- Does the Coriolis effect contribute to headland sandbank growth?
- How does the headland geometry and the surrounding slope of the seabed affect sandbank initiation?

Objective 2. *Establish an optimized process-based model capable of simulating both headland-associated processes and the regional-scale sediment transport processes that could contribute to the initiation and growth of a near-shore headland sandbank in the Bristol Channel, U.K.*

- What is the ideal size and resolution of the model grid required to represent the important regional and local-scale processes that control headland dynamics and sandbank growth?

- Which 'model reduction' methods are most suitable and how can these be optimized in the present case study?

Objective 3. *Investigate regional sediment transport processes in the central Bristol Channel in order to determine potential bank re-nourishment and maintenance pathways in the present-day hydrodynamic climate.*

- Does a potential mechanism exist whereby sediment can be transported in an up-estuary direction in the coastal fringes of the Bristol Channel and hence nourish the Nash Sands and other large foreshore and bank deposits of sandy material?
- If a mechanism does exist, is it possible to describe its exact nature and give an estimate of the likely sediment transport that can be imported over a given time period?

Objective 4. *Investigate the mechanisms that control the Nash Sands, a headland associated 'banner-type' bank in the central Bristol Channel*

- Was the initial growth of the bank controlled by headland-associated processes or is it a purely relict feature?
- Are secondary currents significant in the initiation and maintenance of the sand bank?
- Does the bank generate its own self-supporting hydrodynamic mechanism, manifested in the residual tidal current field around the headland?
- Do significant transport pathways exist between the sandbank and other large sand-rich deposits in the local area?

The outline of the thesis reflects the four main objectives formulated here: **Chapter 2** includes the idealised modelling aimed at demonstrating the sensitivity of headland associated sandbank building to various parameters. In the first experiments, an idealised Gaussian-shaped headland is used to assess sensitivity to tidal eddies, Coriolis force and the surrounding seabed slope. A second half-Gaussian headland shape is then modelled, the shape of which has some similarity to the promontory close to the Nash Sands. Sediment convergence under varying forcing conditions is simulated in order to

identify the potential for bank building in the real system. **Chapter 3** focuses on experiments that were conducted to establish an optimised model that could resolve both regional and local-scale wave-current and sediment transport processes in an efficient way. The regional sediment transport in the central Bristol Channel and sediment supply to the sandbank is investigated in **Chapter 4**. The work explores both current- and wave-driven processes in order to prove the validity of the proposed mechanism of sediment importation and hence the potential to 'feed' the bank and surrounding area with marine derived material. **Chapter 5** investigates the likelihood that the sandbank was initiated and grew in response to headland processes (investigated in Chapter 2) and instability mechanisms, respectively. A number of approaches are taken in order to achieve this, including 2-D modelling experiments with the bank removed from the model bathymetry and 3-D modelling to provide comparisons of surface and near-bed current fields. The results, in the form of sediment transport pathways, are then compared with those inferred from sedimentological and bedform data. **Chapter 6** summarises the results and discusses the main conclusions.

2. Modelling Sandbank Growth Around Headlands

2.1 Introduction

The following chapter describes an idealized numerical modelling study that has been carried out to investigate the initiation and growth of sandbanks close to coastal headlands. Two types of headland shapes have been investigated including a Gaussian headland, comparable to Portland Bill, Dorset, U.K. and a semi-Gaussian headland, more comparable with Nash Point, Bristol Channel, U.K. These ideas are then further developed in later chapters to help improve understanding of the formation and maintenance of the Nash Sands, a banner-type bank that exists to the west of Nash Point.

2.1.1 Headland Dynamics

Coastal headlands have important impacts on shore-parallel tidal currents. They induce flow accelerations that affect the vertical structure of the water column and have significant impacts on the distribution of sediments. The adjacent seabed, therefore, is often characterized by an area of enhanced scour close to the headland and significant zones of deposition further away. These areas of sediment accretion often grow into more permanent sandbank features. Such phenomena account for a significant proportion of near-shore sandbanks found in the U.K. This chapter investigates the physics behind the formation and growth of these features.

Previous studies of headland sandbanks have related secondary hydrodynamic mechanisms to the initiation and growth of these phenomena. Pingree (1978) proposed that the Coriolis effect has an impact on flow convergence at the centre of residual tidal eddies which affects sediment accretion. This was further developed by Pingree & Maddock (1979) who attributed the asymmetry between sandbanks found at either side of Portland Bill, U.K to Coriolis acceleration either enhancing or reducing flow convergence at the bottom of tidal eddies (see Figure 1.3).

Park & Wang (1991) analyzed the influence of the Coriolis effect on topographic vorticity production around headlands. They showed that around one side of a headland, topographic vorticity is reduced by the Coriolis effect. This, they suggested, alters the vorticity balance and affects flow convergence and, hence, sediment accretion.

Other authors including Kalkwijk & Booij (1991) and Alaee et al., (2004) have proposed that secondary flow and up-welling can occur in the absence of flow separation and circulatory headland flows. They showed that in a flow deflected and accelerated abnormally by a topographic obstruction, up-welling and transverse flow occurs at a variety of spatial scales. The Coriolis effect was shown to significantly alter the magnitude of these secondary flows.

Signell and Harris (1999) used an idealised model of a coastal headland to investigate the 'tidal stirring' mechanism proposed by Pingree (1978) and its effect on sandbank building. They used coastline geometry and tidal forcing comparable to that found at coastal headlands where sandbanks are known to occur. They demonstrated that the positions of sandbank formation and growth were unrelated to the position of tidally averaged eddies, a finding that conflicted with the tidal stirring hypothesis of Pingree (1978). The idealised model also predicted symmetrical deposits of sediment either side of the coastal headland, questioning the role of the Coriolis effect on sandbank growth at this scale.

In the following work, a similar methodology is adopted with the aim of, first, repeating, and then expanding the work of Signell and Harris (1999) using a more sophisticated process-based model. In addition to comparing the tidally averaged eddies with sediment accumulation, much effort is dedicated to the analysis of transient eddies and how these effect headland sandbank building. The work also inspects more closely the secondary currents produced throughout the tidal cycle with the aim of detecting upwelling currents- another symptom of tidal stirring. The impact of the Coriolis effect is also revisited using techniques that compare the vorticity balance around the headland at different stages of morphological development.

Coastal headlands are typically surrounded by a sloping seabed of varying gradient. This may have important impacts on the distribution of sediment and is investigated in the following work.

The headland shape is also important in determining the distribution of sediments and this is investigated using a second type of headland, a half-Gaussian shape. The shape is comparable to the coastal geometry of a number of headland sandbanks, including the Nash Sands.

2.2 Experimental Approach

The coupled hydrodynamic/morphological package *Delft-3D* was used for the numerical experiments (see Appendix 2, for full details of the underlying model physics and rationale). The model provides a dynamic feedback between the flow and the bed changes and uses a sigma layer approach to discretize the vertical domain (see Figure 2.1) where

$$\sigma = \frac{z-\zeta}{D+\zeta} = \frac{z-\zeta}{H} \tag{2.1}$$

z is the vertical co-ordinate in physical space, ζ is the free surface elevation above the reference plane (at $z=0$), d is the water depth above the reference plane and H is the total water depth ($H = D+\zeta$). At the bottom $\sigma = -1$ and at the free surface $\sigma = 0$. This system ensures that the vertical co-ordinates are always fitted to the bottom and the free surface boundaries. Partial derivatives in the original Cartesian co-ordinate system are expressed in σ co-ordinates by the chain rule, introducing additional terms in the equations of motion.

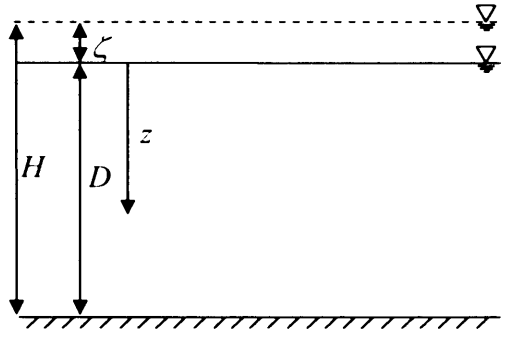

Figure 2.1. Parameters used in the transformation from fixed Cartesian co-ordinates to boundary adjusting σ co-ordinates.

The modelling experiments used two types of idealised headland shapes. The first was a 'Gaussian-shaped' headland which intruded northward into an oscillatory tidal flow moving parallel to an East-West oriented coast (see Figure 2.2 (a)). The headland geometry was defined using the following equation

$$y = \frac{M}{A}\sqrt{4\pi\Gamma}e^{-x^2/4\Gamma} \qquad (2.2)$$

where x and y define the co-ordinates of the coastline, $M = 2000$, $\Gamma = 5\times10^6$ and $A = 0.00012$. This geometrical arrangement has been used for the majority of the tests. The second experiment, aimed at testing the effect of headland geometry on sandbank growth, used a 'half-Gaussian' shaped headland consisting of a constricted upper channel with a wider downstream channel (see Figure 2.2 (b)). Both headland shapes were surrounded by a shallow coastal sea of uniform depth (20 m). Open boundaries to the east and west of the headland were both driven by a tidal range of 1 m. The two driving boundaries were offset by an appropriate phase difference to give a near-headland velocity maximum of approximately 1 ms^{-1}. The land boundaries were defined as 'non-slip' as the offshore boundaries were considered as being far enough away to preclude any frictional influence on the flow. This is justified given the large scale of the simulation. The sediment type used in the models was non-cohesive sand of mean diameter 0.27 mm. This is comparable to the size of sediment found on headland type banks in the U.K., including the Nash Sands. The sediment was uniformly distributed across the model domain and had an infinite thickness (see Table 2.1 for details of the model setup).

The curvilinear model grid was optimised for efficiency. This included high resolution around the headland (where the eddies form) and gradually reducing in resolution moving towards the model boundaries. A number of grid sizes were tested to ensure that a sufficient number of grid points were provided to resolve the tidal eddies. Based on previous literature (including that of Signell and Harris, 1999), the diameter of the eddies was expected to be a minimum of 5 km. A model of resolution of 300 m would thus provide at least 15 grid points to resolve the eddy. The sensitivity tests

demonstrated that the eddy was indeed captured at 300 m grid resolution. However, in addition to capturing the eddies, another aim of the study was to resolve the more localised bed changes around the headland. For this reason a model grid of 150 m spacing was tested. This high resolution grid captured more details of the near-headland dynamics. Further sensitivity tests using grids of 100 m and 50 m spacing made only minor changes to the morphological predictions. Their use was not justified given the extra computational expense.

Other authors including Huthnance (1982), Idier and Astruc (2003) have reproduced sandbank generation using 2-D models. In this study, preliminary modelling experiments showed that generation of sandbanks was indeed possible with a 2-D model. However, these results differed noticeably from those predicted by the 3-D model. The difference increased with the prescription of additional vertical layers and appeared to reach an asymptote in tests using 13 and 14 sigma layers (Figure 2.3). Based on the assumption that more resolution in the vertical provided a better description of the hydrodynamics, it was concluded that a 3-D model gave a more accurate description of the bed changes and was, therefore, used in the ensuing experiments.

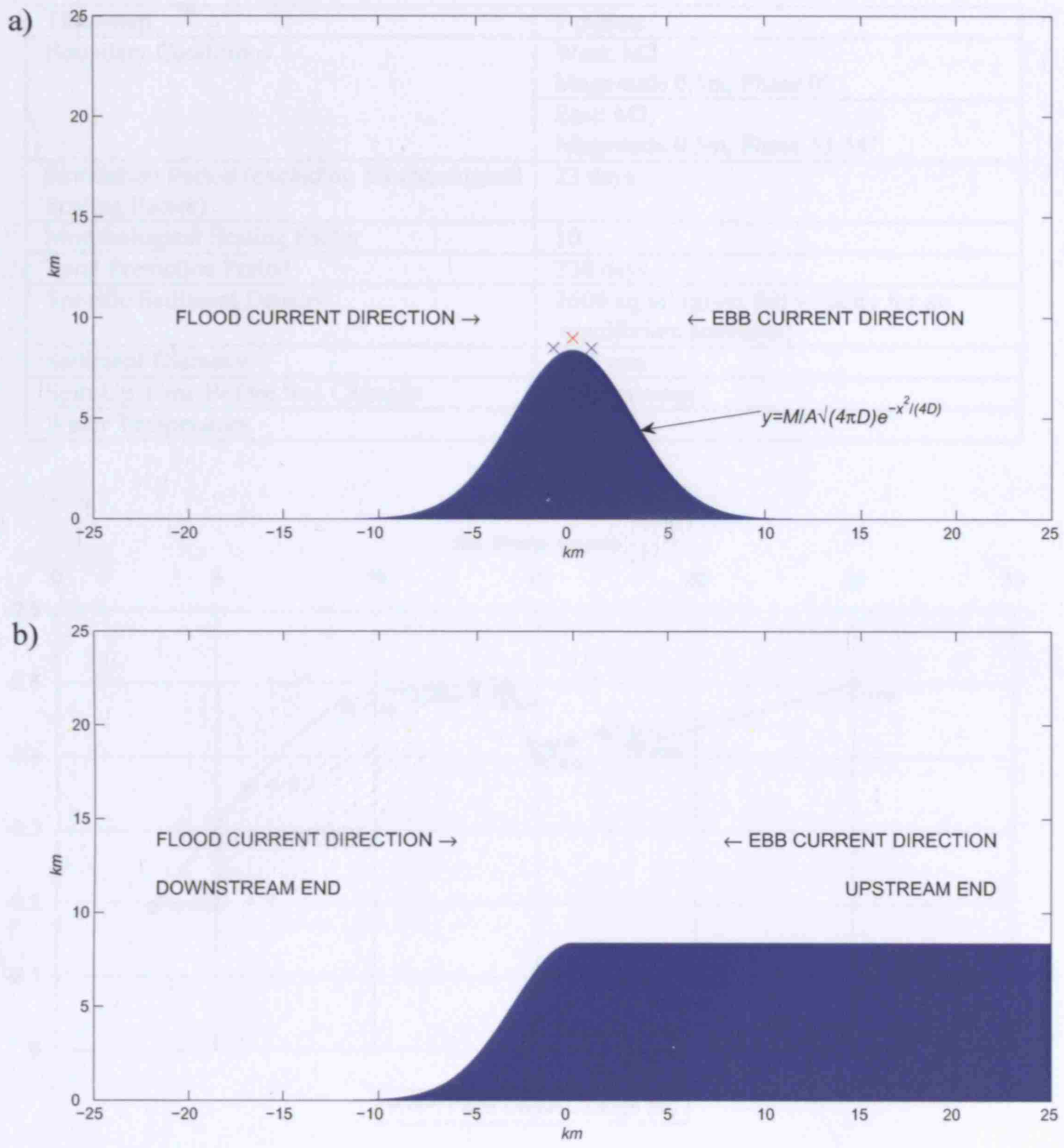

Figure 2.2. (a) Gaussian model domain. The red cross marks the position from which the bed changes in Tables 2.2 and 2.3 are extracted. The blue crosses mark the eastern and western positions from which the maximum and minimum vorticity is extracted in Section 2.4 and 2.5. (b) semi-Gaussian model domain.

Table 2.1. Critical modelling parameters.

Time-step	1 minute
Boundary Conditions	West: M2, Magnitude 0.5m, Phase 0°
	East: M2, Magnitude 0.5m, Phase 33.54°
Simulation Period (excluding Morphological Scaling Factor)	23 days
Morphological Scaling Factor	10
Total Prediction Period	230 days
Specific Sediment Density	2600 kg/m^3 (gives fall velocity for an equilibrium sediment)
Sediment Diameter	0.27 mm
Spin-Up Time Before Bed Changes	2880 minutes
Water Temperature	10 °C

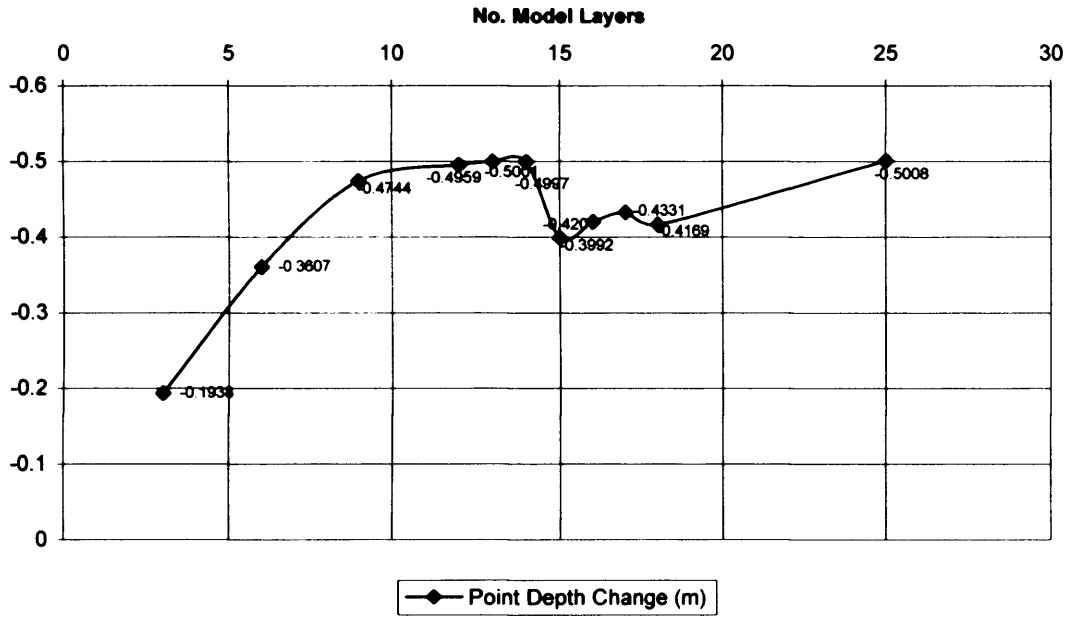

Figure 2.3. Bed changes near the headland tip from predictions with logarithmically derived vertical layer distributions.

The number of layers prescribed in a hydrodynamic model controls the three-dimensionality. Increasing the number of layers increases the vertical resolution, providing a more accurate model prediction over the water column. However, this improved accuracy is at the expense of an increase in model run-time. Increasing the number of layers, from 1 to 3 for example, increases the run time by approximately 50

percent. One aim of this study was to find a compromise between resolution and efficiency. As well as altering the number of layers in a model, it is also possible to change the vertical distribution of the model layers. The *Delft-3D* model uses sediment transport vectors from the near-bed layer to compute rates of bed evolution via the Sediment Balance Equation (Exner Equation).

$$-(1-n)\frac{\partial z}{\partial t} = \frac{\partial Q_x}{\partial x} + \frac{\partial Q_y}{\partial y} \qquad (2.3)$$

where z is the bed level, n is the porosity of the bed and Q_x and Q_y are the x- and y-components of sediment transport in the near-bed layer.

Therefore it is sensible to increase the resolution of the model (increase the number of layers) near the bed. Sensible scaling of this vertical distribution of model layers thus helps to increase the efficacy of the model.

Using the idealised Gaussian-shaped case study, twelve initial model runs were conducted using different numbers of log-distributed layers (Table 2.2). The sediment transport and morphological change predicted by all of these models was extracted from the model results. The model was 'spun up' (i.e. the flow module was run independently from the morphological model) over a period of four days. This removed the effects of early hydrodynamic instabilities on the predicted morphology. The model runs gave predictions over a 230-day period.

Table 2.2. Tests to obtain optimum model set-up.

MODEL RUN	Number of Layers	Distribution (LOG = Logarithmic)	Depth Change Near Headland Tip (m)
1	3	LOG	-0.1938
2	6	LOG	-0.3607
3	9	LOG	-0.4744
4	12	LOG	-0.4959
5	13	LOG	-0.5001
6	14	LOG	-0.4997
7	15	LOG	-0.3992
8	16	LOG	-0.4207
9	17	LOG	-0.4331
10	18	LOG	-0.4169
12	25	LOG	-0.5008

The largest gradients in the vertical velocity profile occur near the bed. For this reason all model tests used layers that decreased in thickness toward the bed, ensuring that the model resolution also increased in this region. The tests incorporated layers distributed according to a logarithmic profile and showed significant differences in the morphological change predicted. To quantify the depth changes predicted by the various model set-ups, a location was selected close to the headland from which predicted bed changes were extracted from the 12 model runs. This position marks an area in which the largest depth variations were found for all model test runs. The point depth changes are plotted in Figure 2.3.

Large differences in predicted bed changes were found between the 3- and 6-layer models (see Figure 2.3). The differences were less between 6- and 9-layer models and reduced again between 9- and 12-layer models. With 13 and 14 layers, only minor improvements were noted. This suggests that at 14 layers, an optimum number of layers has been achieved where resolution is not improved by the inclusion of extra layers. However, results from the 15 layer, showed a significant difference between the bed changes predicted by a 14-layer and a 15-layer model.

The possible implications of this are that either the 15-layer model is providing a more reliable prediction or, given the sudden jump in predicted changes from 14 to 15 layers, the lowest layer of the model is too close to the bed, causing a breakdown in some of the governing assumptions in the model.

The sediment transport model computes the transfer of sediment between the bed and the flow using source and sink terms in the 'reference cell'. The 'reference cell' refers to the lowest layer above Van Rijn's Reference Height (henceforth VRRH). (See Figure 2.4 and Appendix 2).

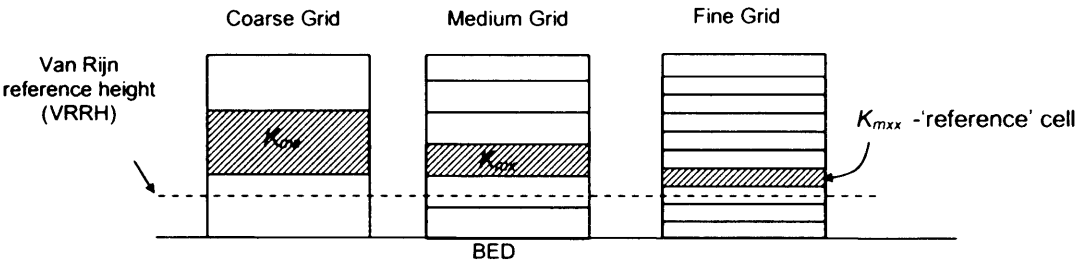

Figure 2.4. Positions of the 'reference' cell- K_{mx}, (for a model with uniform grid spacing in the vertical) from which source and sink terms are computed.

Below the VRRH all sediment is assumed to behave as bed-load and, therefore, is subject to the effects of bed slope and computed using van Rijn's bed-load transport formula. The purpose of the 'reference cell' is to provide an intermediate zone that behaves as both a source and a sink cell for bed-load and suspended load computations. By ensuring that the 'reference cell' is always the layer immediately above the near-bed layer, transfer of computational material from the reference cell into the near-bed layer will be instantaneous. In the 15-layer model, an extra layer existed between the near-bed layer and the 'reference cell' (as seen in the 'Medium' grid in Figure 2.4), a lag between the material being passed from the reference cell and into the bed-load computations was created producing spurious results, as shown in Figure 2.3.

Upon switching from a 14 to a 15-layer model set-up, the 'reference cell' switches from one layer to another and, therefore, so does the layer used for the source and sink terms. This is the probable cause of the broken trend seen in Figure 2.3. The position of the VRRH relative to the model layers is included in Figure 2.5. The VRRH in the 14-layer model falls within the near-bed layer and, therefore, the layer directly above it is used as the 'reference cell' in which source and sink terms are calculated. In the 15-layer model however, the VRRH is in the second layer from the bed and, therefore, the

third layer from the bed is used as the 'reference cell'. It is this abrupt change and jump in 'reference cell' position that is the cause of the significant changes predicted by the two models.[1] These results support the use of a 14-layer model. The VRRH is in the near-bed layer and the predicted bed changes between consecutive predictions (i.e. 13 layers and 14 layers) appear to have reached an asymptote.

However, a 14 layer model is computationally expensive: the increase in run-time between a 12 and a 15-layer model can be as much as 40%. In response to this, two model runs were set up with the aim of reducing the computational time while still maintaining the predictive validity. This required selecting a lower number of model layers that still captured the resolution in the lower portion of the water column without including a model layer lower than the VRRH.

Two models were constructed, a 9- and a 12-layer model with vertical layers distributed according to a power distribution, in which the distance between vertical layers was proportional to the layer number to the power of 2/3 (layer 1 corresponding to the near-bed layer). The predicted depth changes at the headland tip as well as the maximum and minimum depth changes are presented in Table 2.3.

Table 2.3. Predicted depth changes from three model runs.

MODEL TEST	Number of Layers	Distribution	Depth Change Near Headland Tip (m)	Min Depth Changes (m)	Max Depth Changes (m)
13	9	POWER	-0.4967	-0.5001	1.1552
14	12	POWER	-0.4911	-0.4943	1.3399
6	14	LOG	-0.4997	-0.5014	1.0054

Table 2.3 reveals that results from a 9 and 12-layer POWER distributed profile produce bed change predictions comparable to the more computationally expensive 14-layer LOG distributed model. This justifies the use of a 9-layer POWER distributed layer profile for the remainder of this study. The bed change predictions have been extracted from a location in the model bathymetry which is the most dynamic. Therefore, if the 9-layer model is suitable in this location (i.e. the VRRH remains in the

[1] The results of these experiments were passed on to Delft Hydraulics and form the basis of a warning note in the *Delft-3D* User Manual.

near-bed layer throughout the duration of the simulation) then it is assumed that it will also be suitable over the remainder of the model bathymetry where the depth changes are much less.

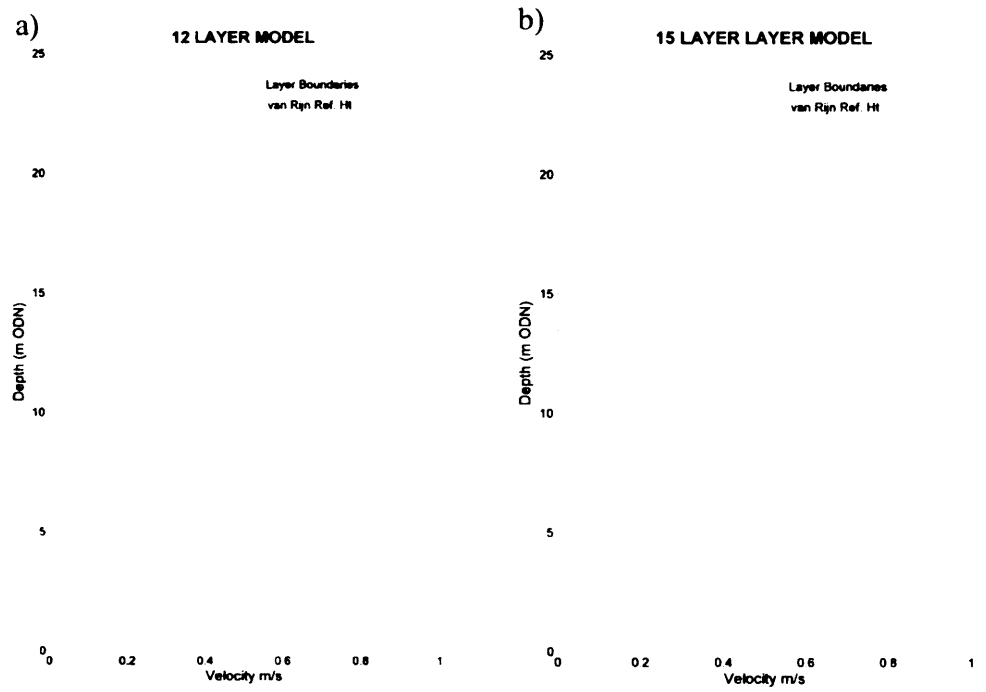

Figure 2.5. Vertical layer distributions and velocity profiles from near the headland tip during peak tidal velocity for: a) 12- layer and; b) 15- layer log distributed vertical grids. In the 12-layer model, VRRH is in the near bed layer, while in the 15 layer model it is in the second layer from the bed.

2.3 Investigating Secondary Headland Dynamics

2.3.1 Tidal Stirring

The 'tidal stirring' mechanism rests on the assumption that residual eddies produce the sandbanks found close to many coastal promontories (Pingree and Maddock, 1979). Using the results from the Gaussian-shaped 9-layer 'power profile' models, values of residual velocity were calculated to test the validity of this proposed mechanism. Figure 2.6 (a) and 2.6 (b) show the predicted positions of residual current velocity gyres and

sediment accretion, respectively. It can be seen that the positions of the residual near-bed velocity gyres do not coincide with the positions of the offshore sandbanks.

Values of instantaneous velocity were also extracted from the Gaussian 9-layer power-profile model results during key parts of the tidal cycle, in order to test the relationship between instantaneous tidal gyres and offshore sediment accretion. These are presented as vector arrows superimposed on the locations of sediment accretion centres (Figure 2.7).

Figure 2.7 demonstrates that in addition to being completely detached from residual tidal gyre location, the sandbank-building mechanism has little association with transient (instantaneous) tidal gyres. Further, the transient tidal gyres only develop significant size during the latter parts of the flood and ebb periods where values of instantaneous velocity are too low to have an important impact on sediment transport. The majority of sediment transport occurs during peak flood and ebb velocity (Figures 2.7 (a), 2.7 (b)). Further inspection of the peak velocity vectors reveals that the positions of the offshore accretion zones to the west and east of the headland coincide exactly with the point at which the peak velocity vectors begin to reduce in intensity (Figure 2.7). The model predicits that for this type of sediment the deposits form as a result of gradients in the instantaneous velocity fields as opposed to the centres of tidal eddies, supporting the findings of Signell and Harris (1999).

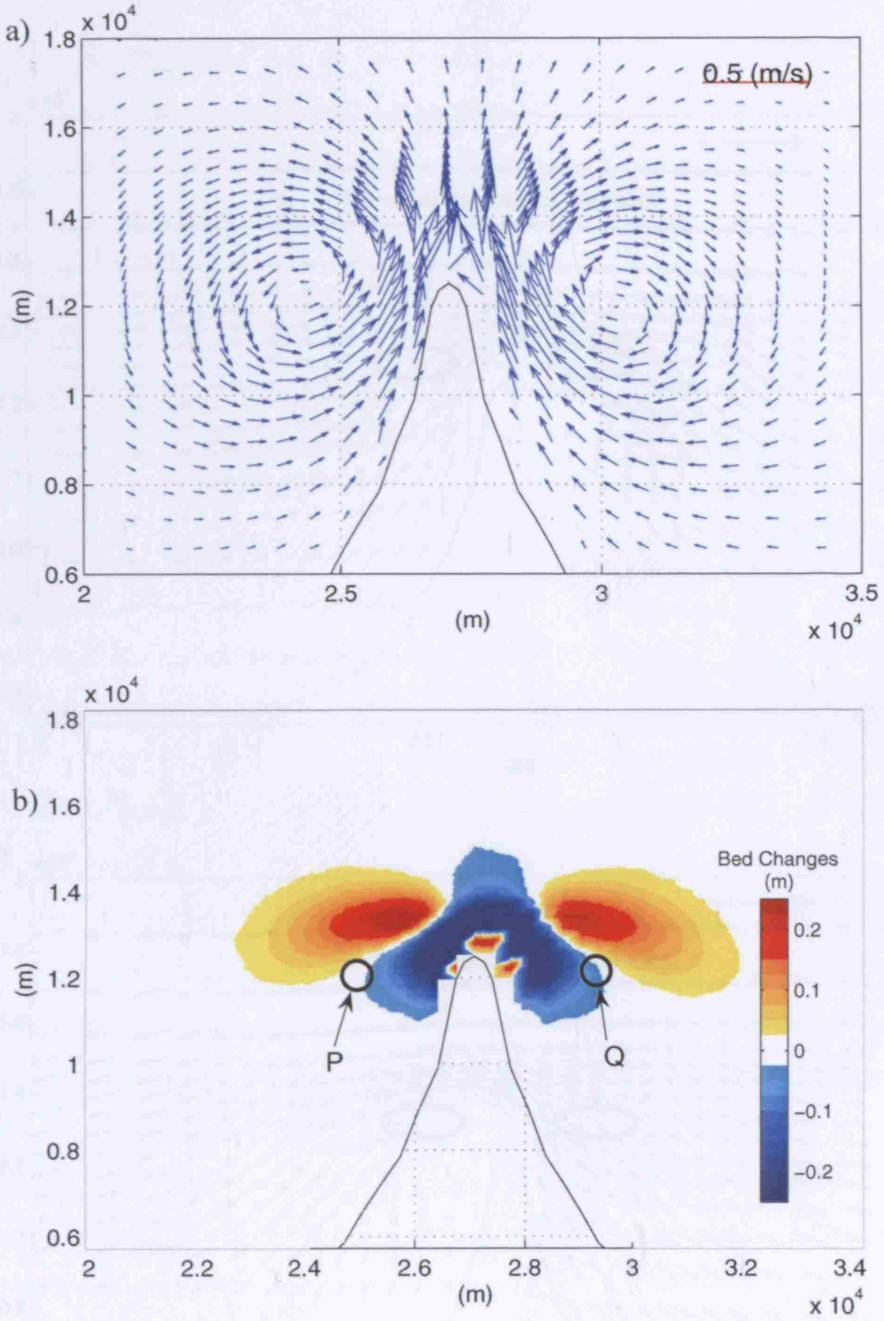

Figure 2.6. a) Residual near-bed velocity vectors; b) morphological change with position of residual gyre centres P and Q, superimposed. Idealised Gaussian headland.

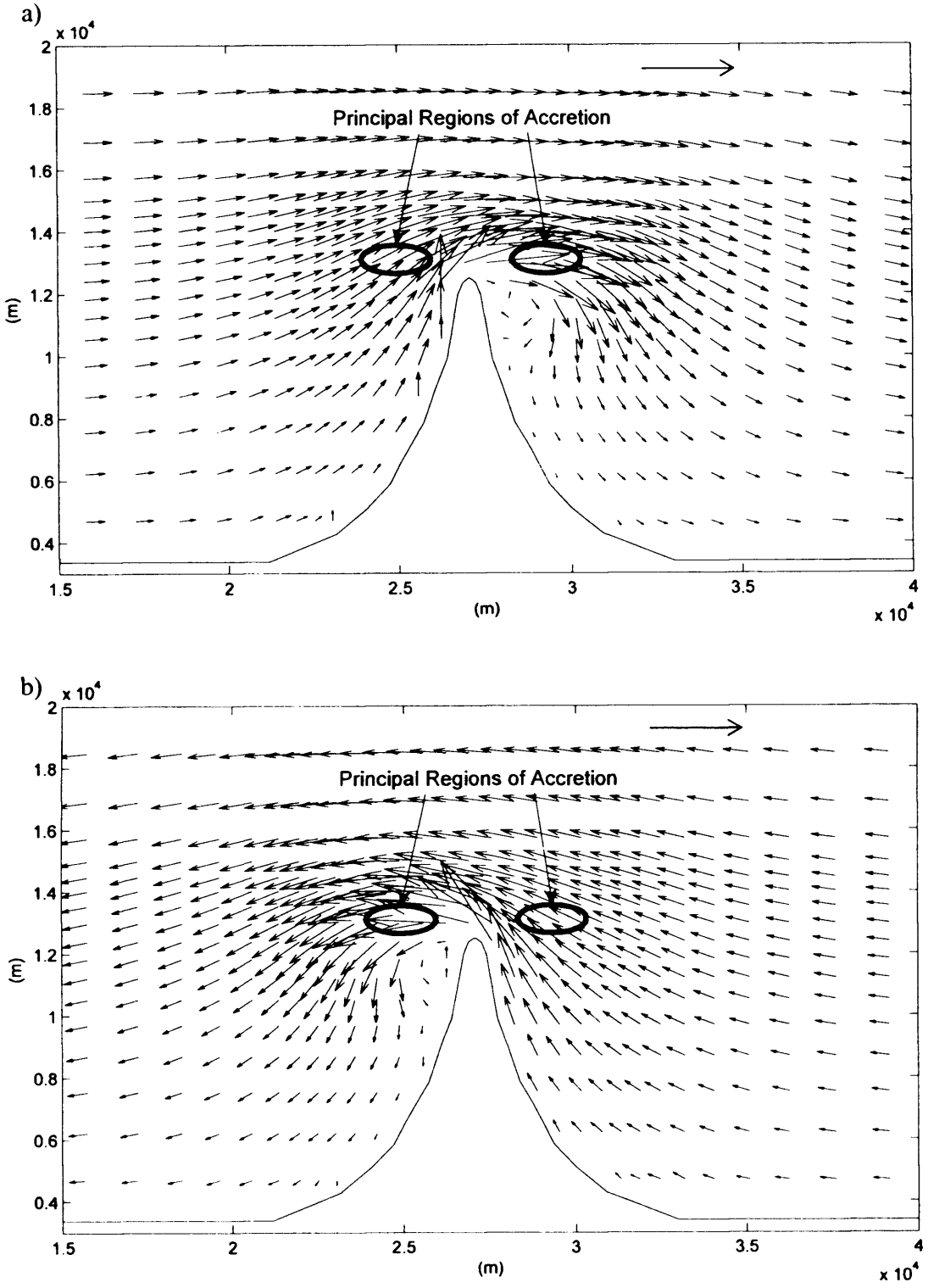

Figure 2.7. Maximum near-bed velocity vectors during: a) peak flood and; b) peak ebb. Idealised Gaussian headland.

These findings suggest that secondary circulation in headland eddies is not a major factor in sandbank creation. It also suggests that the actual mechanism responsible for offshore sandbank accretion is a large transient current velocity, scouring intensely near the headland and depositing further offshore.

2.3.2 Secondary Flows

The study now focuses on the influence of other types of secondary flows on sandbank development. In particular, patterns of transverse flow and up-welling predicted by Kalkwijk and Booij (1991) and Alaee et al (2004) are investigated. This type of secondary flow is produced in response to flow acceleration and curvature close to the headland.

Vertical velocity magnitudes predicted by the model (henceforth 'up-welling') during peak flood and peak ebb periods are presented in Figures 2.8 (a) and 2.8 (b). When flow approaches the headland from the west, up-welling is primarily to the west of the headland tip. When approaching from the east, up-welling occurs principally to the east of the headland tip.

At the start of the simulation, the model predicts equal values of vertical velocity during peak flood and ebb periods (see Figures 2.8 (a) and (b)). This suggests that near-headland up-welling does not cause an asymmetry in the sediment distribution. This is further confirmed by trends in peak values of up-welling throughout the early simulation period (Figure 2.9).

In Figure 2.9, consecutive vertical velocity peaks are approximately equal over the first 60 days of the simulation, suggesting either that up-welling is unaffected by the Coriolis force or that it is too small to be detected. As the simulation progresses, there is a rise in vertical velocity magnitude and consecutive peak values become increasingly more unequal. This indicates that up-welling is becoming increasingly unbalanced as the simulation progresses. The fact that this inequality is not present at the start of the simulation suggests that unequal up-welling is a symptom of the bed changes and that up-welling trends adjust to bed changes rather than precipitate them. This is the case for the medium sand tested in these experiments. The upwelling velocities, reaching a maximum of approximately 8 mms^{-1}, will be insufficient to overcome the settling

velocity for this type of sediment (approximately 25 mms^{-1}). For smaller sediment fractions and, indeed, cohesive sediment, this will not be the case and upwelling may be considerably more important to the headland sediment dynamics.[2]

Further evidence of primary tidal current effects on sandbank development is provided by analysis of instantaneous bed-load and suspended load over a tidal cycle. Early in the model simulation, maximum bed-load transport occurs very close to the headland tip (see Figures 2.10 (a) and (b)). As the simulation progresses and the bed evolves, maximum bed-load transport moves further offshore. After 200 tides, significant bed-load transport covers a large offshore area (see Figures 2.10 (c) and (d)). A similar trend can be observed in patterns of suspended load transport during peak flood and ebb flows (see Figure 2.11). This observed migration of sediment accretionary zones indicates sediment transport patterns that evolve over time in response to bed changes.

Most crucially, these bed-load and suspended load contour plots demonstrate the process of bed evolution around the headland. The accelerated near-headland flow or 'tidal jet' produced during both peak flood and peak ebb, scours sediment from the near side of the headland and initially deposits it in an accretion zone close to the headland tip. As this near-shore depositional zone develops, accretionary zones begin to develop further offshore and further to the east and west.

[2] A balancing downwelling component is also detected in the model predictions but the values have lower magnitude and are less localised than the up-welling velocities. For this reason it is difficult to include them on the same contour plots as Figures 2.8 (a) and (b).

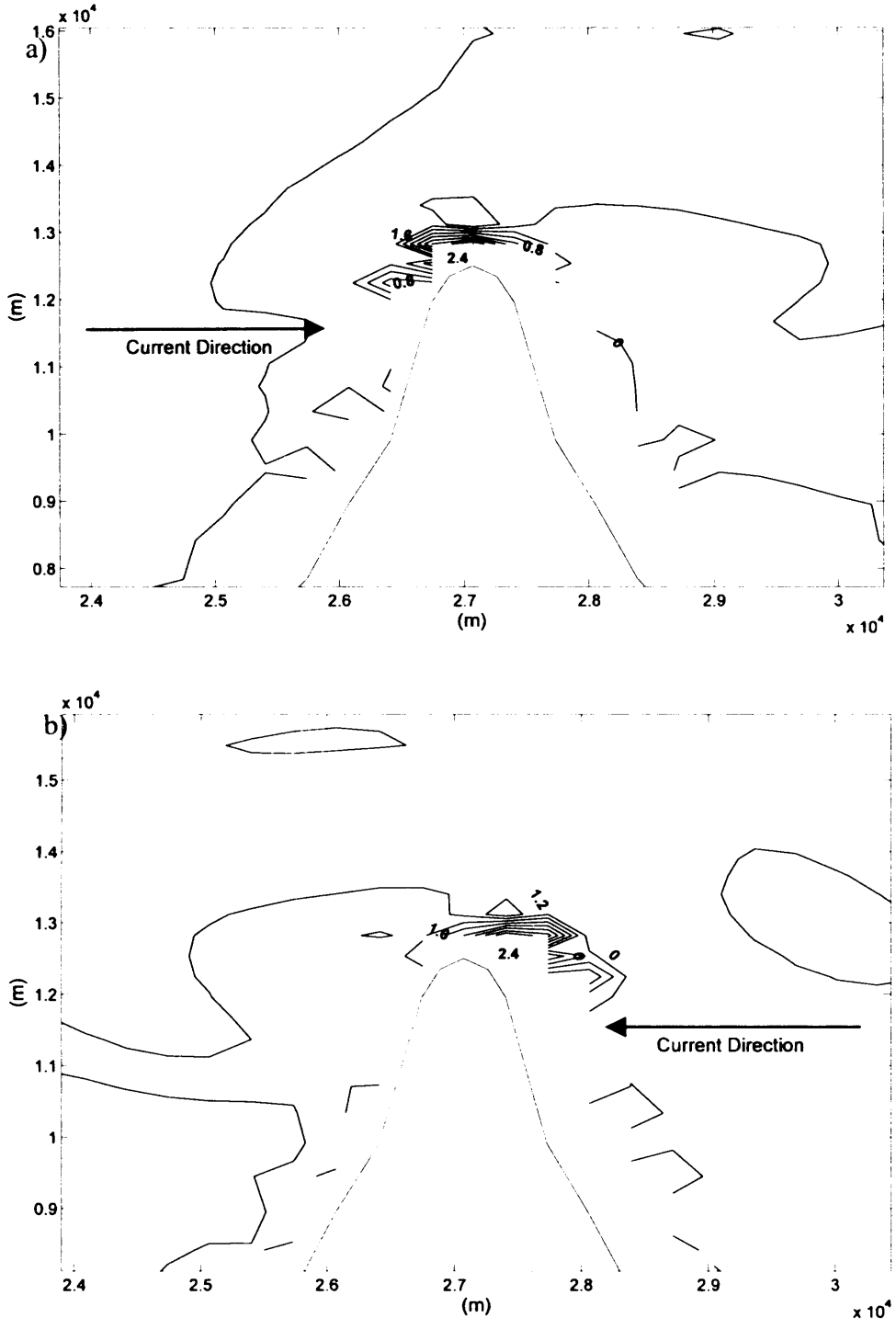

Figure 2.8. Contours of vertical velocity (after only 5 tides) during periods of peak tidal current. Labels are of velocity in mms^{-1} and the contour interval is 0.4 mms^{-1}. Vertical velocity is taken at mid-depthf (model layer 8). Positive values indicate upwelling.

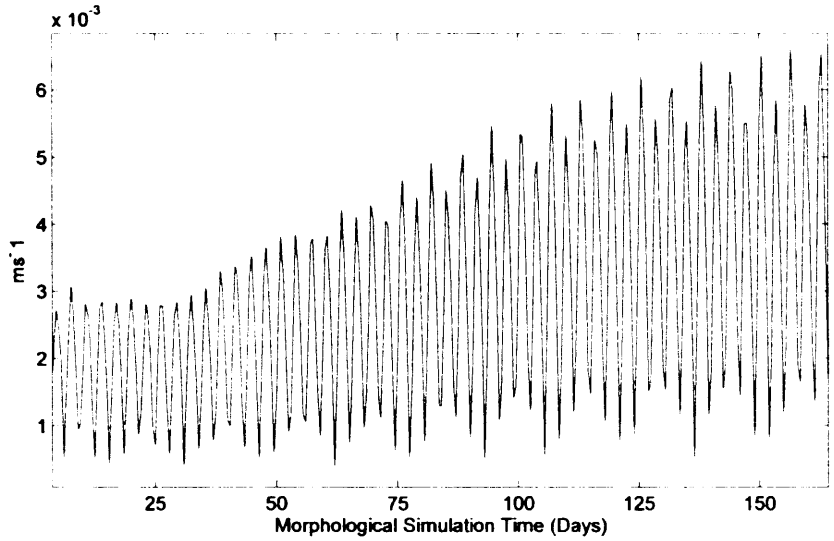

Figure 2.9. Vertical velocity peaks, 170 days of morphological time.

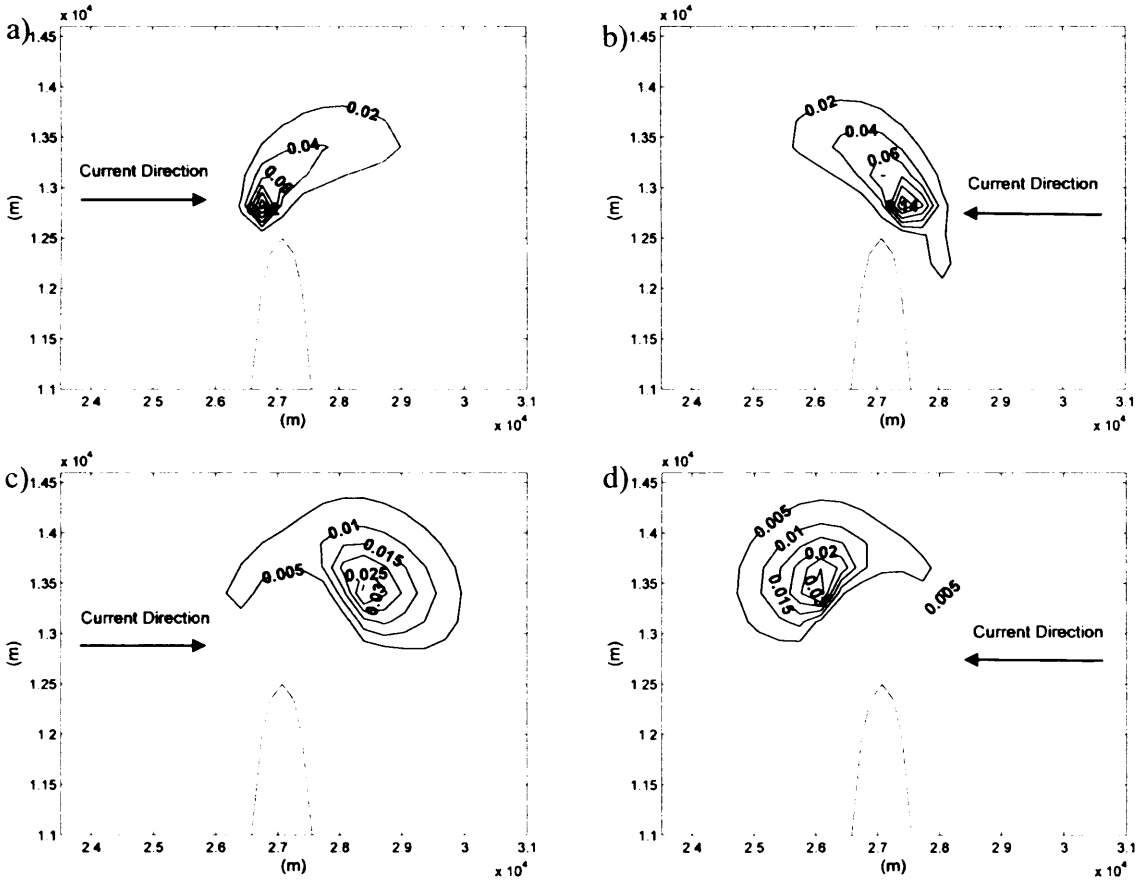

Figure 2.10. Instantaneous peak bed-load contours after 10 tides (a and b) and 200 tides (c and d). Units are 1×10^{-4} $m^3/m/s$.

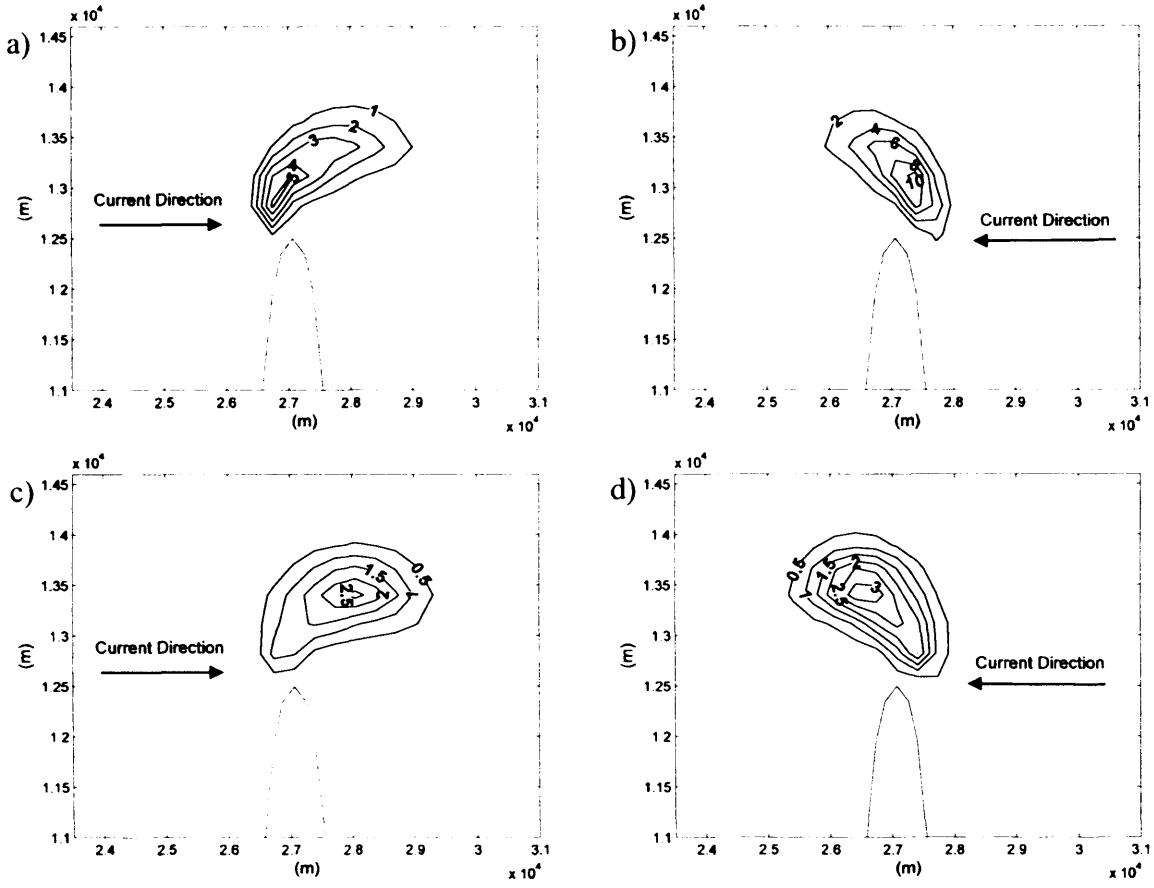

Figure 2.11. Instantaneous peak suspended load contours after 10 tides (a and b) and 200 tides (c and d). Units are 1×10^{-4} $m^3/m/s$.

Figures 2.10 and 2.11 reveal that transport by suspension is significantly larger than transport by bed-load. This helps to explain the disparity in magnitude between near-shore and offshore accretion: larger magnitude suspended load transport appears attached to the headland for most of the duration of the simulation, contributing mainly to near-headland, large magnitude accretion. Only toward the end of the simulation does it begin to correlate with offshore accretion. Conversely, bed-load transport migrates noticeably away from the headland tip and coincides well with regions of offshore accretion.

It is also possible to observe differences in the relative magnitude of eastern and western sediment transport (see Figures 2.12 and 2.13). More specifically, values of bed and suspended load transport during the ebb phase are larger that those observed during

the flood phase. In the following section the possible impact of the Coriolis effect on this phenomenon is investigated in more detail.

2.4 Coriolis Effects

To assess the influence of the Coriolis effect, the model was run for the same Gaussian shaped geometry, but at two different latitudes to reflect conditions in the northern and southern hemispheres (Table 2.4).

Table 2.4. Coriolis model tests.

MODEL RUN	Latitude	Prediction Period
CORIOLIS TEST 1	51° NORTH	230 Days
CORIOLIS TEST 2	51° SOUTH	230 Days

In both cases a large concentration of sediment accretion was predicted immediately in front of the headland (see Figure 2.12), coupled with the accretion of two large offshore lobes to the east and west of the headland. There is a subtle difference between the amount of accretion in the western and eastern offshore deposits in the two test cases: for the 51° N case, there is greater accretion in the western offshore deposit; for the 51° S test case, there is greater accretion to the east.

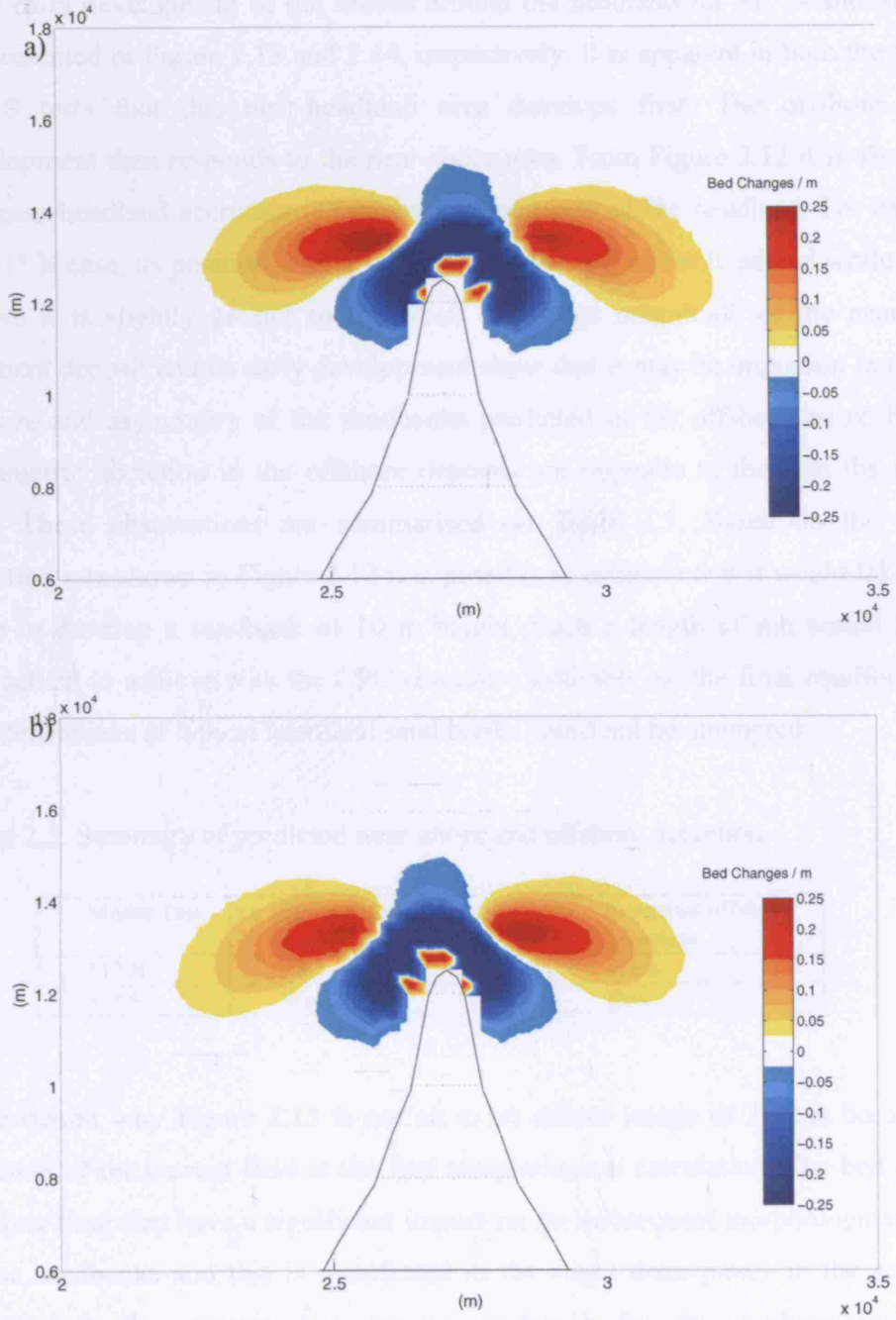

Figure 2.12. Predicted morphological change at (a) 51° N; (b) 51° S for initially flat bed after 460 tides.

The early development of the seabed around the headland for 51° N and 51° S cases are presented in Figure 2.13 and 2.14, respectively. It is apparent in both the 51° N and 51° S tests that this near-headland area develops first. The offshore sandbank development then responds to the near-shore area. From Figure 2.12 it is also apparent that near-headland accretion is favoured on one side of the headland. For example, in the 51° N case, its position is slightly greater to the east of the headland while in the 51° S case it is slightly greater to the west. The large magnitude of the near-headland sediment deposit and its early development show that it may be important in controlling the size and asymmetry of the sandbanks predicted in the offshore areas. Patterns of asymmetric accretion in the offshore deposits are opposite to those in the near-shore area. These observations are summarised on Table 2.5. Based on the maximum accretion rate shown in Figure 2.12 it is possible to estimate that it would take about 25 years to develop a sandbank of 10 m height. Such a length of run would have been impractical to achieve with the CPU resources available, so the final equilibrium shape and dimensions of typical headland sand banks could not be attempted.

Table 2.5. Summary of predicted near-shore and offshore accretion.

Model Test	Favoured near-headland accretion	Favoured offshore accretion
51° N	East	West
51° S	West	East

The reason why Figure 2.13 is not an exact mirror image of 2.12 is because of the direction of the current field at the first morphological calculation. The bed changes at this first time step have a significant impact on the subsequent morphological evolution of the sandbanks and this is manifested in the slight discrepancy in the accumulated sediment in the western and eastern sandbanks for the northern and southern hemisphere predictions, respectively.

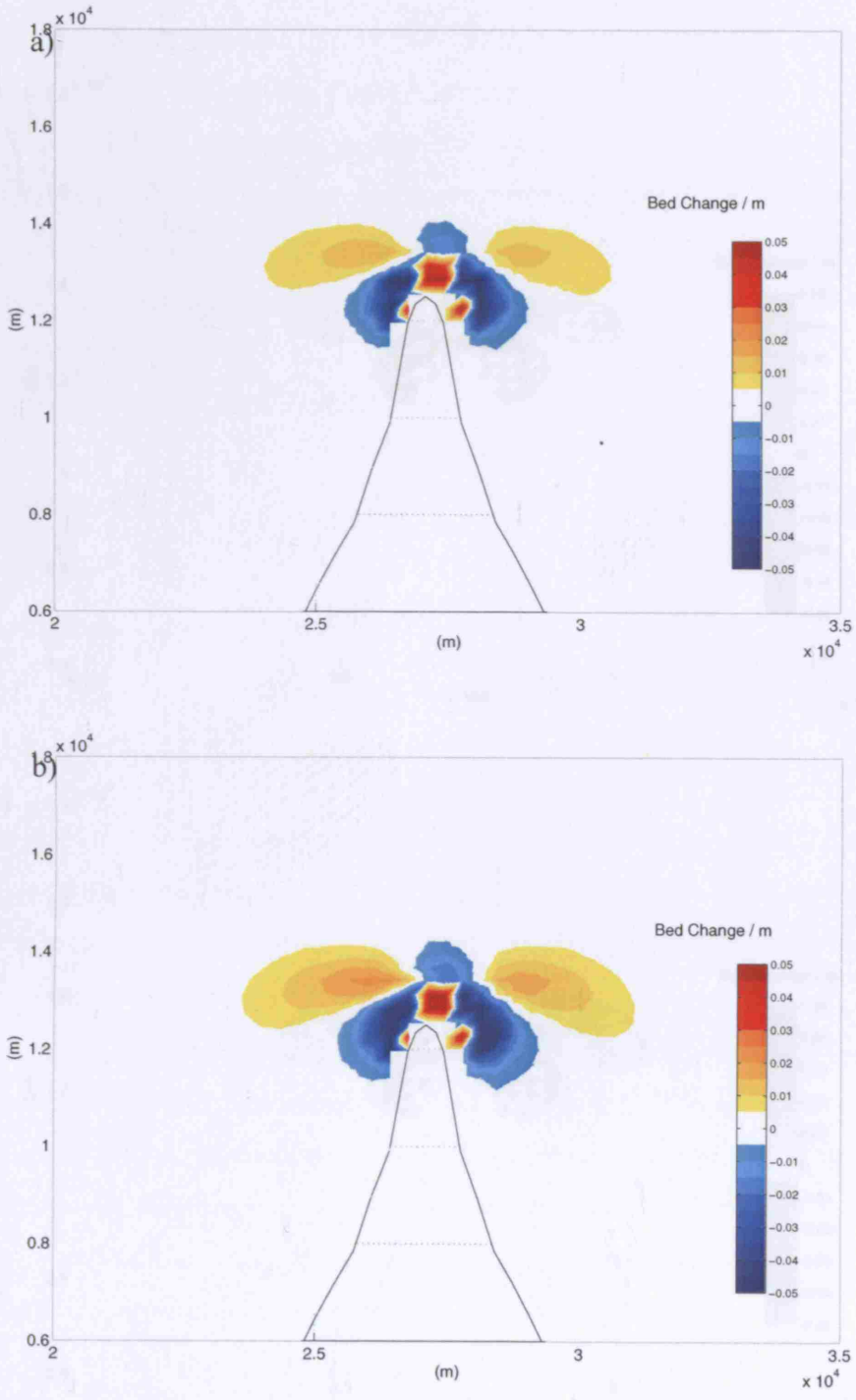

Figure 2.13. Early morphological evolution for model tests conducted at 51° N after (a) 2 morphological tides; (b) 4 morphological tides.

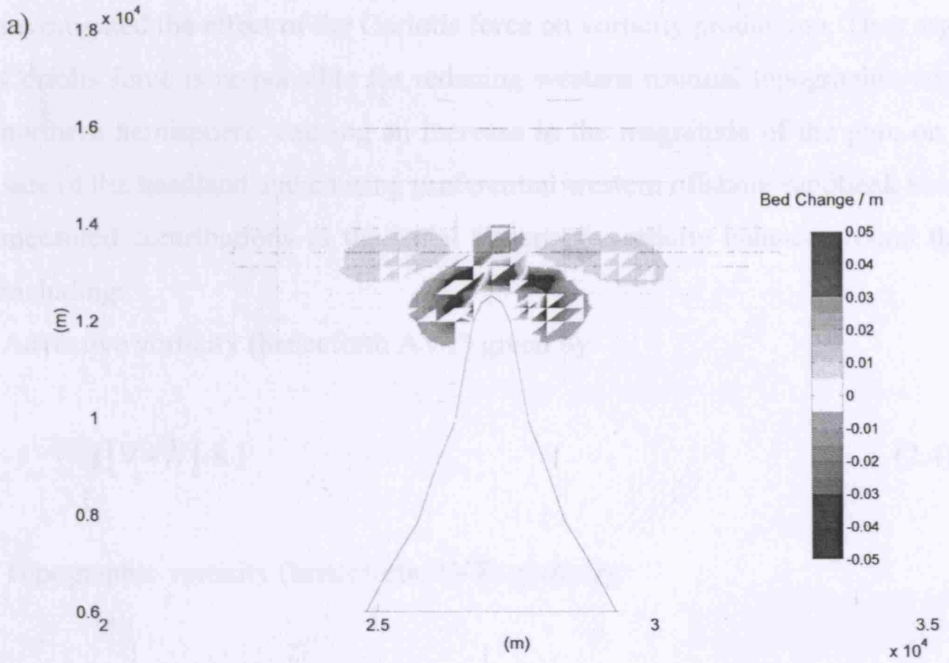

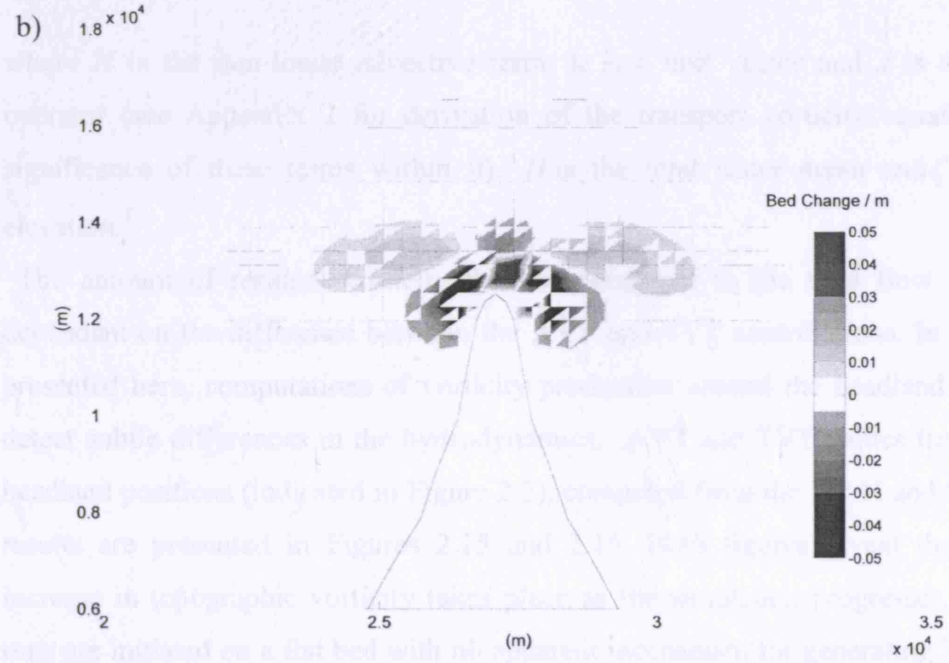

Figure 2.14. Early morphological evolution for model tests conducted at 51° S after (a) 2 morphological tides; (b) 4 morphological tides.

In their comprehensive study of headland dynamics, Park and Wang (2000) investigated the effect of the Coriolis force on vorticity production. They argued that the Coriolis force is responsible for reducing western residual topographic vorticity in the northern hemisphere, causing an increase in the magnitude of the gyre on the western side of the headland and causing preferential western offshore sandbank accretion. They measured contributions to the 'total transport' vorticity balance around the headland, including:

Advective vorticity (henceforth AVT) given by:

$$\left(\left[\nabla \times N\right]\cdot \mathbf{k}\right) \tag{2.4}$$

Topographic vorticity (henceforth TVT) given by:

$$\left(-gJ(H,\zeta)\right) \tag{2.5}$$

where N is the non-linear advective term, $\mathbf{k}$ is a unit vector and J is the Jacobian operator (see Appendix 2 for derivation of the transport vorticity equation and the significance of these terms within it). H is the total water depth and ζ the surface elevation.[3]

The amount of residual vorticity that is transferred to the tidal flow is primarily dependant on the difference between the AVT and TVT contributions. In the analysis presented here, computations of vorticity production around the headland are used to detect subtle differences in the hydrodynamics. AVT and TVT values from the near-headland positions (indicated in Figure 2.2), computed from the 51° N and 51° S model results are presented in Figures 2.15 and 2.16. Both figures reveal that a general increase in topographic vorticity takes place as the simulation progresses. The model runs are initiated on a flat bed with no apparent mechanism for generating TVT (i.e. no bed gradients). As the bed evolves, TVT is produced in areas where evolution has occurred.

[3] A full derivation of these and the remaining terms in Park and Wang's 'transport vorticity' equation is provided in Appendix 1.

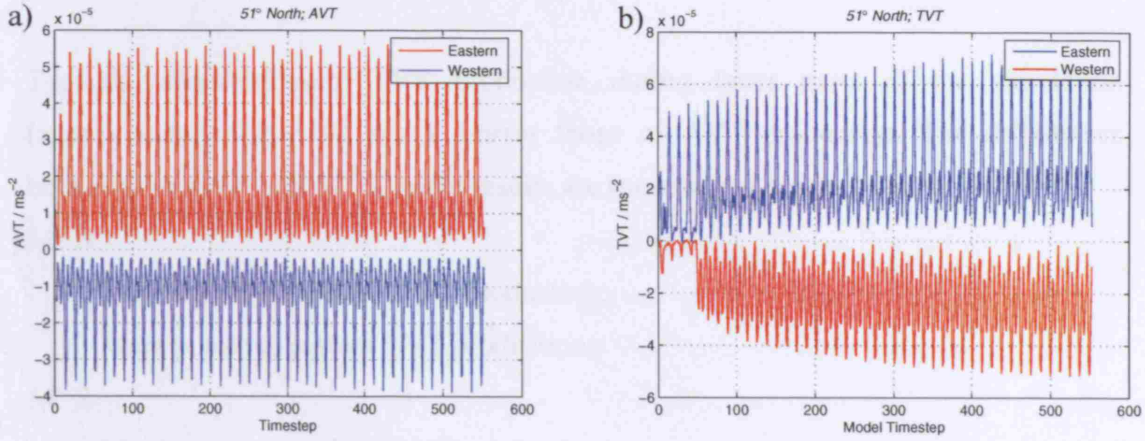

Figure 2.15. (a) AVT production; (b) TVT production at 51° N. Western and eastern positions indicated in Figure 2.2 (a).

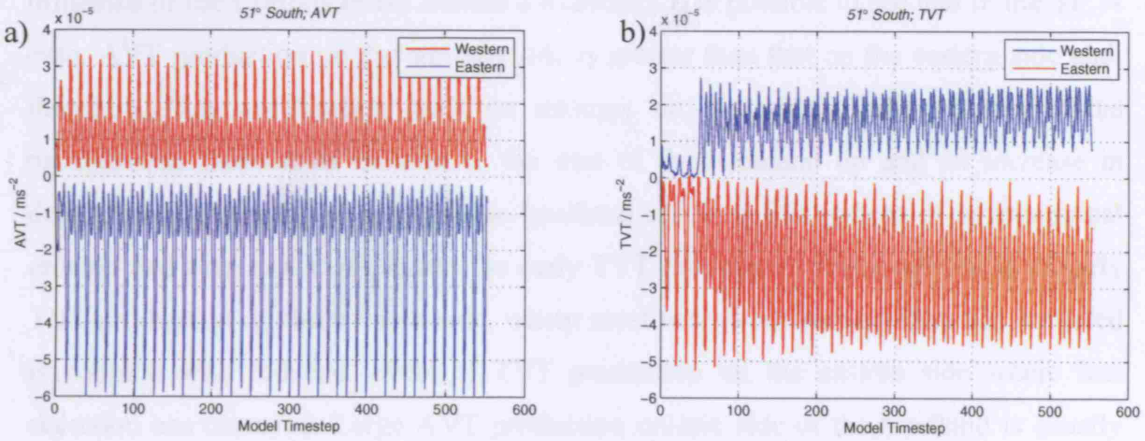

Figure 2.16 (a) AVT production; (b) TVT production at 51° S. Western and Eastern positions indicated in Figure 2.2 (a).

It is also evident from the figures that the vorticity is not completely in balance. In Figure 2.15 for example, although positive and negative AVT production is generally symmetrical, values of positive TVT production far outweigh those of negative TVT production. Also, AVT clearly dominates the vorticity balance early on in the tidal cycle. As the system develops, increasing amounts of sediment are deposited in the near-headland tip region and the levels of TVT on both sides of the headland increase.

Toward the end of the simulation vorticity balance begins to be established. This can be observed in plots of TVT production around the coastal headland in Figure 2.16 (b).

Typical values of max TVT production during latter parts of the simulation (approximately 7.2 $\times 10^{-5}$ ms^{-2}), mirror those of AVT production. The differences between the 51° N and 51° S model results are summarised below:

51° N

- More positive, western AVT production;
- More positive, eastern TVT production;

51° S

- More negative, eastern AVT production.
- More negative, western TVT production.

Analysing the instantaneous patterns of vorticity provides a method of detecting the influence of the Coriolis effect around a headland. It is possible to see that in the 51° N case, AVT production on the western side is greater than that on the eastern side and, therefore, flow acceleration must be stronger on that side of the headland. This promotes an increase in erosion to the east of the headland tip and an increase in deposition slightly to the west of the headland tip. It is this pattern of asymmetrical erosion and accretion that dictates the early TVT production. Enhanced levels of early TVT production on the western side, where most near-headland accretion has occurred is coupled with reduced levels of TVT production on the eastern side where less accretion has occurred. Large AVT production on one side of the headland is usually coupled with low TVT production on that same side. In the early stages of morphological development the Coriolis effect exerts a much greater influence adjusting AVT rather than affecting TVT production.

In the Northern hemisphere, the Coriolis effect provides a perpendicular component that acts to the right of the primary flow. In the geometry adopted for the present case study, it thus provides an onshore component to the flood current and an offshore component to the ebb, which are proportional to the flow velocities. Also, the influence of the Coriolis effect is greatest where tidal jetting occurs near the headland tip. It is here that, rather than being directed onshore, the Coriolis effect induces a long-shore component. This enhances the flood tidal jetting, promoting greater erosion on the western side of the headland tip and greater sediment accretion to the east. The ebb tidal

jetting near the headland is not augmented in this way and a disparity in eastern and western accretion near the headland is produced.

The asymmetry in near-headland sediment accretion then provides an asymmetry in offshore sediment supply. An increase in sediment accretion to the east of the near-headland area provides the ebb flow with a larger and more readily erodible source of sediment. Subsequently, a western offshore sandbank produced during the ebb is slightly larger than the flood-generated eastern offshore deposit (Figure 2.17). The situation in the southern hemisphere is reversed as the Coriolis effect induces an offshore-directed component during the flood and an inshore-directed component during the ebb. The result is preferential western near-shore accretion coupled with preferential eastern offshore accretion.

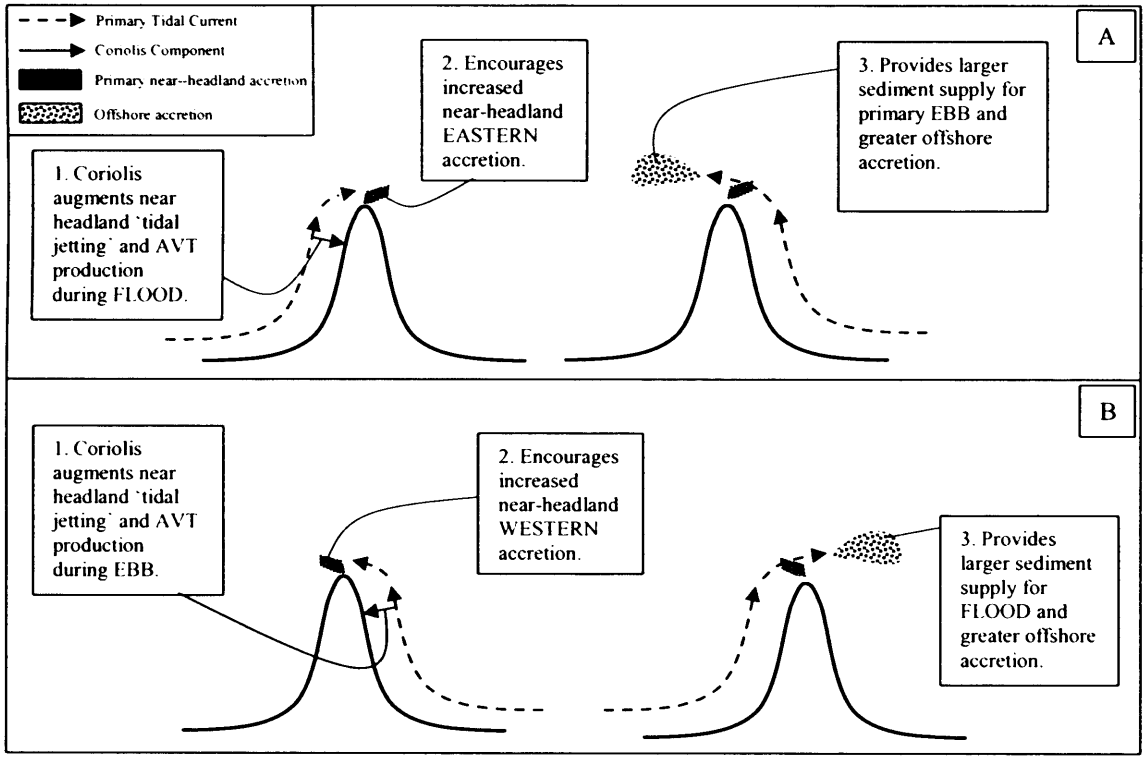

Figure 2.17. Proposed mechanism of preferential patterns of accretion at (a) 51° N; (b) 51° S.

2.5 Impact of a Coastal Slope

In reality, coastal promontories are not surrounded by a flat seabed; most often, a sloped apron encircles the headland. In this section the contribution of this apron to headland sediment dynamics is investigated and, in particular, the effect on offshore sandbank generation.

Numerical simulations have been used to compare the theoretical predictions of three idealised Gaussian models of varying sloped shelving. Model conditions were similar to those of the previous flat bed runs, with forcing from a single semi-diurnal tidal constituent, phase-shifted at each boundary. The first model test incorporated a flat model bathymetry and the second a gently sloping coastal apron surrounding the headland. The apron ran from a depth of -10 m at the shore to -20 m, 3 km offshore. The third test case again used the same idealised Gaussian headland shape with the addition of a steep-sloped coastal apron. The apron ran from a depth of zero metres at the coast to -20 m depth at a distance of 3 km offshore. The two sloped model runs represent steep and gentle coastal slopes. The bathymetries are illustrated in Figure 2.18. Modelling parameters for the flat bed and two slope runs are summarised in Table 2.6.

Table 2.6. Baseline and slope test model bathymetry and simulation time.

Headland Shape	**Test**	**Bathymetry**	**Simulation Time**
Gaussian	BASELINE	Uniform flat bed	230 Days
Gaussian	SLOPETEST1	Steep-slope from zero to -20 m Depth at 3 km offshore	230 Days
Gaussian	SLOPETEST2	Gentle-slope from -10 m to -20 m depth at 3 km offshore	230 Days

The changes in bathymetry predicted for the two slope tests are shown in Figures 2.19 (a and b). Several features of the predicted patterns of sediment accretion and scour are identified:

a) Levels of sediment accretion immediately in front of the headland increase with increasing coastal slope gradient;

b) Increasing gradient is coupled to a decrease in offshore sediment accretion;

c) Primary scour zones to the east and west of the headland tip generally become deeper and wider with increasing gradient.

d) A reduction in asymmetric offshore accretion with increasing coastal slope gradient;

e) An increase in levels of asymmetric near-headland scour and near-headland accretion with increasing coastal slope.

The flat-bed case (see Fig. 2.7 (b)) is characterized by little near-headland asymmetry while the gentle slope model predicts a shift toward enhanced eastern near-headland accretion and scour. In the steep slope case the large magnitude near-headland deposits are connected to the eastern offshore sandbank deposits.

During times of peak ebb and flood velocity when maximum sediment transport takes place, large flow acceleration and streamline concentration occur along the sides of the promontory. Evidence for this is provided in the transient velocity vector plots in Figure 2.7. Accelerated velocities or 'tidal jetting' occurs to the left and the right of the headland tip. Moving past the headland tip, the concentrated streamlines diverge and a rapid flow deceleration occurs. This rapid reduction in flow velocity close to the headland tip promotes local sediment accretion.

The quantity of sediment that accretes in this near-headland tip area is directly related to the extent of flow deceleration. In addition to the flow being influenced by the shape of the headland, it can also be altered by the slope of the bed. The seabed slope will act to increase streamline divergence and flow deceleration, encouraging enhanced levels of sediment accretion near the headland tip. The results from the three Gaussian slope tests corroborate this hypothesis. The steep slope case is characterized by large amounts of accretion in front of the headland tip. The headland and its surrounding coastal slope generate a concentration of streamlines in both the horizontal and the vertical planes.

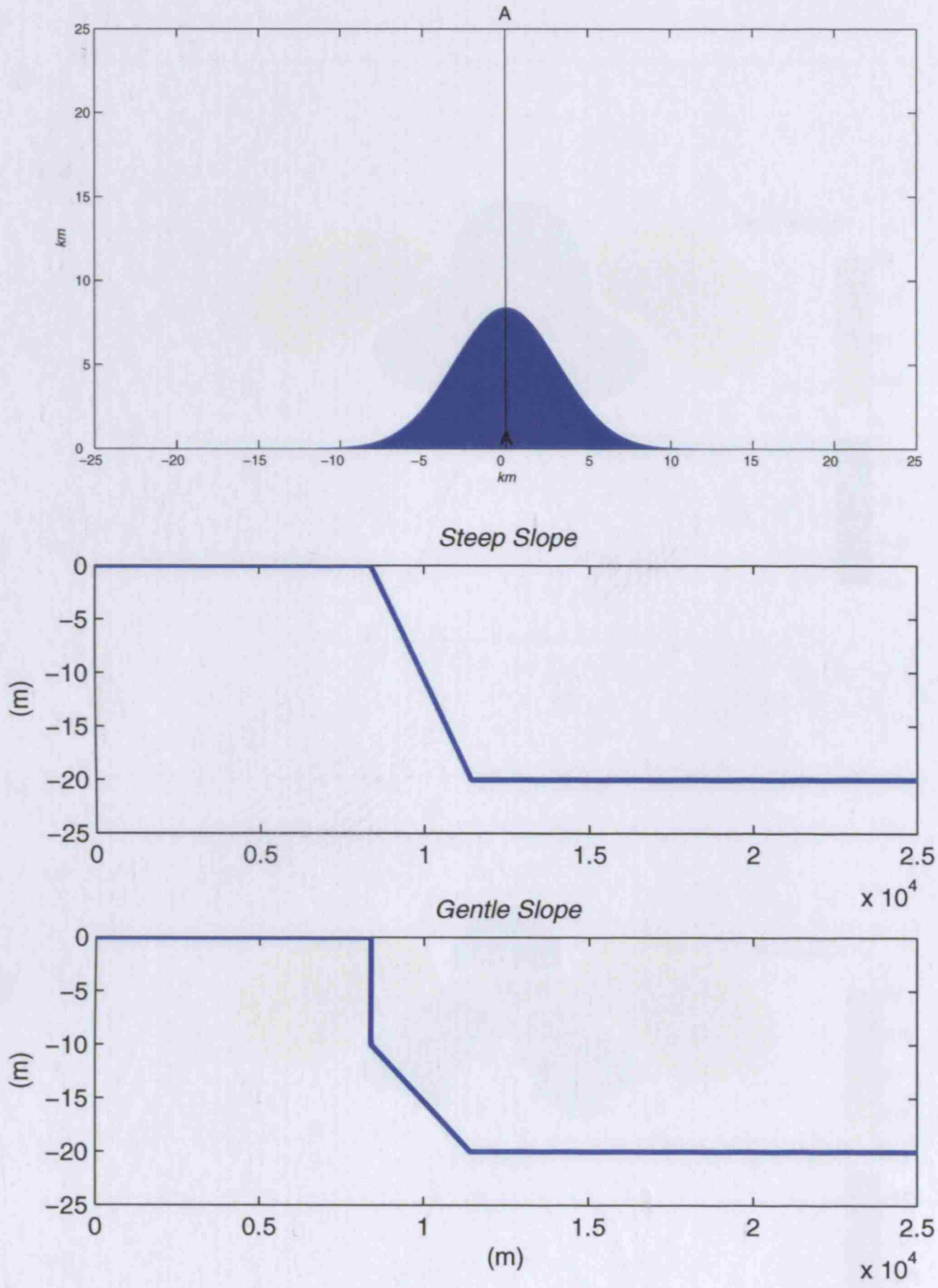

Figure 2.18. Steep and gentle slope bathymetries from Section AA.

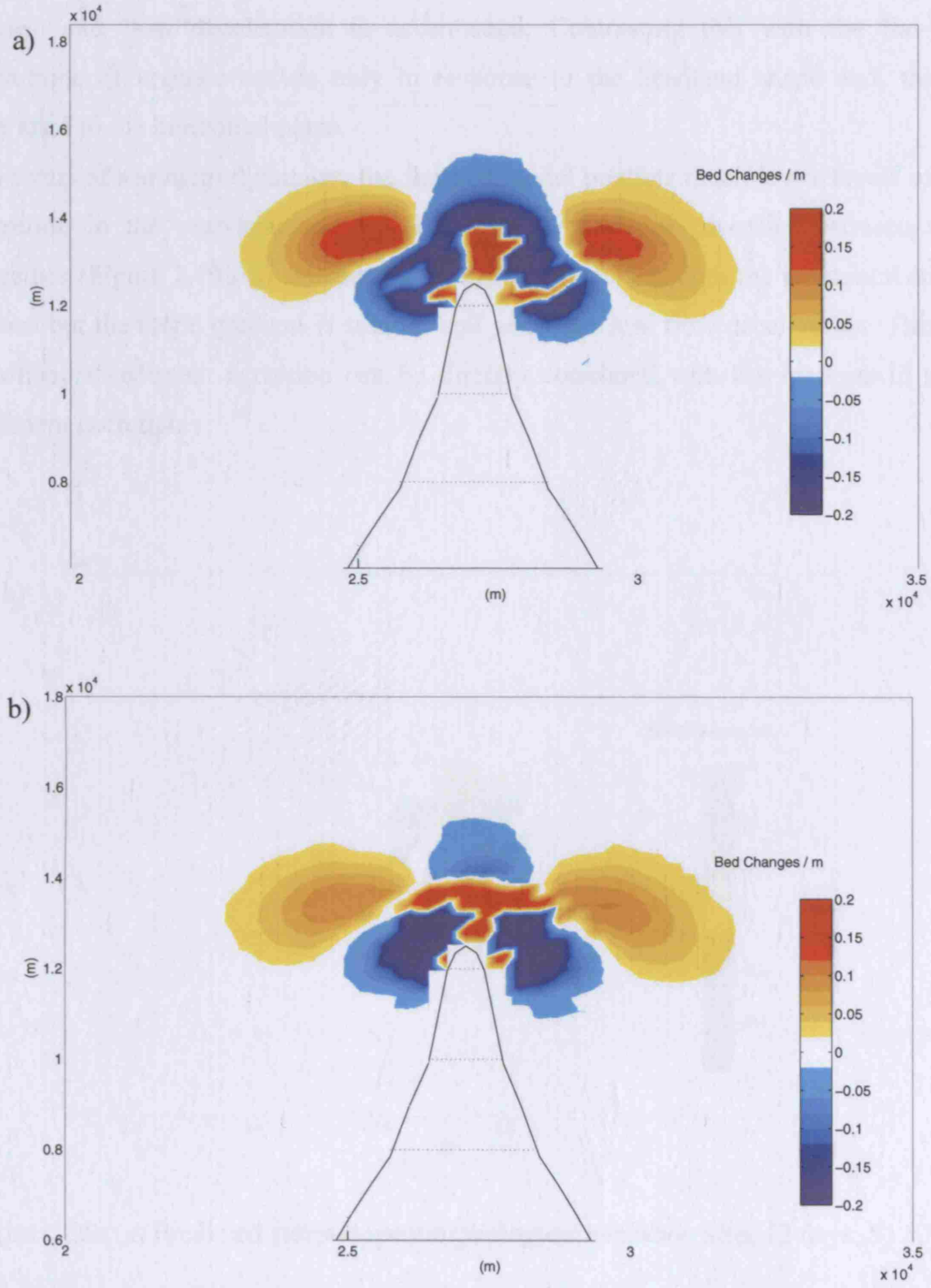

Figure 2.19. Morphological change predicted over 230 days using: (a) gently sloped bathymetry; (b) steeply sloped bathymetry at 51° North.

As the flow reaches the headland tip, streamlines diverge in the horizontal and vertical planes, and flow deceleration is accentuated. Contrasting this with the flat-bed case, streamline divergence occurs only in response to the headland shape and, therefore, is restricted to the horizontal plane.

In terms of sediment dynamics, the flat-bed model predicts much lower levels of sediment accretion in the near-headland tip area. The gentle-slope case lies between these two extremes (Figure 2.19 (a)). Streamline divergence occurs in both the horizontal and vertical planes but the slope gradient is smaller and generates less flow deceleration. This decrease in offshore sediment accretion can be directly correlated with the increase in near-shore sediment accretion.

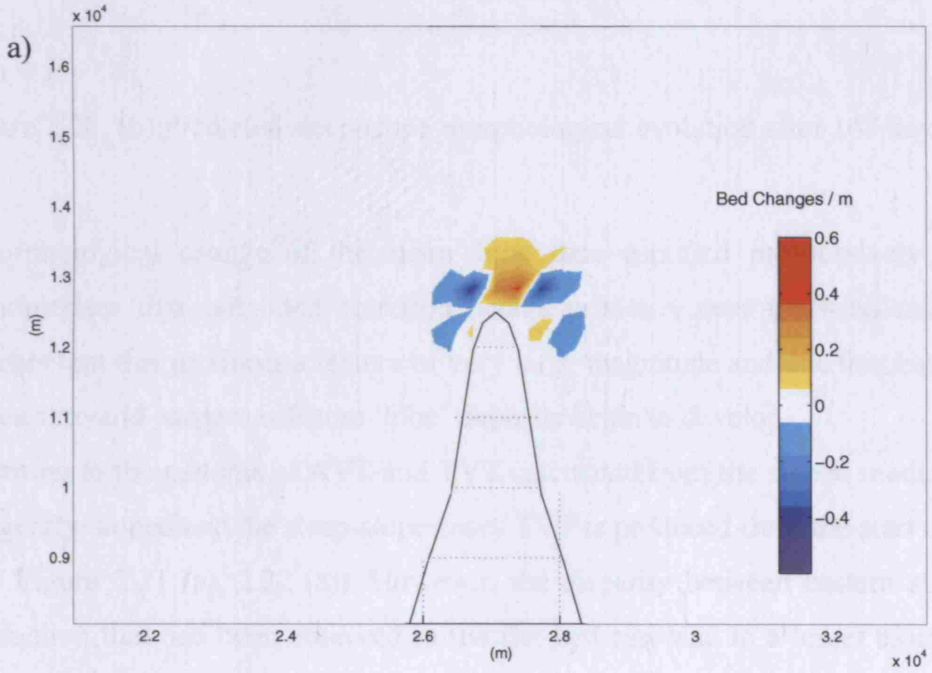

Figure 2.20. (a) Predicted steep-slope morphological evolution after 42 days. 51 ° N

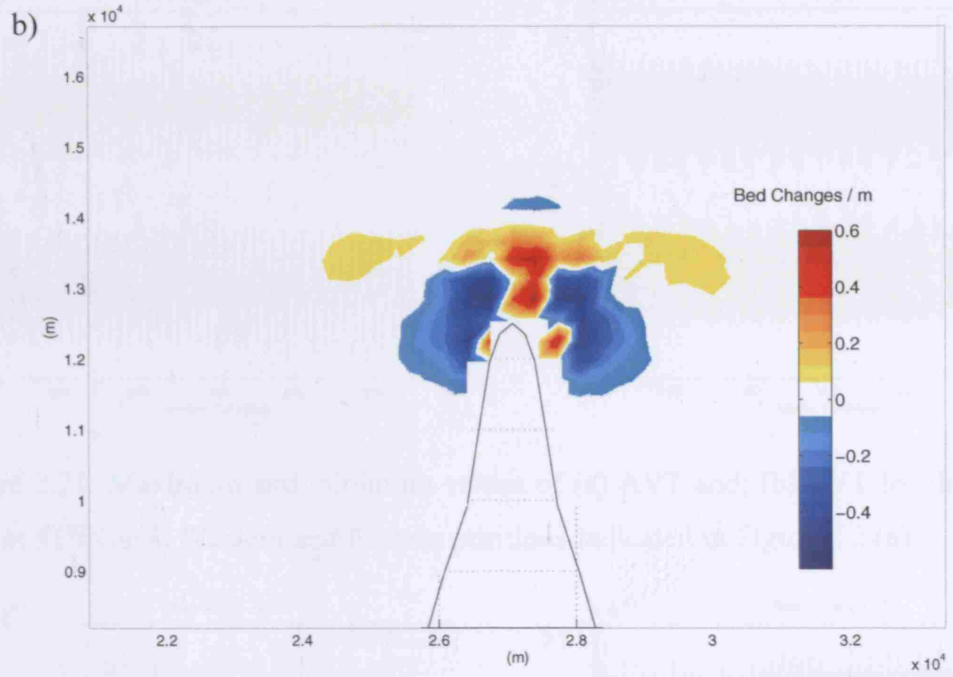

Figure 2.20. (b) Predicted steep-slope morphological evolution after 167 days. 51 ° N

Morphological change of the steep-slope case captured progressively in Figure 2.20 demonstrates that early bed accretion occurs primarily near the headland tip. Further, it appears that this produces a feature of very large magnitude and one that has matured before the eastern and western offshore 'lobe' deposits begin to develop.

Turning to the patterns of AVT and TVT calculated from the sloped model results, in both the gently-sloped and the steep-slope cases TVT is produced from the start of the simulation (see Figure 2.21 (a), 2.22 (a)). However, the disparity between eastern and western TVT production that had been observed in the flat-bed case and to a lesser extent in the gently-sloped case, appears to be absent in the steep-slope case. A shift toward a more symmetrical production of TVT is observed. A noticeable feature of the trend in TVT production in the steep-slope case is the relative magnitude of the levels of maximum and minimum TVT production. TVT production far outweighs AVT production throughout the entire simulation (Figure 2.22 (b)). The introduction of a slope has generated a shift in the vorticity balance toward being TVT dominant.

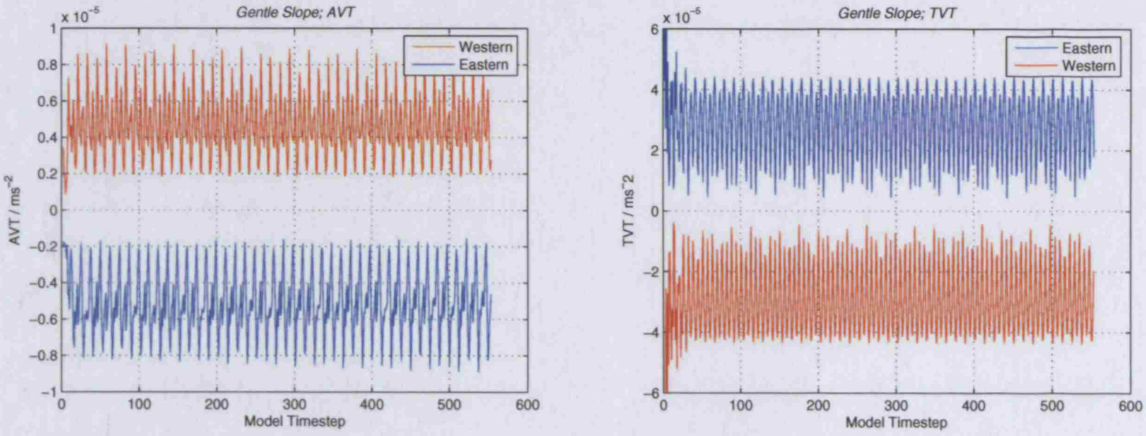

Figure 2.21. Maximum and minimum values of (a) AVT and; (b) TVT for the gentle slope case at 51° North. Western and Eastern positions indicated in Figure 2.2 (a).

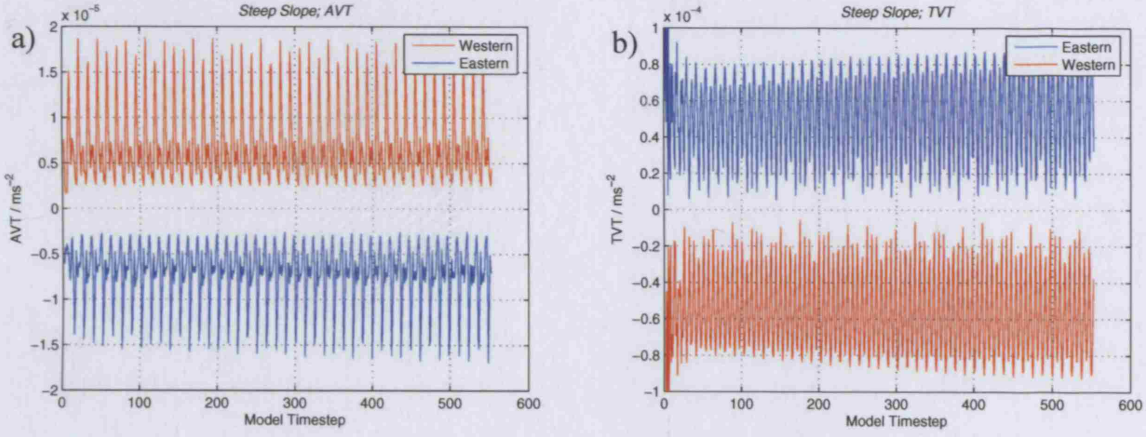

Figure 2.22. Maximum and minimum values of (a) AVT and; (b) TVT for a steep-slope model at 51° North. Western and Eastern positions indicated in Figure 2.2 (a).

This also provides an insight into the contribution of the Coriolis effect and the observed patterns of preferential eastern and western offshore accretion observed in the 51° N case and the 51° S case. The Coriolis effect only appears to be important when dealing with coastal systems in which the vorticity balance is established or close to being established. In a regime where the hydrodynamics are dominated by the influence of a slope and TVT production far exceeds AVT production, the Coriolis effect has much less influence on headland morphology.

2.6 Semi-Gaussian Headland Geometry

In the following set of numerical experiments, erosion and accretion around a semi-Gaussian shaped headland (see Figure 2.2 (b)) is investigated. This type of headland is common in U.K. coastlines and has often been associated with 'banner' bank growth (see Dyer and Huntley, 1999). The shape promotes similar hydrodynamic responses to those of the Gaussian-shaped headland. The main difference, however, is that flow velocities on one side of the headland will always be much faster than on the other. This has important implications on sandbank building around the headland.

In the first test, a flat bed was used and driving boundary conditions were identical to those used in earlier experiments (i.e. phase shifted semi-diurnal constituents, see Table 2.1). This particular model set-up produced a near-headland peak velocity of approximately 1 ms^{-1}. Vectors of predicted peak velocities are shown in Figure 2.23. Flow separation at the headland tip can be observed; however, the transient gyres are much smaller, particularly to the east of the headland (the flood gyre). The geometry promotes a more uniform current field (relative to the Gaussian case) and less potential for flow separation (i.e. less lateral shear). However, gyres in the residual current field are more pronounced (see Figure 2.24). These have been plotted on top of the 10 month predicted bed changes.

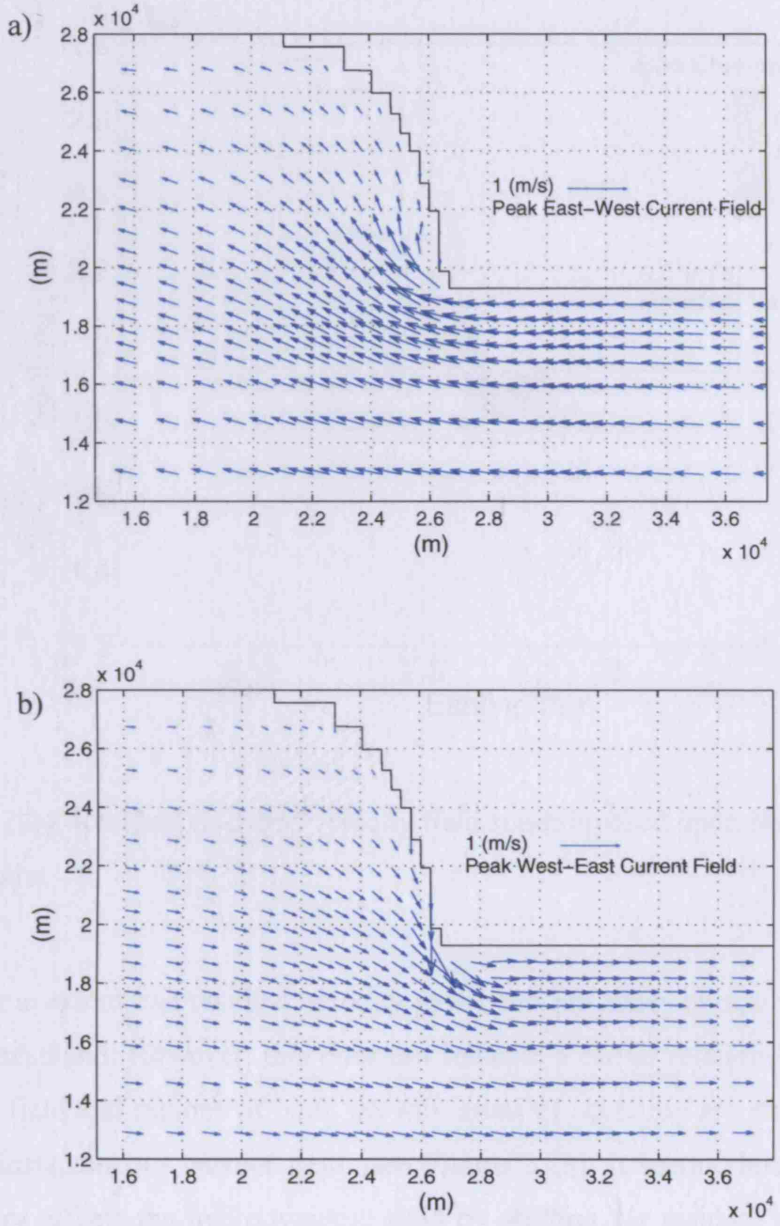

Figure 2.23. Peak (a) Ebb and; (b) Flood velocity fields for a semi-Gaussian headland test case on a flat bed. (Near surface velocity vectors).

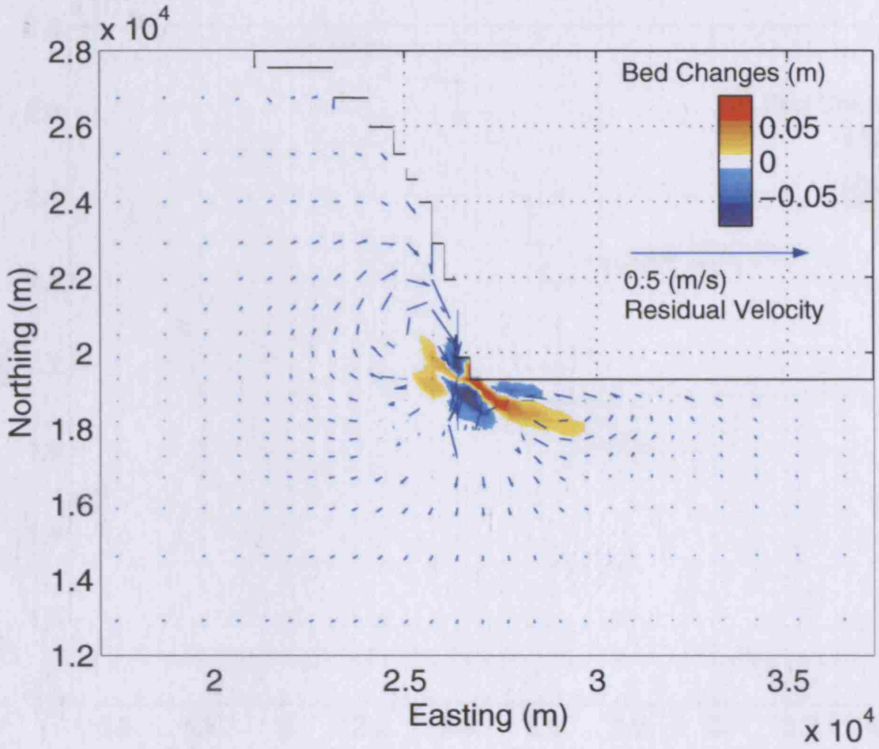

Figure 2.24. Residual near-bed velocity field superimposed upon bed changes predicted over 13 months.

To some extent, the residual velocity gyres overlap zones of accretion to the left and right of the headland. However, this does not indicate a causal relationship between the residual current field and regions of bank growth: areas of accretion are strictly related to gradients in the instantaneous current field)see Figure 2.23). It seems, however, that the headland geometry affects the hydrodynamic field by shifting the residual gyres to positions which are close to areas of sediment accumulation)see Figure 2.24). This is also repeated in the residual sediment transport plot)Figure 2.25). This may have important effects on the future development and maintenance of the sandbank and is relevant to the case study reported in Chapters 5 and 6.

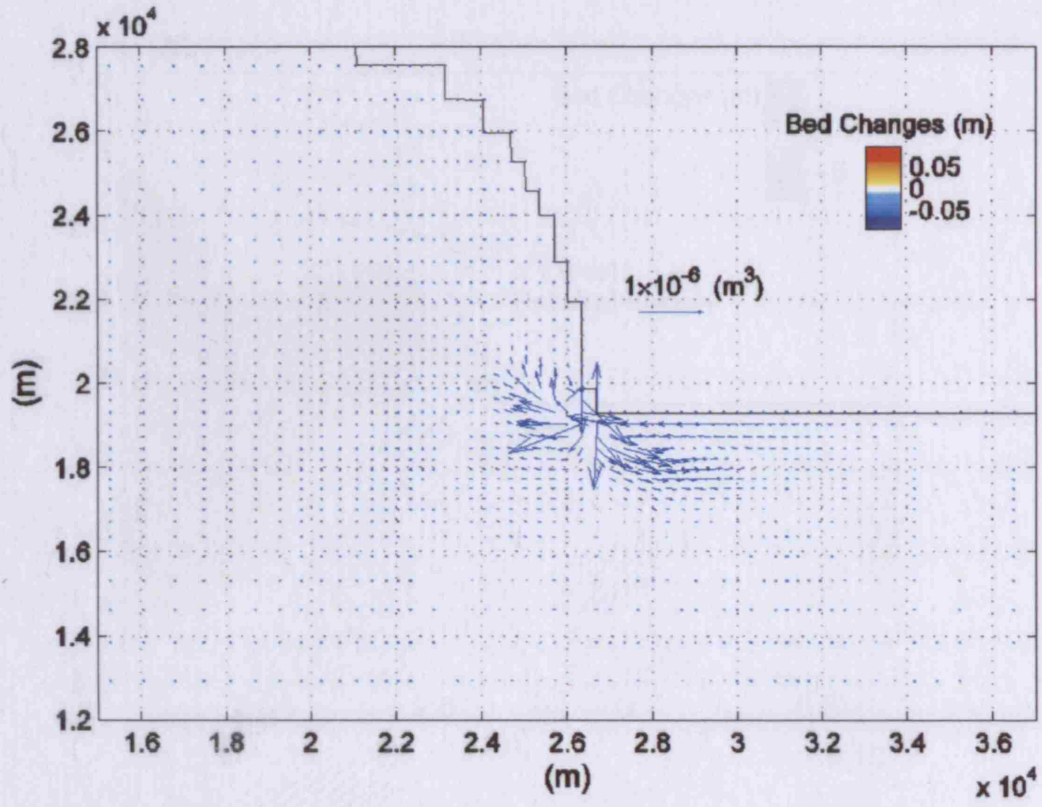

Figure 2.25. Residual sediment transport vectors.

An additional experiment tested the impact of increased tidal currents on bank growth. The amplitudes of the boundary conditions were adjusted to produce a maximum near-headland current velocity of approximately 1.8 ms^{-1}, corresponding to current speeds recorded at the Nash Point, Bristol Channel, U.K. The corresponding residual current field can be seen in Figure 2.26. Sediment accretion to the right of the headland is reduced due to the higher current velocities in that region.. Material deposited during lower energy periods of the tide is scoured away during the next flood or ebb period.

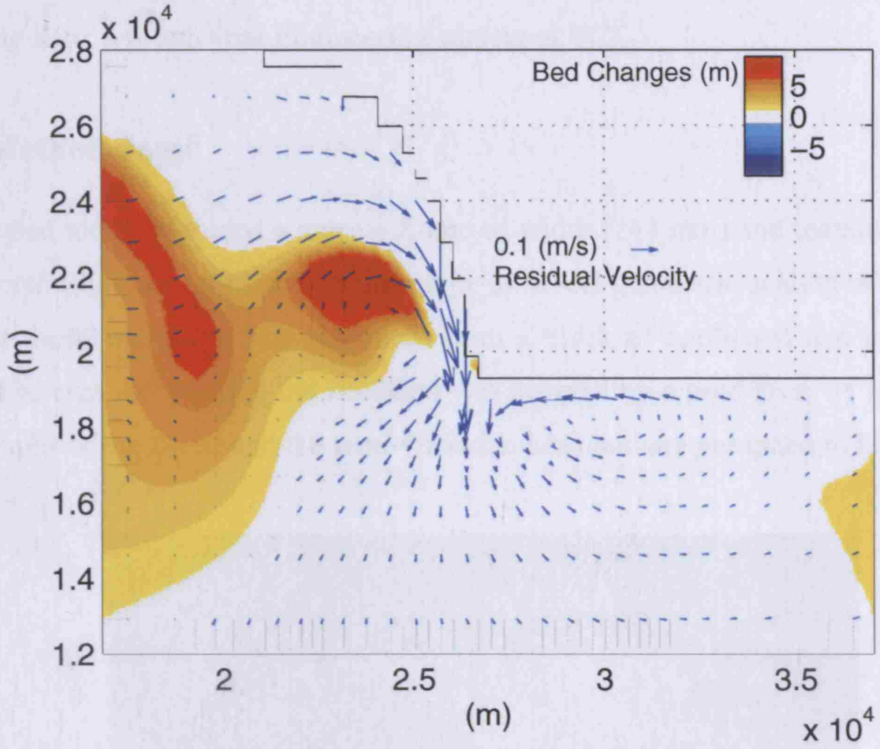

Figure 2.26. Residual near-bed velocity field superimposed upon 13 month bed changes for the high current speed test.

The situation presented in Figure 2.26 resembles the pattern of sand accumulation and scoured bed-rock regions found around the Nash Point, Bristol Channel, U.K. The eastern channel is free of deposited sediment while there is an accumulation of material (the Nash Sands) to the north-west of the headland which also coincides with a residual current circulation.

2.7. Physical Modelling

Before embarking on an extensive numerical modelling study of the Nash Sands and surrounding system, it was decided to perform a few simple physical modelling experiments. The aim of these was to reproduce the patterns of sediment erosion and accretion predicted by the numerical modelling of the semi-Gaussian headland, above.

The experiments were conducted in collaboration with an MSc project being undertaken by Min-Jung Kim, a fourth year Engineering student at UCL.

2.7.1 Methodology

The scaled model included a narrow flume of width (244 mm) and maximum permissible water depth (300 mm) providing a prototype to model geometric scaling of 133:1. A semi-Gaussian headland shape was machined from a block of hardwood and inserted into the flume. The area surrounding the headland was covered by a sand layer of 10 cm thickness. Photographs of the flume and the semi-Gaussian headland are presented in Figure 2.27.

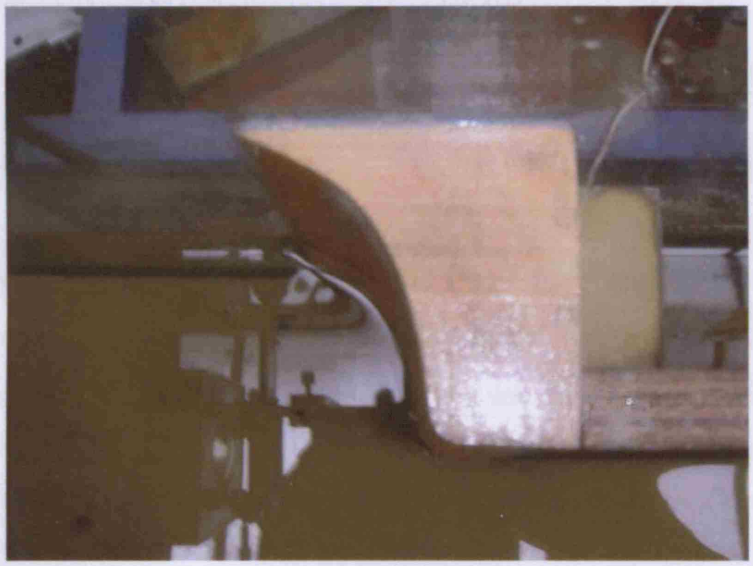

Figure 2.27. Plan view of the semi-Gaussian headland shape used in the physical model tests.

The flume was adjusted to give a constant flow velocity (0.043 ms^{-1}) in the channel over a period of 1.07 hrs. The flume was reversed to simulate flood and ebb periods. The flow velocity and the period were calculated using Froude number scaling of the numerical modelling parameters described above:

$$(F_r)_p = (F_r)_m \qquad 2.6$$

where subscripts p and m represent the prototype and model parameters, respectively. This can be written as

$$\frac{V_p}{\sqrt{g_p \cdot H_p}} = \frac{V_m}{\sqrt{g_m \cdot H_m}} \qquad 2.7$$

where V_p and V_m are the prototype and model velocities and H_p and H_m are the water depths. Gravity is constant in both the model and the prototype giving

$$\frac{V_p}{V_m} = \sqrt{\frac{H_p}{H_m}} \qquad 2.8$$

The prototype water depth is 20 m and the mean flow velocity is 0.5 ms^{-1}. The prototype mean flow velocity, V_p, is 0.5 m/s. The model water depth, H_m, is limited by the available apparatus to 0.15 m. The model flow velocity, V_m, can then be calculated as 0.043m/s.

The model tidal periods are calculated using the same Froude number scaling where

$$\sqrt{\frac{H_p}{H_m}} = \frac{V_p}{V_m} = \frac{H_p / T_p}{H_m / T_m} \qquad 2.9$$

T_p and T_m are the prototype and model tidal periods. Hence

$$\frac{T_p}{T_m} = \sqrt{\frac{H_p}{H_m}} \qquad 2.10$$

giving an M_2 model time period of 1.07 hours.

To determine the model grain size, the particle Reynolds number, $R*$, gives a relationship between the model and prototype shear velocity, viscosity and grain size:

$$\left(\frac{u*d}{\nu}\right)_p = \left(\frac{u*d}{\nu}\right)_m \qquad 2.11$$

Since viscosity of the model and prototype are equal, equation (2.11) reduces to

$$\frac{u*_p}{u*_m} = \frac{d_m}{d_p} \qquad 2.12$$

If equation 2.12 is now used to define the grain size it will provide a model grain size larger than the prototype grain size. This is because the friction velocity of the model will be smaller than that of the prototype. Clearly this is impractical because it will be more difficult to move larger grains in the model which has lower current speeds. If the grain size scaling were to follow this similarity rule, the grain size used in the model will be either too large or too small to reflect reality. In this experiment, therefore, the geometric similarity is ignored and a mean grain diameter of 0.18 mm of sandy material has been used. The choice was based on sediment availability at UCL laboratories and also on a number of trial experiments, in which the patterns of erosion and accretion were closely inspected to ensure they replicated the prototype threshold for sediment erosion during times of peak tidal flow. The sinusoidal variation of the current speed could not be replicated in the flume. Table 2.7 summarises the physical modelling parameters.

Table 2.7. Prototype and model parameters.

Parameter	Prototype	Model
Water depth	20 m	0.15 m
Width	25 km	0.244 m
Grain size	270 μm	180 μm
Depth-averaged velocity	1 ms^{-1}	0.043 ms^{-1}
Period	12.42 hrs	1.07 hrs

2.7.2 Results

The patterns of erosion and accretion that occurred around the headland were monitored over four tidal cycles. The flow was reversed by switching the position of a weir gate from one end of the flume to the other and pumping water in the opposite direction. Bed changes around the headland were monitored by projecting a grid image onto the bed and recording the change at regular intervals. The projected grid can be seen in Figure 2.28.

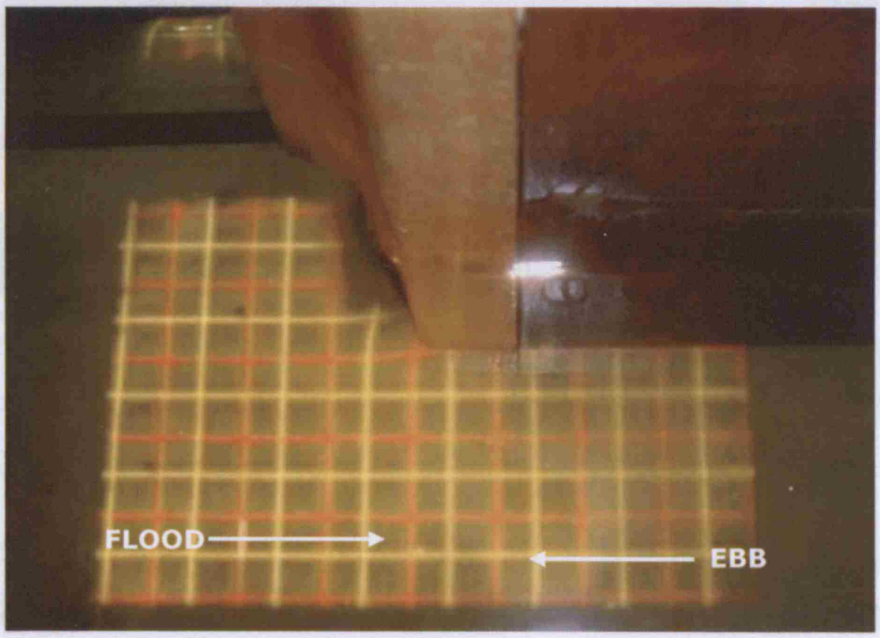

Figure 2.28. Grid image projected onto the sand bed around the semi-Gaussian headland. Also included are the ebb and flood tidal directions.

Observations of the streamlines were made by injecting a dye tracer at locations around the headland. These revealed the presence of a low velocity zone behind the headland during the ebb phase. In addition, the dye tracer demonstrated the presence of secondary currents close to the headland tip, established in response to flow curvature and the horizontal pressure gradient field.

During the ebb phase there is an overall deceleration in the velocity field due to continuity effects and, hence, very little in the way of bed erosion. During the flood phase however, the flow velocity increases to as much as 0.12 ms^{-1} close to the headland which is four times the mean current speed. This caused a significant pressure gradient field and a strongly erosive secondary current that was detected by the dye tracer. The secondary currents could be observed to scour sediment from the headland tip and carry both suspended and bed-load material further downstream. Deposition of the material occurs approx. 5-10 cm downstream. The development of the seabed during four tidal cycles can be seen in Fig. 2.29

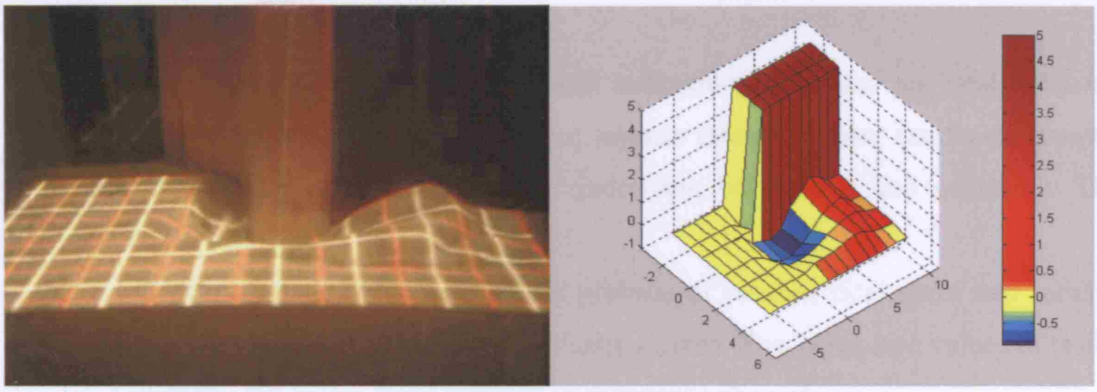

Figure 2.29 (a) Photographed and (b) plotted bed changes (in cm) from around the headland after four tidal cycles. (Both images were made by MSc student Min-Jung Kim who was working closely with me).

In contrast to the numerical experiments, described earlier, the physical experiments predict a large amount of sediment accumulation on the eastern side of the headland. In the numerical experiments, the ebb tidal flow was too fast to permit the build up of any significant deposit. Further, the mechanism generating the sediment transport in the

physical tests was the strongly erosive secondary currents that were local to the headland tip. In the numerical experiments, sediment erosion was due mainly to the primary currents.

The secondary mechanism described above clearly dominates the morphological regime in the physical experiments. To the west of the headland (i.e. in the area comparable to the location of the Nash Sands) there is no build up of sediment.

The results demonstrate that the experimental facilities that were available are insufficient to simulate the physical processes that occur at the real scale of headland sandbank formation. The main problem is that the ebb velocity is insufficient to erode sediment in the upper channel, a phenomenon which is present both in the numerical experiments and in the upstream and downstream channels of the area surrounding the Nash Sands.

2.8 Summary

Numerical modelling of water flow and sedimentation around an idealised coastal headland has demonstrated a number of aspects related to how sandbank growth is initiated in response to tidal forcing, underlying bathymetry and geometry. These include the following:

- A causal relationship between the position of residual tidal gyres and sandbank generation does not exist for the situation tested. This is because values of residual velocity fall below those relevant to sediment transport;
- There is a lack of correlation between instantaneous gyre positions and sediment accretion and the primary zones of sediment accretion are much more closely related to the positions of large gradients in the peak current fields.
- The Coriolis effect can affect the distribution of sediment around a headland as it can affect tidal jetting near the headland tip. This is what influences accretion very close to the headland and, therefore, affects the supply of sediment to offshore areas in which sandbank accumulation occurs. Tests conducted at negative latitudes (i.e. the southern hemisphere) demonstrated a switch in the orientation of the mechanism in response to the Coriolis effect.

Analysis using advective and topographic vorticity computations demonstrated that the Coriolis effect enhances advective vorticity on one side of the headland and that the response of the bed is then reflected in the trend in topographic vorticity production that develops as the simulation progresses: as more sediment is pushed to the opposite side of the near-headland area, there is an increase in topographic vorticity production on that side.

An investigation into the influence of coastal slopes on these types of headland has further revealed the impact of the Coriolis effect in advective vorticity production. It has been shown that in regimes where the ratio of advective to topographic vorticity production is close to unity, the influence of the Coriolis effect is more important and this is expressed in the asymmetry of the bed. In regimes where topographic vorticity is more dominant because of a seabed slope, the Coriolis effect becomes less important compared to the antecedent geology (including the slope and the headland shape). Therefore, the impact of the Coriolis effect is very small and is not the cause for the asymmetric accumulations of material that are found around many prominent coastal headlands.

Numerical tests conducted using a semi-Gaussian headland shape predicted much smaller transient gyre formation and asymmetric patterns of sediment accretion. The positions of residual gyres, however, coincided much more closely with those of sediment accumulation. Upon increasing the magnitude of the ambient current field, sediment accumulation on the narrow side of the semi-Gaussian headland ceased with accretion on the opposite side increasing and moving further away from the headland. The resulting hydrodynamic field and predicted region of erosion and accretion were comparable to those found around the Nash Point in the central Bristol Channel which exhibits a similar headland geometry. Coincidence of the residual sediment transport field and the zone of sand accumulation to the north-west of the headland suggest a possible relationship between then as the sandbank develops. This final point is explored further in Chapter 5.

3. Construction and Verification of a Process-based Model for the Bristol Channel/Swansea Bay Area, U.K.

3.1. Introduction

The following chapter focuses on the construction and optimization of a process-based model designed to capture important sediment transport processes around an existing headland sandbank and its surrounding area. The Nash Sands of the central Bristol Channel (see Figure 3.1) is used as a case study where both strong tidal and wave effects need to be described by the model at a range of spatial scales. This introduces a significant computational overhead and thus it is the aim of the following experiments to provide a model that is capable of:

a) capturing *all* significant processes and

b) doing so in an efficient and practical way.

The resulting model set-up is then employed in Chapters 4 and 5.

3.1.1 Model Reduction

Process-based models make predictions by solving discretised empirical or Newtonian equations using numerical techniques. Therefore, the accuracy of the predictions is directly related to the sophistication of the incorporated equations. State of the art systems are reliable at predicting complex hydrodynamics but application to morphodynamical simulation becomes increasingly unreliable over longer time-scales (see Leont'yev, 2003). This is a reflection of our current knowledge of longer-term processes and interactions. This study focuses on the design of a coupled modelling system, set up to improve understanding of a particularly complex coastal environment.

A number of techniques have been developed that assist the validity of process-based morphological simulations (see De Vriend et al., 1993; Latteaux, 1992). These include the use of both input and model 'reduction' techniques. In this study we focus primarily

on making a contribution to the latter. Recent studies, including Sandpit (2005), tested a number of 'state of the art' morphodynamic modelling systems and suggested large differences in predictions despite the similarities in the underlying equations and assumptions of each model. These differences were attributed to the varying input and model reduction approaches taken by the individual modellers.

Model reduction involves taking advantage of the difference in time scales between hydrodynamic and morphological change. This helps to reduce the complexity of the model and improve the long-term efficiency. There are two main approaches to process-based model reduction. The first usually involves an increase of the morphological time-step and is employed in large coupled models. The second, sometimes referred to as 'formal model reduction', involves a more fundamental analysis of the underlying equations and assumptions that drive processes at the coastline. The subject forms a branch of modelling that is useful in understanding the processes behind cyclical morphological features. In the present study this type of approach is not valid because the feature of interest is an isolated headland sandbank feature.

Increasing the morphological time-step involves a combination of:

- An increase in the time-step between consecutive calls of the sediment transport and morphological models. In between the calls, the bed is updated by extrapolating incremental bed changes computed at a previous time-step by establishing relationships between the waves/flow and bathymetry. (See De Vriend et al., 1993, for further details);
- The 'Online' method. This involves multiplying the bed changes computed during one hydrodynamic time-step by an acceleration factor (see Roelvink, 2006).

MIKE 21/3 FM, used in this study, updates the bed using the 'Online approach'. The sediment transport rates are updated at a user-defined interval of the hydrodynamic computations.

3.1.2 Further Model Reduction

Restricting the number of simulated wave conditions to only those responsible for sediment transport also helps to minimise the computational effort. This study aims first, to identify and include only wave conditions that are significant to sediment

transport, and second, find the minimum frequency at which the wave field needs to be recomputed. Additional improvement of the model efficiency is then sought by simple optimization of the mesh geometry. This includes reductions in both the grid resolution and domain size.

3.1.3 The Study Area

The Bristol Channel is a large macro-tidal inlet in the western U.K. The region is subject to a diverse range of the wind and wave conditions and has one of the highest tidal ranges in the world. This provides the backdrop to strong wave-current interaction and complex tidal and wave-driven sediment transport.

A number of studies (Harris and Collins, 1985; Harris and Jones, 2005) have hypothesised that in spite of the ebb-dominated tidal transport, there exists a wave-induced easterly directed transport pathway providing a potential mechanism for importing marine derived sediment into the north eastern part of the central Bristol Channel.

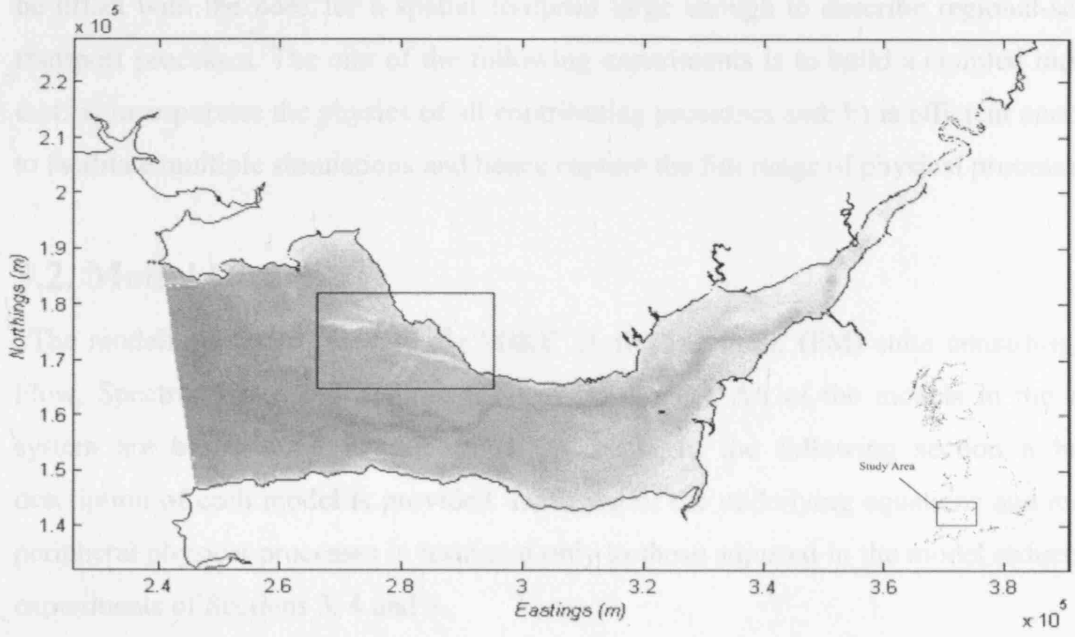

Figure 3.1 . The Bristol Channel study area. The boxed area marks the location of the Nash Sands.

Waves induce a time-averaged mass and momentum flux within fluid in which they propagate (see Longuet Higgins and Stewart, 1964, van Rijn, 1993). With progressively shallower water, non-linearities of the propagating waves become more pronounced and the asymmetry of the waves increases. This generates vertical and horizontal gradients in the mass and momentum fluxes. If waves approach at an oblique angle, this excess flux is driven parallel to the coastline in the form of a long-shore current. Longuet Higgins and Stewart (1964) explain this phenomenon using the 'radiation stress concept'. In addition to the radiation stresses, waves also affect sediment transport by increasing the near-bed orbital velocity and shear stress. The present model scope needs to include all of these wave-induced sediment transport processes as well as describing the effects of tidal currents and wave-current interaction.

3.1.4 Model Aims

Capturing these processes within a reasonable computational time-scale requires extensive model optimization and reduction. High resolution in the breaking zone must be offset with the need for a spatial footprint large enough to describe regional-scale transport processes. The aim of the following experiments is to build a coupled model that: a) incorporates the physics of all contributing processes and; b) is efficient enough to facilitate multiple simulations and hence capture the full range of physical processes.

3.2. Model Design

The modelling system used is the MIKE 21 flexible mesh (FM) suite consisting of Flow, Spectral Wave and Sediment Transport models. All of the models in the FM system are based on a flexible mesh approach. In the following section a brief description of each model is provided. Inclusion of the underlying equations and more peripheral physical processes is restricted only to those adjusted in the model reduction experiments of Sections 3, 4 and 5.

3.2.1 Model Coupling

In the coupled wave / current approach of this modelling study, the effects of wave setup and momentum gradients are incorporated by extracting the radiation forces (S_{xx}, S_{yy} and S_{xy}) from stationary wave simulations (see Fig. 3.2). The resulting tensor field is then passed on to a coupled hydrodynamic/sediment transport model (henceforth, HD/ST) in which the radiation stress gradients, ($\partial S_{xx}/\partial x, \partial S_{yy}/\partial y, \partial S_{xy}/\partial y$) drive momentum and mass fluxes, promoting wave-induced currents and long-shore transport. Simulating the wave-induced sediment transport in the HD/ST model depends on the detail in which wave decay is resolved in the near-shore zone by the wave model. Resolving this correctly requires an accurate description of the near-shore bathymetry. The approach also requires the simulation of a large number of combined wave and water level conditions to capture the full range of potential wave conditions.

During the final HD/ST simulations, the sediment transport rate invoked by the effects of both wave-induced currents and tidal forcing are derived by interpolation from a pre-computed look up table, calculated using the DHI *Sediment Transport Program* (see Section 3.2.4).

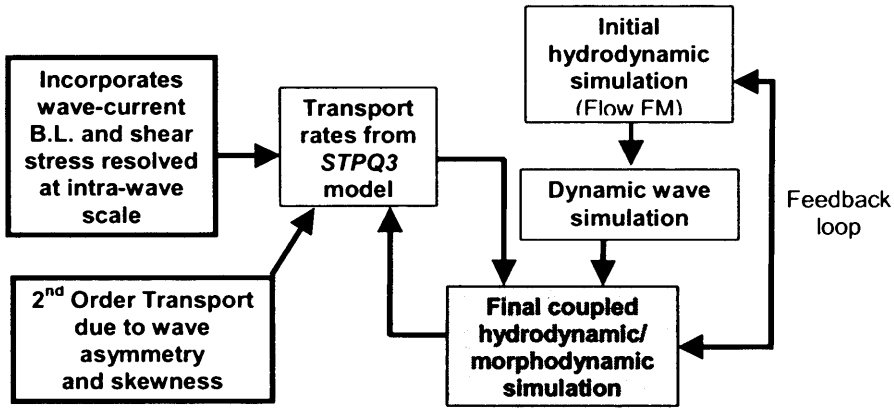

Figure 3.2. Details of the model coupling procedure.

3.2.2 The Wave Model

The MIKE 21 SW Spectral Wave model includes two types of algorithm which vary in their level of sophistication. To reduce computational run times, this study uses the

parametrically decoupled version of the model (henceforth DS module). The DS module solves the wave action balance equation (see Komen et al., 1994) as a stationary or in-stationary (time dependent) solution over frequency, direction and space employing two paramaterisations to improve efficiency. Results of a validation exercise are presented comparing the performance of the DS model with real measurements from the Bristol Channel.

3.2.3 The Flow Model

The hydrodynamic model solves the two dimensional Reynolds averaged Navier-Stokes equations invoking the approximations of Boussinesq and hydrostatic pressure. This involves continuity, momentum, temperature, salinity and density equations (DHI, 2005). Results of a full calibration exercise is presented in Appendix 3.

3.2.4 The Sediment Transport/Morphological Model

In order to capture the combined effects of wave and current action on bed shear stress and sediment transport, it is necessary to resolve the boundary layer in as much detail as possible. The physics of the boundary layer, however, becomes increasingly complicated under the combined influence of waves and currents (see Bakker & Van Doorn, 1978; Kemp & Simons, 1983). In the present study, an approach is sought that incorporates modifications to the boundary layer from orbital wave motion and also adjustments to the vertical balance of forces induced by the action of wave breaking and setup (gradients in radiation stresses).

For this purpose DHI's *Sediment Transport Program*, henceforth *STPQ3*, is employed which provides a quasi-3D description of the hydrodynamic force balance through the water column and hence an improved description of the wave-current boundary layer. The approach resolves the spatial and temporal variation of shear stress, flow velocity and sediment concentration using the integrated momentum approach of Fredsøe (1984). The main drawback with this approach is the effort required to re-compute the boundary layer characteristics at every call to the sediment transport model. Therefore to reduce this, a form of model reduction is employed in which a detailed look-up table is pre-computed for a range of wave/tide/sediment combinations that cover the

conditions of the modelling study. During the simulation, sediment transport rates are interpolated from the look-up table at each call to the sediment transport model.

3.3. Mesh and Domain Optimisation

3.3.1 Choice of Mesh size

The hydrodynamic model solves the Reynolds-averaged Navier-Stokes equations at the centre of each element in the model domain. The size and spacing of the elements determine the limits of the 'resolved' and 'unresolved' domains (Abbott & Minns, 1998). In order to incorporate the influence of the sub-grid or 'unresolved' flow on the 'resolved' flow, the model uses a turbulence closure scheme to dissipate energy from the system. Models with larger element sizes require more energy to be diffused at the sub-grid scale and hence introduce more uncertainty into their predictions. The model uses the approach of Smagorinsky (1963) to dissipate energy at scales smaller than the mesh spacing (Δx_n). The method assumes that the ability of a fluid to sustain internal shear stresses is related to the mean strain rate tensor ($\partial\overline{u}_i/\partial x_j + \partial\overline{u}_j/\partial x_i$) by a 'turbulent eddy viscosity' υ_t,

$$\tau_{ij} = \upsilon_t \left(\frac{\partial \overline{u}_i}{\partial x_j} + \frac{\partial \overline{u}_j}{\partial x_i} \right) \tag{3.1}$$

υ_t is computed as a function of a characteristic length scale, h, based on the mesh spacing,

$$h = [(2\Delta x_1)(2\Delta x_2)(2\Delta x_3)]^{1/3} \tag{3.2}$$

and is itself a function of the intensity of the rate of shearing in the fluid (S_{ij})

$$\upsilon_t = a_1^2 h^2 \sqrt{S_{ij} S_{ij}} \tag{3.3}$$

Equation 3.3 suggests that the turbulent eddy viscosity tends to zero as the second power of the grid size (Abbott and Minns, 1998). The shear stress (τ_{ij}) and, therefore, the sub-grid energy removed from the system also tends to zero with the second power of the grid size. As the grid spacing gets smaller, the diffusive effect of the turbulence closure scheme reduces. Ideally the turbulence closure scheme should dissipate energy to the same extent as infinitesimally small grid spacing. However, this is not the case, due mainly to the selection of the constant, a_1. In highly variable flow fields, it is unclear what value to assign for a_1 and the sub-grid energy dissipation is miscalculated.

The purpose of the following experiment was to find, under dynamic forcing conditions, a grid resolution in which the turbulence closure scheme is not invalidated by the assumptions described above. A constant $a_1 = 0.28$ was used in all tests (as suggested by the DHI user manual (DHI, 2005) and grids of 15 m, 25 m, 45 m, 65 m and 85 m and 105 m. For the model domain, a region around the Nash Sands in the central Bristol Channel is isolated (see Fig. 3.1 (a)), and using each grid in turn, an 8 m tide is propagated from the western boundary. Boundary conditions used to define the 8 m tide include deep water constituents obtained from the KMS global tidal model (Andersen, 1995), calibrated using TOPEX and POSEIDON satellite altimetry data. Velocity measurements are recorded at 10 observation positions inside the model (positions indicated in Fig. 3.3 (a)).

Comparison of mean current speeds of the different grid resolution models (Fig. 3.3 (b)), suggest that the 15 m, 25 m, and 45 m predictions are similar. Mean velocity predictions of the larger node separation models (65 m, 85 m and 105 m), however, show deviation from those of the higher resolution. The mean velocity standard deviations of the 25 m and 45 m lower resolution models compared to the 15 m node separation model, are 0.03 m/s and 0.05 m/s, respectively. For the lower resolution models, however, this rises to 0.13 m/s, 0.16 m/s and 0.18 m/s for the 65 m, 85 m and 105 m resolution models respectively. These results suggest that, at this water depth, a node separation of 45 m is preferable.

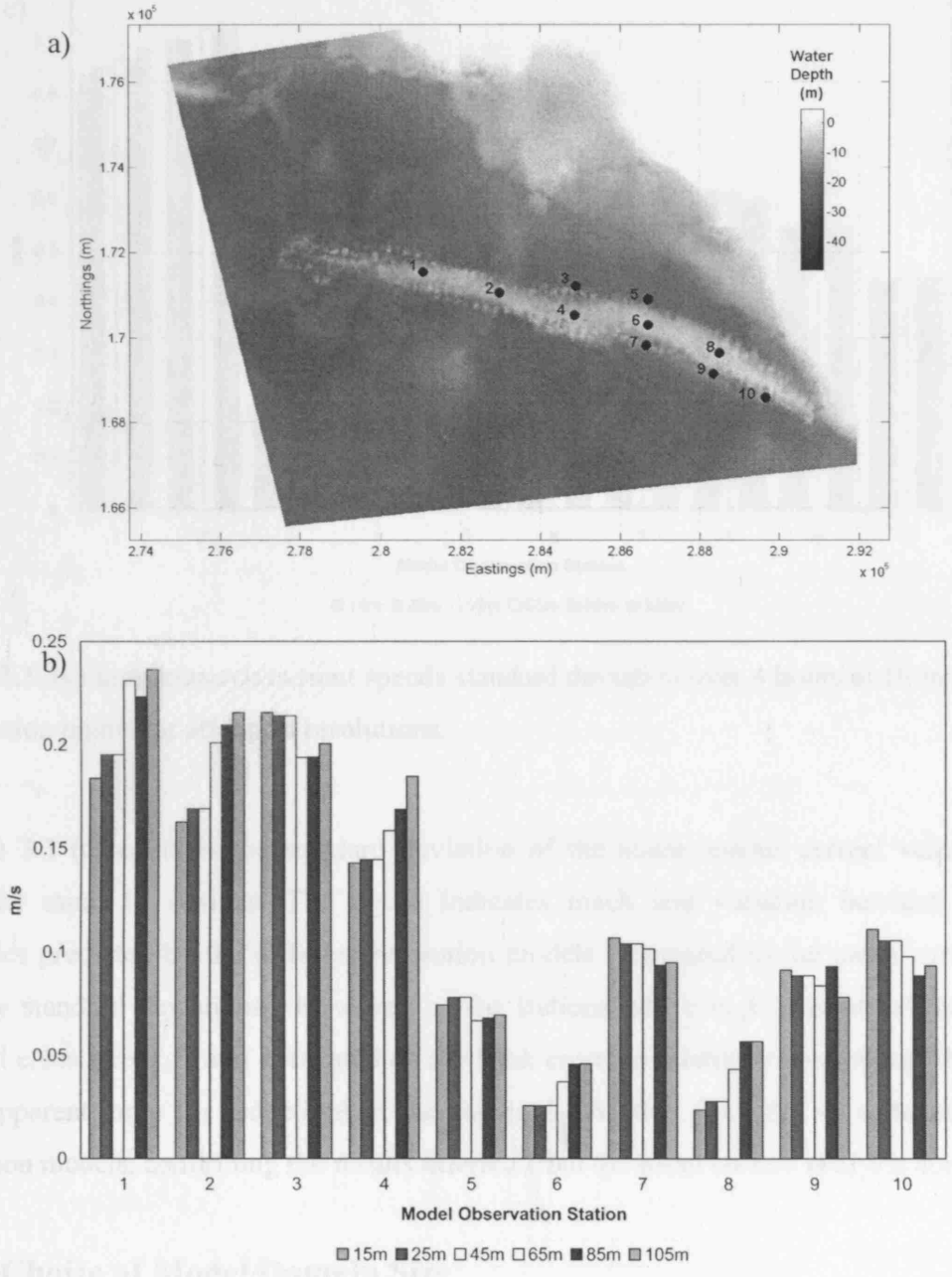

Figure 3.3. . (a) Region selected for grid resolution tests including positions of model observation points. (b) Mean current speed over 4 hours at 10 model observation points for all 6 grid resolutions.

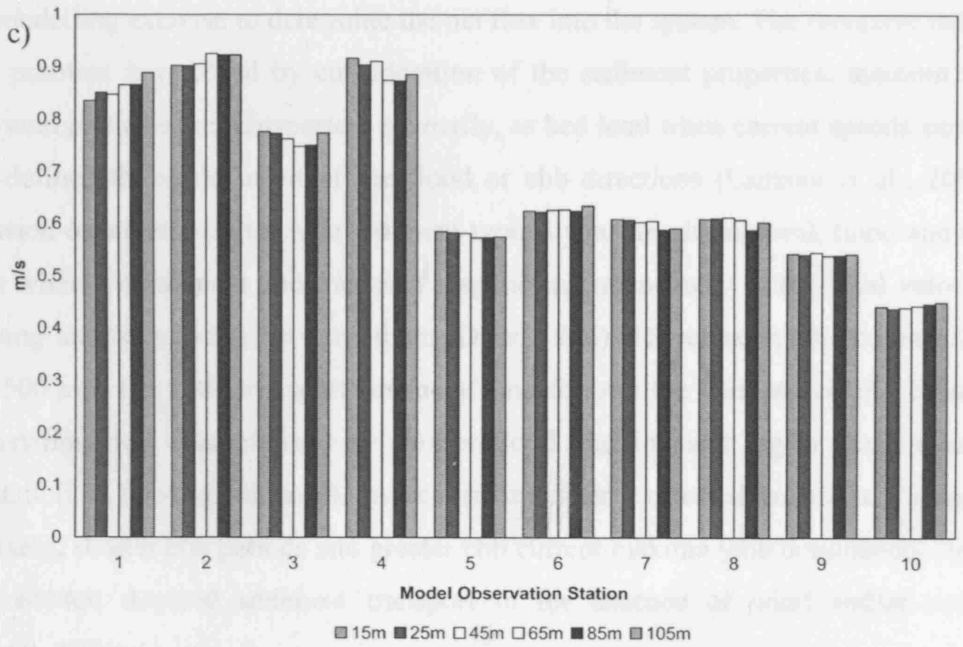

Figure 3.3. (c) Instantaneous current speeds standard deviation over 4 hours at 10 model observation points for all 6 grid resolutions.

Figure 3.3 (c) contains the standard deviation of the instantaneous current velocity from the same 10 stations. The figure indicates much less variation between the velocities predicted by the different resolution models (compared to the mean current velocity standard deviations). However, at the stations where high current velocities persist i.e. stations 1, 2 and 4, located on the bank crests in relatively deep water, there is an apparent jump (or reduction) in the standard deviation from the 45 m to 65 m resolution models, confirming the results inferred from the mean current analysis above.

3.3.2. Choice of Model Domain Size

The next test focuses on minimizing the size of the modelling domain. The argument in favour of using a large macro-scale model in the Bristol Channel is that it can provide a better description of the regional sediment fluxes: the sediment has more time and space to adjust to the dynamic forcing and reach an equilibrium state that is representative of the real conditions. In this study, very few observational data are available from which to derive a flux boundary condition; indeed, it is one of the aims

of the modelling exercise to determine the net flux into the system. The recursive nature of this problem is resolved by consideration of the sediment properties: medium and coarse sand particles are transported, primarily, as bed load when current speeds exceed a well-defined threshold in either the flood or ebb directions (Lanzoni et al., 2002). Suspension of medium and coarse sediment typically occurs during peak flood and ebb periods where entrainment and transport respond instantaneously to the fluid velocity, displaying almost zero lag between them (Dyer, 1986). Therefore, medium sand (250 μm to 500 μm) has little transport 'memory' and follows the current velocity closely. Flow asymmetries, characterized by shorter flood duration and higher flood current maximum (i.e. flood dominance), induce an up-estuary directed sediment transport. Conversely, shorter ebb periods and greater ebb current maxima (ebb dominance) cause a net seaward directed sediment transport in the absence of wind and/or waves (Dronkers, 1986).

The above argument is derived in order to propose the use of a curtailed regional model of the Bristol Channel, its western boundary extending to a line connecting Bull Point with the Gower Peninsular (see Fig. 3.4). It is also assumed that, given an adequate model warm-up period, the system will achieve an equilibrium sediment concentration that is representative of the regional conditions. To validate this, two grids are tested including a larger regional domain and a smaller curtailed domain, the western boundary of which is detailed by the white dashed line in Figure 3.4.

A particularly energetic period of wave action was selected from February 2004 in which wave heights exceeded 4 m (H_s) and wave periods were in the range of 9 to 18 s (T_{peak}) (4 month return period). The experiment consisted of the following steps:

1. An initial hydrodynamic model simulation was run using deep water tidal constituents (Andersen, 1995) defined at the western boundary at a resolution of 0.25 degrees;
2. A wave simulation was run using the large computational grid over the dynamic water levels and currents computed in Step 1). This provided an unsteady radiation stress field that varied due to both the external wave forcing and the internal water levels and currents;

3. A final coupled flow and sediment transport model was run over the same period utilizing the radiation stress field and integral wave parameters previously computed in Step (2) to drive the sediment transport.

The coupling between the wave and the current calculations consisted of the wave field being re-calculated at 15 minute intervals using feedback from the water levels and currents. A uniform grain size of 270 μm was used in the tests. The same procedure was then repeated using the curtailed computational mesh. Total load transport averaged over one tide for the large and curtailed model domains has been plotted in Figure 3.5 (a) and (b) respectively. The difference between the large and curtailed model gross transport predictions is plotted in Figure 3.5 (c). The results demonstrate that there is a negligible difference between the large and the curtailed model predictions. The overall difference in the gross transport predicted by the two models is only 2.2 %.

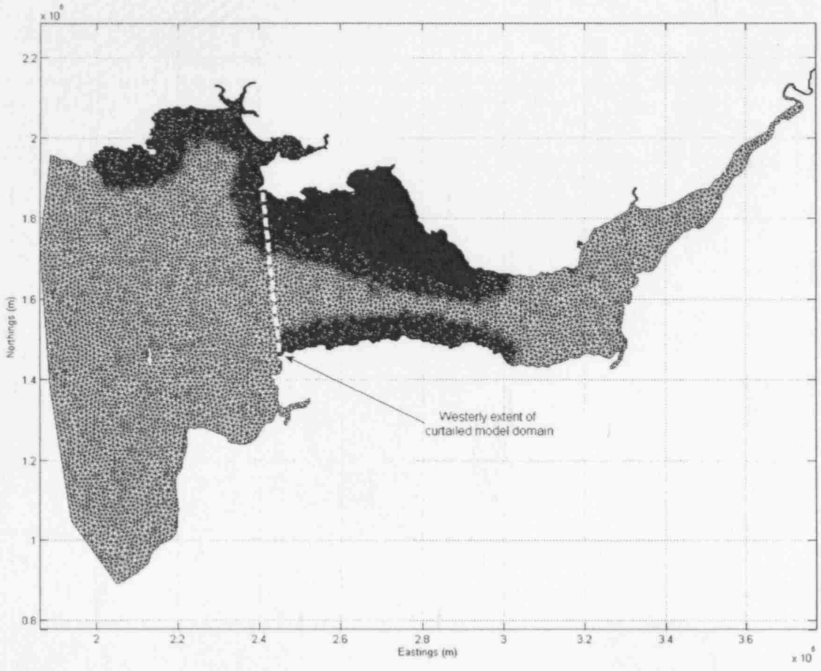

Figure 3.4. Larger regional mesh, initially constructed for the complete modelling study. Figure includes the western boundary of the curtailed mesh, proposed for optimising model CPU time.

In addition to examining the spatial difference in the gross transport predicted by the two models, predictions at coastal locations, where there exist strong non-linear effects due to wave-current interaction, were also examined. Ten locations at which the water depth was less than 10 m were selected (see Figure 3.6) and the predictions from both models compared. The results indicated a difference in the predicted total load magnitude (summed over 1 tide) of less than 10% (see Figure 3.7). The tests also confirm that the prescription of an initial boundary flux is not a requirement because of the equilibrium character of the sediment transport in this particular situation.

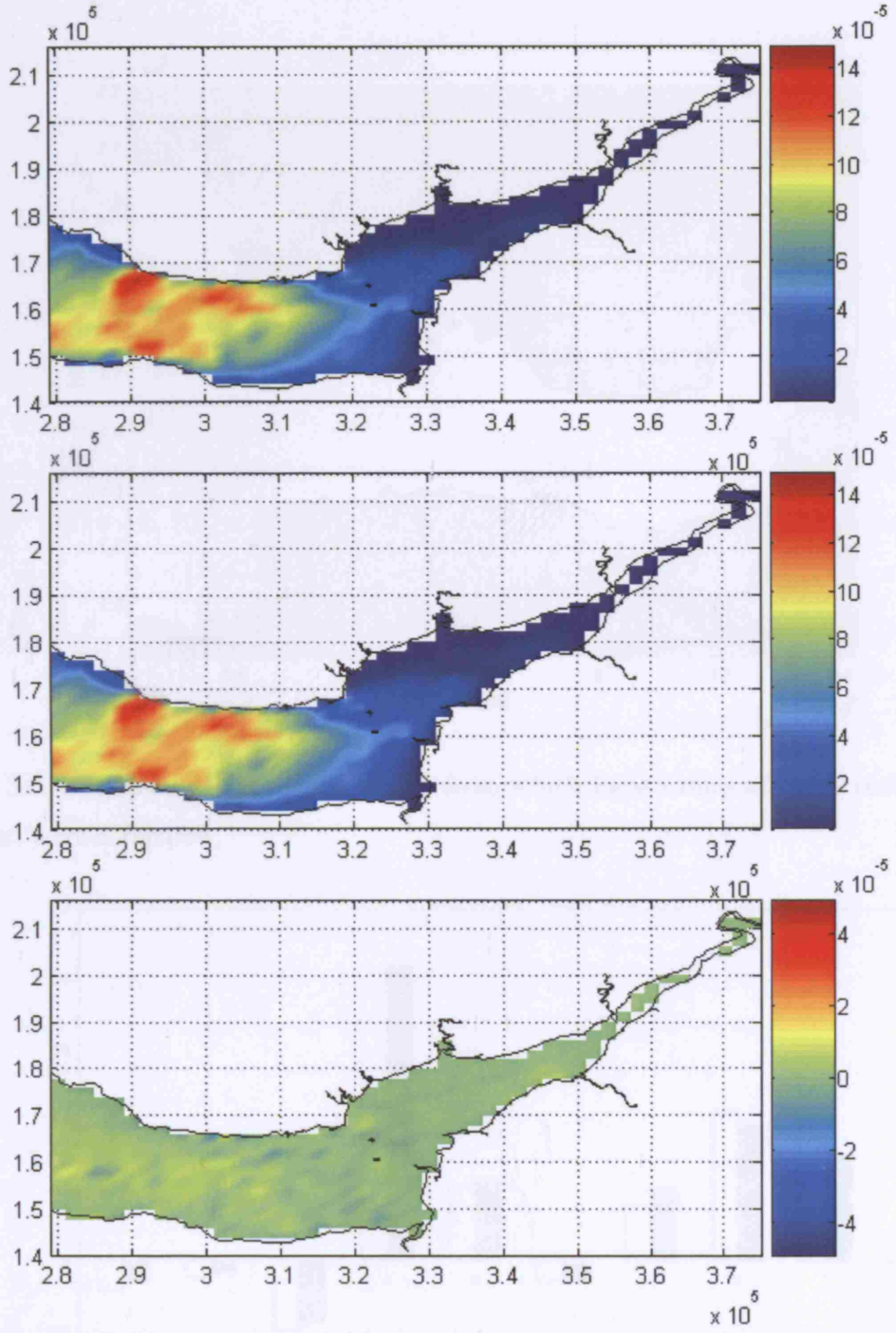

Figure 3.5. Predictions of total load magnitude summed over one tide for: (a) the large model domain and; (b) the curtailed model domain. (c) Difference in total load magnitude summed over one tide predicted by the two models. Units are m^3/m.

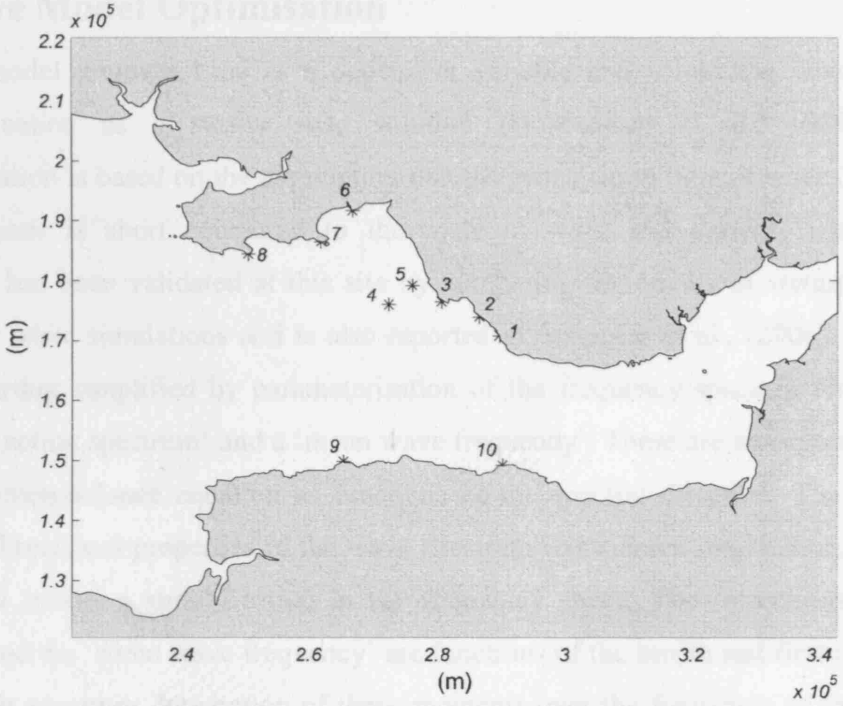

Figure 3.6. Locations of the coastal points from which local values of gross sediment transport were compared.

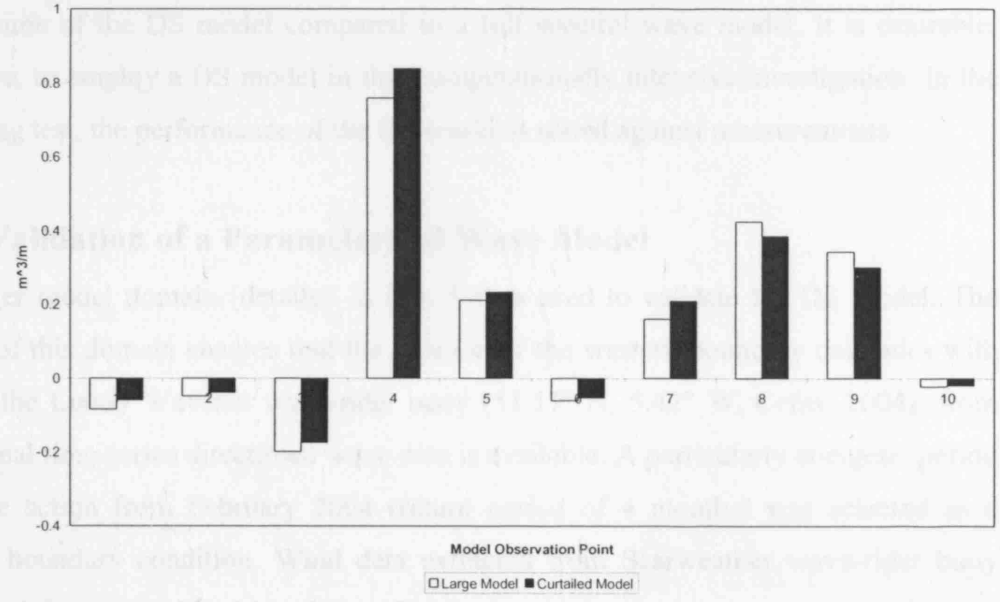

Figure 3.7. Predictions of total load magnitude summed over a single tide at the near-shore locations indicated in Figure 3.6. Positive values indicate accretion.

3.4. Wave Model Optimisation

The DS model removes time as a dependent variable and solves the wave action balance equation as a steady state solution (Holthuijsen et al., 1989). This parameterisation is based on the assumption that the propagation time of waves through coastal regions is short compared to the scale of wind and current fields. This assumption has been validated at this site by comparing the results of stationary and instationary wave simulations and is also reported in Sørenson et al., (2006). The DS model is further simplified by parameterisation of the frequency space in terms of a 'directional action spectrum' and a 'mean wave frequency'. These are incorporated into the wave action-balance equation as functions of the spectral direction. The method retains the directional properties of the wave spectrum (considered important in coastal regions) but makes a simplification in the frequency space. The 'directional action spectrum' and the 'mean wave frequency' are functions of the zeroth and first moments of the action spectrum. Integration of these moments over the frequency of the wave-action spectrum provides spectral dependency of the wave propagation in the DS model (see Holthuijsen et al., 1989 and Sørensen et al., 2006). The two paramaterisations reduce the number of degrees of freedom from 125 to 25, and provide a 5-fold decrease in run time of the DS model compared to a full spectral wave model. It is desirable, therefore, to employ a DS model in this computationally intensive investigation. In the following test, the performance of the DS model is tested against measurements.

3.4.1 Validation of a Parameterised Wave Model

A larger model domain (detailed in Fig. 3.4) is used to validate the DS model. The choice of this domain ensures that the position of the western boundary coincides with that of the Lundy Wavenet wave-rider buoy (51.17° N, 5.42° W, Cefas, 2004), from which real time-series directional wave data is available. A particularly energetic period of wave action from February 2004 (return period of 4 months) was selected as a driving boundary condition. Wind data extracted from Scarweather wave-rider buoy (51.39° N, 3.91° W, U.K. Met. Office, 2005) over the same period is applied uniformly across the domain.

Wave simulations are performed by propagating a time-series of wave height, period and direction, recorded by the Lundy wave-rider buoy, over a dynamic water level and current field. Wave-action transformations in the frequency domain are a result of changes in the bottom topography, ambient current (from the hydrodynamic model) and also from wave breaking. The wave breaking formulation used in the model is based on the approach of Battjes and Janssen (1978) where the source term due to depth-induced breaking is a function of the total wave energy, the relative mean frequency of the waves, the fraction of breaking waves and the wave height to water depth ratio (γ_b). Ruessink et al., (2003) have presented a new empirical method of calculating γ_b in which

$$\gamma_b = 0.76kD + 0.29 \tag{3.4}$$

where k is the wave number and D is the local still water depth. It was demonstrated that the prediction of wave heights on barred and planar beaches could be greatly improved using this formulation. The DS wave model uses this same formulation for the breaking parameter γ_b.

The performance of the model is assessed by comparing predictions of integral wave parameters with measurements at a wave-rider buoy in the upper Bristol Channel (for position see Figure 3.10 (a)). Results (see Fig. 3.8 (a) and (b)) show good correlation between model predictions and measurements. It is possible to see that towards the end of the simulation, where the wind direction shifts to a north-westerly direction, the model predictions of the peak wave period are less good (an error of at least 40 % is apparent). This can be attributed to the fact that the wave model was not set up to resolve waves from that direction. The main interest was in simulating wave propagation from a south westerly direction and so the number of directions defined in the model was reduced to improve efficiency. However, given the level of correlation between the measurements and predictions for the other wave directions (a maximum error of 10 % can be measured for waves propagating in a south westerly direction), the study proceeded with the PD wave model.

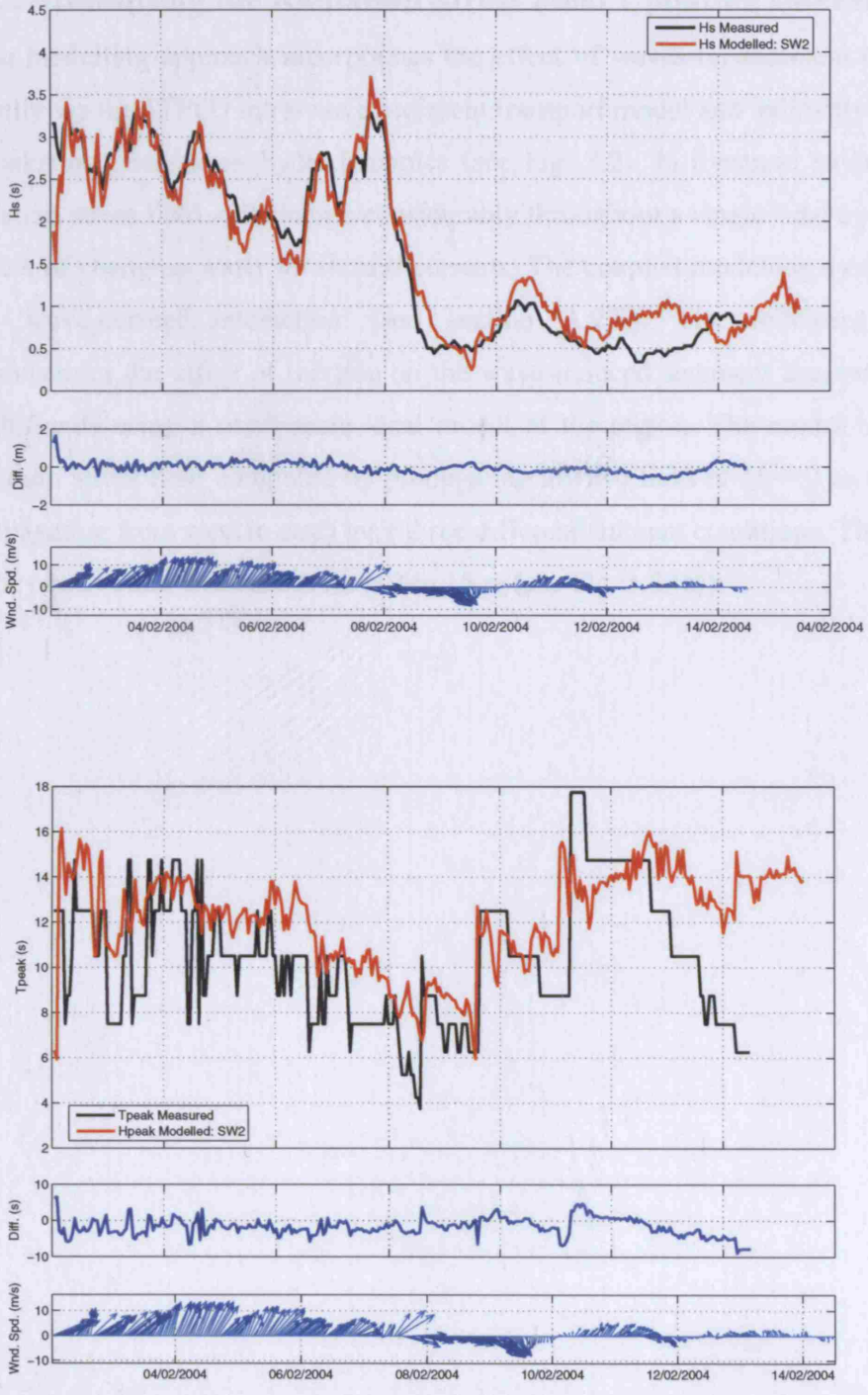

Figure 3.8. Comparison of measured and modelled (a) Significant wave height and; (b) peak wave period. Also plotted are time-series of calculated difference and wind speed/direction.

3.4.2 Minimising the Radiation Stress Field Updating Interval

The modelling approach incorporates the effect of waves on sediment transport both directly via the *STPQ3* intra-wave sediment transport model and indirectly via the effect of radiation stresses on hydrodynamics (see Fig. 3.2). In dynamic environments, the radiation stress field will change considerably throughout a single tidal cycle due to the effects of changing water levels and currents. The coupled modelling system simulates this wave-current interaction (see section A.2.3). The following experiment demonstrates the effect of the tide on the wave-induced sediment transport around the Nash Sands using a small-scale local model of the region. The model is driven by a radiation stress field computed by propagating a wave field of H_s = 2 m and T_p = 10 s (propagating from west to east) over three different ambient conditions. The water depth of the observation sites varies from 2 to 15 m (see Fig. 3.3 (a)).

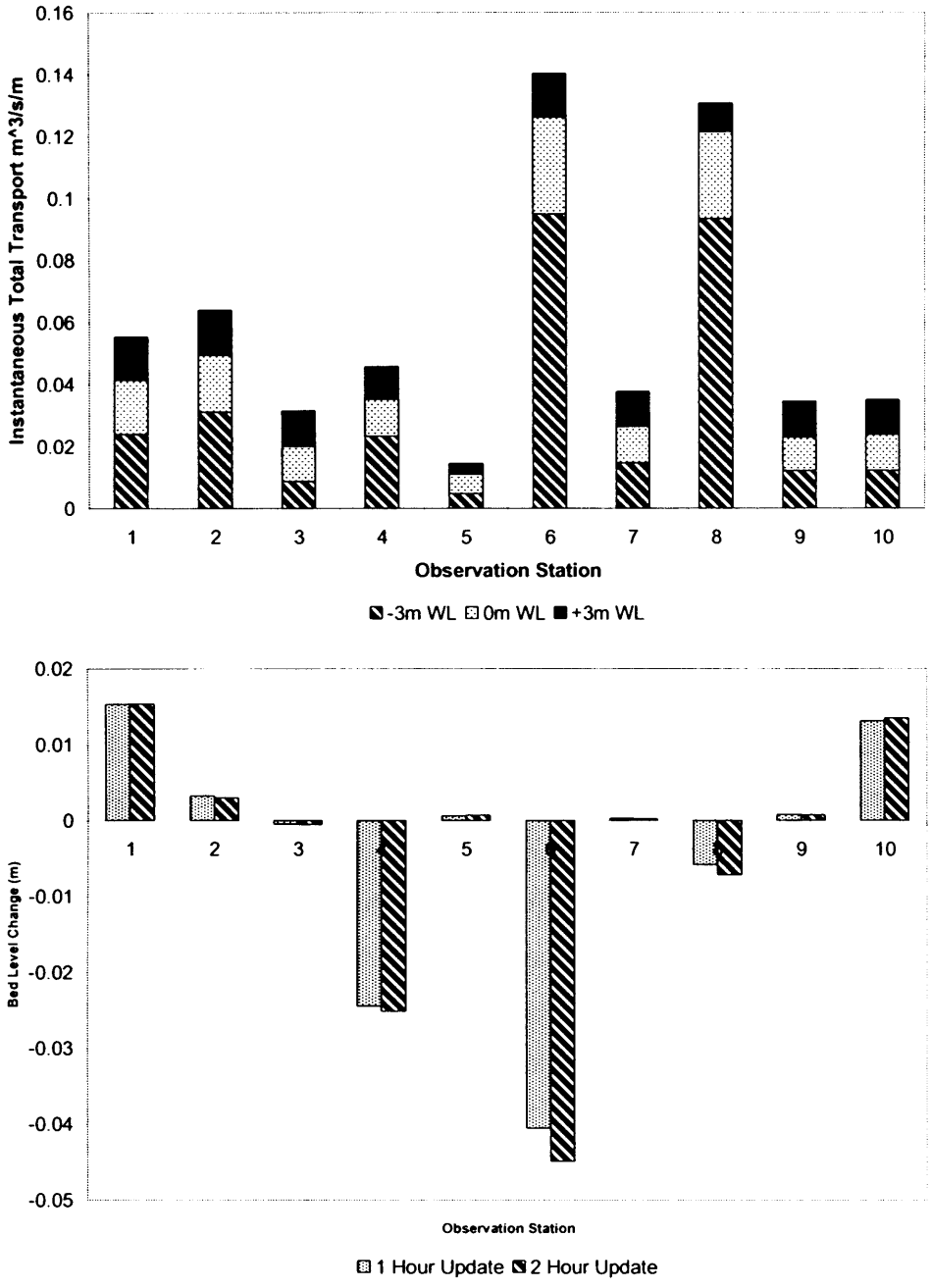

Figure 3.9. (a) Westerly component of sediment transport predicted for three tidal levels and; (b) bed level changes predicted at observation points under a 2 m (H_s), 10 s (T_{peak}) monochromatic wave.

The predicted rates of sediment transport (Fig. 3.9 (a)) indicate that a reduction in the water depth of 3 m can be related to a doubling in the sediment transport rates. The effect is even greater in shallow water locations. For example, at observation stations 5 and 6 situated at the crest of the sandbank, the predicted sediment transport increases by more than a factor of 3 for a reduction in water depth of 3 m. In addition to highlighting the importance of computing the radiation stresses on a dynamic water level, the test also highlights the need to re-compute radiation stresses a number of times within a complete tidal cycle. This idea is developed further in the next section.

Radiation stresses are computed at two update intervals of 60 and 120 minutes over a spring tide using the DS wave model and curtailed mesh validated in Sections 3.4.1 and 3.4.2. The resulting radiation stress fields are then utilised by the coupled HD/ST model.

Results from the two tests suggest that increasing the updating period from 60 to 120 minutes has only a limited impact on predictions. Comparisons of bed level changes from point locations at the Nash Sands (see Fig. 3.9 (b)) suggest only a fractional adjustment (maximum of 0.005 m). The difference is relatively minor, given that the test has been conducted under strong forcing conditions (spring tides and 5 m waves). The effect on the regional sediment transport is also negligible: comparison of the gross sediment transport at two cross-sections (see Figure 3.10 (b) and 3.10 (a) for positions) demonstrates an almost unnoticeable difference in the predicted transport. The results suggest that a relaxation of the updating interval, from 60 minutes to 120 minutes, is acceptable in this situation.

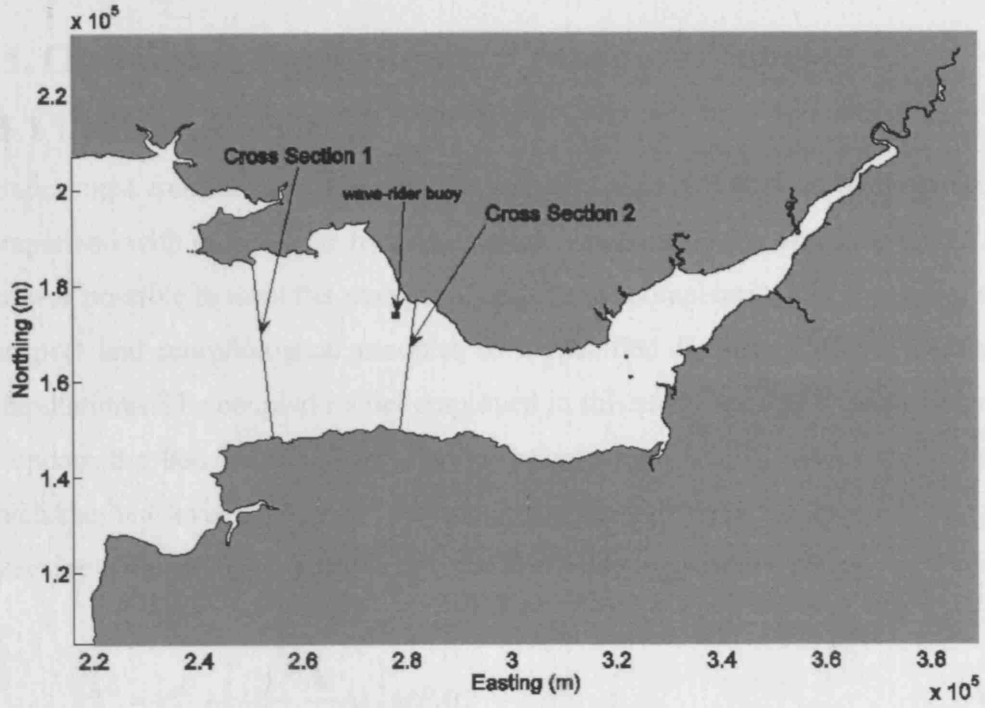

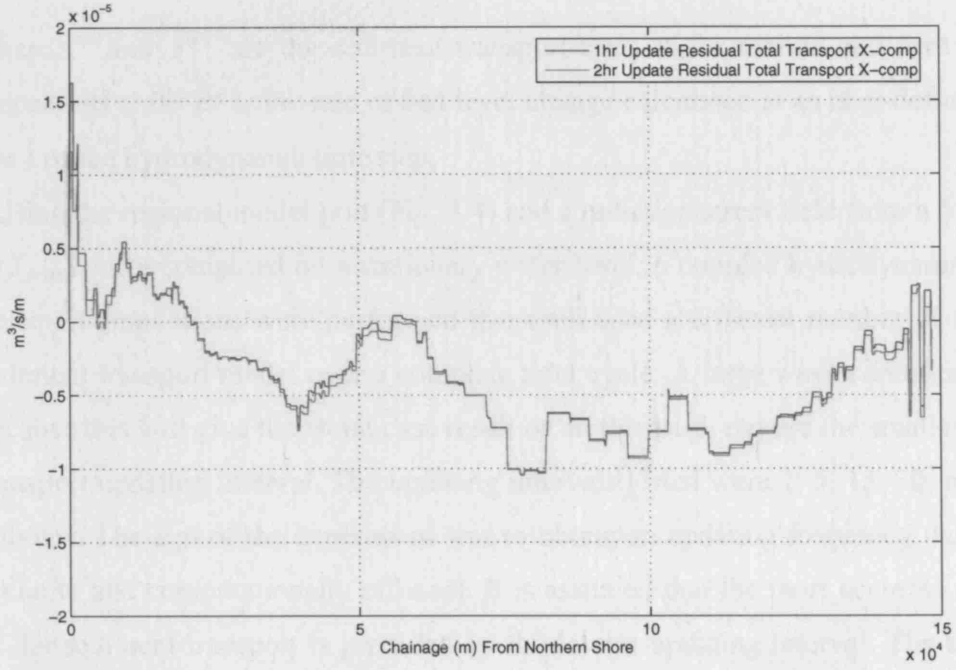

Figure 3.10. (a) Positions of 2 cross-sections at which sediment transport fluxes are computed. (b) Westerly component of residual sediment transport from cross-section 1, computed over 1 tidal cycle.

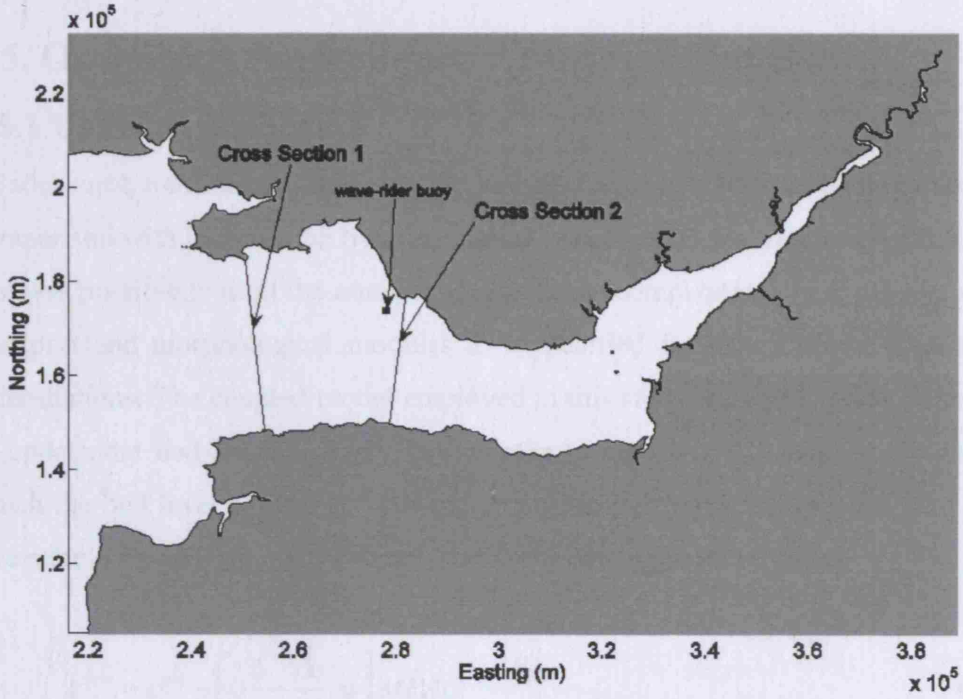

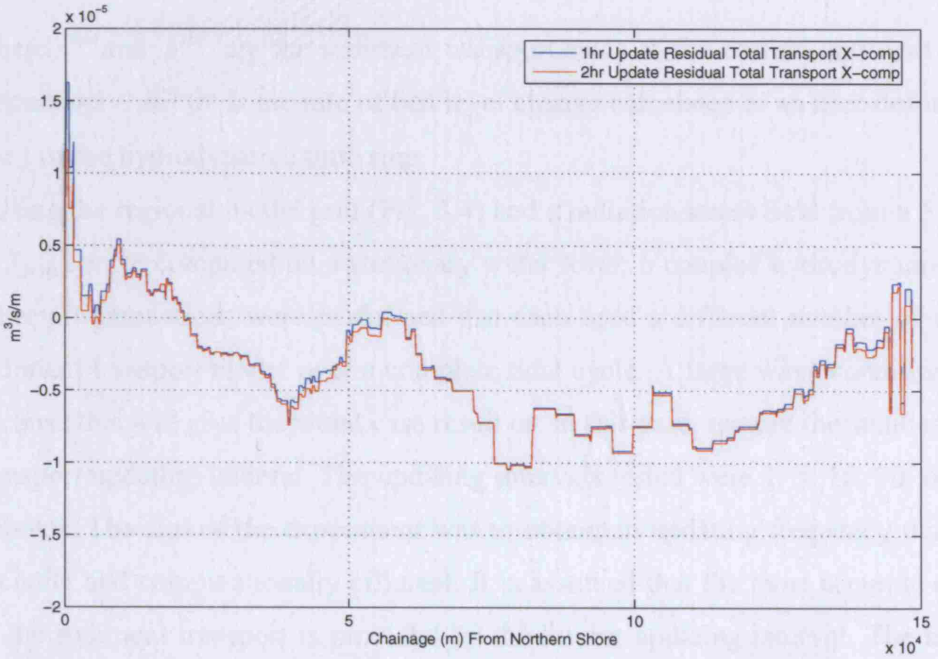

Figure 3.10. (a) Positions of 2 cross-sections at which sediment transport fluxes are computed. (b) Westerly component of residual sediment transport from cross-section 1, computed over 1 tidal cycle.

3.5. Optimising the Sediment Transport Models

3.5.1 Updating Frequency

Under most conditions, changes to the sediment transport and morphology are slow in comparison with those of the hydrodynamics (van Rijn, 1993). Intuitively, this suggests that it is possible to limit the number of calls to the computationally expensive sediment transport and morphological modules to a specified frequency of the hydrodynamic computations. The coupled model employed in this study uses an explicit Euler scheme to update the bed level at every hydrodynamic time step but relaxes the interval at which the bed level change and the sediment transport rates are updated. The new bed levels are obtained using a forward in time differencing scheme stating

$$z^{new} = z^{old} + \left[\frac{1}{1-n} \frac{\partial z}{\partial t} \Delta t \right] MFAC \tag{3.5}$$

where z^{new} and z^{old} are the sediment transport rates at the current and next time-steps respectively, $\partial z / \partial t$ is the rate of bed level change calculated at an user-defined interval (Δt) of the hydrodynamic time step.

Using the regional model grid (Fig. 3.4) and a radiation stress field from a 5 m (H_s), 12 s (T_{peak}) wave computed on a stationary water level, 6 coupled hydrodynamic/sediment transport simulations were performed that each used a different number of calls to the sediment transport model over a complete tidal cycle. A large wave condition was used because this will give the worst case result or, in this case, require the smallest sediment transport updating interval. The updating intervals tested were 1, 5, 15, 30, 60, and 120 minutes. The aim of the experiment was to obtain an updating frequency that was both accurate and computationally efficient. It is assumed that the most accurate description of the sediment transport is provided by the lowest updating interval. The accuracy of the remaining updating intervals tested will therefore be measured by comparison to the 1 minute interval predicted transport rates.

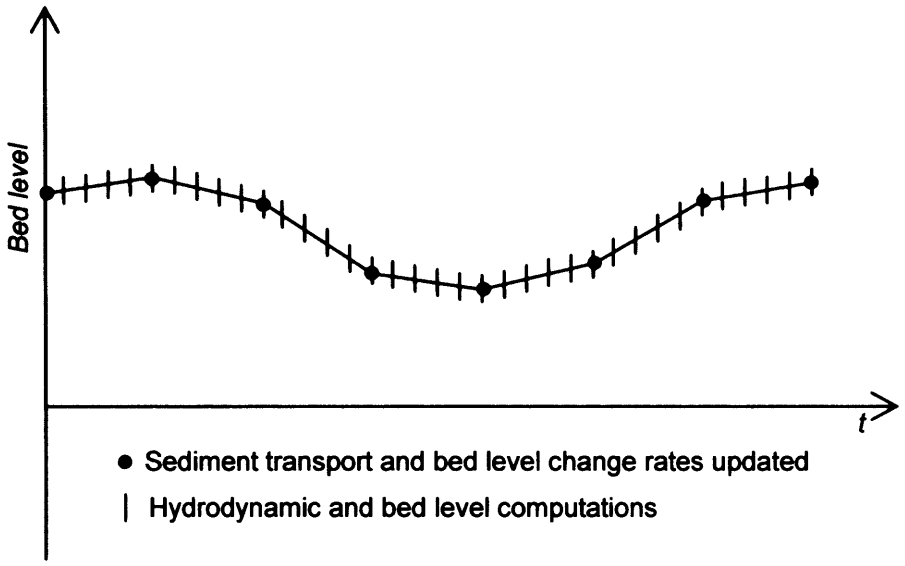

Figure 3.11. Procedure used to reduce the number of calls to the sediment transport module.

Figure 3.12 demonstrates that the predicted sediment transport is extremely sensitive to the updating interval. Both the 5 and 15 minute updating intervals predict residual sediment transport that is comparable to the 1 minute updating test. However, an increase of the updating interval to 30 minutes is accompanied by a significant difference in both the pattern of residual transport across the estuary and the total transport computed over a tide (see Figure 3.13). This suggests that in order to resolve both the inter-tidal dependency of the wave-induced currents, and the equilibrium response of the sediment transport to the ebb-dominated tidal currents, a high updating frequency is required. The use of a minimum 15 minute updating interval is, therefore, used for subsequent modelling experiments in this environment.

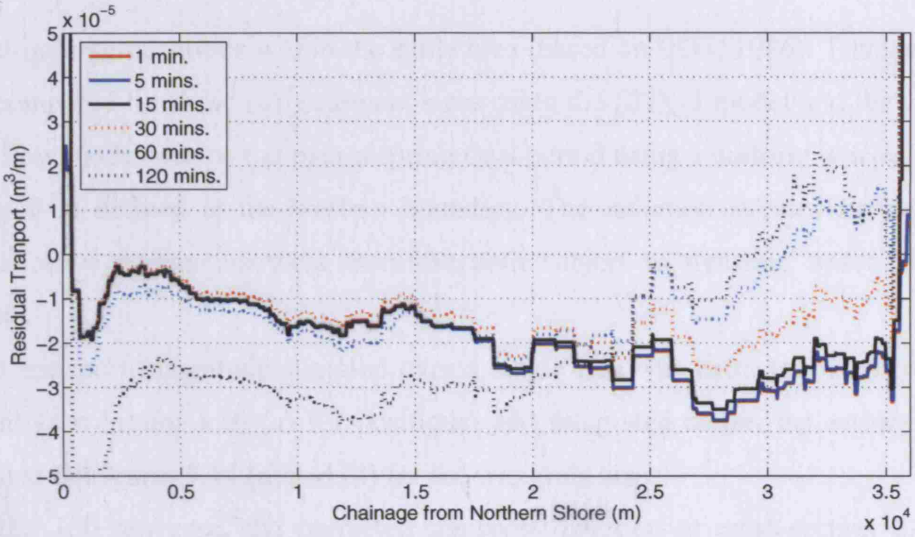

Figure 3.12. Residual sediment transport (westerly component) for varying sediment transport updating intervals, over 1 complete spring tide. Cross-section 1 (see Fig. 3.10 (a)).

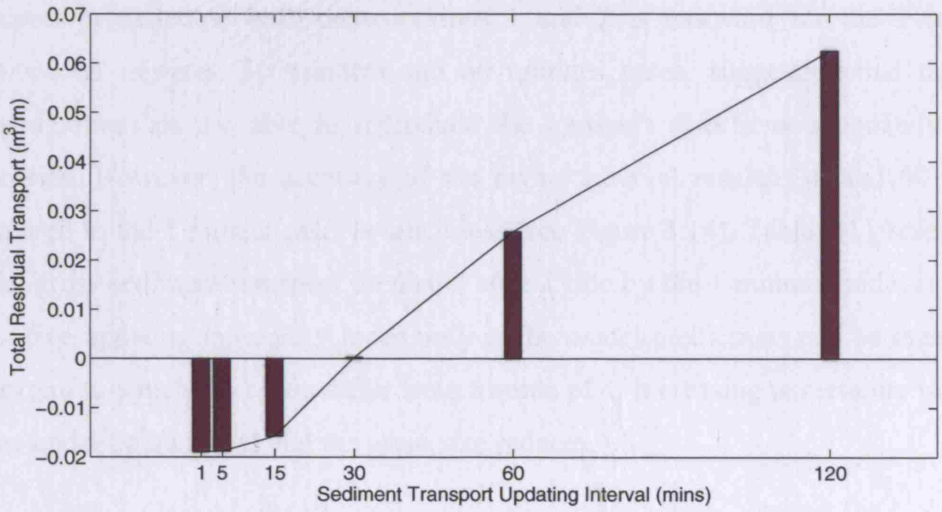

Figure 3.13. Residual sediment transport integrated over cross-section 1 for 6 different updating intervals.

3.5.2 Updating Interval as a Function of Grain Size

Additional tests were also conducted to establish the dependency of the updating frequency on the grain size. Two grain sizes were selected, 150 μm and 270 μm, both

present in large quantities within the study area (based on BGS, 1986). Transport tables were computed for these two sediment sizes using the *STPQ3* model and the combined wave-flow model was re-run over a spring tidal period using a uniform wave (H_s = 2 m; T_{peak} = 9 s) defined at the western boundary. The radiation stresses as well as the integral wave parameters were therefore both subject to dynamic water levels and currents.

Total transport magnitude summed over a single tide was extracted from two cross-sections (see Figure 3.10 (a) for positions) and integrated across the estuary. This is presented in Figures 3.14 (a) and (b) for the two grain sizes.

For the 150 μm case, the predicted transport direction at cross-section 2 reverses between the 5 minutes and the 15 minutes updating intervals. This shows that, for this grain size, a relatively short updating interval is required (at least 5 minutes) in order to capture the reversal in the transport direction predicted by the 1 minute model.

For the experiments involving the larger 270 μm sand grains, the direction of total transport predicted at both cross-sections 1 and 2 is eastward for the 1 minute, 5 minutes, 15 minutes, 30 minutes and 60 minutes cases, suggesting that the higher updating intervals are able to reproduce the transport directions adequately for this grain-size. However, the accuracy of the higher interval results (30 and 60 minutes) compared to the 1 minute case, is much less (see Figure 3.14). Table 3.1 presents ratios of the gross sediment transport predicted after 1 tide by the 1 minute model runs to the other five updating intervals. Uncertainty in the model predictions can be measured by the extent to which the ratios differ from a value of 1. Increasing uncertainty is detected as the updating increases and the grain size reduces.

Table 3.1 Dependency of Sediment Transport Updating Interval on Grain Size.

Updating Freq. (/min)	1	5	15	30	60	120
270 µm; Line 1	1.0000	0.9422	0.9047	1.0306	1.1353	0.2768
270 µm; Line 2	1.0000	0.9695	0.9607	0.3032	1.1004	0.4496
150 µm; Line1	1.0000	1.0235	1.0340	0.9792	0.8193	0.7474
150 µm; Line2	1.0000	0.9829	-1.2695	-1.1481	0.9624	0.6464

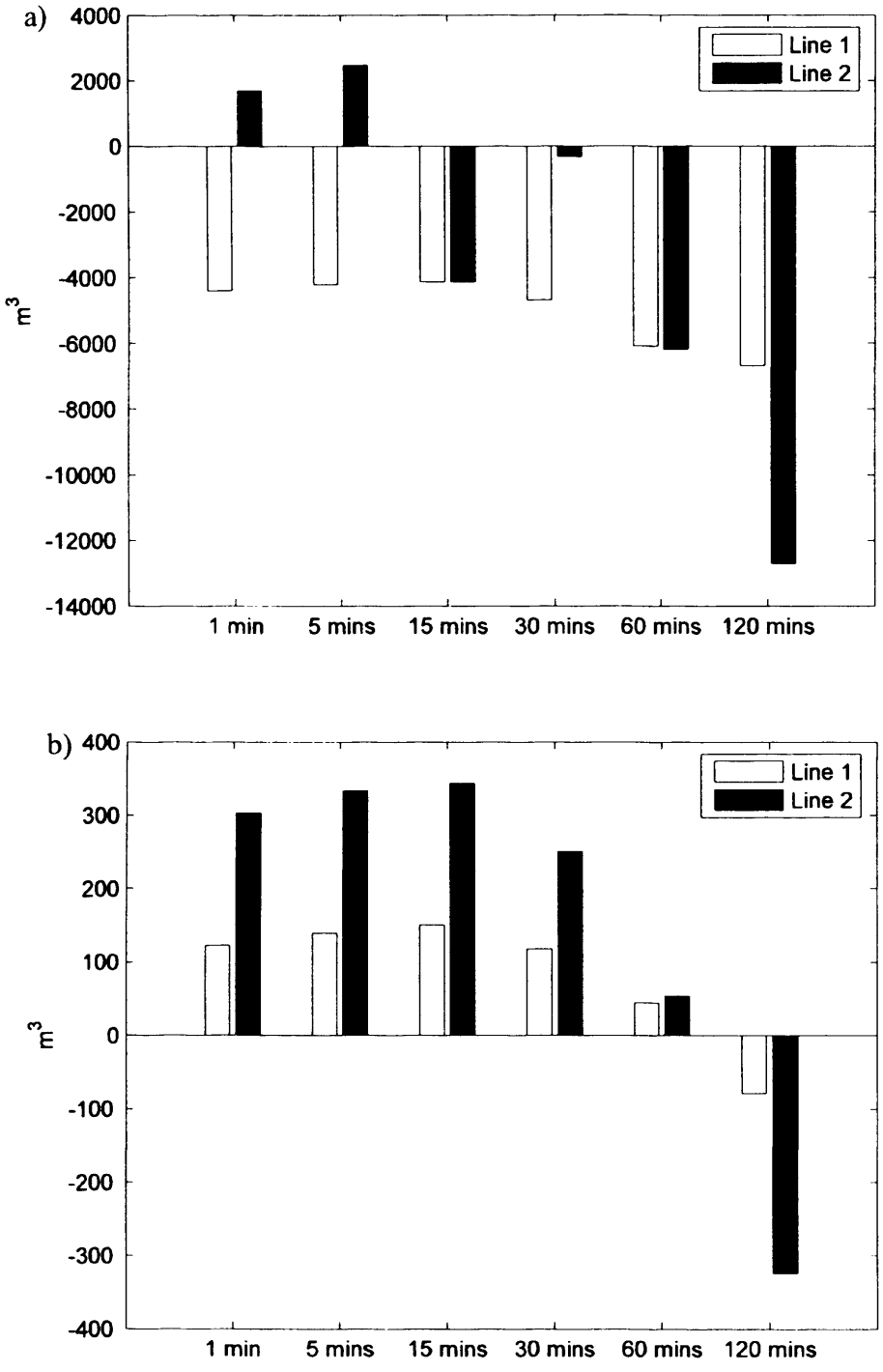

Figure 3.14. Predictions of total load magnitude summed over a single spring tide at cross-sections 1 and 2 for grain size of (a) 150 μm and; (b) 270 μm.

Overall, the results indicate that as the grain size reduces, the updating frequency prescribed by the user must increase to accommodate the additional time in which the smaller sediment fraction remains suspended in the water column after periods of peak current velocity.

3.5.3 Updating Interval as a Function of Wave Height

The sensitivity of the updating interval to wave height was also tested. Waves of 1 m, 3 m and 5 m (H_s) and period of 9 s (T_{peak}), were propagated from the western boundary of the model during a single spring tide. A grain size of 270 μm was used in the tests. The total load magnitude summed over a single spring tide predicted at cross-sections 1 and 2 is presented in Figures 3.15 (a), (b) and (c) for the 1 m, 3 m and 5 m wave conditions respectively. The ratios of the gross sediment transport predicted after 1 tide by the 1/1 minutes model runs to the other five updating frequencies is presented in Table 3.2. Again, the uncertainty in the results (relative to the 1/1 minutes updating frequency) increases with the updating frequencies (for all wave conditions), however, no clear relationship exists between the maximum permissible updating frequency and the wave height. The results show that an updating interval of 15 minutes produces results that differ from those predicted by a 1 minute updating interval by only a maximum of 10 %. Based on this it is considered acceptable to proceed with a 15 minute updating interval for the entire range of wave conditions tested in Chapters 4 and 5.

Table 3.2. Dependency of sediment transport updating frequency on wave height.

	$\Sigma Q\|_{Update=1\,min}^{tide} \quad \Sigma Q\|_{Update=5,15,30,\ldots}^{tide}$					
	1 min	5 min	15 min	30 min	60 min	120 min
H_s = 1m; Line 1	1.0000	0.9531	0.9126	0.9577	1.1222	1.4922
H_s = 1m; Line 2	1.0000	0.9763	0.9662	1.0216	0.8894	0.5594
H_s = 3m; Line 1	1.0000	0.9215	0.9870	0.9656	1.0815	0.2331
H_s = 3m; Line 2	1.0000	0.9580	1.0075	1.0046	1.1661	0.4701
H_s = 5m; Line 1	1.0000	0.9678	0.9310	0.9431	0.9037	0.6791
H_s = 5m; Line 2	1.0000	0.9774	0.9574	0.9892	0.9770	0.4280

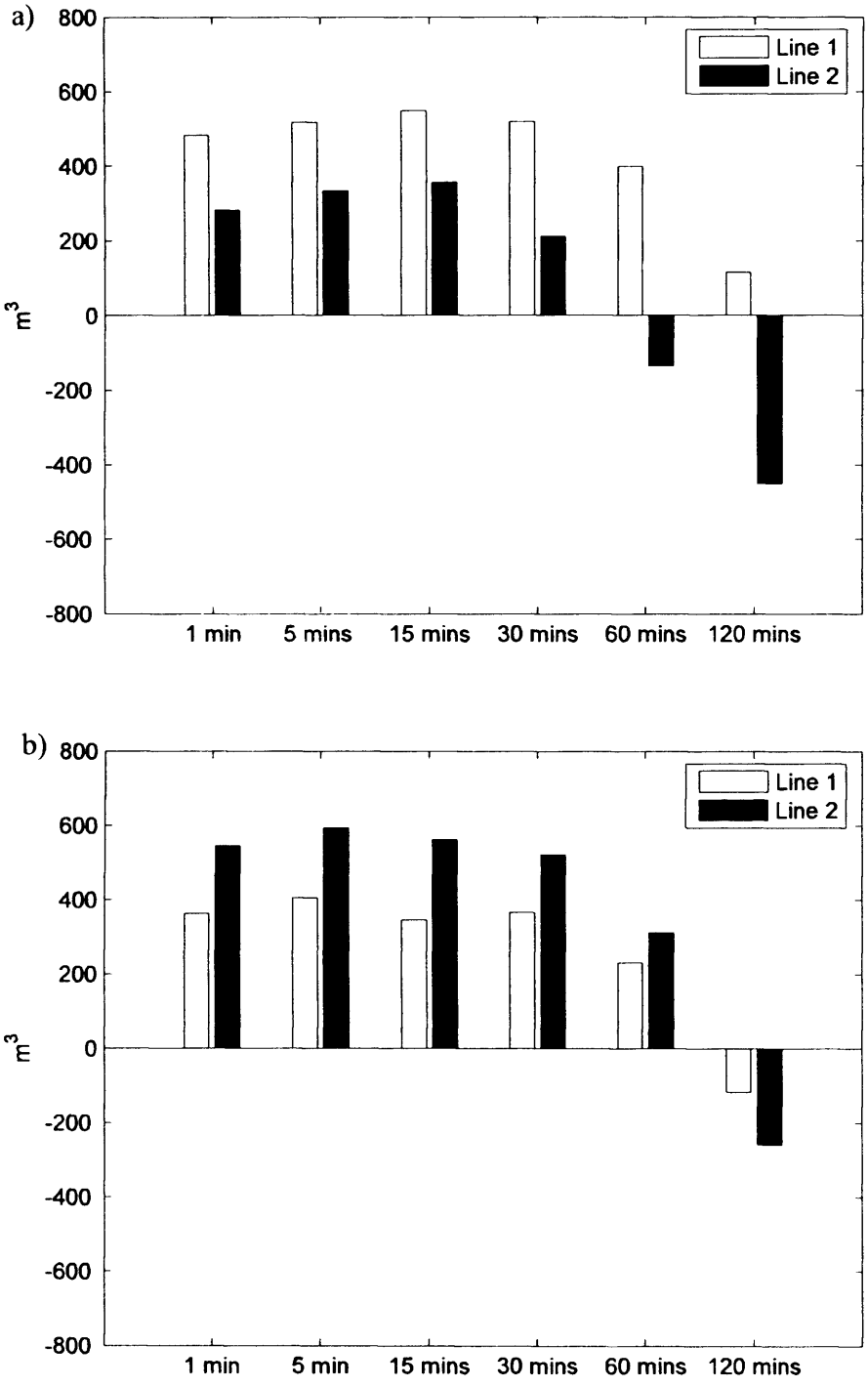

Figure 3.15. Predictions of total load magnitude summed over a single spring tide at cross-sections 1 and 2 for wave heights of (a) 1 m; (b) 3 m.

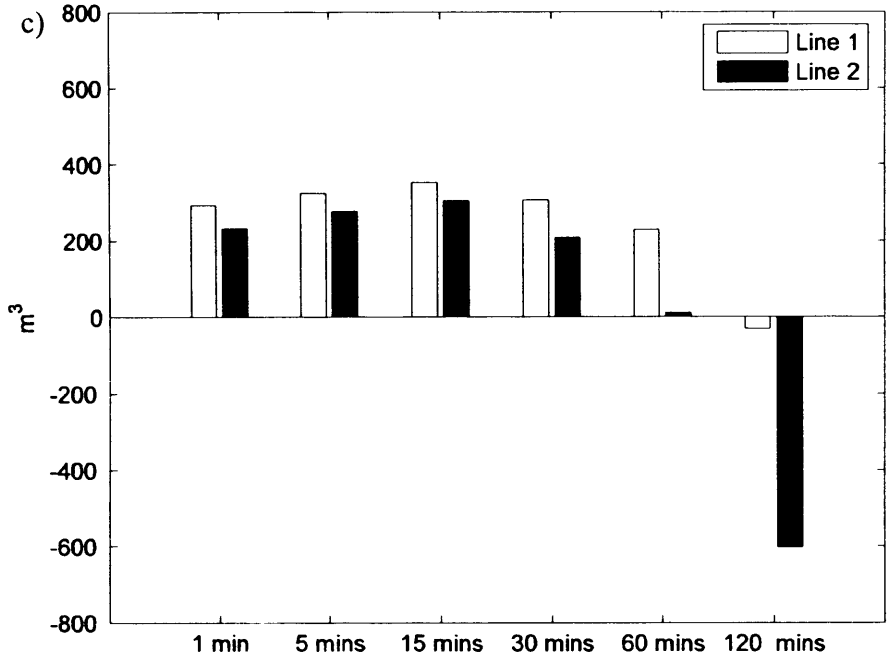

Figure 3.15. (c) Predictions of gross sediment transport over 1 spring tide at cross-sections 1 and 2 for wave heights of 5 m. Positive values indicate transport into the system.

3.6. Summary

The experiments carried out in this study have provided a model set-up that can be applied in a large-scale, regional study where important wave and current processes occur at a variety of spatial scales. The model has been optimized at a number of levels. Initially, an ideal mesh resolution was established by assessing the dissipation of sub-grid level energy by model domains of varying resolution. The results suggested a 45 m node separation model produces similar current fields to a 15 m node separation model in this environment. This demonstrated the validity of the turbulence closure scheme at the lower resolution and provided justification for using a 45 m node separation model in subsequent experiments. Further improvement of the computational efficiency was then added by reducing the spatial footprint of the mesh. Comparisons of regional sediment transport and local bed changes demonstrated the equilibrium character of the

regional sediment transport and hence, provided evidence to suggest that a smaller (and therefore more efficient model) was capable of resolving large-scale transport processes in sufficient detail.

A number of tests were then performed to improve the efficiency of the model coupling. By restricting the number of calls to expensive parts of the flow or wave models, optimisation of both the radiation stress field and the sediment transport updating intervals was attempted. Under high wave and tidal forcing it was shown that a radiation stress field updating interval of 120 minutes is sufficient to capture adjustments made to the wave-induced current field by a dynamic tide in this environment. Attempts to optimise the sediment transport rates under similar forcing, however, suggested that at least a 15 minutes updating interval is required.

Overall the experiments demonstrated that consideration and understanding of the dynamics of a region is helpful in order to select model parameters that accurately describe the physical processes. Relaxation of the model coupling should be performed carefully with numerous test simulations being conducted in order to assess whether the contributing processes are being captured properly. In the above scenario, the primary interest was combined wave/current induced sediment transport which required simulation of the complex regional tidal currents and wave-induced currents in shallow-water areas. The results presented here aim to provide some direct guidance to modellers / coastal engineers working in comparable environments that are subject to both high tidal and wind / wave energy. Although the settings and optimizations may not be directly transferable to all situations, the study provides a methodology as to how the validity of the many assumptions and shortcuts required in real coastal modelling projects can be tested.

4. Identifying Potential Mechanisms of Sediment Supply to 'Banner Banks' in the Bristol Channel, U.K.

4.1 Introduction

Using the 'optimised' model established in the previous chapter, large-scale wave and current-induced sediment transport in the region around the Nash Sands (see Figure 4.1) is now investigated. The experiments aim to demonstrate the potential for episodic up-estuary transport capable of re-nourishing sandy deposits in the central Bristol Channel, including the Nash Sands.

4.1.1 Hydrodynamic Setting

The Bristol Channel is a large macro-tidal inlet, bounded to the south by the English counties of Somerset, Devon and Cornwall and to the north by south Wales (see Figure 4.1). The mouth of the Bristol Channel is connected to the Celtic Sea. To the east the Bristol Channel joins the Severn Estuary which has one of the largest tidal ranges in the world: The mean spring tide range varies from 6 m in the outer Bristol Channel to approximately 12 m at Avonmouth. The tidal regime is strongly semi-diurnal in character, typically producing two high and low waters each day.

The tidal streams within the main channel run parallel to the coastline, approximately, and peak tidal currents increase moving up the channel. Typical mean spring current speeds at Lundy Island in the outer channel are around 0.7 m/s, increasing to approximately 2.4 m/s within the Severn Estuary. Within the outer and central Bristol Channel tidal currents are ebb dominant, whilst upstream of Avonmouth in the Severn Estuary the tidal currents are flood dominant. Around headlands, within the embayments and over large bed-form features such as sandbanks, the circulation patterns are far more complex.

Generally, freshwater discharges into the Bristol Channel are relatively small when compared to the tidal flows. As a result, fluvial flows give rise to only very localised effects close to the river confluence, where salinity gradients can influence sediment movements (Heathershaw and Hammond, 1980). Therefore, the Bristol Channel is considered to be a well mixed system. Based on this assessment, the effects of density gradients are ignored in the modelling.

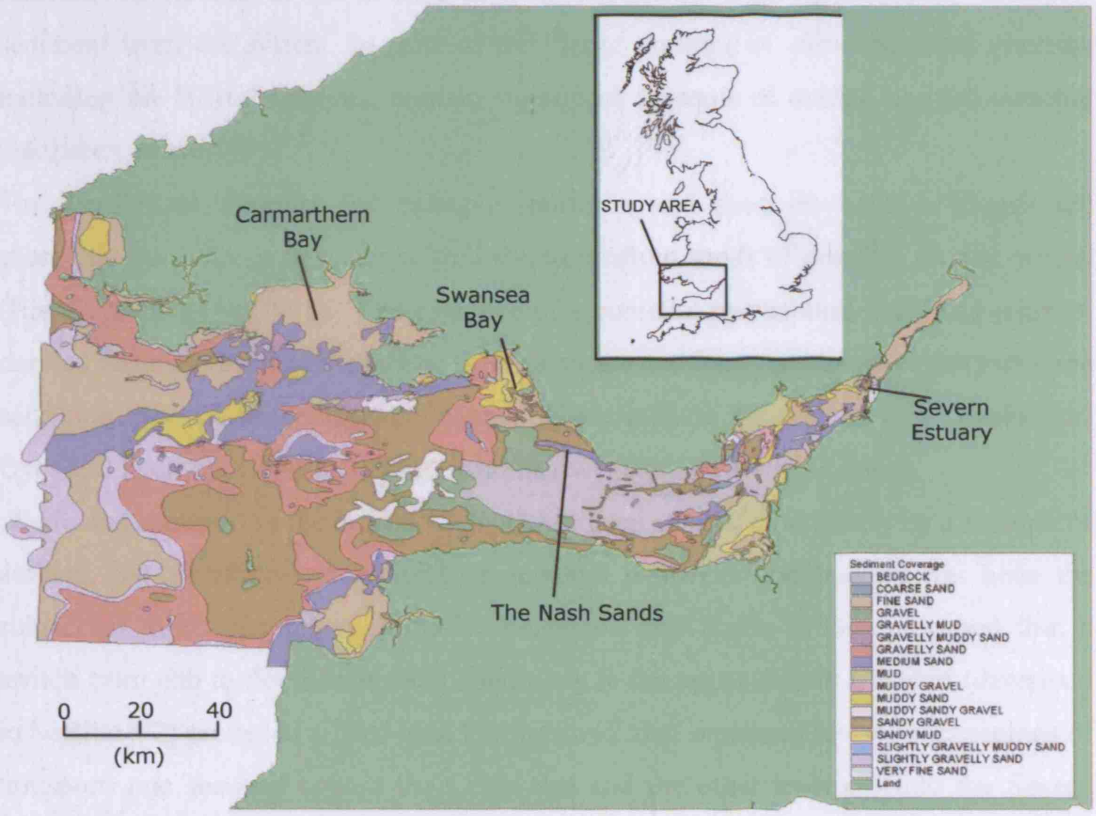

Figure 4.1. Surficial sediment distribution and regional setting based on data from the BGS (1986).

The wave climate consists of large swell and locally generated wind waves, approaching principally from the west and south west (see Figure 4.5). Measurements of wave heights in excess of 15 m have been recorded in some outer locations of the channel (UKMO, 1997).

4.1.2 Sediment Transport

The direction of sediment transport in large estuaries is controlled principally by differences in flood and ebb velocities (Dronkers, 1986). Therefore, the nature of the tidal asymmetry is of fundamental importance to estuarine morphology. In many U.K. estuaries, including the Mersey and Humber systems (see O'Connor, 1987), an inundation of marine derived sediment occurs in response to the flood dominated character of the tide. In ebb-dominated estuaries, there is a strong propensity to export sediment from the system. In spite of this, large portions of ebb-dominated systems, including the Bristol Channel, contain significant amounts of marine derived material (McLaren, et al., 1993).

In the Bristol Channel for example, northern and southern coastal fringes are characterized by large deposits of well-sorted medium sands of possible marine origin. (Harris and Collins, 1988). The presence of a potential mechanism importing marine-derived sediment has significance to the sustenance and long-term sustainability of large sand-rich deposits in the Bristol Channel. These include the 'banner-type' banks (see Dyer and Huntley, 1999) including Nash, Scarweather and Helwick Sands.

Sediment transport in the Bristol Channel has been studied extensively by a number of authors, but a definitive consensus on regional pathways and budgets has been the subject of much contention. Initially, Belderson and Stride (1966) proposed that a switch from ebb to flood dominated conditions in the upper Bristol Channel (described in Section 4.2) produced a 'Bed-load Parting zone' that separated two distinct regions of transport: one seaward toward the Celtic Sea and the other eastward into the Severn Estuary. Evidence for this included asymmetrically oriented flow-aligned sandbanks as well as current meter data (Heathershaw and Hammond, 1980).

The finding of marine foraminifera in the Severn Estuary (Murray and Hawkins, 1976) added confusion to the 'bed-load parting zone' hypothesis which was further compounded by the presence of large deposits of marine-derived medium sands in the coastal embayments of the northern Bristol Channel. The evidence suggested that as well as a dominant westward transport path in the lower Bristol Channel originating from the bed-load parting zone, some material was being transported up-estuary.

Culver (1980) incorporated this apparent up-estuary transport of marine derived sediment in a two-layered conceptual model. The model proposed that in the lower Bristol Channel, the sediment regime could be described as having net bed-load transport and suspended sediment transport occurring in opposing directions. In the two-layer system, coarse material was transported westward, away from the parting zone as bed-load (consistent with previous conceptual models) and fine material was transported in suspension in the upper water column by wind-driven currents. Culver's Bristol Channel, therefore, was characterised by the net export of coarse sediments and the net import of fines. By inference, then, the estuary became progressively finer moving eastward, a pattern that is evident in the Bristol Channel.

Culver's interpretations were later refuted by the work of Collins (1983) in which satellite images collected over a range of meteorological conditions were used to identify areas of high, medium and low suspended sediment concentrations. These images were then used to infer that suspended sediment transport in the Bristol Channel was predominantly westward and not eastward. Further work by Collins and Ferentinos (1984), that used the release and recovery of drifters, also supported the satellite interpretations.

Coupled with sonar images and bedform interpretations from across the central Bristol Channel region, the drifter release experiments of Collins & Ferentinos (1984) showed clear switches in the direction of sediment transport moving across the estuary. Based on these observations, a revised conceptual model was proposed including the concept of 'mutually evasive' sediment transport pathways. This is refers to a coastally restrained, easterly directed transport pathway to the north and south of the system and a westerly directed transport direction in the channel centre (see Figure 4.2).

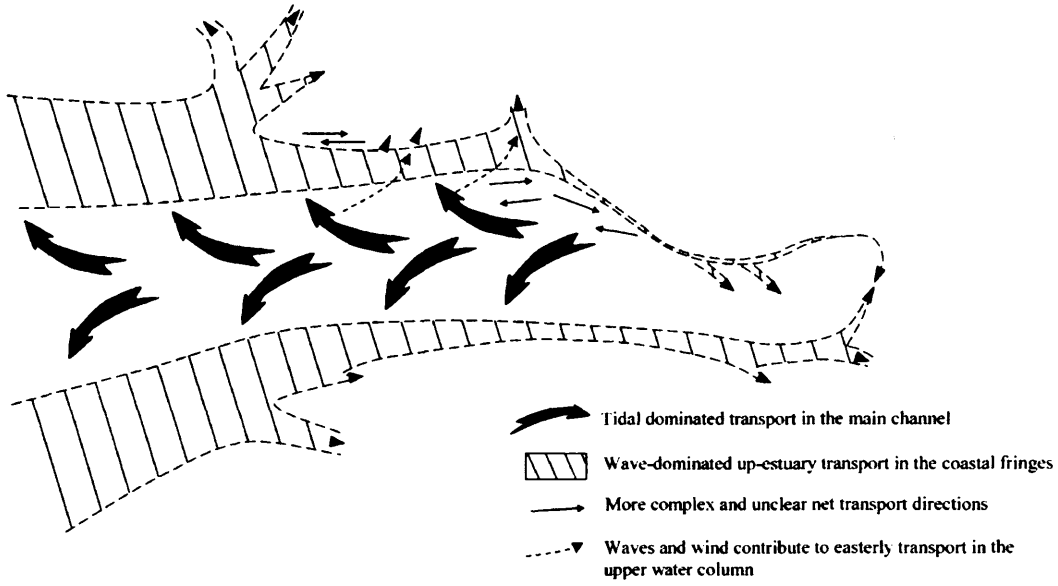

Figure 4.2. Near-bed sediment drift pattern proposed by the 'Mutually Evasive' conceptual model of by Collins & Ferentinos (1984).

The revised conceptual model provided a mechanism for bringing sandy material toward the bed-load parting zone. It was also able to explain the finding of Celtic Sea sediments in the upper estuary. Further evidence from side-scan sonar images (Harris and Collins, 1988), showed eastward oriented asymmetric sand waves and features which were indicative of eastward directed transport pathways in the coastal zones. Based on estimates of bed-load transport inferred from current measurements, the 'mutually evasive' hypothesis could then be expanded (Harris and Collins, 1988) to include the effects of wave-induced bed shear stresses enhancing easterly directed transport in the coastal regions to the north and south of the main channel. A summary of the evidence supporting a 'mutually evasive' transport mechanism is presented in Figure 4.3.

Citing the hydrodynamic modelling of Uncles (1982) and also their own observations of currents and sand transport, Stride and Belderson (1990) rejected the concept of 'mutually evasive' sediment transport pathways. The authors offered alternative interpretations of the observational evidence presented by earlier authors. For example,

they contended that the extension of the flood dominated zone based on tracer results (Pattiaratchi and Collins, 1984) conflicts with peak current measurements and sand transport directions (see Figure 4.4 for a summary of Stride and Belderson's (1990) re-interpretation of the observational evidence).

Overall, previous work based on field measurements and observations has proven to be inconclusive due to complex local circulations and the conditions under which the data was collected. Therefore, in the present study, a modelling approach is applied in an attempt to demonstrate the regional scale processes that dominate the system. A process-based modelling study seems an obvious approach to help extrapolate the sparse observations over a large area. The key component of the model is that it includes both the effects of waves and currents on sediment transport. Previous modelling studies have used tidal forcing only and hence have been unable to resolve the processes adequately. The regional-scale sediment transport of medium sands (270 microns) is investigated as well as the wave-induced transport hypothesis. A large number of wave and current combinations are simulated in order to identify a potential sediment importation mechanism. A further aim of the study is to test the application of a 'representative wave', derived by condensing the wave climate into a characteristic form (Chesher and Miles, 1992).

The coupled modelling system that is used incorporates the effects of both tides and waves and includes contributions to sediment transport from the wave-current boundary layer, wave-induced current field and second order mass transport. The key aspects of the model have been described in Chapter 3 where the model has been optimised for the experiments conducted in Chapters 4 and 5. For the purposes of the present chapter, the crucial process that needs to be well-represented by the model is wave-current interaction as this has important implications to the sediment transport field. In the following Section (4.2) aspects of the modelling system that are most relevant to wave-current interaction are described.

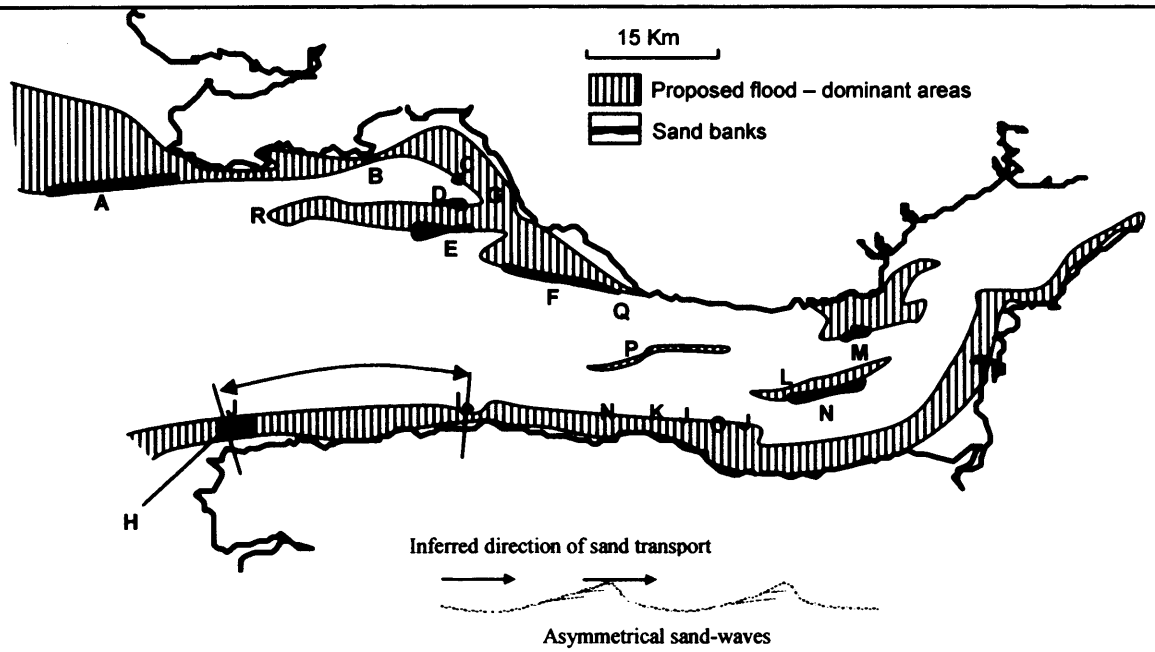

A, E and F: Helwick, Scarweather and Nash Sands (clockwise from left): Side-scan sonar data revealed eastward oriented asymmetric sand-waves on Helwick, Scarweather, Nash and on other smaller sand deposits (Collins, 1987). These were attributed to a flood dominant up-estuary sand transport pathway.
B: Mixon Shoal
C: Kenfig Patches
D: Hugo Bank
G: 'Proto-bank' or nascent sandbanks nr. Hutchwins Point: Northward facing lee slopes on sand-waves detected. Interpreted as indicators of flood dominated transport in northern coastal regions.
H: 'Proto-bank' nr. Bull Point
I: Shoal off of Foreland Point
J: Easterly facing lee slopes found on sand-waves. Interpreted as indicators of a near-coastal flood-dominated zone.
J-I: Heavy mineral deposits including chlorite and siderite, discovered offshore between Bull Point and Lundy - thought to have been transported east from minero-rich areas of Barnstable Bay by flood-dominated, easterly currents (Harris & Collins, 1988).
K: Sand-waves with easterly facing lee slopes.
L: Culver Sands
M: Mckenzie Shoal
N: Easterly current measurements (Harris & Collins, 1988). Further evidence in support of a southerly flood-dominated zone.
O: Small area with max. easterly directed maximum bed shear stress.
P: Current measurements from the Breaksea Valley suggest a flood dominant area in this central estuary location (Harris & Collins, 1988).
Q: Drifter Recovery from this area (Collins, 1987), suggested southward extension of the flood dominated zone.
R: Tracer study results, (Collins & Pattriatchi 1984) detected eastward water transport in this location. This extended the predicted flood dominated zone 12Km west of Scarweather Sands.

Figure 4.3. Summary of observational evidence in support of the 'mutually evasive' sediment transport pathways hypothesis.

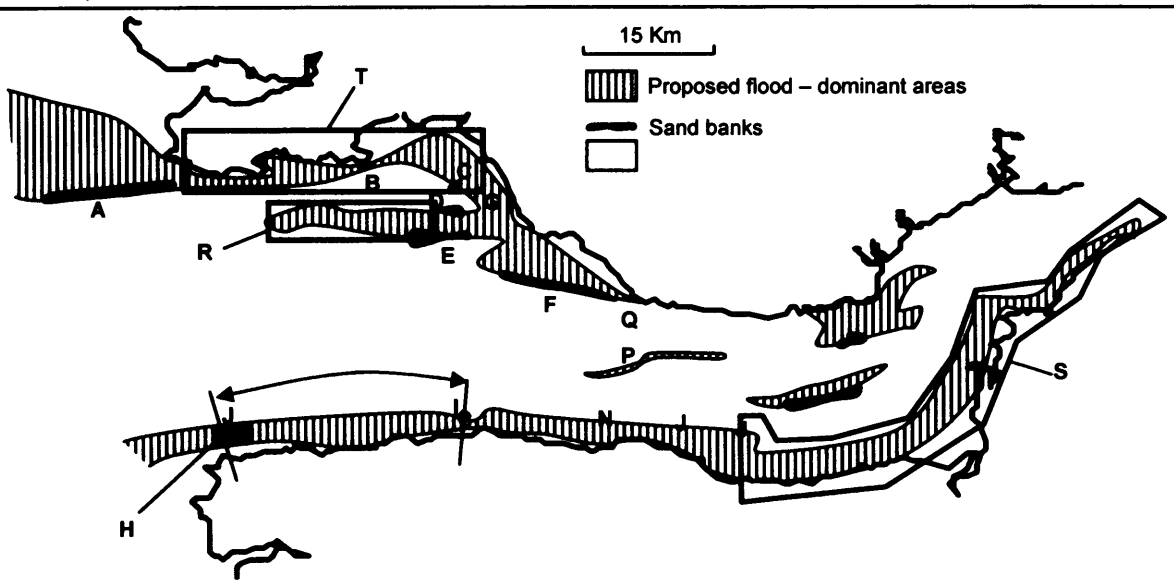

A, **E**, and **F**: Eastward oriented asymmetric sand-waves on Helwick, Scarweather and Nash Sands, reinterpreted by Stride and Belderson (1989) - henceforth S & B - as being a product of the oblique orientation of sandbanks: One side is exposed to preferential flood tidal current and the other side ebb, thus producing opposing net sand transport on both sides of the banks and a local deviation from the regional pattern.

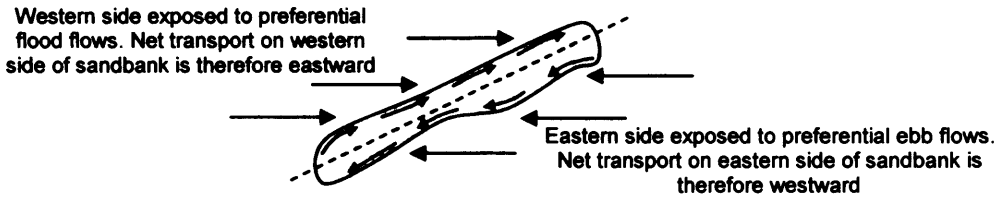

G and **H**: S & B dismiss the use of 'proto-bank' bed-forms as transport indicators suggesting the bed-forms are relict features.
J: Easterly facing lee slopes found on sand-waves at locations labeled 'J' and also current measurement re-interpreted by S & B as products of local topographic variation as opposed to indicators of flood dominated transport zone.
J-I: S & B suggested that the River Lyn is the source of heavy mineral deposits in this area. This dismisses the concept that an easterly transport mechanism is responsible for mineral transport from Barnstable Bay.
P: S & B suggested that these easterly-directed current measurements were the product of local effects perhaps due to a vertical eddy that developed in the Breaksea Valley during ebb tide.
Q: S & B questioned the accuracy of drifter study results taken from here
R: S & B suggested that the extension of the flood-dominated zone, based on tracer results (Collins & Patriatchi 1984), conflicts with peak current measurements and sand transport directions.
S: Proposed area of flood-dominated transport, questioned by S & B
T: S & B contended that it is incorrect to extrapolate local sand-wave crest-lines as regional indicators of boundaries between flood and ebb dominance. Based on this, they proposed that this area of flood dominance should be discounted.

Figure 4.4. Summary of observational evidence used to refute the 'mutually evasive' sediment transport pathways hypothesis.

4.2 Model Setup

4.2.1 Wave Current Interaction

In shallow water regions wave action has important impacts on the current field including the following:

- *Enhancement of the bed shear stresses which modifies the bed-roughness and affects the tidal current speed;*
- *Increase in turbulence generation due to white-capping, wave-breaking and energy dissipation at the bottom which enhances vertical mixing;*
- *A net mass flux in the direction of wave propagation (Stokes Drift), which can often be complicated by return flows;*
- *Wave decay which generates momentum fluxes in the surf zone (due to gradients in radiation stresses), setting up long-shore currents;*
- *Wave streaming due to downward directed momentum fluxes in the wave boundary layer.*

It is important that these processes are simulated correctly in this study to capture the combined effects of waves and currents on sediment transport. In addition, these processes should be incorporated in an efficient way to ensure that a large number of wave-current combinations can be simulated.

The study uses DHI's *STPQ3* sediment transport model, coupled to the spectral wave model, *MIKE-21 SW*, and a 2-D hydrodynamic flow model, *MIKE-21 FM* (DHI, 2005). See Chapter 3, Figure 3.2 and Appendix 2 for a further description of the model components. The 2-D model has been optimised in Chapter 3 and is justified on the basis that we are considering the sediment transport in a well-mixed estuary where a logarithmic velocity profile is a valid approximation.

The *STPQ3* model is a point model which solves the full wave-current boundary layer by integrating the momentum equation over a wave period using the approach of Fredsøe (1984). The bed shear stresses and the thickness of the boundary layer are found by iteration. The procedure is to run the *STPQ3* first for a range of wave and current conditions and the results are written to a look-up table. When the 2-D coupled wave-current model is run, it looks to the sediment transport table at each time-step to provide the rate of sediment transport for a given water depth/wave period/wave

height/wave steepness/current speed combination provided by the flow and wave models.

The approach captures:

- The enhanced bed roughness due to waves;
- The increased mixing in the vertical due to bottom dissipation and wave breaking;
- A contribution to the bed shear stress from wave breaking;
- A contribution from the.mean wave motion (Stokes Drift), and;
- A contribution from gradients in the water surface.

Wave streaming in the boundary layer, caused by a net downward transfer of momentum producing a positive shear stress in the direction of wave propagation, is also included within the *STPQ3* computations.

The approach simulates the influence of ripples on sediment transport by calculating:

- The dimensions of the ripples as a function of the characteristics of waves and currents;
- The increased roughness experienced by the flow due to the presence of ripples;
- The contribution to the eddy viscosity from the ripples and;
- The mean concentration at the level of the ripple crest.

Wave-induced currents driven by radiation stress gradients are handled outside the sediment transport model by the coupled wave-current model. They affect the directions and magnitudes of the current fields that are fed into the *STPQ3* model. The *STPQ3* model also incorporates an additional contribution to the eddy viscosity by breaking-induced turbulence. The production of turbulent energy is computed using the model of Battjes and Janssen (1978).

When defining the range of parameters over which to compute the potential for sediment transport within the *STPQ3* model, it is possible to select a suitable wave-theory with which to compute the instantaneous orbital velocities. These are then used to solve the momentum equation and obtain the bed shear stresses and potential transport rates. This study derived a table using a combination of Stokes and Cnoidal 5^{th} -order wave theories (see Fenton 1985; Fenton, 1990). Both theories incorporate a current induced Doppler shift by including the current flux in the calculation. The approach captures the refraction of waves by an ambient current field: in the presence of

a current the wave model solves a modified version of the linear dispersion relation by subtracting the product of the wave number vector and the ambient current vector from the angular frequency of the waves (see Appendix 2.2.2). This gives an angular frequency which is 'relative' to the current velocity i.e. as observed in a frame of reference moving with the current velocity.

Stokes 5th-order theory is valid in deep water, and for non breaking waves, where higher order terms are small. In areas of increased wave steepness (shallow water), higher order terms become significant and Cnoidal 5th order theory is more appropriate. The *STPQ3* model differentiates between the two conditions and computes the transport rates accordingly by reference to the *Ursell* number, U^{no}

$$U^{no} = \frac{H_s \lambda^2}{D^3} \tag{4.1}$$

where H_s is the significant wave height, λ, the wavelength and D the water depth. For U^{no} values of 25 and less, Stokes theory is applied and for those of more than 25, Cnoidal theory is applied.

4.2.2 Sediment Transport

The sediment transport is calculated as the sum of the suspended and bed-load transports. In the *STPQ3* model, the friction velocity calculated over each wave period is used to derive the Shields parameter and the bed concentration. Using the Shields parameter, the bed-load transport is then calculated following the approach of Engelund and Fredsøe (1976) which gives bed-load transport in the direction of the mean current and normal to the mean current. The bed load transport is influenced by the effect of both a longitudinal slope and a transverse slope.

The model uses a reference concentration concept in which sediment concentrations for source and sink terms are computed at a reference level. Below the reference level all sediment is assumed to behave as bed-load and subject to the effects of bed slope. The position of the reference level and the amount of sediment in suspension is

governed by the friction velocity, which is computed from the boundary layer model (*STPQ3*).

Suspended load transport computations follow the approach of Zyserman and Fredsøe (1994). First, a time-averaged bed concentration is found from the Shields parameter. This accounts for the effects of bed slope by adjusting, θ_{cr} the critical Shields parameter in the calculation. This value is then used as a bottom boundary condition for the initial concentration profile. The turbulent diffusion equation is then solved iteratively to give the time-varying and time-averaged concentration profiles. The suspended sediment transport is calculated as the product of this instantaneous concentration and the instantaneous flow velocity. The time integration of the diffusion equation is repeated until a periodic solution is obtained.

The main advantages of the *STPQ3* model are:

a) The inclusion of many more points in the vertical than a standard sigma- layer coastal model, capturing the velocity and concentration profiles inside the wave-current boundary layer.

b) The wave orbital motion and turbulence are computed at the intra-wave scale and hence the wave-current interaction is resolved at an appropriate temporal scale.

The *STPQ3* model uses the detailed spatial and temporal hydrodynamic information that it calculates to obtain directly the sediment transport rates. It is important to note that the hydrodynamic information is not fed back into the flow and wave models. Therefore, processes like return flow from wave breaking and mass transport will only affect the sediment transport rates, and not be present in the current and water level calculations made by the 2D-H flow model MIKE 21 FM. A further disadvantage is that the *STPQ3* model uses a depth-averaged estimate of the current velocity to compute the boundary layer kinematics. Therefore, it does not distinguish between surface and bottom flows.

4.3 Model Tests

In this study, the response of the system to the full range of wave and tidal conditions is tested. Characteristic waves are identified in the historical time-series of wave data

from the Scarweather wave-rider buoy (UKMO, 2005, see Figure 4.5), and used as boundary conditions for the wave model. Conditions that are a) below 1 m (H_s) and; b) from directions that have no component in the direction of sediment import or export are ignored. Omission of wave heights that are less than 1 m (H_s) is based on the principle that we are seeking to identify a mechanism rather than quantify the total annual transport.

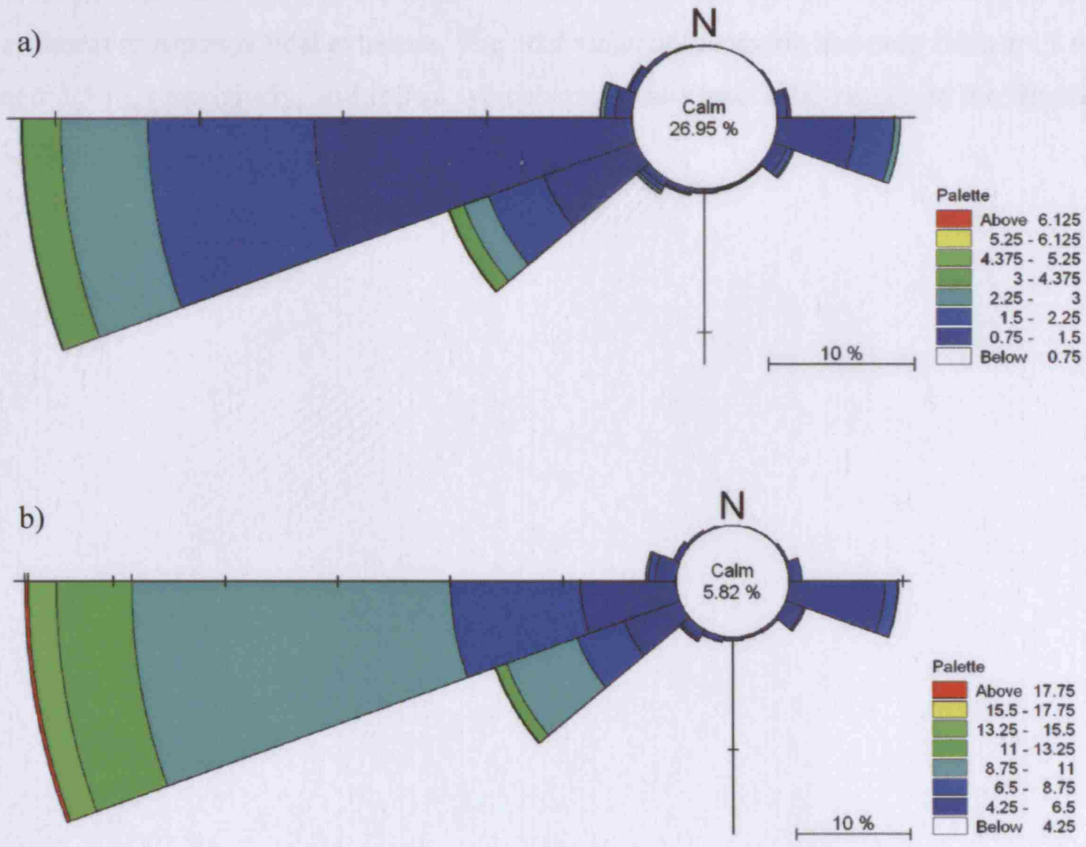

Figure 4.5. (a) Significant wave height and; (b) peak wave period, recorded at the Scarweather Wave Rider (UKMO, 2005) 51.39° N 3.91° W; 01/06/2000 – 31/12/2004.

A total of 32 combinations of wave height, period and direction are incorporated in the modelling study. These combinations reflect the range of wave conditions that can be observed in the system and cover the four dominant directions of wave propagation (see Table 4.1).

Each wave condition is simulated over both a semi-diurnal spring and a neap tide (12.42 hours) requiring a total of 64 initial wave-current simulations to generate the hydrodynamic field, followed by 64 coupled ST/HD simulations. Construction and optimisation of the unstructured mesh used in these experiments is described in Chapter 3. The mesh used is shown in Figure 4.6 below. Peak neap and spring tides are used in order to minimize the total number of simulations and provide indications of the sediment transport at tidal extremes. The tidal range of the spring and neap tides are 8 m and 3.5 m, respectively, and reflect typical spring and neap tidal ranges in the Bristol Channel.

Figure 4.6 Model grid used in tests.

Table 4.1. Hourly recordings of integral wave parameters at the Scarweather Wave Rider Buoy (UKMO, 2005) 51.39° N 3.91° W; 01/06/2000 – 31/12/2004. Units of peak wave period (T_{pk}) are seconds and units of significant wave height (H_s) are meters.

Θ=105° H_s \ T_{pk}	3	6	9	12	15
1	917	1332			
2		383			
3					
4					
5					

Θ=225° H_s \ T_{pk}	3	6	9	12	15
1	200	207			
2		262			
3		49			
4		2			
5					

Θ=255° H_s \ T_{pk}	3	6	9	12	15
1	612	5639	2343	1229	20
2		2090	837	885	7
3		762	109	255	11
4		75	19	2	
5		1	3		

Θ=285° H_s \ T_{pk}	3	6	9	12	15
1	226	265			
2		153			
3		22	7		
4			1		
5					

The complete modelling methodology consisted of the following steps:

1. An initial calibrated hydrodynamic model was run over both single spring and neap tides on the grid system of Figure 4.6. The model used eight deep water tidal constituents from the global KMS model (Andersen, 1995) to drive the offshore tidal boundary. This model provided a dynamic flow field on which wave computations could be performed;
2. Radiation stresses for the 64 total conditions were computed. For wave directions between 180° and 360° degrees, wave forcing was imposed at the western boundary. For waves approaching from 105°, however, it was necessary to synthesize a wave field by applying a wind stress across the domain. The magnitude of the wind stress needed to generate each required wave period and height combination was estimated by reference to the Shore Protection Manual (U.S. Army Corps of Engineers, 1984) and then further improved by calibration (i.e. adjustment of the wind speed and air-water interface) to provide the required conditions.
3. The sediment transport look-up table was derived using the *STPQ3* model. Table 4.2 details the range of parameters for which the sediment transport table is

computed. The sediment grain size used was 270 μm of relative density 2.65. A critical Shields parameter value of 0.05 was used.

4. The flow model is re-run with both tidal forcing and forcing from the pre-computed radiation stress fields. The flow model interpolates values from the sediment transport table at a defined interval of the flow time-step (15 minutes).

Wind stresses were only applied in the wave model and were not applied to the flow model in stages 1 and 4.

Table 4.2. The ranges of principal parameters from which the tabulated transport rates are computed by the *STPQ3* model. (V = current velocity; H_{rms} = root mean square wave height; H_{rms}/D = wave height/water depth - criterion for wave breaking; T_{pk} = peak wave period; γ = angle between waves and currents).

Parameter	Lower Bound	Upper Bound	Increment
V (m/s)	0.010	3.01	0.1
H_{rms} (m)	0.1	8.1	0.4
H_{rms}/D	0.1	0.8	0.1
T_{pk} (s)	3	20	2
γ (°)	0	360	30

4.3.1 A Wave-induced Transport Mechanism

Prior to running the full array of simulations, the study concentrated primarily on a selection of typical wave conditions (see Table 4.3), approaching from the prevailing wind and wave direction (255°). This approach helped to demonstrate the 'mutually evasive' transport mechanism.

Over each complete tidal cycle, sediment transport fluxes were extracted from the model results and used to compute residual transport over 3 cross-sections inside the Bristol Channel (see Figure 4.7 for Cross-Section positions). Cross-sections to the west of the Nash Sands were chosen because the modelling aimed to demonstrate a mechanism of supplying material to the sandbank from source areas further west. Results for both bed-load and suspended load transport are now presented sequentially.

Table 4.3. Description of the combined wave-current simulations conducted for separated bed-load and suspended-load.

Model Simulation Numbers	1 and 2	3 and 4	5 and 6	7 and 8	9 and 10	11 and 12	13 and 14
Wave Conditions	0 m, 0 s	1 m, 6 s	1 m, 15 s	2 m, 9 s	2 m, 15 s	3 m, 9 s	3 m, 15 s
Tide Conditions	Springs/ Neaps	Springs/ Neaps	Springs/ Neaps	Springs/ Neaps	Springs/ Neaps	Springs/ Neaps	Springs/ Neaps

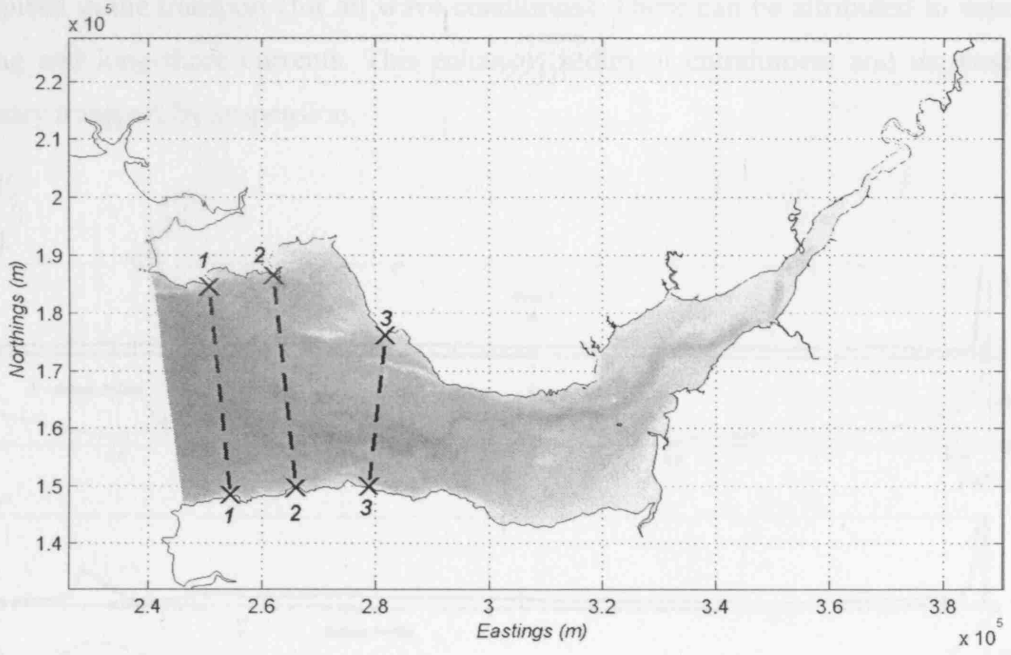

Figure 4.7. The central and upper Bristol Channel. Cross-sections used for analysis of residual sediment transport are labelled 1, 2 and 3.

4.3.2 Neaps, Suspended Load

With reference to Figure 4.8 which includes the cross-sectional sediment flux integrated and averaged over a tide, the model indicates a transport direction that is out of the estuary for tide-alone conditions. A switch to up-estuary suspended load transport for almost all wave conditions is predicted across the entire Bristol Channel during neap tides, particularly for low frequency waves (1 m, 15 s; 2 m, 15 s; and 3 m, 15 s). The water depth relative to the wave period and height affects the wave asymmetry and

controls the amount of mass transport in the direction of wave propagation. In the coastal fringes of the Bristol Channel (15 m < water depth < 25 m) the majority of waves are sufficiently affected by the bathymetry to produce a residual mass transport in the direction of wave propagation and alter the overall direction of transport to up-estuary. In the centre of the main channel (water depth > 25 m) only the longer period waves are sufficient to 'feel' the bottom and affect the direction of sediment transport.

Figure (4.8) also includes a profile of the bathymetry at each cross-section. Of particular interest around regions of locally shallow water (i.e. water depth < 15 m), are large spikes in the transport (for all wave conditions). These can be attributed to wave breaking and long-shore currents. This enhances sediment entrainment and increases up-estuary transport by suspension.

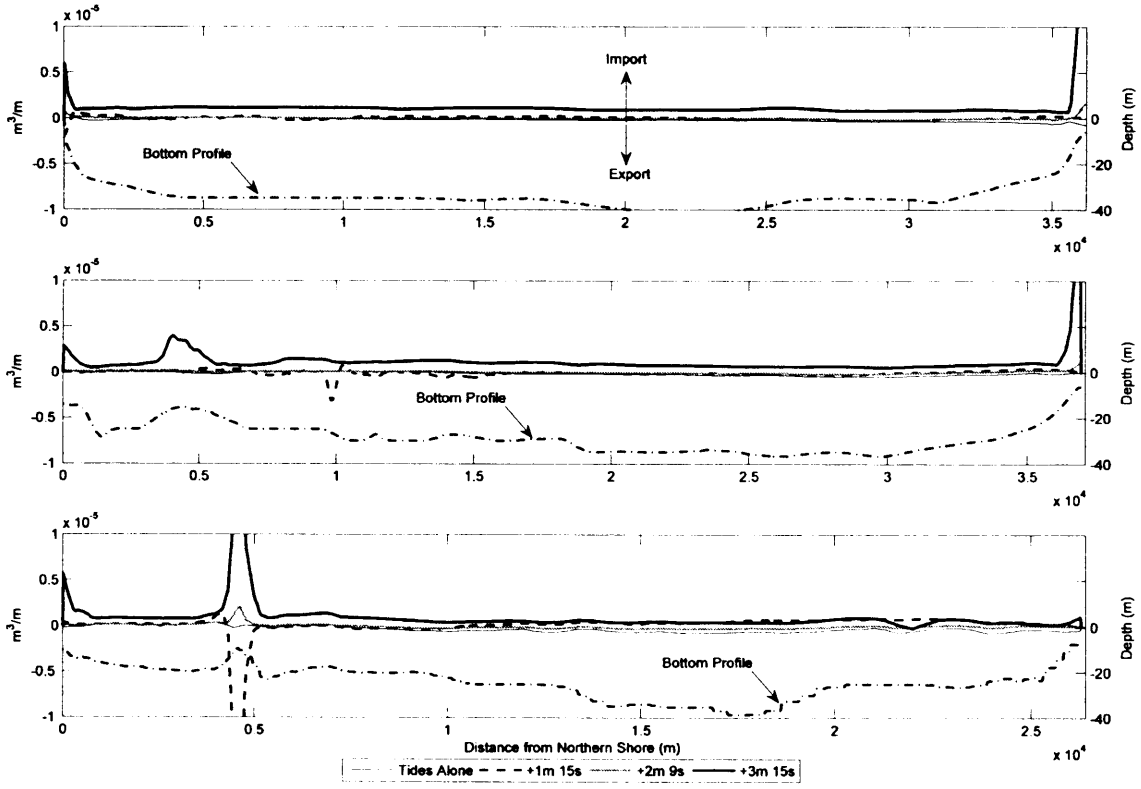

Figure 4.8. Tidally averaged suspended sediment transport under Neap tides predicted at: a) cross-section 1; b) cross-section 2 and; c) cross-section 3. Positive values indicate an up-estuary transport direction.

4.3.3 Neaps, Bed-load:

The most significant aspect of the predicted bed-load transport (see Figure 4.9) is the fact that the transport under waves follows closely the transport predicted under tidal currents alone: In the large areas of the coastal fringes (15 m < water depth < 25 m), the model predicts large regions of flood-dominated transport (due possibly to local circulation effects) and these are simply enhanced by wave action.

There are also interesting deviations from the trends described that are worthy of further discussion. These are caused mainly by the 1 and 2 metre waves with long periods. In both the coastal fringes (15 m < water depth < 25 m) and the deeper main channel (water depth > 25 m), the 1 m, 15 s wave produces an increase in the amount of sediment exportation (relative to the tide alone transport). The 2 m, 9 s wave also produces the same effect although this can be detected only in cross-section 3. A possible explanation is that the waves are long enough to 'feel' the bottom (thus increase the bed shear stress) but not asymmetric enough (due to the large water depth) to alter the direction of transport. The result is that the long period waves simply amplify the net-tidal transport. It is possible that the 3 m, 15 s waves are large enough both to 'feel' the bottom and to induce sufficient asymmetry in the crest and trough orbital velocities to counter the tidally directed transport.

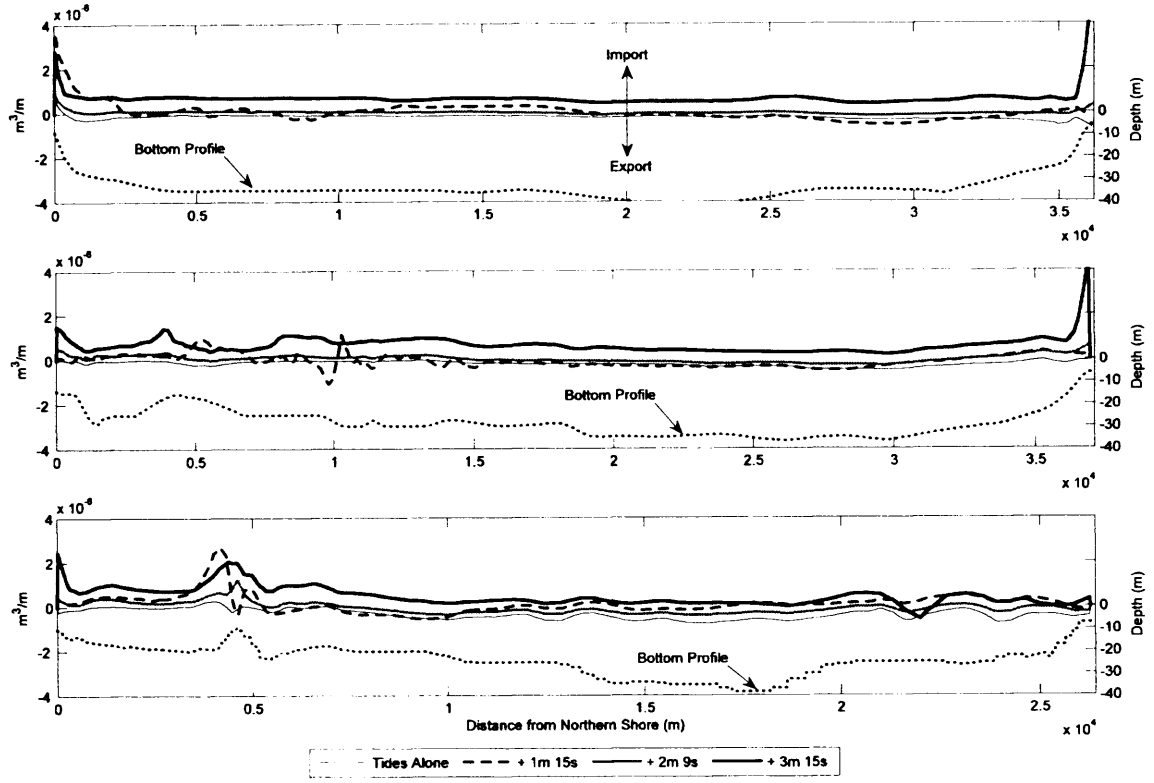

Figure 4.9. Tidally averaged bed-load transport under neap tides predicted at: a) cross-section 1; b) cross-section 2 and; c) cross-section 3. Positive values indicate an up-estuary transport direction.

4.3.4 Springs, Suspended-load

Even under no wave action, it is possible to detect a shift in the direction of transport (for cross-sections 2 and 3): tidal transport changes from strong export in the channel centre to import in the slightly shallower coastal fringes (see Figure 4.10). The superposition of waves on to the tidal signal augments the tide alone transport (with some exceptions, notably the 2 m, 9 s wave at cross-section 1). This can be ascribed to the fact that the waves serve to enhance the bed shear stresses, increasing sediment entrainment and total tidal transport in the coastal fringes and export in the deeper channel.

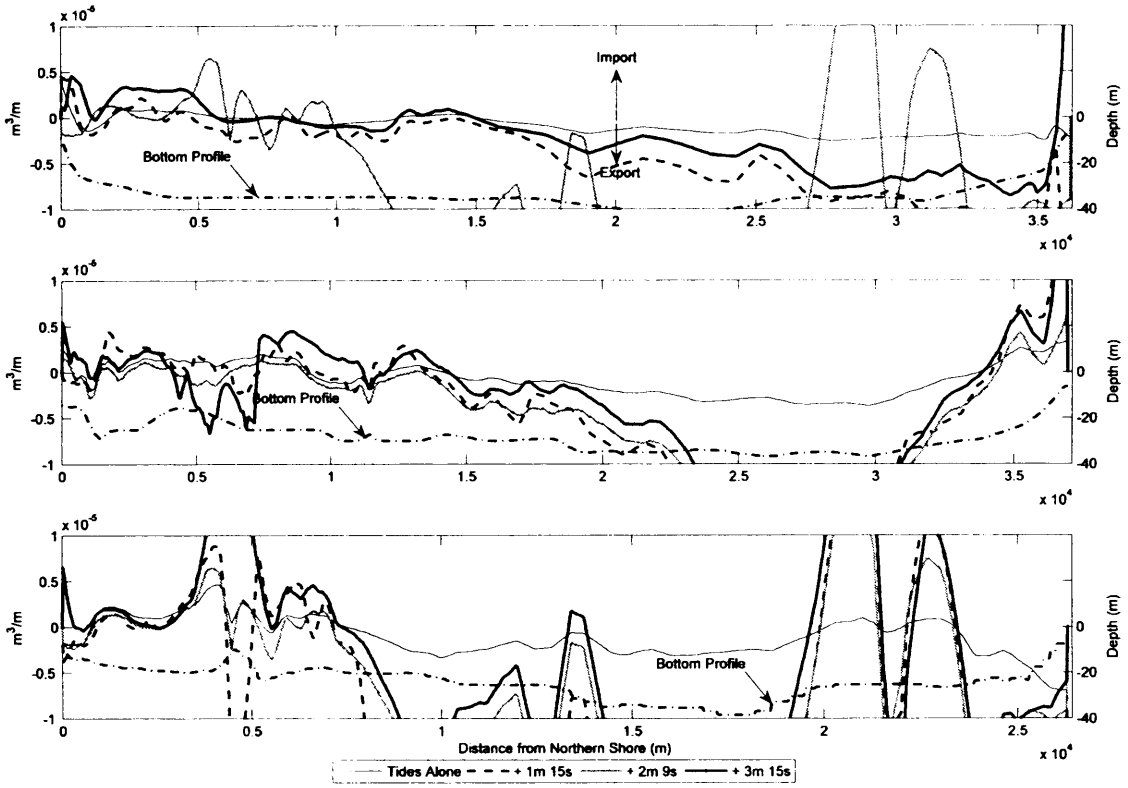

Figure 4.10. Tidally averaged suspended sediment transport under spring tides predicted at: a) cross-section 1; b) cross-section 2 and; c) cross-section 3. Positive values indicate an up-estuary transport direction.

4.3.5 Springs, Bed-load

Bed-load transport is similar to suspended load transport under spring tides in which the overall transport direction is tidally dominated and the waves serve simply to increase the bed shear stresses and enhance the magnitude of the transport in the direction of the tide (see Figure 4.11).

Again in shallower regions the wave-induced transport deviates considerably from the tide-alone transport. This could be attributed to the increasing disparity between crest and trough wave orbital velocities with decreasing water depth.

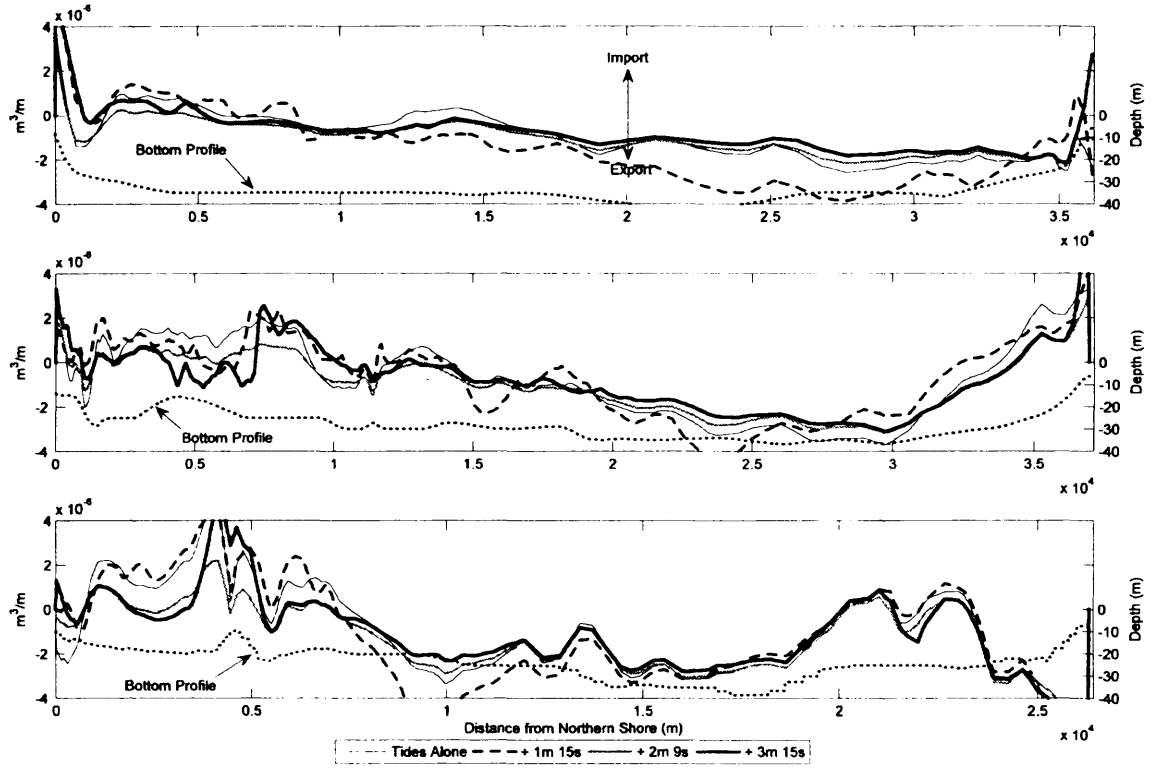

Figure 4.11. Tidally averaged bed-load transport under spring tides predicted at: a) cross-section 1; b) cross-section 2 and; c) cross-section 3. Positive values indicate an up-estuary transport direction.

4.3.6 Computation of the Representative Wave

Using real or synthesized tidal data that includes every minor fluctuation in a long-term or large-scale modelling prediction, lends itself to generating only "one single visualisation of a whole range of possible outcomes of the non-linear process" (De Vriend et al., 1993). This has led to the development of techniques that reduce the required data input and computing requirements to provide a less detailed but more robust prediction.

The most common method is to run the model using representative conditions (Dong and Chen, 2001). These can be either representative of tidal or wave conditions. Rather than driving the model with a real time-series of data, long-term records of wave and tidal data are schematised into typical or 'representative' conditions. A number of studies have been conducted using this type of approach including those of Latteux

(1987; 1992) and Chesher and Miles (1992). The validity of the long-term prediction can be improved and a greater understanding of the underlying trends derived. The approach is also useful in event-based or scenario type modelling: a representative tide or wave can be run in conjunction with short temporal scale events to assess the sensitivity of a system.

Having computed transport rates for all waves approaching from 255°, further simulations were conducted for the three other prevalent wave directions, 105°, 225° and 285°. Based on these predicted transport rates, and following the approach of Chesher & Miles (1992), a representative wave height, H_θ, was computed for the region where

$$H_\theta = \left[\sum fq.H_s^{\,p} / \sum fq\right]^{1/p} \tag{4.2}$$

p is the exponent of the wave height in the sand transport formula. A value of 2 was used by Chesher and Miles (1992) and is also used in this study. H_s is the wave height for a given frequency, fq. The approach yields a representative wave height of 1.52 m for this system, after weighting the wave heights computed for the different directions. Based on a comparison with values of sediment importation predicted using 1 and 2 m waves, this is clearly insufficient to sustain any substantial up-stream mechanism, either in the near-shore or offshore regions. In this dynamic environment, therefore, the application of a 'representative wave' is not appropriate because it contains no dependency on the wave period.

4.4 Summary

The present study has provided strong evidence in support of a wave-induced mechanism of sediment import into an ebb-dominated estuary. In near-shore regions (depth < 15 m) of the Bristol Channel case study, the mechanism is persistent during both spring and neap tides and is particularly prevalent when long period swell waves approach perpendicular to the estuary mouth.

In the coastal fringes (15 m < water depth < 30 m), up-estuary transport is significant under a range of wave conditions. This is principally the result of the differential between instantaneous peak and trough wave orbital velocities which pushes sediment up-estuary. In the near-shore zone (depth < 15 m), transport can be attributed to wave-induced currents which are set up in response to wave breaking and decay. During Spring tides, transport in the near-shore and in the coastal fringes is still affected by tidal action though; in regions of high current speeds, the waves act to augment transport out of the system.

Overall, the study demonstrates that there are a number of processes that can cause up-estuary transport in a large macro-tidal ebb-dominated system and it is stressed that the study merely attempts to identify potential mechanisms, hence the use of a uniform sediment distribution throughout the system.

In the case of the Bristol Channel, the supply of marine sands into the upper estuary can be produced by: wave decay and long-shore transport in the breaking zone; local flood-dominance in the coastal fringe regions; suspended transport by Stokes Drift in the deeper water regions; and enhanced up-estuary directed bed-shear stresses and bed-load transport due to asymmetry in wave orbital velocities in intermediate water depths.

The complexity of these transport mechanisms means that the concept of a representative wave is difficult to employ in such an environment. Most importantly, the study demonstrates the potential for event-based replenishment of coastal sediment sinks in which 'ephemeral transport pathways' link sand rich deposits. This indicates that the rare extreme events are important in maintaining a long-term equilibrium of the near-shore sandbanks deposits and seasonal changes are due to fluctuations in such events.

5. Modelling Formation and Maintenance Processes Around a Near-shore Sandbank

5.1 Introduction

Having demonstrated a potential mechanism for supply in the coastal fringes of the central Bristol Channel in Chapter 4, the following chapter uses the same optimised model established in Chapter 3 to investigate the local complexities in the hydrodynamic and sediment transport field around the Nash Sands. Potential mechanisms for the initiation and maintenance of the 'banner'-type headland bank are investigated as well as local sediment transport pathways and their modification under the action of waves.

5.1.1 Physical Description of the Nash Sands

The long sandy perturbation in the northern part of the central Bristol Channel which constitutes the Nash Sands (see Fig. 5.1) is exposed to an extreme hydrodynamic climate including a spring tidal range of 8 m, large Atlantic swell and locally generated wind waves. The bank is situated close to a prominent headland (Nash Point). Following the most contemporary classification system of Dyer and Huntley (1999), the bank is considered a 'Type 3 Headland Associated Banner Bank', formed "in response to an acute change in coastal topography where the headland is resistant to erosion". The Nash Sands fulfils a number of the criteria outlined by Dyer and Huntley to warrant its Type-3 classification: the shallower part is nearer the headland and the crestal depth gradually reduces moving away from the headland. The side of the bank facing the sea has a steeper slope than that on the landward side.

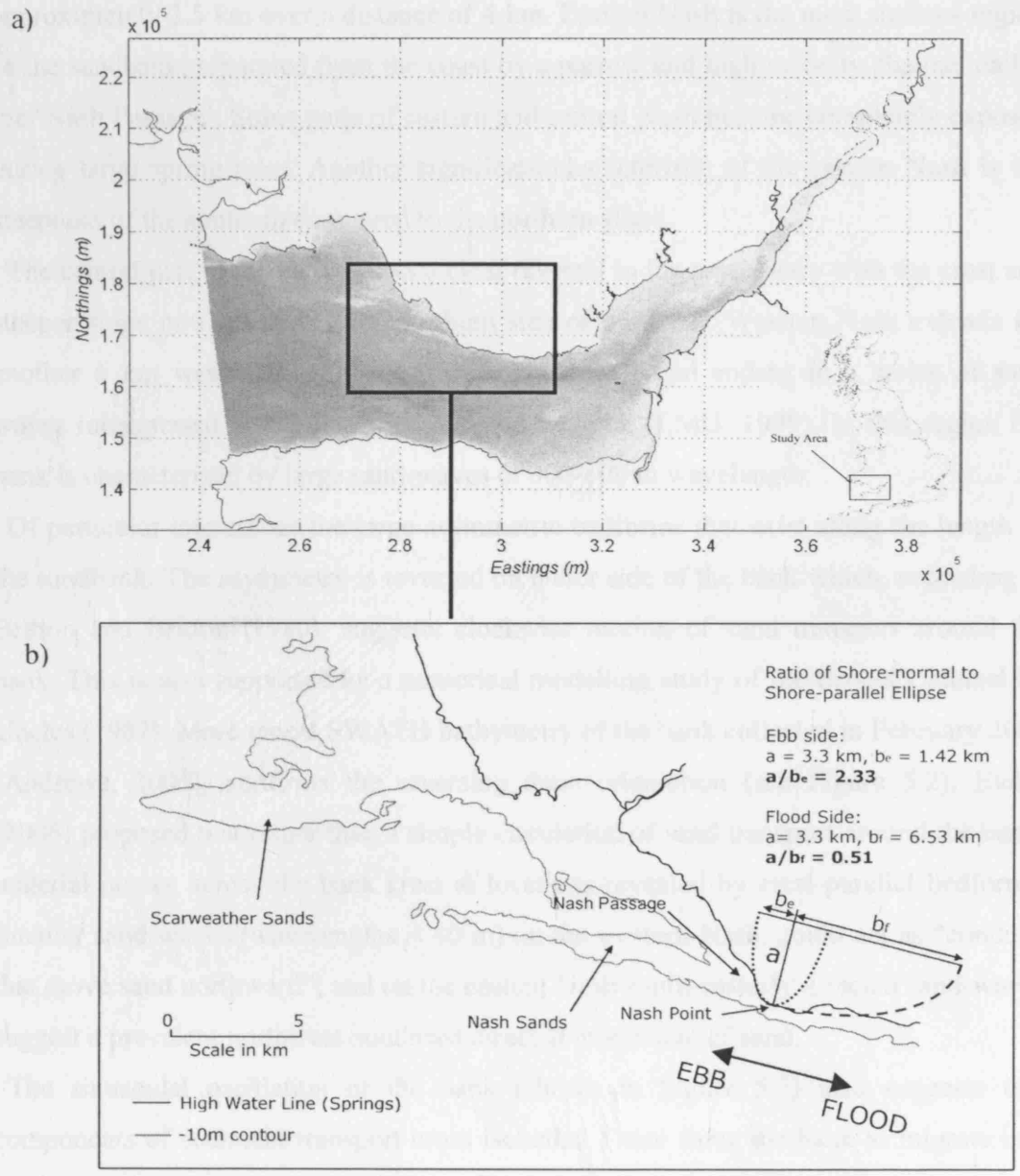

Figure 5.1. (a) Modelling domain and location; (b) Local bathymetry.

Less clear, however, are the mechanisms responsible for both the bank's initial growth and its maintenance in the present-day hydrodynamic environment. One recent report by Thompson et al. (2002) suggests that the sandbank forms part of a 'closed system' and that its volume has been loosely fixed since its original formation. The sandbank begins from a point approximately 200 m west of Nash Point and gradually widens to

approximately 3.5 km over a distance of 4 km. Eastern Nash is the most shallow region of the sandbank, separated from the coast by a narrow and high velocity channel called the 'Nash Passage'. Some parts of eastern and central Nash become completely exposed during large spring tides. Another significant characteristic of the eastern Nash is the steepness of the southern compared to the northern slope.

The central part of the bank shows a clear reversal in the asymmetry with the crest and steeper slope now located to the northern side of the bank. Western Nash extends for another 6 km westward, gradually becoming deeper and ending in a series of sand waves interspersed with patches of exposed bedrock (EMU, 1999). In this region the bank is characterized by large sand-waves of 300-600 m wavelength.

Of particular interest are the large asymmetric bedforms that exist along the length of the sandbank. The asymmetry is reversed on either side of the bank which, according to Britton and Britton (1980), suggests clockwise motion of sand transport around the bank. This is also supported by a numerical modelling study of the Bristol Channel by Uncles (1982). More recent SWATH bathymetry of the bank collected in February 2005 (Andrews, 2005), confirms the reversing dune orientation (see Figure 5.2). Evans (2006) proposed that rather than a simple circulation of sand transport around the bank, material moves across the bank crest at locations revealed by crest-parallel bedforms. Smaller sand-waves (wavelengths < 40 m) on the western Nash, could act as "conduits that move sand northward"; and on the eastern Nash south-easterly directed sand-waves suggest a prevalent northwest-southeast directed movement of sand.

The sinusoidal oscillation of the bank (shown in Figure 5.3) also suggests that components of sediment transport cross isobaths. These force the bank to migrate in a north-south direction.

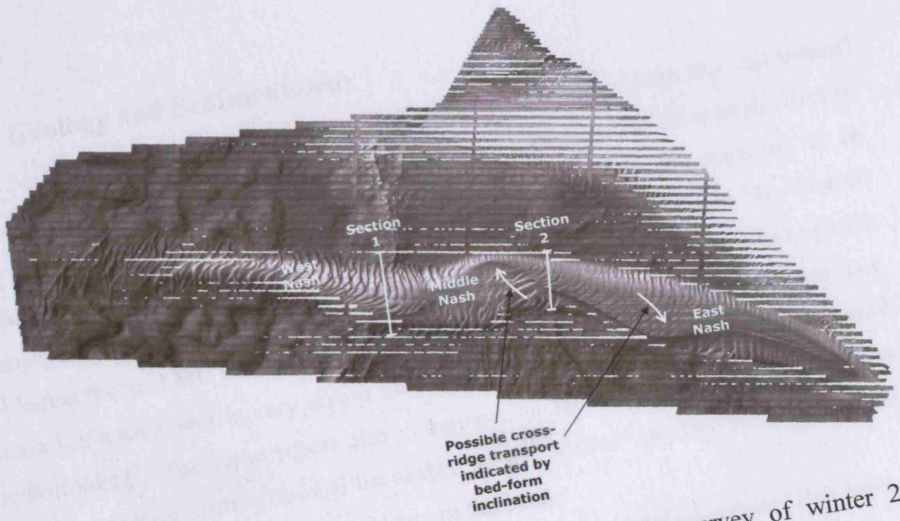

Figure 5.2. Interpolated surface from SWATH bathymetry survey of winter 2005 (Andrews, 2005).

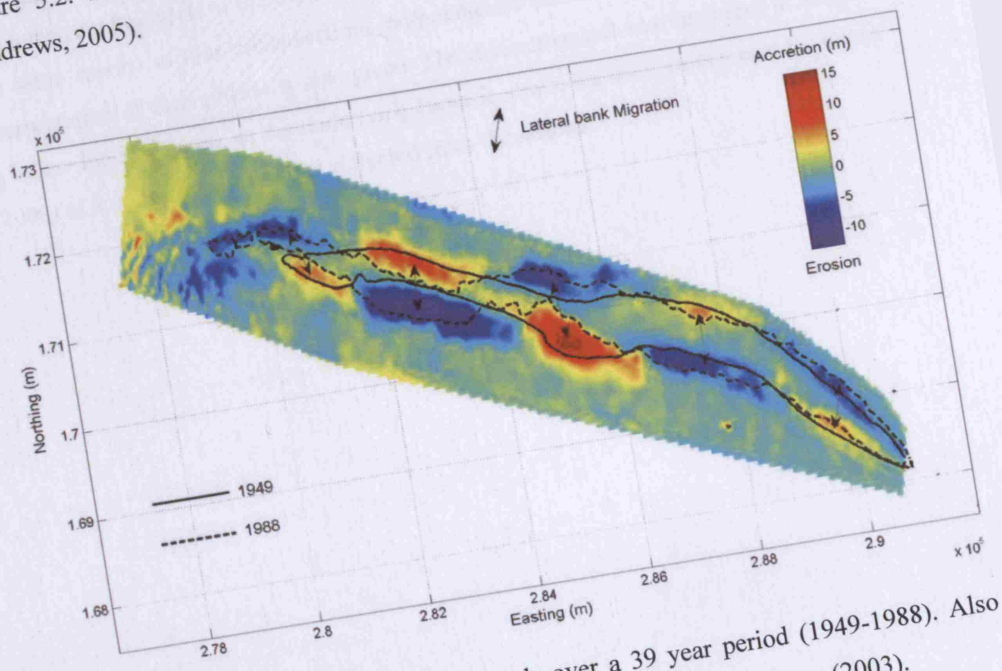

Figure 5.3. Bed changes at the Nash sands over a 39 year period (1949-1988). Also plotted is the 5 m contour line from 1948 and 1988. Data from Cudemo (2003).

5.1.2 Geology and Sedimentology

The Nash Sands rests upon an uneven rock platform that slopes from the east toward the south and west (Coastal Geophysics, 1995). From a thickness of 12 m at the eastern and middle regions of the bank, the sediment gradually thins. The presence of an underlying bed-rock core is difficult to confirm from seismic evidence. The Coastal Geophysics (1995) report states that there is no underlying bedrock while other reports, including that of EMU (1999), state that "The strike or alignment of the underlying rock strata has been found to vary across the length of the bank due to faulting and small scale folding". The same report also comments on the existence of "more resistant layers of rock, projecting through the seabed up to 2 metres" and that there is a distinct thickening of the sandy gravel basal layer of the bank.

Recent interpretation of the same seismic survey (Evans, 2006) concludes that there is no underlying bed rock to the bank. Figure 5.4 shows a corrected seismic profile (from the same report) at two cross-sections perpendicular to the bank crest. A schematic interpretation of each profile is also given. The distinctive reflector apparent at about 6 m below the bank crest, in the underlying Jurassic strata, has been interpreted by Evans (2006) as a multiple of the signal reflected from the seabed.

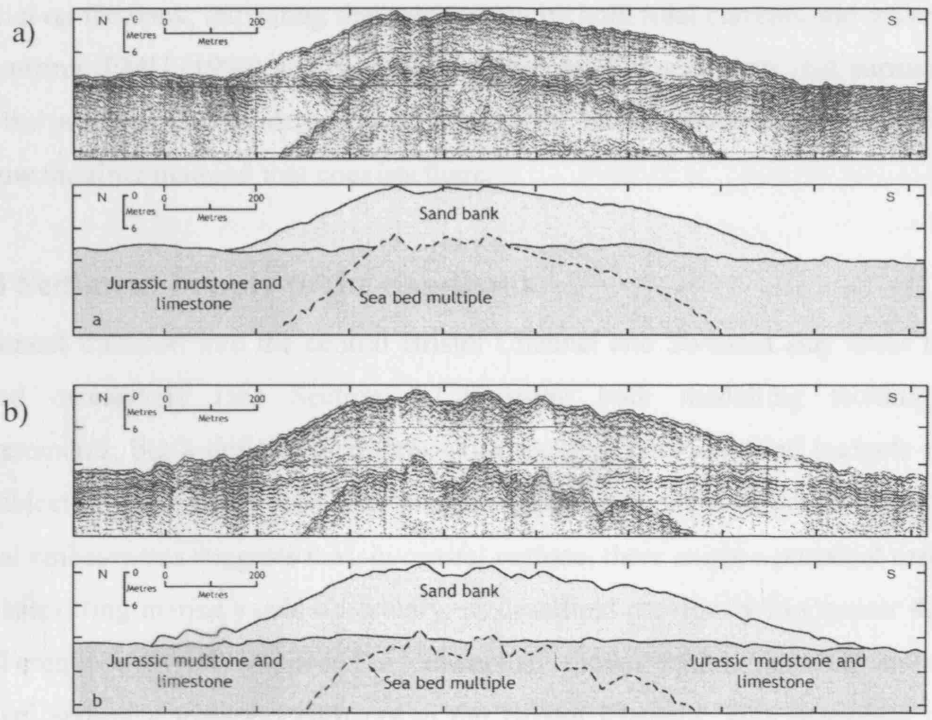

Figure 5.4. Seismic profiles and interpretations from Evans (2006) for: (a) section 1 and; (b) section 2. The profiles were taken at sections perpendicular to the bank crest (positions indicated in Figure 5.2)

Evans (2006) also suggested that the bank is dominated by two main processes: tidal currents which "control its location and shape and promote the formation of dunes"; and waves, which "flatten the dunes".

5.1.3 Surficial Sediments

Sediment grain sizes on the bank range from 0.23 to 0.37 mm (Gau and Collins, 1995). The exposed western end of the Nash Sands contains slightly coarser (0.4 mm) and well-sorted sediment reflecting the increased exposure of this side of the bank. Moving east along the bank, sediment characteristics remain almost constant up until the eastern Nash where fining up is observed on the northern face.

The eastern end of Nash contains the coarsest and best sorted sediments (EMU, 1999) where well-sorted sediments of up to 0.4 mm exist. There is a noticeable absence of fine

material on the bank, indicating that winnowing by both tidal currents and wave activity is occurring. EMU (1999) also suggest that the gravelly sediments that surround Nash have the potential to provide sandy material to the bank if wave energy is sufficient to winnow the finer material that coexists there.

5.1.4 Sediment Supply to the Sandbank

Sediment transport into the central Bristol Channel and Swansea Bay areas has been studied extensively (see Section 4.1.2) using both modelling techniques and measurements, but a definitive consensus on regional pathways and budgets has been the subject of much contention. The presence of large deposits of medium sands in the coastal embayments suggests that, in coastal regions, there exists a potential mechanism for transporting marine sands up-estuary, as described previously in Chapter 4. Collins and Ferentinos (1984) proposed a conceptual model which included a 'mutually evasive' sediment transport pathway in the Bristol Channel. This described coastally constrained, easterly directed transport pathways to the north and south of the system, and a westerly directed transport in the ebb-dominated main channel. This has been investigated in the previous chapter using numerical modelling. It was demonstrated that a strong mechanism exists, reliant on a wave-related switch in the direction of peak bed shear stresses and due to, primarily, low frequency swell waves. The work suggested that waves could provide a means of replenishing coastal sediment sinks that would otherwise deplete under the ebb-dominated tidal action.

5.1.5 Possible Mechanisms of Formation and Maintenance

Pingree (1978) and Pingree and Maddock (1979) first suggested that secondary currents produced by tidal eddies affect sediment transport and may be responsible for the production of topographic features around headlands. In Chapter 2 it was shown that near-headland sandbanks are controlled principally by gradients in the instantaneous bed shear stresses rather than residual or transient circulations, supporting the work of Signell and Harris (2000) and Bastos et al. (2002). Kenyon and Cooper (2004) suggested that, for near-headland banner-type banks, it is "bed-load convergence and the near closed system of sand circulation that make it possible for the banks to exist in

places where the current speeds are high and where grain sizes of bank sediments are below the equilibrium size for that current speed". This is a useful way of describing the process by which sediments can become trapped in regions where they would otherwise not accumulate due to the high current speeds. In contrast., Berthot and Patiaratchi (2005) suggested that secondary currents could be important "when associated with the instantaneous tidal flow, particularly at maximum currents". This suggests that secondary currents, produced by tidal eddies, could modify the peak instantaneous current vectors and alter the net sediment transport.

For the Nash Point headland, the formation of a tidal eddy can be predicted by simple consideration of the headland geometry and the tidal streamlines. Signell and Geyer (1990) fitted an ellipse with current-normal and current-parallel axes to the headland geometry and calculated the resulting 'aspect ratio' for each stage of the tide. The 'aspect ratio' of each ellipse is the ratio of shore-normal to shore-parallel ellipse axes. For a residual eddy to form, Signell and Geyer (1990) suggest that the aspect ratio must be greater than 4/3. In the case of the Nash Sands, the aspect ratios are estimated to be 2.33 and 0.5 for the ebb and flood phases, respectively (see Figure 5.1), suggesting that an eddy forms on the western side of the headland.

The modelling work of Uncles (1982) indicated the presence of a large residual eddy on the western side of the Nash Point headland. The eddy closely follows the isobaths of Nash Sands, suggesting a relationship between the eddy and the sandbank. In the current work, the relationship of the eddy to the growth and maintenance of the Nash Sands is investigated using the numerical modelling system established in Chapter 3. The principal question relates to whether the eddy is a product of headland-associated tidal dynamics (described earlier and in Chapter 2) or whether it is induced by the presence of the sandbank. If the latter is true then the observed circulation may be a symptom of a hydrodynamic mechanism of bank maintenance, first demonstrated by Zimmerman (1978) and Huthnance (1982). The mechanism was shown to be prevalent on tidal sandbanks that are aligned anti-clockwise to a reversing tidal flow. It can be explained by considering a ridge, or sandbank, situated in a shallow coastal sea, inclined anticlockwise to the tidal streamlines (see Figure 5.5). Moving from deeper to shallower water, a parcel of fluid particles will be increasingly affected by frictional interaction

with the seabed and fluid moving onto the sandbank will be moving faster than fluid moving off of it. This will affect the spatial deflection (or curve) of the moving fluid particles either side of the sandbank crest.

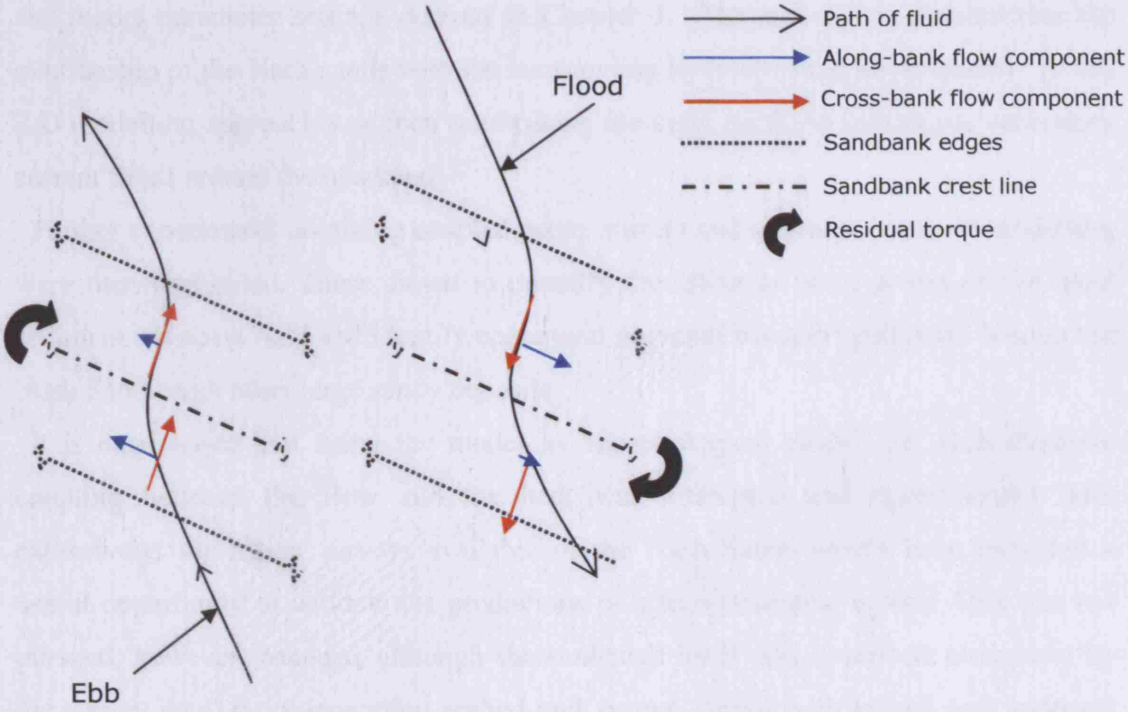

Figure 5.5. Streamlines crossing a ridge aligned anti-clockwise to the undisturbed flow.

Dronkers (2005) describes the mechanism in terms of the inertial response of a parcel of fluid particles moving across a ridge: during the ebb phase, flow adaptation to friction on the upstream side of the ridge is delayed by the relatively high inertia of the fluid. Streamlines are deflected toward the crest with a spatial lag. The result is an overall increase in the along-ridge flow component. On the downstream side frictional effects slowly reduce with increasing water depth and the response of the fluid parcel is delayed (spatially) due to its relatively low inertia. The result is an increase in the west-east along-ridge flow component. The overall effect is a residual current field consisting of mutually opposing along-ridge flow components. The presence of such a mechanism on the Nash Sands is investigated in Section 5.3 by computing the frictional contribution to vorticity production over a tidal cycle.

5.2 Model setup

A depth-integrated (2-D) model was first applied, which used the unstructured mesh and model parameter settings derived in Chapter 3. The aim was to demonstrate the relationship of the Nash sands with the surrounding hydrodynamic environment. A full 3-D modelling approach was then used (using the same mesh) to investigate secondary current fields around the headland.

Further experiments involving coupled wave, current and sediment transport modelling were then performed. These aimed to quantify the effect of wave action on the local sediment transport field and identify ephemeral potential transport pathways linking the Nash Sands with other large sandy deposits.

It is emphasised that using the model in 'morphological mode', i.e. with dynamic coupling between the flow and the bed, was attempted and experimented with extensively: the repeat surveys available of the Nash Sands would have provided a useful opportunity to validate the predictions of a morphological model. This was not pursued, however, because, although the sandbank itself was described accurately by the survey data, the surrounding seabed and system lacked both spatial and temporal resolution. Inserting the sandbank into the model bathymetry surrounded by a patchwork of survey data from the surrounding system (from different decades and of varying quality) led to bed changes that were simply model adjustments as it tried to achieve a steady state i.e. one in which the bathymetry and the forcing were in equilibrium. It became impossible to differentiate cause-effect relationships or establish long-term trends which could be validated by the high resolution survey data available.

The approach taken in the following experiments used trends in the hydrodynamic and sediment transport predictions to infer the potential for changes to the bank bathymetry.

A brief description of the model parameters is given in Section 5.2; Section 5.3 describes the pure current and sediment transport modelling experiments; combined wave-current and sediment transport modelling is presented in Section 5.4 and Section 5.5 discusses the main findings in a geological context. The work is summarised in Section 5.6.

The modelling experiments have been carried out using the MIKE 21/3 FM (Flexible Mesh) coupled modelling system. The modelling system includes a dynamic coupling

between flow and spectral wave models and is based on an unstructured finite volume technique. Node separation of the unstructured mesh ranges from 2.5 km in offshore areas to 45 m in a near-shore region including the Nash Sands and the eastern side of Swansea Bay (see Figure 5.1). For a full description, see Chapter 3 where the model has been extensively validated in and then employed in the regional transport studies of Chapter 4. Only a brief description of the individual modules is provided below.

5.2.1 Flow Model

The flow model solves the Reynolds-averaged Navier Stokes equations and assumes hydrostatic pressure is valid and that the Boussinesq hypothesis is representative of the turbulent stresses (see Appendix 2). The effect of the waves on the flow field is taken into account by the radiation stress concept (Longuet-Higgins and Stewart 1964). Both 2- and 3-D flow models have been used in the present work. The 3-D model uses sigma co-ordinates to separate the vertical into discrete layers and solves the shallow water equations for each layer with transfer of mass between the layers provided by continuity. The model uses an eddy viscosity concept to resolve sub-grid level turbulence, including a k-ε model (Rodi 1984) and the approach of Smagorinsky (1963) for the vertical and horizontal eddy viscosities, respectively.

Boundary conditions for the flow model were provided by tidal elevation data based on global tidal analysis which gave eight deep water constituents (Andersen 1995). The flow model was calibrated over a spring-neap cycle. Model predictions are compared with measured current velocities and water surface elevations in Appendix 3.

5.2.2 Wave Model

The wave model has been applied in 'parametrically decoupled' mode where the wave action-balance equation is solved by describing the frequency domain in terms of a mean wave frequency (Holthuijsen et al., 1989). Wave computations are performed as a set of discrete 'stationary' solutions at pre-defined intervals to give a dynamic, time dependant solution that includes the effect of wave-current interaction. The approach has been extensively validated in the Bristol Channel by Sørenson et al. (2006)

5.2.3 Sediment Transport Model

The sediment transport rates are calculated using a 1-D (Vertical) point model (*STPQ3*) which uses an integrated momentum approach to solve the wave-current boundary layer over a complete wave cycle (see Fredsøe 1984). Oscillatory bed-load and suspended-load transport rates are obtained via the Shields parameter and a reference concentration approach, respectively. The 1-D model is first run for the complete range of water depths and wave and current combinations that are expected in the domain. This is done prior to the main flow and wave computations and the results written to a 'transport table'. During the 2-D coupled wave and flow simulations, transport rates are interpolated from the transport table at a pre-defined multiple of the hydrodynamic time-step.

The advantage of this approach is that it provides a better description of the sediment transport rates without sacrificing the overall computational speed of a depth-averaged or sigma layered model (see Chapter 3 for further details).

5.3 The Effect of Tidal Currents on Sandbank Morphology

Model tests were conducted over separate spring and neap semi-diurnal (12.42 hrs.) tidal periods. Simulations were performed both with and without the Nash Sands present in the bathymetry (see Figure 5.6). The bed was artificially excavated to the level of the surrounding sea bed. For the simulations performed with the Nash Sands present, survey data of the bank from 1988 was interpolated into the model bathymetry. 1988 data was used because it was the closest year to 1987, the year in which data was collected by the Admiralty for the central Bristol Channel (which has been used as bathymetry for the area that surrounds the bank in the model).

Plots of instantaneous spring current vectors, during both peak flood and ebb tides, are presented in Figure 5.7. The plots demonstrate the way in which the bank affects the tidal currents: as the tidal current moves on to the bank (from deep to shallow water) it is immediately deflected clockwise by frictional torque. As the flow moves off the bank (from shallow to deep water), reducing frictional torque deflects the flow anti-clockwise.

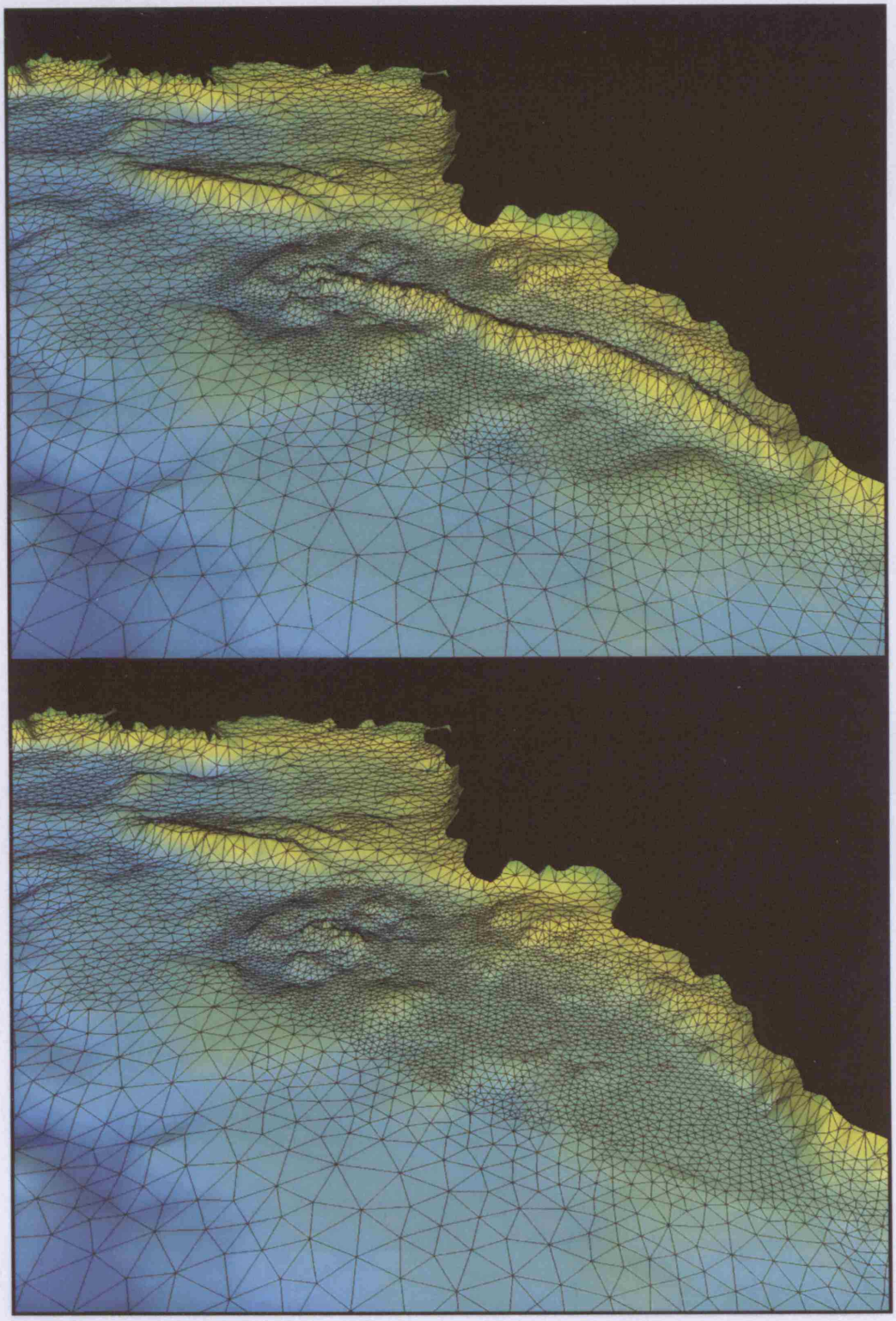

Figure 5.6. 3-D images of the unstructured mesh, (a) with the Nash Sands and; (b) without the Nash Sands present in the model bathymetry.

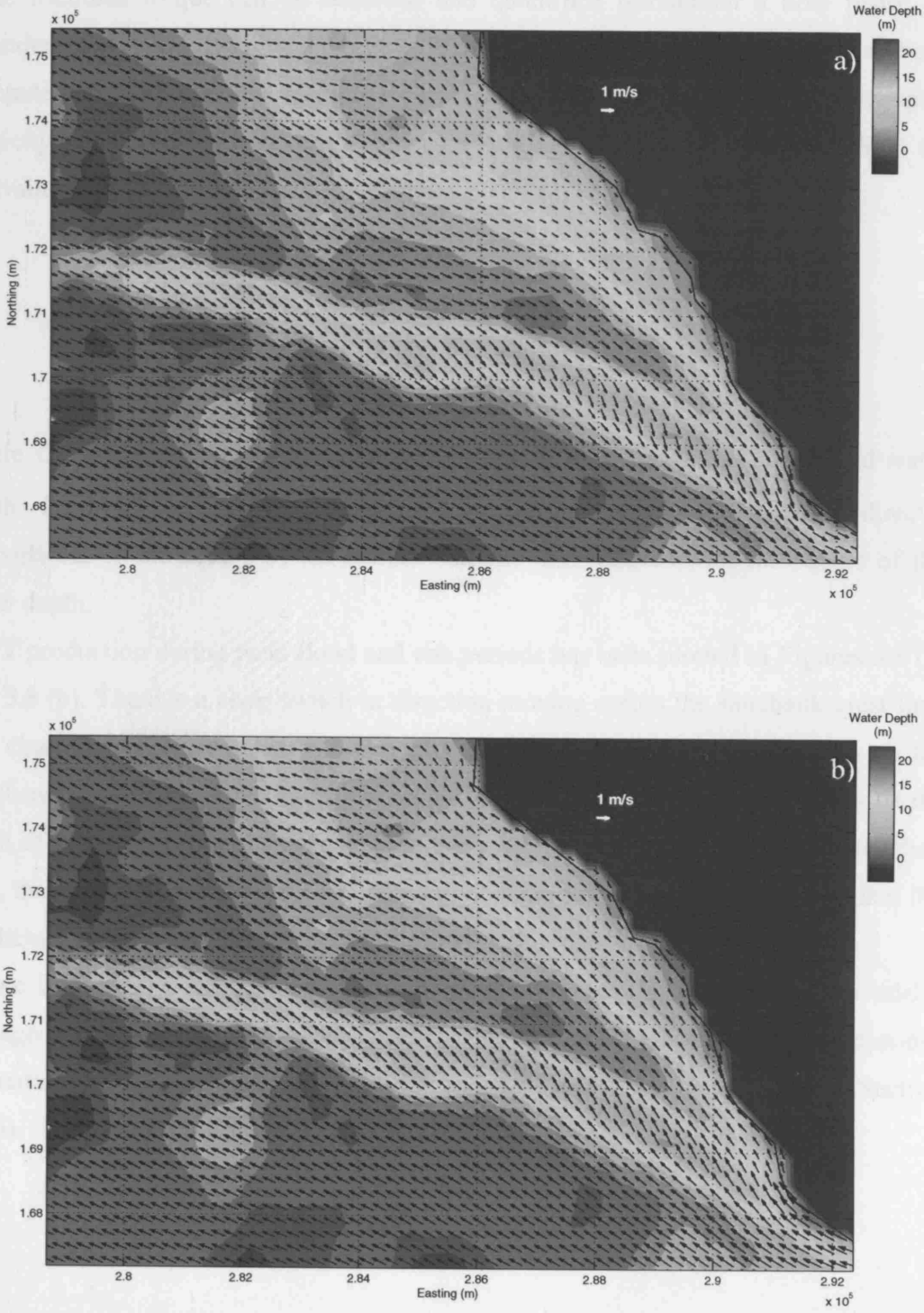

Figure 5.7. Model predictions of peak spring (a) flood and; (b) ebb current velocities (depth-averaged).

The frictional torque can be observed and quantified throughout a tidal phase by consideration of the 'frictional vorticity transport' (hereafter, *FVT*), which has been computed from the model results. *FVT* describes the contribution to the transport vorticity balance by the frictional torque (see Park and Wang 2000 and Appendix 1 for derivation) and is computed as

$$FVT = C_D \left[\nabla \times \frac{\mathbf{U}|\overline{U}|}{H^2} \right] \cdot \mathbf{k} \qquad (5.1)$$

where C_D is a frictional coefficient, U is the current velocity and H is the total water depth. From the expression, it can be seen that the frictional torque is directly proportional to the square of the current velocity and reduces with the square of the water depth.

FVT production during peak flood and ebb periods has been plotted in Figures 5.8 (a) and 5.8 (b). There is a clear switch in direction moving across the sandbank crest-line. The change is also illustrated by comparing the *FVT* components at two points on the sandbank slopes whose positions are indicated in Figure 5.8 (c). One point is to the north of the bank crest (P1) and one is to the south (P2). The figure demonstrates that, first, there is a clear switch in *FVT* production as the tide reverses, and second that the northern and southern slope productions always act in opposition.

More importantly, the residual *FVT* production (Figure 5.8 (c)) indicates a tidally averaged rotation that is clockwise. This is a result of the unbalanced frictional response to inertia that occurs during both the flood and the ebb phases (as described in Section 5.1.5).

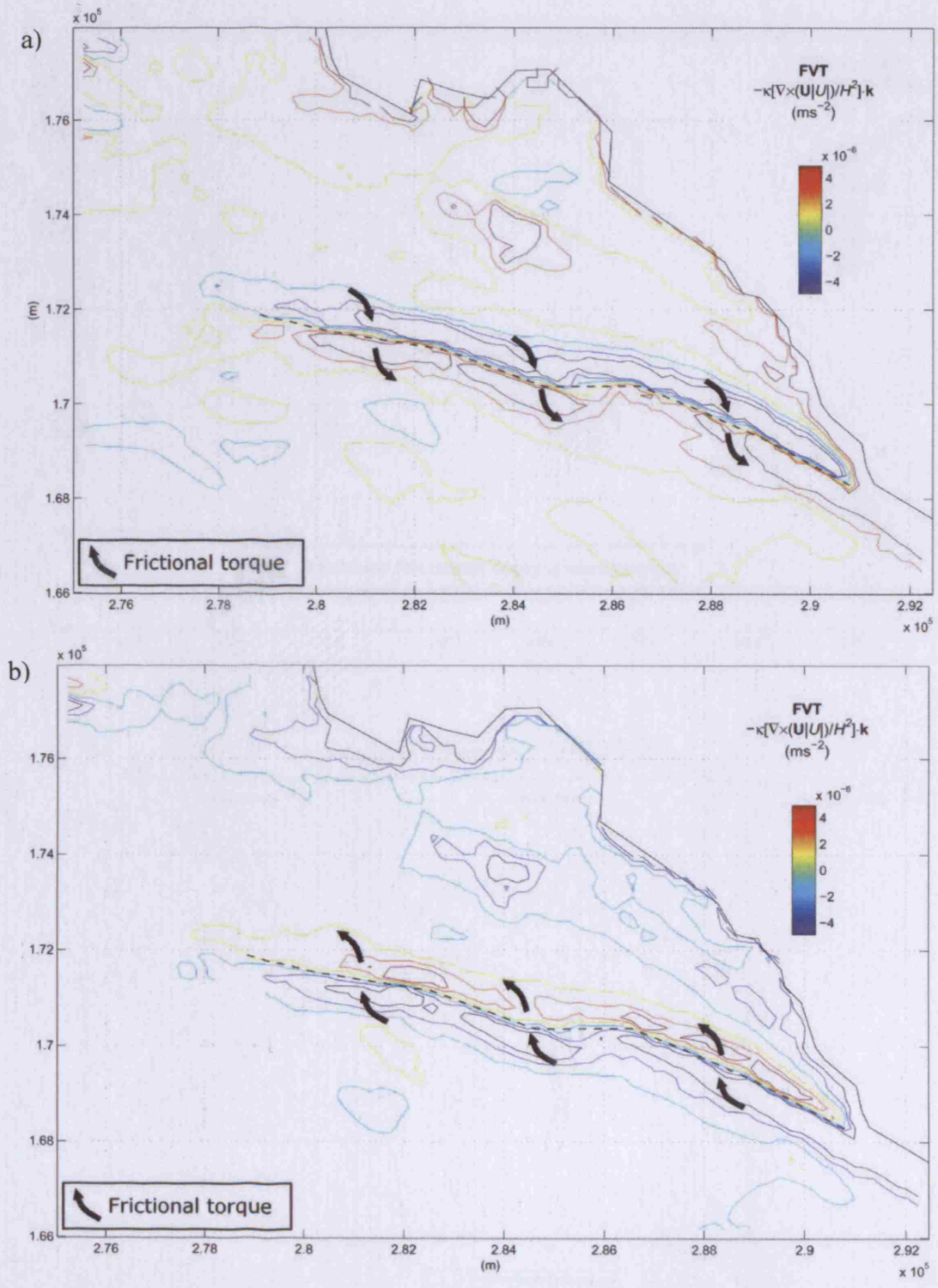

Figure 5.8. Frictional transport vorticity (FVT) production at: (a) peak flood and (b) peak ebb. Dashed line indicates the bank axis position.

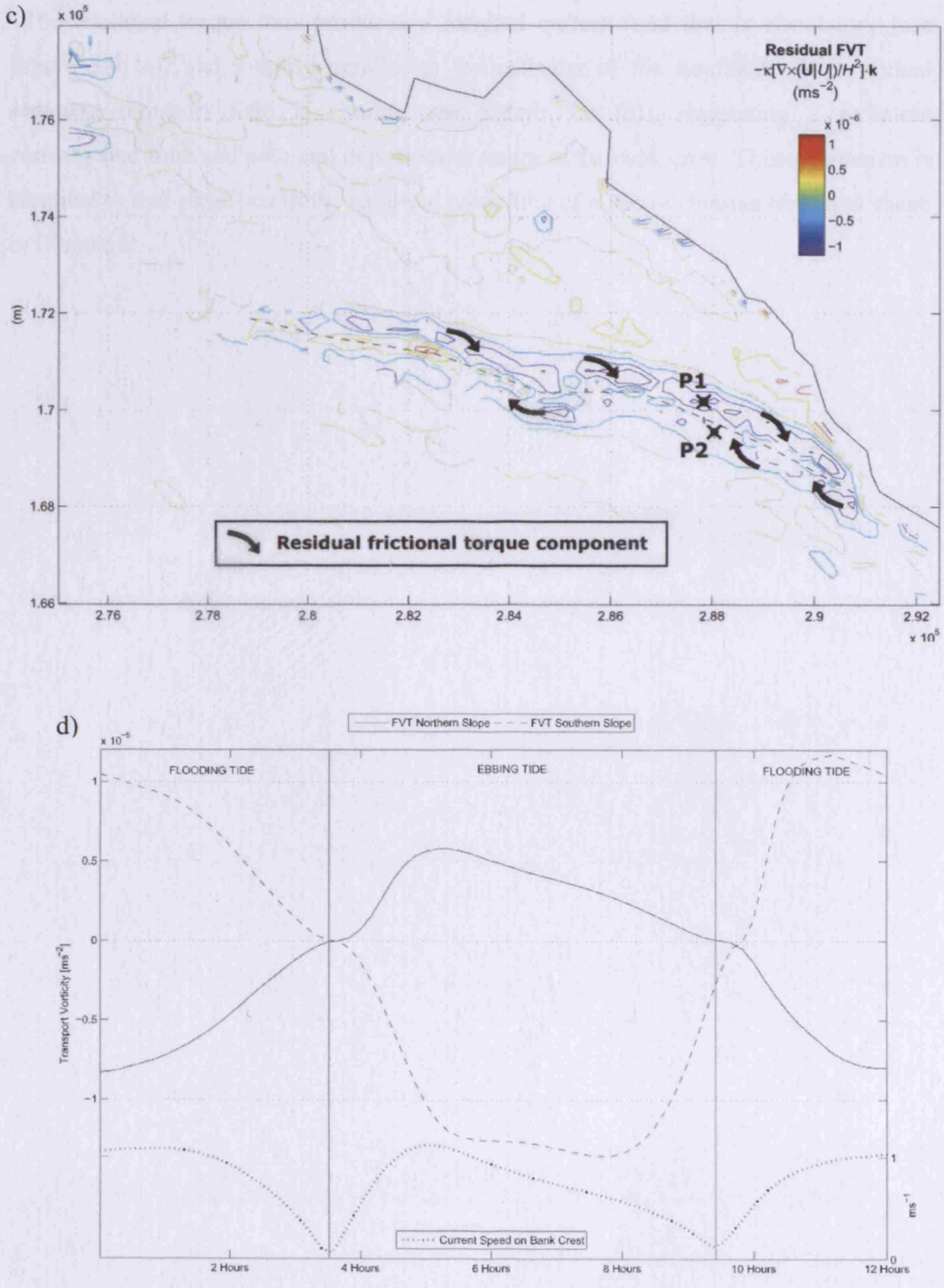

Figure 5.8. (c) Residual FVT production and (d) FVT production at point P1 and P2 (positions indicated in (c)).

The frictional torque thus produces a residual current field that is circulatory (see Figure 5.9 (a)) and roughly parallel to the isobaths of the sandbank. The residual sediment transport field is similar (see Figure 5.9 (b)), suggesting a sediment convergence zone and potential depositional centre at the bank crest. This mechanism is identical to that identified in the idealised modelling of a semi-Gaussian headland shape in Chapter 2.

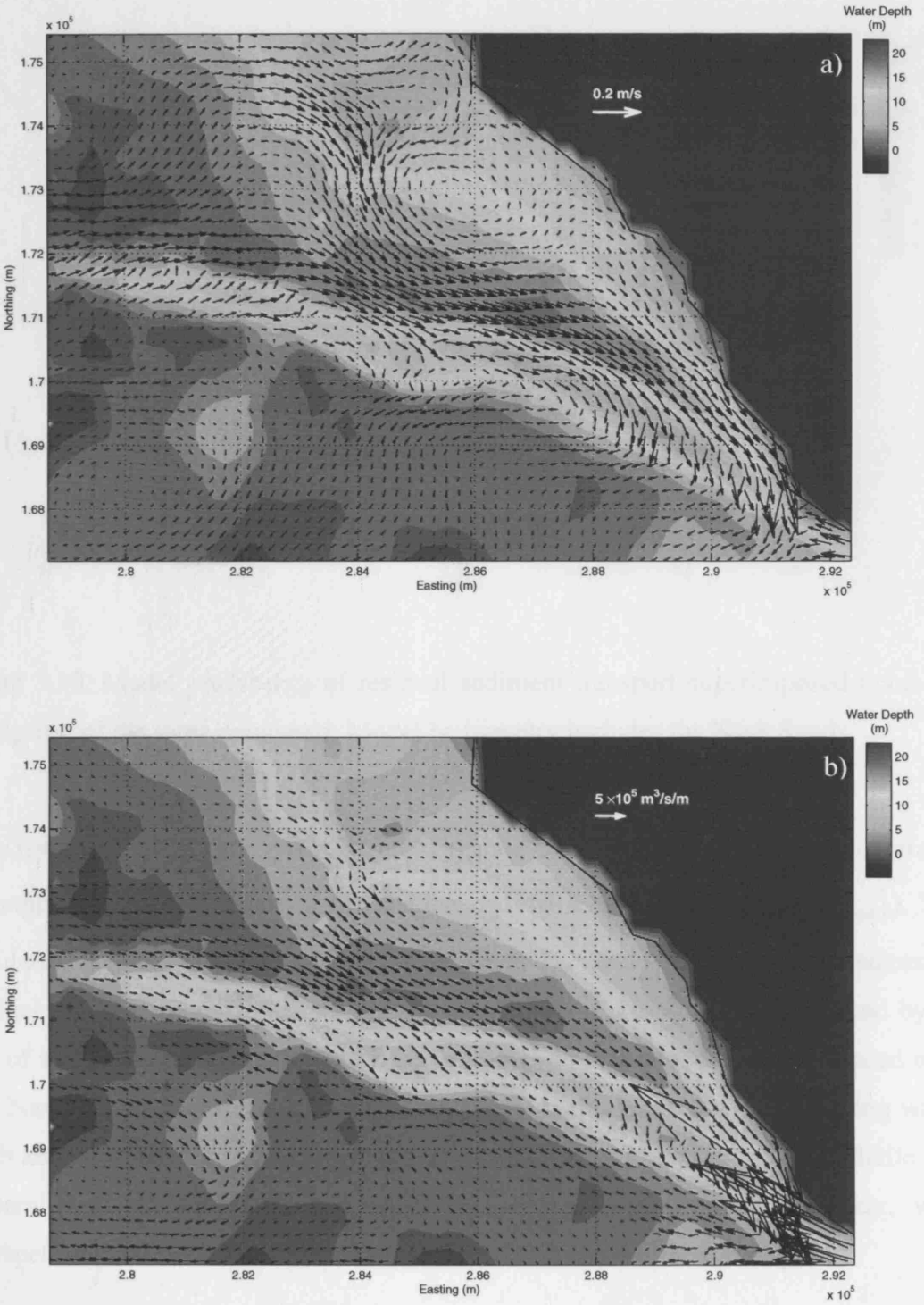

Figure 5.9. Model predictions of residual spring (a) current and; (b) total load transport pathways.

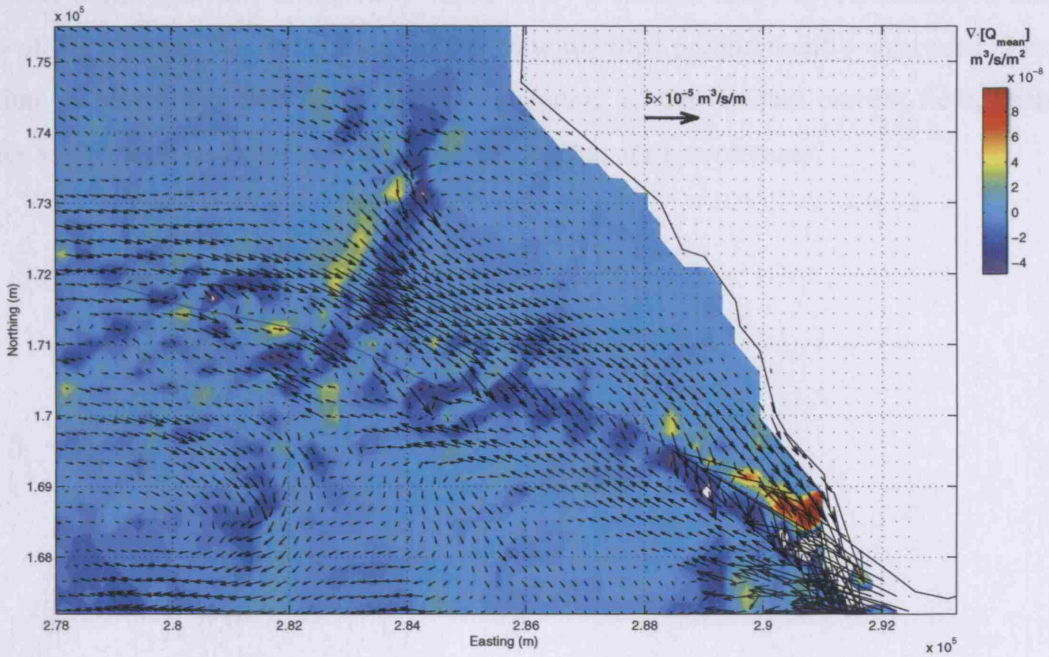

Figure 5.10. Model predictions of residual sediment transport superimposed upon the divergence of the same parameter. Model bathymetry includes the Nash Sands.

The resulting potential for sediment convergence at the bank crest can be demonstrated by computing the divergence of the residual sediment transport field ($\nabla \cdot [Q_{mean}]$). The calculated values are plotted in Figure 5.10 and include superimposed vectors of residual sediment transport. The centre of the sediment transport eddy is marked by an area of sediment convergence (dark blue colour). The feature is most pronounced over East Nash. Moving westward, frictional torque gradually reduces with increasing water depth and the sediment convergence subsequently reduces in intensity. Over middle and western Nash, therefore, the pattern of sediment convergence is less clear, with interspersed patches of convergent and divergent residual sediment transport.

Model experiments conducted with the Nash Sands removed from the bathymetry suggest a significant difference in the residual current (Figure 5.11 (a)) and sediment transport fields (Figure 5.11(b)). The circulatory flow field that previously enveloped

the Nash Sands has now disappeared replaced by a smaller eddy, approximately 2 km west of Nash Point. The local flow field is now directed predominantly westward. The residual sediment transport field reflects the pattern of the residual current field, with eddies to the north and south (of the Nash sands) that are less obvious.

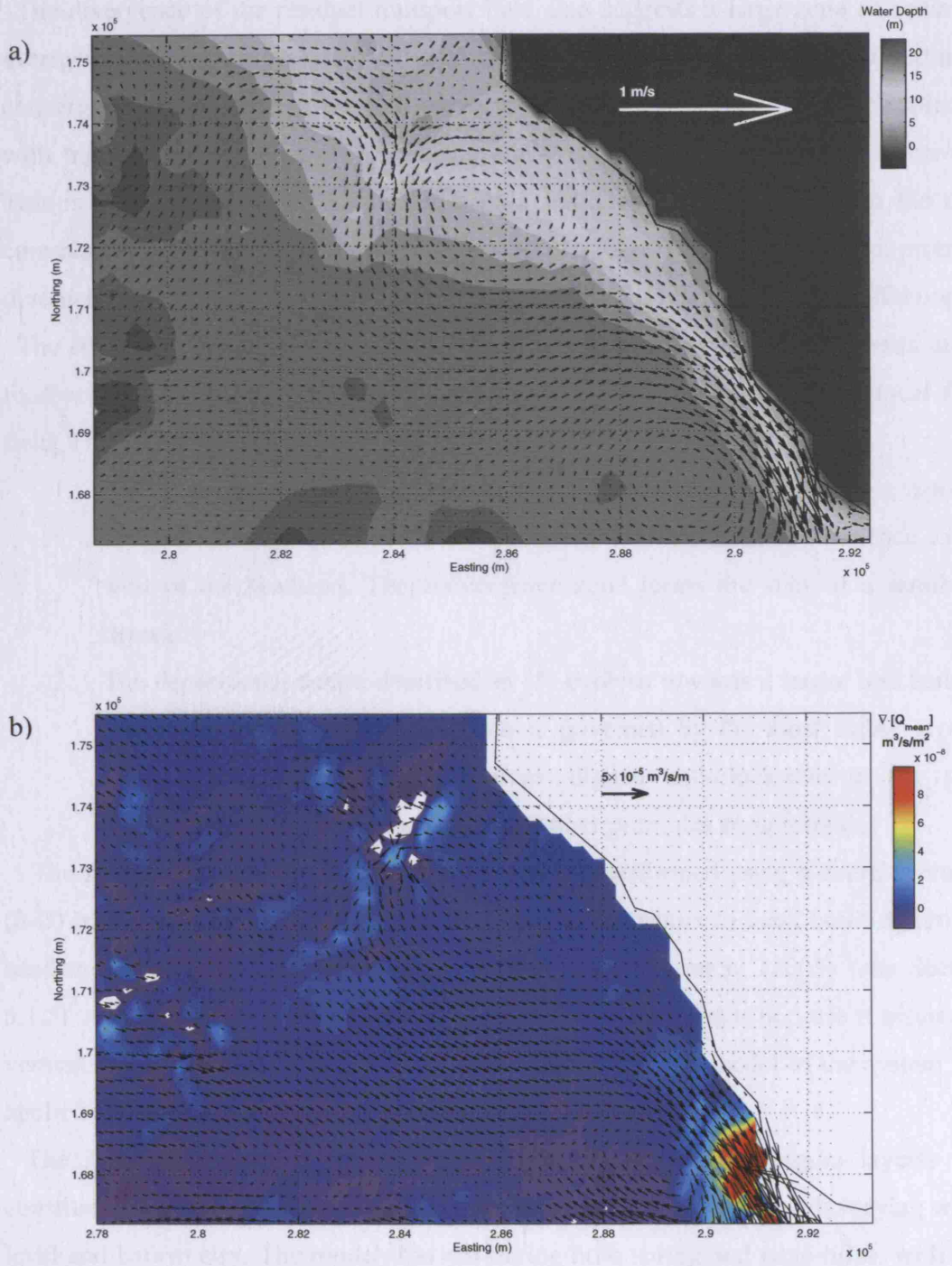

Figure 5.11. (a) Residual current field and; (b) residual total load transport vectors superimposed upon the divergence of the residual total load transport field. The Nash Sands is excluded from the model bathymetry.

The divergence of the residual transport field also suggests a large zone of sediment divergence (in Figure 5.11 (b)) close to the headland and a large zone of sediment convergence approximately 3 km to the west of the headland. The two zones coincide with transport vectors that are increasing and decreasing in magnitude, respectively. This is a key factor in explaining the bank's initiation: strong gradients in the tidal currents, induced by continuity-induced flow acceleration around the headland, promote divergence of sediment transport near the headland and convergence further offshore.

The sediment convergence zone will be further modified by the tidal currents and a feedback mechanism (described earlier) between the bed changes and the local flow field. The bank's growth is thus a two stage process:

1. Continuity-induced flow acceleration around the headland induces a zone of sediment divergence (close to the headland) and sediment convergence to the west of the headland. The convergence zone forms the start of a sandbank deposit.
2. The depositional centre described in (1) evolves towards a larger bed feature, the shape and orientation of which is governed by the most stable growth mode; that is, an elongated feature aligned anti-clockwise to the tidal streamlines in which frictional torque further promotes bank growth.

The simulations described in this section were all performed using a depth-averaged (2-D) model. The potential for secondary flows to contribute to bank building around headlands has been commented on by Berthot and Pattiaratchi (2005) (see Section 5.1.5). A 2-D model is unable to capture depth-varying flow fields because it assumes a vertical velocity gradient that is logarithmic. Therefore, a 3-D model of the system was applied in order to investigate the contribution of secondary flows.

The 3-D model consisted of 9 horizontal layers (henceforth, sigma layers) that constitute the vertical domain. The sigma layers contract and expand with varying water level and bathymetry. The model was run during both spring and neap tides, with and without the sandbank included in the model bathymetry. Secondary currents would be identified by the presence of dissimilar near-bed and near-surface current fields as well as by local areas of up-welling and down-welling.

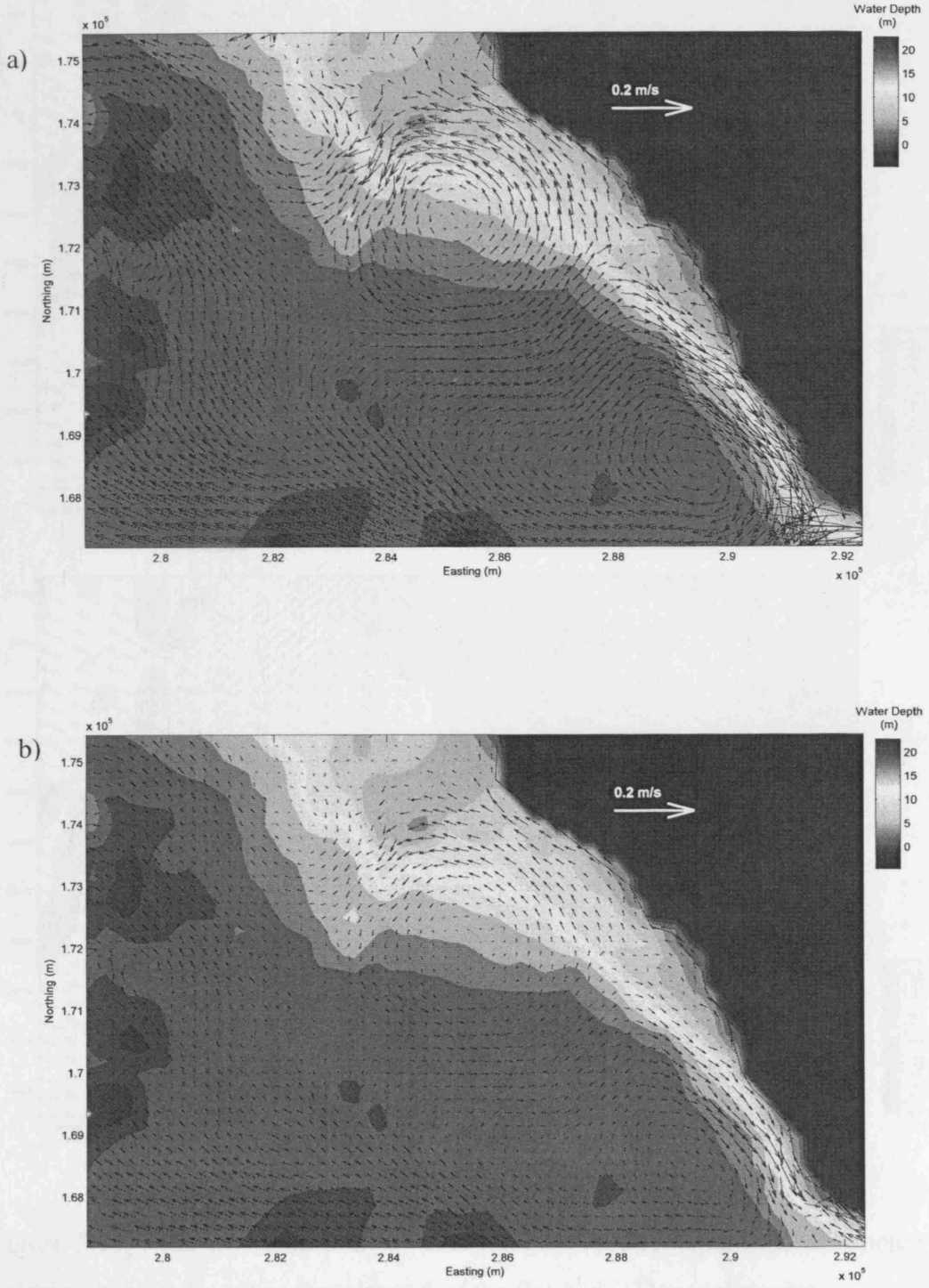

Figure 5.12. a) Near-surface and; b) near-bed residual current fields for simulations performed without the Nash Sands present in the model bathymetry.

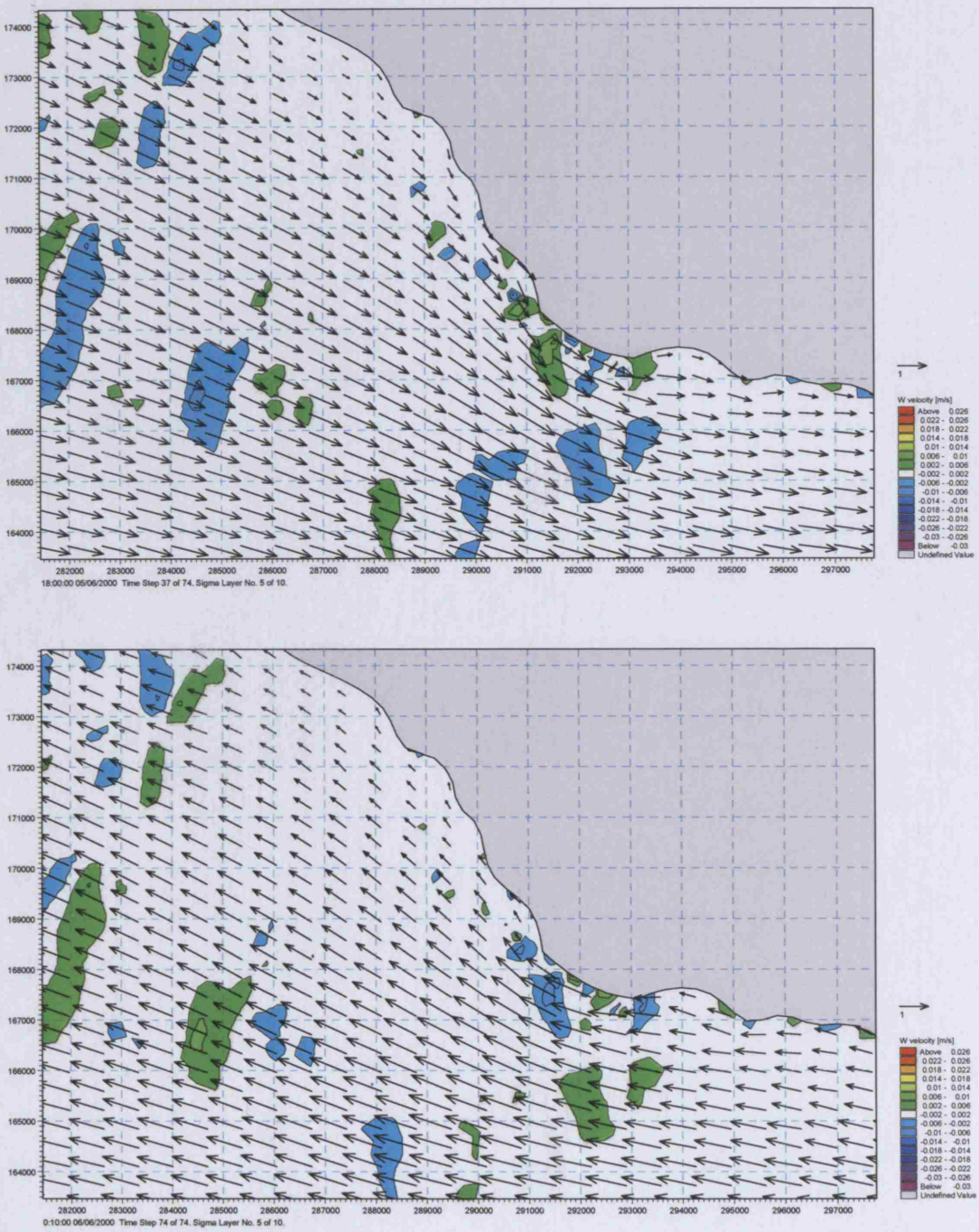

Figure 5.13. Peak (a) flood and (b) ebb velocity vectors superimposed upon vertical velocity magnitudes taken from layer 5 of the flat-bed 3-D model results.

Residual near-surface and near-bed current vectors are included in Figure 5.12 for a model bathymetry that excludes the Nash Sands. The plots show that near-bed velocities are much smaller than near surface velocities but that there is little difference in the current direction. The near-bed vectors are in phase with the near-surface vectors and, hence, it appears that there is no apparent mechanism of generating a secondary current. Further, in the absence of the bank, vertical velocities are small (in comparison to the horizontal velocity magnitudes), except for the very near headland area (0-750 m from Nash Point), see Figures 5.12 (a and b).

Comparison of the vertical velocity magnitude around the headland with empirical estimations of the fall velocity of this type of sediment demonstrates the relative unimportance of the secondary currents. Using an approach proposed by Soulsby (1997) the settling velocity sand particle in water can be related to the grain diameter, the grain density and the viscosity of water. The approach requires the calculation of a dimensionless grain size, $D*$

$$D* = \left[\frac{g(s-1)}{\upsilon^2}\right]^{1/3} d \qquad (5.2)$$

where g is the acceleration due to gravity, υ is the kinematic viscosity of water, d is the grain size and s is the ratio of densities of grain and water. By optimising two coefficients in a combined viscous plus bluff-body drag law against data for irregular grains, Soulsby derived a new equation to describe the settling velocity, w_s, of a natural sands

$$w_s = \frac{\upsilon}{d}\left[(10.36^2 + 1.049D*^3)^{1/2} - 10.36\right] \qquad (5.3)$$

Assuming water and grain densities of 1027 kgm^{-3} and 2650 kgm^{-3}, respectively, and that the kinematic viscosity of sea water is $1.36\times10^{-6}\ m^2s^{-1}$, the settling velocity of 260 μm sand grains can be calculated as 0.0321 ms^{-1}. Comparing this value with the peak vertical velocities predicted by the model (see Figure 5.13 (a) and (b)), in which the

maximum vertical velocity value is approximately 0.15 ms^{-1}, suggests that secondary currents produced by flow curvature around the near-headland area are too small to have a significant impact on the sediment distribution.

5.4 Combined Wave and Current Effects

As well as tidal currents, the Nash Sands is exposed to a mixture of long-period Atlantic swell waves and higher frequency locally generated wind waves. The influence of the wave climate on the bank's morphodynamics, particularly during larger storm events, has been commented on by a number of authors including most recently Evans (2006), who suggested that wave action provides a destructive influence on the large-scale bed features.

In the next experiments, a coupled model, with a fully dynamic feedback between waves, currents and sediment transport, has been used to simulate a number of different wave and current combinations. The wave conditions included in the tests broadly reflect the wave climate measured in the local area (see Section 4.1.1) summarised in Table 5.1 below.

Table 5.1. Wave height and period simulated for both spring and neap periods for a prevailing wave and wind direction of 255°. X marks the tested wave conditions.

T_z/H_s	1 m	2 m	3 m	4 m	5 m
3 s	X				
6 s				X	
9 s	X	X			X
15 s			X		

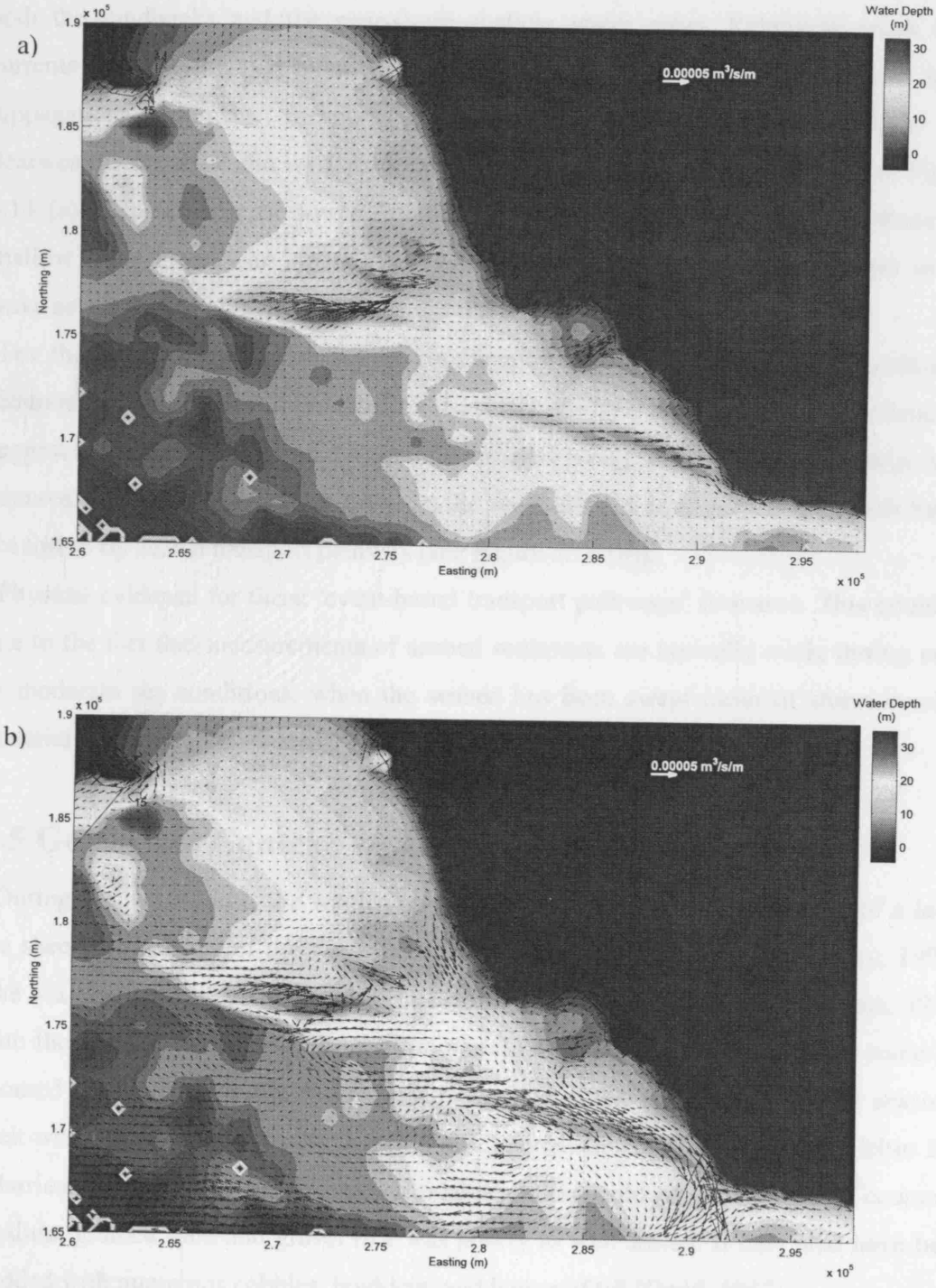

Figure 5.14. Combined wave and current predictions of residual sediment transport rates for: (a) a neap, and; (b) a spring tide with a wave of 3 m (H_s), 15 s (T_{pk}).

Under neap conditions, wave action has a significant effect on the current field over both the sandbanks and the near-shore shallow water areas. Relatively weak tidal currents are overwhelmed by wave-induced currents that are in the direction of wave propagation. Sediment transport along the banks, including Nash Sands and Scarweather Sands to the west, is greatest for the long period waves (15 s, see Figure 5.14 (a)). This is because low frequency waves generate large momentum fluxes in shallow water areas. The direction of sediment transport under neap tides and strong wave action is thus predominantly toward the coast.

For the wave conditions tested in combination with spring tides, the direction of sediment transport is still dominated by the tidal currents. However, there is evidence to suggest that the waves enhance sediment transport along pathways that link large sand features: under long-period wave action, the sandbanks of Scarweather and Nash Sands are linked by such a transport pathway (see Figure 5.14 (b)).

Physical evidence for these 'event-based transport pathways' is scarce. This could be due to the fact that measurements of seabed sediments are typically made during calm or moderate sea conditions, when the seabed has been swept clean of storm-invoked material by the strong local tidal currents.

5.5 Geological Context

During the last ice age, the south Wales coast marked the southerly extent of a large ice sheet covering all of the western and northern areas of the U.K. (Bellamy, 1998). The sea level was an estimated 120 m below the present day value (Jelgersma, 1979) with the position of the coast-line in the middle of the Celtic Sea. Terrestrial material, scoured by the moving ice-sheet, was transported southward by sub-glacial seasonal melt-water and deposited into the Bristol Channel and offshore into the Celtic Sea (Harrison et al., 1998). These glacio-fluvial deposits would have consisted of coarse to medium grained sand and gravel that was poorly to well sorted. It may also have been bedded with numerous cobbles, boulders, and lenses of till (Gadd, 1987)

During the ensuing sea level rise (the Flandrian Transgression), the U.K. continental shelf became progressively flooded and around 10000 years ago, the present-day near-shore regions became inundated (Evans, 2006). It is proposed that during the early

stages of inundation, relatively shallow water would have promoted the dispersion of isolated well-sorted fluvial deposits by wave action. In addition, wave-induced currents would have encouraged the transport of further glacio-fluvial marine deposits into the Bristol Channel. With increasing water level, tidal effects began to dominate the system and natural zones of sediment convergence, including those around headlands, provided depositional centres for the sediment. The zone of sediment convergence that exists west of Nash Point (identified by the model test with the sandbank excluded from the bathymetry) demonstrates the potential for sandbank initiation at this location. With further sea level rise, sediment availability from dispersed glacio-fluvial sediments persisted as did wave-induced transport from the Celtic Sea. The initial growth mechanism would then evolve into a self sustaining sandbank feature.

The internal structure of the sandbank, interpreted from seismic investigation in Figure 5.4, indicates the presence of overlying large and small sand-waves, subject to constant re-working by tidal and wave action (Evans, 2006). This is indicative of a 'Houbolt sand accumulation' model of sandbank growth in which the sandbank rests on a flat, transgressive surface and is related to a convergent pattern of sediment transport (see Houbolt, 1968, and also Bastos et al., 2003). It is further confirmation of a continued growth and maintenance mechanism observed in the present-day regime via numerical modelling (described previously). Similar tidal and wave processes that now affect the sandbank were present since its formation.

5.6 Summary

A numerical modelling investigation, combined with geological interpretation, has demonstrated a number of aspects related to the growth and maintenance of a near-shore 'banner-type' headland sandbank. The growth of the Nash Sands is suggested to have been triggered by the Flandrian transgression and perpetuated by a combination of tidal action and sea-level rise.

After the initial inundation of near-shore regions, Fluvio-glacial material deposited in the Bristol Channel was dispersed by wave action and other deposits from further offshore were transported landward by strong wave-induced currents. With increasing sea level, the sediment was re-worked and deposited in zones of sediment convergence,

characterised by strong gradients in the local current field. Modelling experiments presented here, which excluded the Nash Sands from the bathymetry, demonstrate the existence of a major zone of potential sediment convergence to the west of Nash Point, close to the present-day location of the sandbank.

The mechanism by which this initial zone of sediment convergence could have developed into a larger sandbank feature (by way of hydrodynamic instability) has been demonstrated. The instability is the result of frictional retardation, which, due to the inclination of the bank relative to the tidal streamlines, promotes a residual circulation of water and sediment. This circulation further enhances convergence of re-worked fluvio-glacial sediments towards the bank crest. As sea level rose during the Holocene, the initial accumulation of sediment evolved into a larger bed feature, the shape of which was governed by the most stable growth mode under the present tidal regime.

The model also predicts exchange of sediment across the bank, particularly in the eastern and middle Nash areas. The modelling results are supported by examination of bank characteristics and bed features from high resolution SWATH bathymetry: significant north-south deviation of the bank crest-line can be observed, accompanied by large sand-waves that are orientated in a similar way.

3-D modelling results show that patterns of near-bed and near-surface current fields are identical, confirming that secondary currents are not significant around the headland and do not play a role in the bank's growth.

Combined wave, current and sediment transport modelling has demonstrated the impact of wave-induced currents and wave-enhanced bed-shear stresses on the local sediment transport regime. During neap tides, wave-induced currents are shown to be significant and push sediment in the direction of wave propagation along the bank crests and towards the shore. Given that the prevailing wind and wave direction is from the south west, migration of sediment from the banks to the foreshore, as suggested by the modelling, is possible under neap tides. During spring tide conditions, wave action generally amplifies the tide-alone transport pathways and transport between large sandy deposits becomes a possibility.

Overall, it is proposed that the bank's formation and maintenance can be summarised by the following:

i) Glacial melt-water deposits large quantities of material into shelf seas, including the Celtic Sea and a shallow Bristol Channel;

ii) Wave action, combined with sea level rise, brings material into the central Bristol Channel area;

iii) Tides re-work the glacial material and, where large gradients in the current field exist (around headlands), deposit it. The deposits promote hydrodynamics instabilities which evolve into bank deposits with continued tidal action;

iv) Storms maintain a supply of material to the region and also provide links between discrete sediment deposits.

6. Discussion and Conclusions

The principal aim of this study was to improve the understanding of near-shore sandbanks that are located close to prominent coastal headlands. Two approaches were followed, both involving process-based numerical modelling techniques. Firstly, the initial response of the seabed (over 1 to 2 years) around a highly idealised coastal headland was investigated using the process-based model, *Delft-3D*. The simple approach provided a practical method of assessing the sensitivity of near-shore sandbank growth to a number of variables. Secondly, the initiation and potential growth mechanisms of a real near-shore sandbank were investigated using the process-based modelling system, *MIKE 21/3 FM*. The *Delft-3D* model was replaced by *MIKE 21/3 FM* because, at the time of the experiments, coupled wave and current simulations could not be run on the *Delft-3D* system. This is also the reason that coupled wave-current simulations were not performed on the idealised modelling conducted in Chapter 2.

As has already been described, the dynamic nature of the Nash Sands on the south Wales coast provided the initial motivation behind this study. The bank's unstable character was demonstrated by a series of repeat surveys, which showed considerable oscillation of its footprint over relatively short time-scales compounded by marine aggregate dredging of significant volumes of material. A potential supply of sediment to the bank was not immediately obvious given the strongly ebb dominant character of the system, the large areas of exposed bedrock surrounding the bank and the cohesive nature of the up-stream sediment. In order for the processes outlined in Chapter 2 to be relevant (including the effects of headland eddies, geometry and slope) , it was first necessary therefore to identify a potential mechanism for supplying material to the bank.

A distinct lack of available measurements and the variety of scales at which the transport processes operated meant that a process-based model of the region was felt to be the best method of resolving the contentious sediment transport pathways in the Bristol Channel. Thus, such a model was set up, the construction of which involved a

full sensitivity analysis of the model parameters in order to optimise and tailor the modelling system around the key processes.

It was found that the frequency of available bathymetric data was insufficient to facilitate calibration of a morphological model. Adjustments to the bank due to stochastic (waves and storm) and deterministic (tidal) forcing occurs at temporal scales that are much less than the frequency of repeat surveys. Further, the temporal nature of the data sets that constitute the model bathymetry, including the bank and the surrounding seabed, implies that the bathymetry is made up of a mosaic of data from surveys undertaken at different times, sometimes decades apart. This leads to inconsistency in areas where the various surveys overlap, and unnatural adjustments of the seabed that are orders of magnitude larger than the bank processes of interest. This is down to the bed and the tidal forcing adjusting towards an artificial equilibrium state and makes it impossible to provide real quantitative predictions of bed change. Consequently then, for the morphological simulation of such large-scale bed features, process-based models should only be applied in 'diagnostic' mode.

Despite this, however, process-based modelling has proven to be extremely useful in the work presented here, highlighting clear cause-effect relationships between various sediment transport and sandbank processes. Taking on the role of a 'numerical lab', the approach avoids the scaling problems associated with the real laboratory providing a spatially integrated insight into complex physical interactions that would otherwise not be possible.

Problems do exist, however; for example, small scale processes may have an accumulating effect on larger-scale processes and are often 'cut off' by the grid-size of the model (sub-grid effects). With advances in both computational power and theoretical understanding, process-based modelling should continue to offer an ever-improving tool in understanding of the coast.

In the following section, the objectives and research questions formulated in Chapter 1 are addressed through a discussion of the main results presented in Chapters 2-5.

Objective 1. *Identify the principal factors that control the initiation of near-shore sandbanks around coastal headlands.*

Process-based morphological modelling of an idealised coastal headland surrounded by a uniform sandy bed of infinite thickness, has demonstrated a strong propensity to erode and accrete sediment close to a coastal headland. In the modelling experiments, erosion of sediment coincided with large continuity-induced accelerations in the near-headland current field. Further offshore, sediment accretion followed large decelerations in the local current field. For a 'Gaussian' shaped headland, this created near-symmetrical 'lobes' of deposited material either side of the headland, combined with smaller zones of deposition that touched the headland. These near-shore deposition zones were interspersed with large scour holes. For a 'semi-Gaussian' shaped headland (comparable to Nash Point in the central Bristol Channel), the pattern of erosion and accretion again closely matched acceleration and decelerations in the instantaneous current field, respectively. The near-symmetrical bed changes predicted in the 'Gaussian' shaped experiments, were absent, replaced by a single zone of deposition on the 'steep' side of the headland and a large, near-headland area of erosion.

The effect of both residual and instantaneous tidal eddies on sandbank initiation around headlands has also been investigated. No firm evidence could be found to link the eddies with bank initiation: the positions of eddies and sediment accretion was not coincident.

For the 'semi-Gaussian' shaped headland, coincidence between the residual tidal eddy and the position of sediment accretion was predicted. This should not be interpreted as a cause-effect relationship, however: sediment accretion is controlled by the gradient in the current field alone, as demonstrated by the 'Gaussian' experiments. In certain cases, the accretion zone happens to be to be coincident with the tidal eddy as a result of the headland geometry.

These types of process-based models are also only designed to give sediment accretion in areas where sediment convergence ($\nabla \cdot Q$) is predicted from the flow field. A Lagrangian approach in which the path of an individual sand-grain is followed over a number of tides, may give a result that is different because it will be more sensitive to subtle changes in the flow field that promote its transport and deposition.

Further, the sediment transport models applied in this study have all assumed 'equilibrium' sediment transport. 'Equilibrium' refers to the fact that there exists no

temporal lag between the flow field and the sediment transport field. Application of a non-equilibrium transport model may give results that are different to those found here. Both these provide interesting opportunities for future work.

A conceptual model of the bank initiation process is proposed, consisting of acceleration or 'tidal jetting' of the incoming shore-parallel tide near the headland which disturbs and erodes the bed. Material is moved by both bed- and suspended load (the proportions of which are dependant on sediment characteristics and current speeds). Accretionary zones close to the headland mark areas of bed-migration which develop prior to offshore bank initiation. The growth of these initial near-headland bed perturbations determines the asymmetry of the offshore 'lobes' which develop later. The offshore deposits are derived from both suspended and bed-load material derived from the near-headland erosion zones and bed perturbations.

The findings described above discount the role of a 'tidal stirring' mechanism in sandbank initiation around headlands. However, the model still predicts sediment accretion around the headland that is asymmetric. The observed asymmetry in the bed morphology is not reflected by the boundary conditions of the model, suggesting that the Coriolis force is still contributing in some way. Analysis of the levels of advective and topographically-induced vorticity production during each phase of tide has provided useful insights in to this phenomenon. Advective vorticity production is greater on one side of the headland, indicating flow acceleration in response to the Coriolis-enhanced pressure gradient force. The result is an increase in the amount of bed material available for transport to offshore 'lobes' during the next phase of the tide.

The impact of the Coriolis force, however, is small in comparison with the effects of other parameters that have been tested. Experiments conducted with varying seabed slopes surrounding the headland show that the Coriolis-induced asymmetry becomes even less pronounced with increasing slope. This indicates that the effect of Coriolis force on sandbank initiation and growth is negligible in comparison with other factors, including antecedent geology and tidal asymmetry.

Objective 2. *Establish an optimized process-based numerical model capable of simulating both headland-associated processes and the regional-scale sediment*

transport processes that contribute to the initiation and growth of a near-shore headland sandbank in the Bristol Channel, U.K.

The complexity of the Bristol Channel, and the variety of spatial and temporal scales at which the key processes occur, required a sophisticated process-based model capable of resolving combined wave and current effects on sediment transport. A number of sensitivity tests were conducted in order to achieve a capable and efficient model set-up. The assumption of equilibrium transport, whereby the tidal forcing and sediment transport fields are assumed to be in phase, permitting a reduction in the overall size of the modelling domain.

Tests were also conducted to assess the maximum allowable relaxation (updating frequencies) between the flow field and both the sand transport and wave-radiation stress fields in this environment. The results suggested that a relatively high (1 in 15 minute) updating of the sediment transport field was required, reflecting the non-linear relationship between tidal currents and sand transport. For the wave forcing, the radiation stresses needed to be updated once in every 30 minutes.

Objective 3. *Investigate regional sediment transport processes in the central Bristol Channel in order to determine potential bank re-nourishment and maintenance pathways in the present-day hydrodynamic climate.*

A large-scale process-based modelling investigation was conducted, using the model grid and parameters described in Chapter 3. A number of potential wave-induced mechanisms for bringing marine-derived sediments into the coastal fringes of the estuary were identified. In near-shore regions, transport by long-shore transport in the breaking zone was shown to be significant under various wave and current combinations. Up-estuary transport is further enhanced by local flood-dominated areas, Stokes Drift and larger up-estuary directed bed-shear stresses (due to asymmetry in the wave-orbital velocities at intermediate water depths).

Of further interest is the finding that wave action is not always capable of inducing up-estuary transport. Specifically during spring tides, and under specific wave-conditions, wave-related effects (described above) are overwhelmed by the tidal currents. The result

is that during spring tides, the transport direction is tidally dominated. Wave action simply enhances the maximum bed-shear stresses and increases the total load transport.

Objective 4. *Determine whether the Nash Sands is controlled by headland-associated processes or whether it is a purely relict feature.*

The process-based model set-up (established in Chapter 3) was again used in this part of the study, taking advantage of the model optimization that had been carried out. Experiments showed that the bank lies in a natural zone of sediment deposition, in which gradients in the local flow field (produced by the headland) promote downstream accretion. The results support the findings of earlier experiments (Chapter 2) which suggest similar relationships between the instantaneous flow field and the locations of sediment accretion and bank initiation.

The headland eddy is shown to coincide with the position of the sandbank, suggesting a relationship between the two. The results, however, show that the bank promotes its own residual eddy due to inertial lags persistent during both phases of the tide. These promote a residual clockwise circulation of water and sediment and a local convergence of sediment toward the sandbank's centre. A headland-induced eddy was also detected in simulations conducted in the absence of the sandbank. However, with the bank present in the model bathymetry, the bank and the headland eddies became part of the same residual sandbank circulation.

Secondary currents are also shown to have an insignificant effect on the growth and development of the Nash Sands. This is demonstrated by a 3-D modelling study of the region which predicted near-bed and near-surface current fields that were coincident.

Combined wave, current and sediment transport modelling focusing on the local Swansea Bay area suggested the presence of ephemeral transport pathways providing a potential link between large sandy deposits under large wave action

6.1 Summary

The main findings of this work are summarised as follows:

1. Sandbank initiation around headlands is the result of continuity-induced gradients in the instantaneous current field. This has been demonstrated both in 'idealised' and 'real' coastal environments;

2. The mechanism can be described as a two-stage tidal process:
   I. Erosion and accretion near the headland during one phase of the tide providing an excess of more readily available material near the headland;
   II. This is then redistributed and transported further offshore during the next phase, forming the start of a headland-type bank.

3. Coriolis force has a minor effect on headland-type sandbank initiation and growth, compared to other parameters including coastal geometry and seabed slope.

4. The mechanism outlined in (1) and (2) above, is shown to exist around Nash Point, a coastal headland in the Bristol Channel U.K. and could be responsible for the initial growth of the Nash Sands, an elongated 'banner-type' bank.

5. The Nash Sands is maintained by a significant residual flow of water and sediment that circulates around it. The circulation is caused by an unbalanced response to friction due to the bank's orientation relative to the principal tidal axis. The mechanism is augmented by the residual tidal circulation.

6. Headland-induced secondary flows are not involved in the initial growth or maintenance of the Nash Sands.

7. Wave action provides a number of potential mechanisms by which sediment can be supplied to the sandbank. These include wave-induced currents from wave-breaking, wave-induced increase of peak orbital velocities in the direction of wave-propagation, Stokes drift and streaming in the boundary layer.

8. Ephemeral sediment transport pathways, active during significant wave forcing, provide a means of linking large sand-rich bank and foreshore deposits and maintaining the long-term equilibrium of the coastal system.

6.2 Proposed Further Work

A number of ideas have been formulated from the work presented in this thesis which could provide fruitful avenues of further research.

6.2.1 Idealised Modelling:

The idealised modelling experiments using *Delft-3D* were focused on the effects of tidal currents alone. Inclusion of wave in the same case study, therefore, would provide a means of quantifying:

1. The effect of wave action on limiting sandbank growth;
2. The importance of long-shore drift on sandbanks found around Gaussian-shaped headland-type headlands.

Another approach that has been explored recently by Berthot and Pattiaratchi (2006), as well as by Signell (2006), is the extension of the simulation periods to time-scales of decades to centuries. This approach has provided a means of analysing the effect of bed/flow interaction and morphological feedback on sandbank evolution. An expansion of this involving stochastic wave forcing could be a useful way of studying chronology effects on sandbank morphodynamics.

6.2.2 Model Optimisation:

One aspect of the model reduction experiments of Chapter 3 that could provide a useful further investigation was the way in which the morphological acceleration factor (*MFAC*) is utilised within combined wave and tidal modelling: is it possible to include a 'dynamic' *MFAC*; i.e. one that adjusts automatically with the severity of the forcing? In which case, which parameter should be used to govern the *MFAC*?

6.2.3 The Nash Sands and Bristol Channel:

At present the modelling conducted on Chapters 4 and 5 captures only the 'potential' for up-estuary transport, assuming a uniform distribution of seabed sediment. Modelling of the Bristol Channel using an accurate description of the sediment distribution as well as grain-size maps would thus be a useful means of quantifying sediment transport rates.

Another aspect, omitted from the modelling study, was the effect of wind-driven currents on sediment transport. Wind driven currents provide a potentially significant contribution to the total amount of material transported as suspended load.

As previously mentioned, the use of a Lagrangian-type model to follow individual sand grains around a headland, may give results that differ from those of a purely Eulerian scheme. The approach would be a useful addition to the purely Eulerian experiments of the present study.

The proposed improvements to the modelling experiments described above, should also be coupled to an extensive program of data collection in the study area. The key issue is the capture of sediment distribution during and after significant wave conditions.

A further useful investigation would involve modelling of the Bristol Channel and Celtic Sea system using adjusted sea levels. This would help to indicate historical sediment transport pathways and, potentially, the original formation of the large headland banks.

As described in Section 5.1.5, running the model in real time using corresponding bathymetry and forcing conditions (waves and tides) was found to be problematic. This was due to disparities between the bathymetric data sets compiled to form the model bathymetry and resulted in the bed and hydrodynamics not being in equilibrium: bed changes predicted by the model were the result of the bed adjusting towards a new state of equilibrium rather than being indicative of the natural response to the forcing conditions.

It might be better to concede that, unless the quality of both the boundary conditions and bathymetry data can guaranteed to produce the same form of 'dynamic equilibrium' as the real system, it is pointless attempting to mimic its morphological evolution using a process-based model. The way forward may then be to accept this inherent problem

and use the model in a 'diagnostic' sense only. In practise this would require first running the model using the most accurate description of the bathymetry and boundary conditions that can be found. The morphological model would be left to run until it had reached a point in which the hydrodynamics and the bathymetry were in a steady-state. At this point it could be assumed that subsequent changes in the forcing conditions will have an immediate effect on the system equilibrium. In the case of a sandbank, this may involve adjustment of the bank's total volume or morphology. Ultimately, the approach would provide a diagnostic means of assessing the likely response of the sandbank to various forcing conditions. It could be used to assess the likely bank response to a large storm or alternatively, to sand mining.

The large amount of time taken for the system to achieve an initial equilibrium state would be the main drawback of this approach. Improving the bathymetry, so that it mirrors more closely the bathymetry of the starting condition, would help, as would the use of a morphological acceleration factor, forcing the bathymetry to adjust much more quickly towards a 'steady' state.

Appendix 1: Derivation of the Transport Vorticity Equation

The generation and dissipation of vorticity around coastal headlands has been described by a number of authors including Heaps (1978), Zimmerman (1978), Tee (1976), Robinson (1981), Signell and Geyer (1990) and Duffy (2006). In the following derivations, the approach of Robinson (1981) is first presented in which a momentum equation is derived that includes terms responsible for the production and dissipation of vorticity around a coastal headland. The more recent 'total transport' equation of Park and Wang (2000), employed in Chapter 2 to detect subtle changes in the hydrodynamics (due to bed changes and the Coriolis Force), is then presented.

Robinson's equation is derived from a depth-averaged version of the two-dimensional momentum equation, appropriate to barotropic motion in shallow tidal seas:

$$\frac{\partial \bar{u}_h}{\partial t} + (\bar{u}_h \cdot \nabla)u_h + 2\Omega \cdot \mathbf{k} \times \bar{u}_h = -\frac{\nabla p}{\rho} - \frac{C_D}{D+\zeta}\bar{u}_h |\bar{u}_h| + \upsilon_H \nabla^2 \bar{u}_h \qquad \text{(A1.1)}$$

$\bar{u}_h$ is a two-dimensional horizontal vector representing the depth-averaged horizontal velocity related to the horizontal velocity, u_h, by

$$\left(\bar{u}_h = \frac{1}{D+\zeta} \int_{-h}^{\zeta} u_h dz \right);$$

Ω is the earth's rotational speed;

$\cdot\mathbf{k}$ is the vertical unit vector;

p is the pressure (incorporating the effect of surface slopes and tide generating potential);

C_D is a non-dimensional bottom friction coefficient;

D is the still water depth;

ζ is the sea surface elevation above the still water depth;

υ_H is the horizontal eddy viscosity

Using cross-differentiation and a number of vector identities, the momentum equation (A1.1) can be expressed in terms of vorticity, Vorticity of a fluid is the vector measure of local rotation in a fluid flow, defined mathematically as the curl of the velocity vector, $\varpi = \nabla \times \bar{u}_h$.

Using the vector identity:

$$\nabla(\bar{u}_h \cdot \bar{u}_h) = 2[\bar{u}_h \times \nabla \times \bar{u}_h + (\bar{u}_h \nabla)\bar{u}_h] \qquad \text{(A1.2)}$$

and rearranging for $(\bar{u}_h \nabla)\bar{u}_h$, gives:

$$(\bar{u}_h \nabla)\bar{u}_h = \nabla(\bar{u}_h \cdot \bar{u}_h / 2) - \bar{u}_h \times \nabla \times \bar{u}_h \qquad \text{(A1.3)}$$

Substituting for $\omega = (\nabla \times \bar{u}_h)$ gives an expression for the advection (inertial) term in the momentum equation in terms of vorticity

$$(\bar{u}_h \nabla)\bar{u}_h = \nabla(\bar{u}_h \cdot \bar{u}_h / 2) - \bar{u}_h \times \varpi \qquad \text{(A1.4)}$$

Substituting this back into the momentum equation gives

$$\frac{\partial \bar{u}_h}{\partial t} + \nabla(\bar{u}_h \cdot \bar{u}_h / 2) - \bar{u}_h \times \varpi + 2\Omega \cdot \mathbf{k} \times \bar{u}_h = \frac{-\nabla_h p}{\rho} - \frac{C_D}{D+\zeta}\bar{u}_h \bar{u}_h + \upsilon_H \nabla^2 \bar{u}_h \qquad \text{(A1.5)}$$

Taking the curl $(\times \nabla)$ of the above equation and using $f = 2\Omega \sin\varphi$, generates a transport equation of the vorticity (Note that the curl of a divergence of a scalar quantity is zero ($\nabla(\bar{u}_h \cdot \bar{u}_h / 2) \times \nabla = 0$))

$$\frac{\partial \varpi}{\partial t} + \nabla \times [(f + \varpi) \cdot \mathbf{k} \times \bar{u}_h] = -\frac{C_D |\bar{u}_h|}{D+\zeta}\varpi + C_D \bar{u}_h \times \nabla\left(\frac{|\bar{u}_h|}{D+\zeta}\right) + \upsilon_H \nabla^2 \varpi \qquad \text{(A1.6)}$$

which is the instantaneous contribution to vorticity from a number of sources described below. Equation (A1.6) can be rewritten as:

$$\frac{d}{dt}\left(\frac{\varpi + f}{D+\zeta}\right) = -\frac{C_D|\bar{u}_h|}{(D+\zeta)^2}\varpi + \frac{C_D\bar{u}_h}{D+\zeta}\times\nabla\left(\frac{|\bar{u}_h|}{D+\zeta}\right) + \frac{\upsilon_H}{D+\zeta}\nabla^2\varpi \qquad \text{(A1.7)}$$

or rearranging for vorticity ϖ :

$$\frac{d\varpi}{dt} = \underbrace{\left(\frac{\varpi + f}{D+\zeta}\right)\frac{d}{dt}(D+\zeta)}_{1} + \underbrace{\frac{C_D}{D+\zeta}\bar{u}_h\times\nabla|\bar{u}_h|}_{2} - \underbrace{\frac{C_D|\bar{u}_h|}{(D+\zeta)^2}\bar{u}_h\times\nabla(D+\zeta)}_{3}$$

$$\underbrace{-\frac{C_D|\bar{u}_h|}{D+\zeta}\varpi}_{4} + \underbrace{\upsilon_H\nabla^2\varpi}_{5} \qquad \text{(A1.8)}$$

Terms 1, 2 and 3 in equation (A1.8) provide three mechanisms of generating vorticity. Potentially all three mechanisms could contribute to headland generated vorticity. Terms 4 and 5 represent dissipative processes that destroy or redistribute the vorticity. Robinson (1981) provides qualitative descriptions of the three vorticity producing terms (1, 2 and 3) which are expanded and illustrated below:

Mechanism 1: Moving from deep to shallow water

- Term 1 in Equation A1.8: $\left(\frac{\varpi + f}{D+\zeta}\right)\frac{d}{dt}(D+\zeta)$

For the conservation of potential vorticity, as depth changes, relative vorticity (ϖ) and planetary vorticity (f) must change in the same sense. Considering a column of rotating fluid moving over bed topography of depth D, as D increases, the column of fluid is stretched. Potential vorticity is conserved because the stretched water column has a smaller moment of inertia and can rotate faster to increase its relative vorticity.

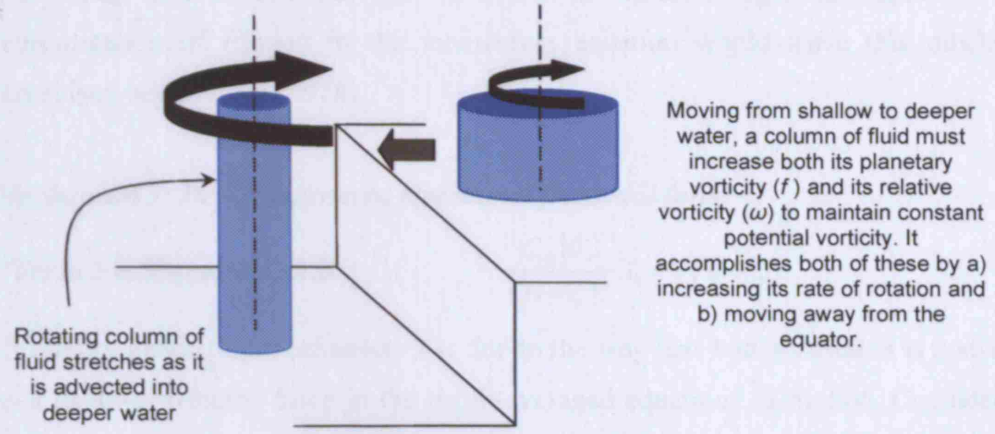

Figure A1.1. Vorticity generating mechanism A: conservation of potential vorticity with changing water depth.

Mechanism 2: Lateral shear in flow and the influence of the quadratic friction law.

- Term 2 in Equation A1.8: $$\frac{C_D}{D+\zeta}\overline{u}_h \times \nabla\left|\overline{u}_h\right|$$

This second vorticity generating mechanism is a product of two contributing factors: firstly, the acceleration of the flow in response to restricted flow at the headland; secondly, and most critically, the quadratic representation of bottom friction in the momentum equation (A1.1).

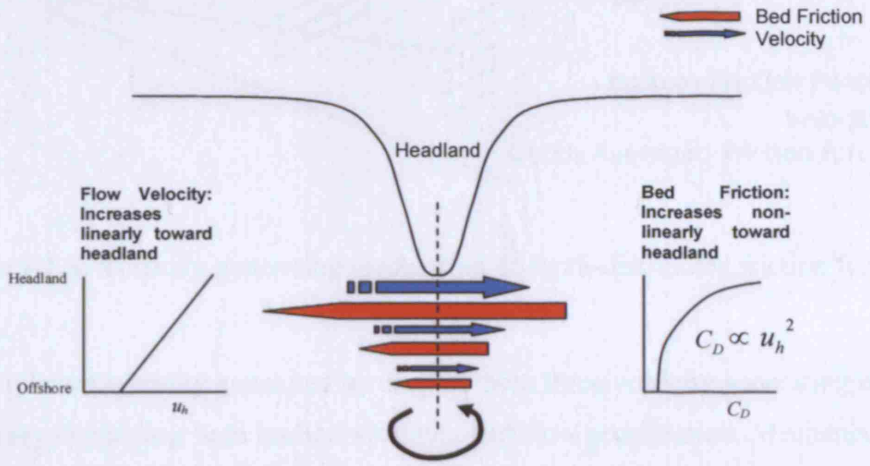

Figure A1.2. Vorticity generating mechanism 2: non-linear increase in bed friction

The result is a mechanism that is active in water of uniform depth. A linear representation of friction in the momentum equation would leave this mechanism redundant -see Pingree (1978).

Mechanism 3: Depth dependent directional frictional force

- Term 3 in Equation A1.8: $$\frac{C_D|\overline{u}_h|}{(D+\zeta)^2}\overline{u}_h \times \nabla(D+\zeta)$$

Vorticity generating mechanism 3 is due to the way that bottom friction is considered as a depth-distributed force in the depth-averaged equations of motion. Considering a straight coastline in which the depth varies in a direction normal to the local velocity: there will be an offshore reduction in the depth-distributed friction force, even in the absence of lateral velocity shear. This will cause an onshore torque and generate vorticity. In contrast to mechanism 2, this mechanism requires no non-linear friction term because it is independent of lateral velocity shear.

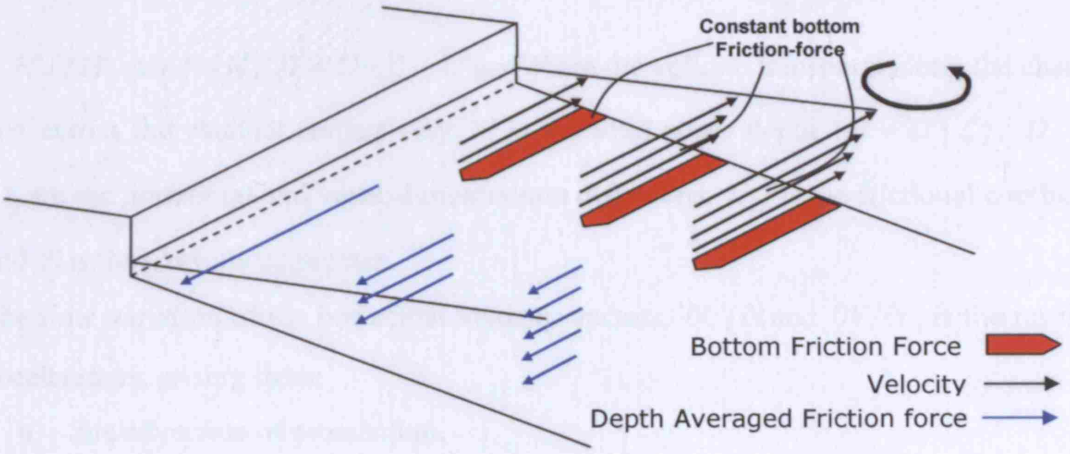

Figure A1.3. Vorticity generating mechanism 3: depth-distributed friction force

The relative vorticity generated by each of these three vorticity generating mechanisms will vary depending both on bottom depth and flow acceleration. Mechanisms 1 and 2 will be inactive over uniform beds while it has been suggested (Pingree and Maddock, 1978) that the contribution of mechanism 2 is much smaller and only important in high velocity flows very close to the headland.

Park and Wang (1991, 2000) have also analysed the vorticity production and dissipation associated with residual flows around headlands and hollows. They suggest that consideration of the ***total transport*** vorticity is critical because the pattern can be quite different from that of vorticity associated with depth-averaged velocity alone. This is because the transport vorticity equation contains terms that are only implicitly included in the vorticity expression considered by Robinson (1981).

The transport vorticity equation is derived by cross differentiating the equations of motion. The equations of motion, in terms of total volume transport, are given by

$$\frac{\partial U}{\partial t}+\frac{\partial uU}{\partial x}+\frac{\partial vU}{\partial y}-fV=-gH\frac{\partial \zeta}{\partial x}-C_D\frac{U(U^2+V^2)^{1/2}}{H^2}+D_x \qquad \text{(A1.9)}$$

$$\underbrace{\frac{\partial V}{\partial t}+\frac{\partial uV}{\partial x}+\frac{\partial vV}{\partial y}}_{\text{A}}+\underbrace{fU}_{\text{B}}=\underbrace{-gH\frac{\partial \zeta}{\partial y}}_{\text{C}}\underbrace{-C_D\frac{V(U^2+V^2)^{1/2}}{H^2}}_{\text{D}}+\underbrace{D_y}_{\text{E}} \qquad \text{(A1.10)}$$

$u=U/H$, $v=V/H$, $H=D+\zeta$, U and V are the volume transports along the channel and across the channel respectively. H is the total water depth ($H=D+\zeta$), D_x and D_y are the horizontal and vertical momentum diffusions, C_D is the frictional coefficient and f is the Coriolis parameter.

The time variation of the horizontal velocity vectors, $\partial U/\partial t$ and $\partial V/\partial t$, is the result of accelerations arising from:

a) the advection of momentum,
b) the effect of the earths rotation,
c) the slope of sea surface,
d) the frictional drag of the seabed,
e) the transfer of horizontal momentum by mixing.

When all of these terms are averaged over a tidal cycle, the non-linear contributions of advection and friction induce local residual currents in the form of large flood and ebb gyres (see Duffy, 2006).

The total transport vorticity equation can then be derived by cross-differentiating the transport equations of motion (A1.9 and A1.10)

$$\underbrace{\frac{\partial \Pi}{\partial t}}_{1} + \underbrace{[\nabla \times N]\cdot \mathbf{k}}_{2} = \underbrace{-gJ(H,\zeta)}_{3} + \underbrace{f\frac{\partial \zeta}{\partial t}}_{4} \underbrace{- C_D\left[\nabla \times \frac{U|U|}{H^2}\right]\cdot \mathbf{k}}_{5} + \underbrace{[\nabla \times D_c]\cdot \mathbf{k}}_{6} \quad \text{(A1.11)}$$

where $\Pi(=\partial V/\partial x - \partial U/\partial y)$ is the transport vorticity. N is the non-linear advective term, $J\,(=\partial(u,v)/\partial(x,y)$ is the Jacobian operator. The five terms are defined below:

1. The local acceleration of transport vorticity
2. The vorticity advection
3. The 'topographic' vorticity tendency
4. Vorticity from sea surface divergence
5. Vorticity from bottom friction
6. Vorticity diffusion

In the total vorticity transport equation above, the topographic vorticity tendency (i.e. the mechanism outlined in Figure A.1.1) is presented explicitly as term (3): $-gJ(H,\zeta)$

Park and Wang (2000) suggested that the advantage of the 'total transport' vorticity approach was that, unlike the 'depth averaged' vorticity approach employed by Robinson (1981), a 'total transport' approach contains a 'topographic vorticity' term that is only implicitly included in the depth averaged vorticity expression. By deriving it explicitly, using a 'total transport' approach, the contribution to the vorticity balance from depth adjustments can be more easily quantified.

The frictional contributions are now more conveniently combined into one term (5). This has been used in Chapter 5 to detect the frictional contribution of a seabed feature (the Nash Sands) to the residual current and sediment transport fields.

Appendix 2: A Comparison of *Delft-3D* and *MIKE-21/3 FM*

The modelling presented in this study has used a combination of tidal, wave, sediment transport and morphological models that involve a number of empirical and continuum expressions to describe the physics. In the following section a brief description of the equations and numerical aspects of *Delft-3D* and *MIKE-21/3 FM* is given.

A2.1 The Tidal Models

Delft-3D and *MIKE-21/3 FM* solve the three-dimensional incompressible, Reynolds-averaged Navier-Stokes equations (A2.3 and A2.4) and the Continuity equation (A2.5) subject to the assumptions of Bousinesq and hydrostatic pressure.

A2.1.1 The Bousinesq Approximation

Process-based coastal models solve the '*Reynolds-averaged*' Navier-Stokes equations meaning that the turbulent processes are parameterised into the model equations. In the natural environment, turbulence is both an energy-extracting and flow redistributing mechanism (Arcilla and Lemos, 1990) and it is important that its effect is incorporated in the form of terms that are able to do that job. Most models use an 'eddy viscosity concept' such that the turbulent stresses are assumed to be proportional to the gradients in the mean velocity field. This is the crux of the Bousinesq approximation: it assumes that the stress or rate of deformation law for turbulent flow has the same form as the Newton-Stokes law for viscous, laminar flow which is:

$$\vartheta = \upsilon_t \frac{\partial u}{\partial z} = -\overline{u'v'} \qquad \text{(A2.1)}$$

where ϑ is the rate of deformation, υ_t is the eddy viscosity, $\partial u / \partial z$ is the vertical gradient in the horizontal velocity and u' and v' are the turbulent fluctuations about the

mean velocity. Various methods, or 'closure schemes', are used to determine the eddy viscosity ranging from a simple 'mixing length hypothesis' to more sophisticated methods that relate the turbulent kinetic energy production and dissipation to velocity and length scales by algebraic or differential relationships. The closure schemes employed by the *Delft-3D* and *MIKE 21/3 FM*, are described in Section A2.1.4 and A2.1.5.

A2.1.2 The Hydrostatic Pressure Assumption

The hydrostatic pressure assumption is applicable to fluid flows in which the vertical depth is much smaller than the horizontal length scale. This 'shallow water assumption' is considered valid because vertical accelerations are negligible compared to gravitational accelerations and are not taken into account. The hydrostatic pressure, p_a, is simply taken as $\rho g h$, indicating that the models do not solve the full three-dimensional Navier-Stokes equation: vertical velocities are computed from the continuity equation only. Vertical accelerations due to buoyancy effects and sudden changes in bottom topography, therefore, are not taken into account (WL|Delft-Hydraulics 2001).

A2.1.3 The Shallow Water Equations

Both models use a so-called σ-coordinate system in the vertical direction. The system is defined as

$$\sigma = \frac{z - \zeta}{D + \zeta} = \frac{z - \zeta}{H} \qquad \text{(A2.2)}$$

z is the vertical co-ordinate in physical space, ζ is the free surface elevation above the reference plane (at $z = 0$), d is the water depth above the reference plane and H is the total water depth ($H = D + \zeta$). See also Figure A.2.1 below. At the bottom $\sigma = -1$ and at the free surface $\sigma = 0$. This system ensures that the vertical co-ordinates are always fitted to the bottom and the free surface boundaries. Partial derivatives in the original

Cartesian co-ordinate system are expressed in σ co-ordinates by the chain rule, introducing additional terms in the equations of motion.

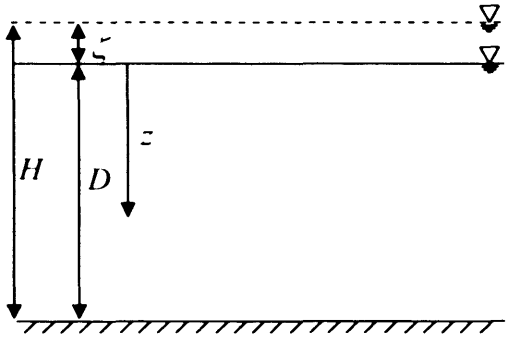

Figure A2.1. Parameters used in the transformation from fixed Cartesian co-ordinates to boundary adjusting σ co-ordinates.

A 3-D simulation consists of a horizontal plane composed of open and closed boundaries and, in the vertical, a number of layers. In a sigma coordinate system, the number of layers is the same at every location in the horizontal plane and the layer interfaces are chosen following planes of constant σ.

The momentum equation is solved over all sigma layers in the x- and y- directions

$$\overbrace{\frac{\partial u}{\partial t}}^{1}+\overbrace{\frac{\partial u^2}{\partial x}+\frac{\partial vu}{\partial y}+\frac{\partial wu}{\partial z}}^{2}=$$

$$\underbrace{fv}_{3}\underbrace{-g\frac{\partial \zeta}{\partial x}}_{4}\underbrace{-\frac{1}{\rho_0}\frac{\partial p_a}{\partial x}}_{5}\underbrace{-\frac{g}{\rho_0}\int_z^{\zeta}\frac{\partial \rho}{\partial x}dz}_{6}+\underbrace{F_u}_{7}+\underbrace{\frac{\partial}{\partial z}\left(\upsilon_t\frac{\partial u}{\partial z}\right)}_{8}+\underbrace{u_s S_c}_{9} \qquad \text{(A2.3)}$$

$$\frac{\partial v}{\partial t}+\frac{\partial v^2}{\partial y}+\frac{\partial uv}{\partial x}+\frac{\partial wv}{\partial z}=$$

$$-fu-g\frac{\partial \zeta}{\partial y}-\frac{1}{\rho_0}\frac{\partial p_a}{\partial y}-\frac{g}{\rho_0}\int_z^{\zeta}\frac{\partial \rho}{\partial y}dz+F_v+\frac{\partial}{\partial z}\left(\upsilon_t\frac{\partial v}{\partial z}\right)+v_s S_c \qquad \text{(A2.4)}$$

as well as the continuity equation

$$\frac{\partial u}{\partial x}+\frac{\partial v}{\partial y}+\frac{\partial w}{\partial z}=S_c \qquad \text{(A2.5)}$$

where t is time; x, y are the horizontal Cartesian coordinates; u, v and w are the velocity components in the x, y and z directions; f (= $2\Omega sin\varphi$) is the Coriolis parameter (Ω is the angular rate of revolution of the earth, φ is the geographic latitude); g is the gravitational acceleration; ρ is the water density; p_a is the atmospheric pressure; ρ_0 is the reference density of water. All of the terms in equations A2.3 and A2.4 describe accelerations that generate forces on the fluid: Term 1 is the unsteady (time-varying) fluid acceleration; Term 2 describes horizontal gradients in the fluid velocity that generate fluid acceleration. Term 3 is the Coriolis acceleration; Term 4 is the acceleration produced by sea surface variation; Term 5 is the acceleration induced by atmospheric pressure gradient; Term 6 is the acceleration due to buoyancy effects; Term 7 represents the imbalance of horizontal Reynolds Stresses (F_u and F_v); Term 8 the is the vertical stresses (from the Boussinesq approximation) and Term 9 is the acceleration due to discharge point sources (S_c is the magnitude of the discharge due to point sources and u_s, v_s are the velocities by which the water is discharged into the ambient water).

A2.1.4 Horizontal Turbulence

As previously described, both *Delft-3D* and *MIKE-21/3 FM* use an eddy viscosity concept (Rodi 1984) to resolve the sub-grid scale turbulence. The approach varies between the models and the methods for horizontal and vertical turbulence are different. For the horizontal turbulence, the Reynolds stresses (F_u and F_v) are related to a horizontal eddy viscosity coefficient, υ_H, and components of the mean rate-of-deformation tensor

$$F_u=\frac{\partial}{\partial x}\left(2\upsilon_H\frac{\partial u_h}{\partial x}\right)+\frac{\partial}{\partial y}\left(\upsilon_H\left(\frac{\partial u_h}{\partial y}+\frac{\partial v_h}{\partial x}\right)\right) \qquad \text{(A2.6)}$$

$$F_v = \frac{\partial}{\partial x}\upsilon_H\left(\frac{\partial u_h}{\partial x}+\frac{\partial v_h}{\partial x}\right)+\frac{\partial}{\partial y}\left(2\upsilon_H\left(\frac{\partial v_h}{\partial y}\right)\right) \qquad \text{(A2.7)}$$

The models differ slightly in their mode of application. The Delft Hydraulics approach calculates the horizontal eddy viscosity coefficient by summing various contributions. A closure scheme is not used. A coefficient of horizontal eddy viscosity must be input directly as a user-specified constant to take into account the effects of

- Horizontal turbulence- associated with unresolved horizontal components;
- 'Shear dispersion' -induced turbulence- related to the vertical variation in horizontal flow velocity (described in Section A2.1.5 below);
- Molecular viscosity- which is a property of the fluid that is dependent on temperature and density.

The DHI approach calculates the horizontal eddy viscosity coefficient at each time-step using the approach of Smagorinsky (1963). It computes an *effective eddy viscosity* related to a characteristic length scale as follows

$$\upsilon_H = c_s^2 l^2 \sqrt{S_{ij} S_{ij}} \qquad \text{(A2.8)}$$

where c_s is a user-specified constant (which can be defined by a map of spatially varying values), l a characteristic length scale and the deformation rate, S_{ij}, is given by

$$S_{ij} = \frac{\partial u_h}{\partial x}+\frac{\partial v_h}{\partial y} \qquad \text{(A2.9)}$$

Theoretically this gives a better schematization of the turbulence effects because it provides a *flow-dependent* eddy viscosity which will adjust to dissipate more energy at higher flow-rates.

A2.1.5 Vertical Turbulence

In 3-D simulations the effect of vertical turbulence on the Navier-Stokes equations is usually parameterised in an appropriate closure assumption. The *closure scheme* computes a flow dependent vertical eddy viscosity, υ_t. Both models provide choices for the turbulence closure scheme (detailed in Table A2.1) which vary in their degree of sophistication.

Table A2.1. Options for resolving sub-grid scale vertical turbulence in *Delft-3D* and *MIKE-21/3*.

Delft-3D	***MIKE-21/3***
Constant eddy viscosity	Constant eddy viscosity
Algebraic eddy viscosity closure model	Log-law formulation
k-L turbulence closure model	*k-ε* turbulence closure model
k-ε turbulence closure model	

The *k-L* model uses one transport equation to solve for *k*, the turbulent energy per unit mass (or T.K.E), while the second-order *k-ε* model solves transport equations for both the turbulent kinetic energy production and dissipation. In this study, the *k-ε* turbulence closure model is used in all experiments. The scheme has been well tested in a number of tidal simulations including those by Baumert and Radach (1992) and Davies and Gerritsen (1994).

A2.1.6 Adjustments for 2-D Modelling

A number of simulations conducted in this study have used a depth-integrated approach. This has mainly been to provide an increase in computational efficiency. Further, the DHI sediment transport model computes the combined effects of waves and currents using a depth-integrated current velocity. A depth-integrated approach has also been used in a number of the *Delft-3D* modelling experiments described in Chapter 2.

Depth-integrated approaches try either to mimic 3-D effects using various schematizations (*MIKE-21/3 FM*) or solve the same set of equations over one σ-layer (*Delft-3D*). Delft Hydraulics recommend that the horizontal eddy viscosity, υ_H, includes a contribution that accounts for the effect of vertical variation in horizontal flow or 'shear-dispersion' (Taylor, 1954). The DHI approach derives two modified

depth-averaged equations by integrating the horizontal momentum and continuity equations over the depth. In the x- direction, the depth-averaged momentum equation reads

$$\frac{\partial H\bar{u}_h}{\partial t}+\frac{\partial H\bar{u}_h^2}{\partial x}+\frac{\partial H\overline{v_h u_h}}{\partial y}=f\bar{v}H-gH\frac{\partial \eta}{\partial x}-\frac{H}{\rho_0}\frac{\partial p_A}{\partial x}-$$

$$\frac{gH^2}{2\rho_0}\frac{\partial \rho}{\partial x}+\frac{\tau_{sx}}{\rho_0}-\frac{\tau_{bx}}{\rho_0}-\frac{1}{\rho_0}\left(\frac{\partial S_{xx}}{\partial x}+\frac{\partial S_{xy}}{\partial y}\right)+\frac{\partial}{\partial x}\left(HT_{xx}\right)+\frac{\partial}{\partial y}\left(HT_{xy}\right)+Hu_sS_c \qquad \text{(A2.10)}$$

and in the y- direction

$$\frac{\partial H\bar{v}_h}{\partial t}+\frac{\partial H\overline{v_h u_h}}{\partial x}+\frac{\partial H\bar{v}_h^2}{\partial x}=-f\bar{u}H-gH\frac{\partial \eta}{\partial y}-\frac{H}{\rho_0}\frac{\partial p_A}{\partial y}-$$

$$\frac{gH^2}{2\rho_0}\frac{\partial \rho}{\partial y}+\frac{\tau_{sy}}{\rho_0}-\frac{\tau_{by}}{\rho_0}-\frac{1}{\rho_0}\left(\frac{\partial S_{yx}}{\partial x}+\frac{\partial S_{yy}}{\partial y}\right)+\frac{\partial}{\partial x}\left(HT_{yx}\right)+\frac{\partial}{\partial y}\left(HT_{yy}\right)+Hv_sS_c \qquad \text{(A2.11)}$$

The resulting momentum equations contain three new terms, T_{xx}, T_{xy} and T_{yy} which are described as the 'lateral stresses'. These include the effects of viscous friction, turbulent friction and shear-dispersion. They are estimated using the eddy viscosity and depth-averaged velocity gradients

$$T_{xx}=2\upsilon_H\frac{\partial \bar{u}}{\partial x},\quad T_{xy}=\upsilon_H\left(\frac{\partial \bar{u}}{\partial y}+\frac{\partial \bar{v}}{\partial x}\right),\quad T_{yy}=2\upsilon_H\frac{\partial \bar{v}}{\partial y} \qquad \text{(A2.12)}$$

Delft Hydraulics include other terms in the 3-D and 2-D momentum equations, M_ξ and M_η, which represent contributions due to external sources of momentum, for example, wave stresses and discharges or withdrawals of water.

The new depth-averaged continuity equation is

$$\frac{\partial h}{\partial t}+\frac{\partial h\overline{u}_h}{\partial x}+\frac{\partial h\overline{v}_h}{\partial y}=HS \qquad \text{(A2.13)}$$

A2.1.7 Numerical Aspects

The partial differential equations presented in the previous sections are solved over both space and time using numerical methods. Appropriate numerical methods have been chosen on the basis of their robustness and speed. In order to solve the equations numerically, the first step is to transform the equations into discrete space i.e. convert them to a form that can be interpreted by a computer.

The *Delft-3D* model uses a finite difference approach in which the physical system is first covered by a rectangular, curvilinear or spherical grid. To discretise the shallow water equations, the primitive variables, including velocity, surface elevation and water depth, are mapped onto the numerical grid using a 'staggered grid' approach (see Figure A2.2 below).

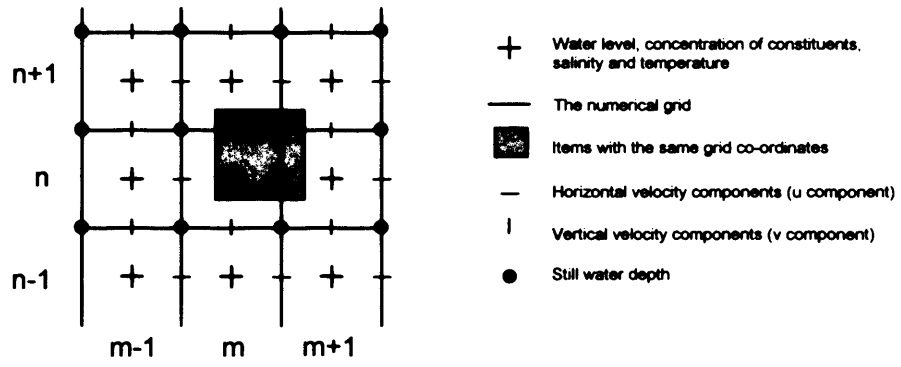

Figure A2.2. Mapping of the primitive variables in *Delft-3D*

The water levels are defined at cell centres and the velocities at cell faces to make a number of *control volumes*. In the vertical, a sigma coordinate system is used in which layers are bounded by two sigma planes which follow the bathymetry and the free surface. The layers can be distributed non-uniformly to allow for more resolution in areas of interest or where the velocity gradient through the vertical is changing more rapidly i.e. in the near-bed area.

MIKE-21/3 FM uses a finite volume-finite difference method to solve the shallow water equations and discretizes the domain into a number of arbitrarily shaped polygons or elements. This unstructured arrangement permits variable element sizes and allows their distribution to be adjusted in order to improve resolution in areas of interest or to fit a land or open boundary. The finite volume method computes fluxes though element faces with the primitive variables mapped to the element centres (see Figure A2.3 below).

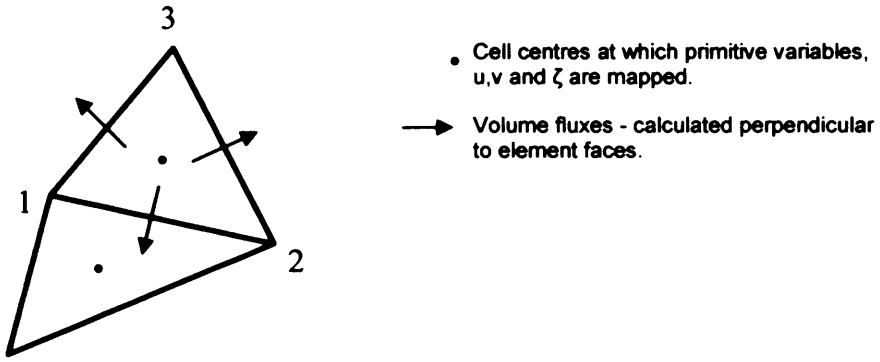

Figure A2.3. Mapping of the primitive variables in *MIKE-21/3*

Having mapped the variables in space, the equations are then solved over time using a numerical method which must be robust, accurate, suitable for time-dependant and steady state problems and computationally efficient.

Generally, numerical methods can be categorised as either *explicit* or *implicit*.

- *Explicit* schemes use already known quantities to make a direct computation of the dependant variables at the next time-step;
- *Implicit* schemes generate unknown quantities which appear on both sides of the coupled equations. They require the use of either a matrix or an iterative technique to compute the dependant variables at the next time-step.

Implicit schemes are both harder to program and require more computational effort; however, they allow for larger times steps because they are numerically more stable (for further details see Abbot and Basco 1989; Chung 2002).

In tidal propagation simulations, explicit schemes are restricted to time-steps of only a few seconds which is often considered unacceptable due to the amount of CPU time

required to compute each time-step (WL|Delft-Hydraulics 2001). The *Delft-3-D* model uses an implicit scheme that employs a Crank-Nicholson finite difference solver. The shallow water equations are formed into a system of non-linear difference equations using a large band-width matrix which is difficult to compute quickly. To solve the equations more efficiently, an 'ADI' time integration method splits one time-step into two stages and solves for the water level gradient and advection terms using alternating implicit and explicit methods. This leads to a much simpler tri-diagonal matrix with a smaller band-width and can be solved quicker.

ADI-methods can only be used for structured grids and the methods are not fully implicit, but 'semi-implicit' (Sørensen, 2006). Structured grids also have further disadvantages. For example, they cannot be easily tailored to suit the positions of boundaries and local refinement is difficult. Both these problems may introduce errors in to the solution, which can only be reduced by using finer grid spacing, hence adding further increases in CPU time.

In the *MIKE-21/3 FM* models an unstructured grid is used because of its flexibility in relation to local refinement. This feature has the advantage of being able to minimize the total number of discrete spatial nodes/elements required and also helps in the construction of boundary fitted meshes. Unstructured meshes are also better suited to modelling flooding and drying because they do not suffer from 'grid blocking' effects, typical of all rectilinear and curvilinear models: inundation and retreat of water may be restricted because the solution propagates along adjacent grid points sequentially. In narrow rivers and tributaries, which may only be represented by one or a small number of grid points, partial flooding along adjacent grid points may block the flow

To achieve improvements in the description of mass conservation, also important for the simulation of wetting and drying in coastal regions, the DHI approach employs a finite volume technique to solve the shallow water equations. One disadvantage of using a finite volume method with an unstructured grid is that it is very difficult to combine with an implicit time integration method. Therefore, the DHI approach uses an explicit method which limits the time-step to a *Courant-Friedrichs-Levy* (*CFL*) number of 1. The *CFL* number is a dimensionless variable that describes the propagation speed of

numerical information from grid cell to grid cell. It is a function of the flow velocity, u, the grid spacing, Δx, and the time-step, Δt:

$$CFL = (\sqrt{gh} + |u|)\frac{\Delta t}{\Delta x} + (\sqrt{gh} + |v|)\frac{\Delta t}{\Delta y} \qquad \text{(A2.14)}$$

If numerical information is propagating too fast relative to the time-step (due to large flow speeds or small grid cells), the model will be unable to find a solution in a given time-step. This will introduce instability and if the condition persists, will often result in the model crashing.

A2.2 The Wave Models

A2.2.1 General Issues

Waves have an important effect on coastal sediments and morphology. They increase sediment stirring leading to increased levels of sediment transport through wave breaking and decay; they drive long-shore currents which have further impacts on near-shore morphology and they also interact with tidal currents to modify the potential for tidal transport. Non-linear wave propagation in shallow water generates other effects on net sediment transport (including 'wave-related' and 'current-related' transport, see van Rijn, 1993). The accurate prediction of wave propagation and decay is thus considered to be an important aspect of this study. Much effort has been dedicated to provide an approach that is both accurate and efficient.

In the Delft and DHI models, a number of Eulerian wave modules are available which can be coupled to the hydrodynamic models. These include both hydrostatic and Bousinesq type models. Bousinesq type models are based on the non-hydrostatic shallow water equations in which the vertical velocity, $w(z)$, is assumed to increase linearly from zero at the bed to a maximum at the free surface following the relationship

$$w(z) = \frac{\partial}{\partial z}\int_{H} u dz \qquad \text{(A2.15)}$$

where U is the depth integrated horizontal velocity, z is a vertical position in the water column at which the velocity, u, is measured. h is the total water depth.

Boussinesq theory involves an extensive set of partial differential equations that must be solved throughout an individual wave cycle. This implies a large computational demand and renders these types of model impractical over larger spatial and temporal scales.

Models based on *the spectral action balance* of the waves are far more appropriate in larger-scale applications. The models are phase-averaged which means that they do not resolve individual wave cycles, but are based on formulations that propagate the absolute wave energy. This makes them much more efficient but also less sophisticated because they do not resolve processes at the oscillatory (intra-wave) scale. For example, wave diffraction or reflection cannot be easily resolved without simplification and parameterisation. This type of model yields phase-averaged quantities such as wave height, period and direction as well as spectral information and is described in the following section.

A2.2.2 The Energy Balance Equation

In the absence of currents, spectral wave models are based on the energy-balance equation where the wave energy density E is written as a function of the absolute angular frequency ω and direction θ. In the presence of an ambient current, the relation between the relative angular frequency, σ (observed in a frame of reference moving with the current velocity), and the absolute angular frequency (observed in a fixed frame), is given by the linear dispersion relation as

$$\sigma = \sqrt{gk\tanh(kd)} = \omega - \mathbf{k}\cdot V_A \qquad \text{(A2.16)}$$

in which $\mathbf{k}$ is the wave number vector of magnitude k and direction θ. d is the water depth and V_A is the current velocity vector. However, in the presence of an ambient

current the most relevant parameter for modelling wave propagation is the action density, A, defined by Whitham (1965) as

$$A(\omega,\theta,x,y,t) = E(\omega,\theta,x,y,t)/\sigma \tag{A2.17}$$

In the Eulerian reference frame the wave action-balance equation is

$$\frac{\partial A}{\partial t} + \frac{\partial}{\partial x}(c_x A) + \frac{\partial}{\partial y}(c_y A) + \frac{\partial}{\partial \theta}(c_\theta A) + \frac{\partial}{\partial \omega}(c_\omega A) = T \tag{A2.18}$$

Or in vector notation

$$\frac{\partial A}{\partial t} + \nabla \cdot (c_{x,y,\theta,\omega} A) = T \tag{A2.19}$$

in which the local rate of change of the action density is represented by the first term in Eq. (A2.19). The second term represents the transport of action in the x, y, θ and ω domains where c represents the celerity. The dissipation and generation of wave action by wind and bed friction are represented by the source function T which is also a function of x, y, θ and ω.

The propagation speeds c_x, c_y and c_θ in the balance equation (A2.19) can be defined by linear wave theory where c_x, c_y are the x- and y- components of the action propagation speed or the group velocity c, where

$$c = \frac{\partial \sigma}{\partial k}\frac{\mathbf{k}}{k} + V_A \tag{A2.20}$$

The rate of propagation in the directional domain (refraction), c_θ, is given as

$$c_\theta = -\frac{1}{k}\frac{\partial \sigma}{\partial d}\frac{\partial d}{\partial \psi} - \frac{\mathbf{k}}{k}\cdot\frac{\partial V_A}{\partial \psi} \tag{A2.21}$$

in which d is the local water depth and ψ is the coordinate in (x, y)-space normal to the spectral wave direction, θ.

Change in the propagation speed, c_ω, represents a change in wave action in the frequency domain. It is caused by time variations in the propagation medium including changing water depth, current speed or direction and is given by

$$c_\omega = \mathbf{k} \cdot \frac{\partial V_A}{\partial t} + \frac{\partial \sigma}{\partial d} \frac{\partial d}{\partial t} \qquad \text{(A2.22)}$$

Both Delft and DHI provide two spectral action balance models which vary in their degree of sophistication. These are often described as 2nd and 3rd generation wave models, henceforth PD and SW. In the Delft system, these models are referred to as *HISWA* (Holthuijsen et al., 1989) and *SWAN* (Booij et al., 1996) respectively. In the DHI system they are referred to as *Parametrically Decoupled* and *Spectral Waves* (Sørensen et al., 2004).

A2.2.3 Spectral and Parametric Formulations

The first difference between the SW and the DS formulations is that the SW models solve equation (A2.19) directly as a time-dependent solution using an unsteady source function, T.

Alternatively, time can be removed as a dependent variable and a steady-state solution to the wave action balance equation is found for different wave and current conditions:

$$\nabla \cdot (c_{x,y,\theta,\omega} A) = T \qquad \text{(A2.23)}$$

This approach is based on the assumption that the propagation time of waves through coastal regions is short compared to the scales of the wind and current field propagation (the 'Stationary' assumption).

Equation (A2.23) is further simplified by parameterising the frequency domain in terms of a *directional action spectrum*, $A_0(\theta)$, and a *mean wave frequency* as a function of

spectral direction, $\omega_0(\theta)$. This is the important distinction between a 3rd and 2nd generation wave model.

This method retains the directional properties of the wave spectrum, important in coastal regions, but makes a simplification in the frequency space. The directional action spectrum, $A_0(\theta)$, and the mean wave frequency, $\omega_0(\theta)$ are given as

$$A_0(\theta) = m_0(\theta) \tag{A2.24}$$

$$\omega_0(\theta) = m_1(\theta)/m_0(\theta) \tag{A2.25}$$

The zeroth (m_0) and first (m_1) moments of the action spectrum are obtained from the definition operator

$$m_n(\theta) = \int_0^{\infty} \omega^n A(\omega,\theta) d\omega \tag{A2.26}$$

Full parameterisation of the action-balance equation is performed by combining equations (A2.26) and (A2.23) to give

$$\nabla \cdot (c^{\bullet}_{0,x,y,\theta} m_0) = T_0 \tag{A2.27}$$

$$\nabla \cdot (c^{\bullet\bullet}_{0,x,y,\theta} m_1) = T_1 \tag{A2.28}$$

in which $c^{\bullet}_{0,x,y,\theta}$ and $c^{\bullet\bullet}_{0,x,y,\theta}$ in equations (A2.27) and (A2.28) are the propagation speeds through (x,y,θ)-space of m_0 and m_1 respectively. T_0 and T_1 are the parameterised source functions for m_0 and m_1 respectively. Notice that the frequency domain (ω) has now been removed from the equations. The full SW (3rd generation) models solve the full wave action balance equation using the two dimensional wave action, $A_0(\omega,\theta)$.

Both the Delft and DHI models account for refractive propagation over arbitrary bathymetry and current fields and the models are driven by boundary conditions and local winds. The following processes are modelled:

1. Wind generation;
2. White-capping (energy dissipation from wind action on wave crests);
3. Quadruplet wave-wave interactions (energy transfer from the peak frequency to lower frequencies. Energy is also transferred to higher frequencies, where it is dissipated by white-capping);
4. Bottom dissipation;
5. Triad wave-wave interactions (the transfer of energy from lower frequencies to higher frequencies, sometimes indicated by the appearance of a secondary high-frequency peak in the free-surface elevation spectrum)
6. Depth-induced wave breaking.

HISWA and SWAN use a semi-implicit numerical propagation scheme on a rectilinear grid while the SW and DS DHI models use a multi-step explicit approach on an unstructured grid. The explicit scheme limits the computational efficiency; however, this can be mitigated somewhat by exploiting the unstructured mesh to its full potential (as described in Section A2.1.5). Recent developments in the numerical methods used in the DHI models have resulted in much improved computational efficiency on an unstructured mesh (see Sørenson et al, 2006).

A2.3 Wave-Current Interaction

A2.3.1 Preamble

In shallow water regions wave action has important impacts on the current field including the following:

1. Enhanced bed shear stresses which modify the bed-roughness and affect tidal current speed;
2. An increase in turbulence generation due to white-capping, wave-breaking and energy dissipation at the bottom which increases vertical mixing;
3. A net mass flux in the direction of wave propagation (Stokes Drift), which can often be complicated by return flows;

4. Wave decay which generates momentum fluxes in the surf zone (due to gradients in radiation stresses), setting up long-shore currents;
5. Wave streaming due to downward directed momentum fluxes in the wave boundary layer.

To capture these effects, DHI and Delft Hydraulics have taken different approaches. The *Delft-3D* model tries to incorporate the physical processes directly into the flow formulations. DHI defer their inclusion to other modules which then calculate the direct impact of wave-current interaction on the processes of interest viz. within a transport or sediment transport module.

One of the reasons DHI choose to model the *effect* of wave-current interaction directly on the processes of interest is that there is a significant difficulty involved in using models that are based on Eulerian fixed co-ordinate systems when modelling wave-current interaction. A standard approach is to resolve the wave-averaged mean motion (Stokes Drift) and the oscillating wave components together and then average them over a wave cycle to give the wave-induced forcing. The wave-averaged mean motion, however, is not always uniform in the vertical (due to return flow and fluctuating water level) and significant errors are subsequently introduced when calculating effects that are dependant on the oscillatory motion i.e. the wave forcing and turbulence. An accurate description of the wave forcing, therefore, needs to include the effects of depth-varying mass fluxes on the oscillatory wave properties.

To overcome this problem, Delft Hydraulics use a "Generalized Lagrangian Mean" approach (henceforth, GLM) to compute the flow quantities (Groeneweg 1999). This follows the mean wave motion due to Stokes Drift. The relationship between the GLM velocity and the Eulerian velocity is given by

$$\vec{u}^{L} = \vec{u}^{E} + \vec{u}^{S} \qquad \text{(A2.29)}$$

where $\vec{u}^{L}$ is the GLM velocity vector, $\vec{u}^{E}$ the Euleriean velocity vector and $\vec{u}^{S}$ is the Stokes drift vector. For more details, refer to Walstra et al., (2000) and Lesser et al., (2004).

The Delft Hydraulics approach, therefore, includes the wave-induced effects of Stokes Drift, radiation stresses and the wave-modified boundary layer directly into the flow formulations.

This approach has a number of advantages including:

- The modelling of sediment transport can be directly coupled to the flow field;
- Secondary flows, including undertow and helical motion, can be modelled directly;
- Other processes, for example density driven currents, can be directly coupled to the model.

Apart from the radiation stress gradients, the DHI approach defers the remaining physics of wave-current interaction to other modules that are coupled to the main hydrodynamic model.

DHI's *STPQ3D* is a separate simulation engine that calculates sediment transport rates for a range of pre-defined wave, current and water depth combinations. The model resolves the wave-current boundary layer and resulting bed shear stresses using the momentum integral method of Fredsøe (1984) (see Section A2.3.2).

The model is run externally to a hydrodynamic simulation, producing tables of potential sediment transport. During a hydrodynamic simulation, sediment transport rates are interpolated from the table.

The following section describes the implementation of all aspects of wave-current interaction in both the Delft Hydraulics (directly coupled) approach and the *MIKE-21/3 FM- STPQ3D* modelling system.

A2.3.2 Enhancement of the Bed Shear Stress due to Waves

Inside the wave boundary layer, the velocity profile of the mean current is affected by turbulence generated by the wave and current motion (Kemp and Simons 1983). The effect of this increased eddy viscosity is to increase flow resistance on the mean current. This is usually described by an 'apparent' bed roughness which is always larger than the real bed roughness. The waves, therefore, will always cause a larger bed-shear stress for a given current. Quantifying the time-varying character of the boundary layer turbulence

and its effects on the bed shear stress, however, remains one of the biggest challenges in seabed mechanics.

Using the momentum integral method of Fredsøe (1984), the *STPQ3* approach of DHI assumes that the time scale for production and decay of turbulent kinetic energy is small compared to the wave period and that a new boundary layer develops each time the flow reverses. The wave boundary layer is therefore computed independently throughout a wave period. During each computation, it is assumed that the turbulent energy is in a state of instantaneous equilibrium and that the velocity profile in the wave-boundary layer is initially logarithmic. This provides a means of solving the boundary layer geometry and resulting bed-shear stress without using an eddy viscosity concept directly. The eddy viscosity and the apparent bed roughness are solved at the end of the computation using the boundary layer thickness and the bed shear stress.

The time varying character of the wave boundary layer over each half wave period is computed by integrating the momentum equation over the wave boundary layer

$$\frac{\partial z_b}{\partial t} = \frac{z_b}{e^{z_b}} \frac{(1+z_b-e^{z_b})}{e^{z_b}(z-1)+1} \frac{1}{U_0} \frac{\partial U_0}{\partial t} + \frac{30\kappa}{k_s} \frac{\sqrt{\kappa^2 U_0^2 + z_b^2 U_{f0}^2 + 2\kappa z_b U_{f0} U_0 \cos\gamma}}{e^{z_b}(z_b-1)+1} \qquad \text{(A2.30)}$$

where κ is von Kármán constant and U_{f0} is the friction velocity for the mean velocity profile in the wave boundary layer. γ is the angle between the current and the waves, k_s is the bed roughness, taken to be equal to 2.5 d_{50} for a plane bed, and 2.5 d_{50} + k_R for a ripple-covered bed. d_{50} is the median grain size and k_R is a ripple-related roughness. z_b is the non-dimensional boundary layer thickness, related to the velocity at the top of the boundary layer (U_0) and the friction velocity (U_f) by

$$z_b = \frac{U_0}{U_f}\kappa \qquad \text{(A2.31)}$$

z_b controls the boundary layer thickness, δ, which varies over a wave period

$$\delta = \frac{k_N}{30}(e^{z_b} - 1) \tag{A2.32}$$

U_f, the time varying friction velocity, can be found by applying a boundary condition at the top of the wave boundary layer ($z = \delta + k_N / 30$)). This condition requires that the vectorial sum of the potential flow velocity computed outside the boundary layer and the mean current profile be equal to the instantaneous velocity. Including a parameter γ, which describes the angle between the mean current direction and direction of wave propagation, the condition yields the following equation

$$\left[\frac{U_f}{\kappa}\ln\left(\frac{\delta + k_N/30}{k_N/30}\right)\right]^2 = \left[\frac{U_{f0}}{\kappa}\ln\left(\frac{\delta + k_N/30}{k_N/30}\right) + U_0\cos\gamma\right]^2 + \left[U_0\sin\gamma\right]^2 \tag{A2.33}$$

[1] [2] [3]

in which term [1] describes the instantaneous velocity profile inside the boundary layer, term [2] the mean current profile inside the boundary layer and term [3] the velocity just outside of the boundary layer computed using potential theory. U_{f0}, the friction velocity due to the current inside the wave boundary layer, is required in both the computations of Eqs. A2.30 and A2.33 and is not known beforehand. Therefore, the two equations are solved iteratively for U_{f0} (using a 4th order Runga Kutta method).

The friction velocity of the mean current, U_{fc}, is then computed using

$$U_{fc} = \sqrt{\frac{1}{T_z}\int_0^T U_f^2 \cos\Theta dt} \tag{A2.34}$$

where T_z is the zero crossing wave period. The mean boundary layer thickness, δ_m, is then computed using

$$\delta_m = 1/2(\delta_{t=T/4} + \delta_{t=3T/4}) \tag{A2.35}$$

And the apparent roughness, k_w, from

$$k_w = k_N \left(\frac{30\delta_m}{k_N} \right)^{1-\left[\frac{U_{fm}}{U_f}\right]} \tag{A2.36}$$

The iteration can be summarised by the following:

1) Compute the mean current friction velocity inside the boundary layer, U_{f0}, using Equation A2.30;
2) Compute the new friction velocity, U_f, using Equation A2.33;
3) Compute a new mean current friction velocity, U_{fc}, using Equation A2.34
4) Repeat until U_{fc} at the end of the iteration is the same as U_{fc} at the start of the iteration (minus a small pre-defined tolerance).

Once the iteration has converged, and the variation of U_f over each wave period obtained, application of the momentum equation in the mean flow direction gives the mean bed shear stress, $\overline{\tau_{wc}}$, in response to combined wave and current motion.

$$\overline{\tau_{wc}} = \frac{1}{T}\int_0^T \rho U_f^2 \cos\Theta dt \tag{A2.37}$$

where Θ is the angle between the instantaneous bed shear stress and the mean current direction, obtained from

$$\cos\Theta = \frac{U_0 \kappa \cos\gamma + U_{f0} z_b}{U_f z_b} \tag{A2.38}$$

The *Delft-3D* model includes the bed shear-stresses due to a combination of waves and currents but in a parameterised way following the approach of Soulsby et al (1993) which primarily aims to establish an inter-comparison between the models available. The combined mean shear stress, $\overline{\tau_{wc}}$, is given as

$$\left|\overline{\tau_{wc}}\right| = y\left(\left|\bar{\tau}_c\right| + \left|\bar{\tau}_w\right|\right) \tag{A2.39}$$

where

$$y = x\left\{1 + bx^p(1-x)^q\right\} \tag{A2.40}$$

and $|\tau_c|$ and $|\tau_w|$ are the bed shear stresses due to current and waves, respectively, and the parameters b, and q are dependent on the friction model used. x is given as

$$x = \frac{\left|\bar{\tau}_c\right|}{\left|\bar{\tau}_c\right| + \left|\bar{\tau}_w\right|} \tag{A2.41}$$

A2.3.3 Enhanced Turbulence Production due to Waves

The wave boundary layer introduces turbulence near to the bed, while wave breaking and white capping add turbulence near the surface. The DHI *STPQ3D* computes the wave-current boundary layer (as described in Section A2.3.2), and parameterises the turbulence, throughout a wave period using an eddy viscosity, υ_{bl}, calculated as

$$\upsilon_{bl} = \kappa U_f z\left(1 - \frac{z}{\delta}\right) \tag{A2.42}$$

where κ is the von Karman coefficient and δ is the instantaneous boundary layer thickness computed by the Fredsøe model described earlier.

For the enhancement of the eddy viscosity due to wave breaking *STPQ3D* uses a dimensionless factor which is defined as the ratio of the actual energy dissipation to the energy dissipation in a steady hydraulic jump. The actual energy dissipation is calculated in different ways for uniform and non-uniform waves using the approach of Deigaard et al (1986). The DHI model includes no turbulence enhancement due to white-capping.

Delft Hydraulics use the same approach to calculate the energy dissipation (viz. Deigaard et al, 1986) but directly incorporate these processes as source terms into the $k-\varepsilon$ equations for turbulent kinetic energy production and dissipation respectively. The contribution due to wave breaking is then linearly distributed over a half wave height beneath the mean water level.

A2.3.4 Radiation Stress Gradients

The Delft and DHI models apply radiation stresses in a similar way. A wave computation (using *SWAN* or *MIKE-SW*) is made prior to a hydrodynamic computation providing a radiation stress tensor, **S**. For 2-D simulations, spatial gradients in the radiation stress tensor provide depth-averaged wave induced forcing, F_x and F_y, which are incorporated into the momentum equations as contributions to the *lateral stresses* (see Section A2.1.6)

$$F_x = \frac{\partial S_{xx}}{\partial x} - \frac{\partial S_{xy}}{\partial y} \qquad \text{(A2.43)}$$

$$F_y = \frac{\partial S_{xy}}{\partial x} - \frac{\partial S_{yy}}{\partial y} \qquad \text{(A2.44)}$$

In 3-D simulations the two approaches differ slightly. *MIKE-21/3 FM* assumes a uniform vertical distribution of the wave-induced forces, while *Delft-3D* applies wave-induced forces over only the top vertical layer.

The *STPQ3D* sediment transport model includes an additional contribution from the radiation stresses by incorporating energy dissipation due to wave breaking. This

provides a vertical transfer of horizontal momentum affecting the momentum balance and bed shear stress.

A2.3.5 Stokes Drift and Mass Flux

The GLM approach used in *Delft-3D* computes the hydrodynamics with respect to the Stokes Drift. A separate calculation of the Stokes Drift, therefore, is not required. It is found simply by subtracting the GLM and Eulerian reference frames and integrating over the wave-averaged total water depth. This gives the total Stokes Drift mass fluxes.

The DHI system calculates the Stokes Drift within the *STPQ3*sediment transport model to give its direct effect on sediment transport. The *STPQ3* model calculates the bed-shear stresses throughout a wave cycle requiring the wave orbital velocities to be resolved at the same interval. The user is able to select from a number of wave theories to calculate the orbital velocity, each of which is valid in a limited set of hydrodynamic conditions. Higher order wave theories can be defined in order to describe the Stokes Drift. The wave induced mass transport then provides a contribution to the mean flow.

A2.3.6 Wave Streaming

Streaming is a small mass flux due to bottom dissipation in the boundary layer that moves in the direction of wave propagation. The phenomenon can be understood by considering the variation in boundary layer thickness along the seabed in the direction of wave propagation: the expansion and contraction of the boundary layer creates a small reversing vertical flow velocity which is small compared to the orbital velocity. Outside of the boundary layer, the additional vertical velocity attains a value w_s while it diminishes to zero at the bed. The existence of a small w_s is key because it means that the product of w_s and the wave orbital velocity when averaged over a wave period is non zero ($\overline{uw_s} \neq 0$). There will be a net momentum flux directed towards the bed which causes a positive shear force at the bed. See Fredsøe and Deigaard (1992) or Mei (2002) for further detail. Both models incorporate contributions to the bed shear stress from streaming using various formulations.

The DHI *STPQ3* model uses the near bed wave orbital velocity, U_0, and the friction velocity, U_f, which have already been computed at half wave cycles using the integrated momentum approach described earlier. The contribution (τ_{str}) to the bottom shear stress from streaming is then computed using

$$\tau_{str} = \frac{\rho}{c}\overline{U_0 U_f |U_f|} \tag{A2.45}$$

in which ρ is the water density, and c is the wave celerity. The over bars denote values averaged over a wave period.

Without resolving the wave-current boundary layer, the Delft model uses an approximate means of computing the streaming effect based on averaging a vertical derivative of the advection terms over a wave period

$$-\frac{\partial \overline{\tilde{u}\tilde{v}}}{\partial z} = \frac{\partial}{\partial z}\left[\frac{D_f k \cos\phi}{\omega}\left(1 - \frac{d+\zeta-z}{\delta}\right)\right] \text{ for } d+\zeta-\delta \le z \le d+\zeta \tag{A2.46}$$

where $\tilde{u}$ and $\tilde{v}$ denote total velocity due to the mean flow and Stokes Drift in the x- and y- directions respectively, ζ is the water surface elevation and D_f is the wave and current dissipation due to bottom friction which is calculated using a parameterised friction factor from Soulsby et al (1993).

A2.4 Sediment Transport

A2.4.1 Suspended Sediment Transport

Both *MIKE-21/3 FM* and *Delft-3D* solve some form of the turbulent advection diffusion equation. In *Delft-3D*, the 3-D advection diffusion equation is solved using output velocity and eddy diffusivity from the hydrodynamic computations. Sediment mixing coefficients are established from the turbulence model. To include the effects of waves on sediment transport, a sediment mixing coefficient for non-cohesive sediment fractions is calculated separately using the parameterised approach of van Rijn (1993).

The *Delft-3D* model also incorporates the effect of suspended sediment on density and settling, something that is not included in the DHI models.

DHI's *STPQ3* model calculates the vertical variation of suspended sediment concentration from the advection diffusion equation using an iterative method presented by Fredsøe et al (1985). The enhanced vertical resolution of the *STPQ3* model provides a more accurate description of the vertical mixing of suspended sediment due to the combined action of waves and tidal currents.

A2.4.2 Erosion and Deposition

The *Delft-3D* sediment transport model computes the transfer of sediment between the bed and the flow using source and sink terms computed in a 'reference cell' (labelled 'K_{mx}' in Figure A2.3). The reference cell is defined as the next layer up in the water column from 'van Rijn's reference height', an arbitrary level calculated as a function of current-related effective roughness and water depth.

Below the van Rijn reference height all sediment is assumed to behave as bed-load and subject to the effects of bed slope. Bed-load transport is computed using the bed-load formula of van Rijn (1993). The purpose of the 'reference cell' is to provide an intermediate zone which behaves as both a source and a sink cell for bed-load and suspended load computations.

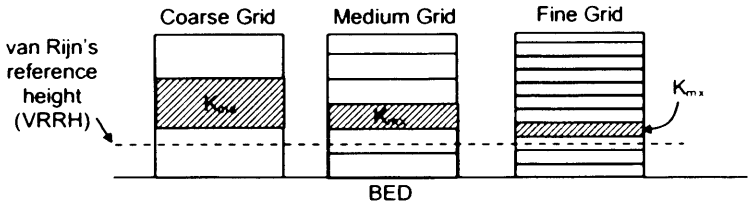

Figure A2.4. Reference level used to compute source and sink terms. Also detailed: position of *van Rijn's reference height.*

The DHI *STPQ3* approach uses a similar approach in which a 'reference bed concentration' is first calculated following the approach of Engelund and Fredsøe (1976): The friction velocity (from the boundary layer dynamics, previously computed)

is used to calculate the Shields parameter. This is then used to compute the probability that all particles in a layer are moving. This governs the linear concentration profile and reference bed concentration. The concentration profile through the vertical is then computed by iteration of the diffusion equation.

The height of the reference level in *Delft-3D* will always be much higher than that used in the *STPQ3* model. This is because in *Delft-3D*, the reference height depends on the position of sigma layers (prescribed by the user). The *STPQ3* model includes many more points in the vertical and hence computes the reference concentration inside the wave-current boundary layer where the complexity exists.

The *Delft-3D* model uses a direct coupling between the flow and the sediment transport models (as it does not use a look-up table). However, the model is highly parameterised and lacks a detailed description of the strongly unsteady conditions in the oscillatory boundary layer.

A2.4.3 Bed-load Transport

The *Delft-3D* model uses one of two formulations presented by van Rijn (1993), depending on whether waves are present. The approach is adjusted for bed-slope.

The *STPQ3* model of DHI uses the bed-load model of Engelund and Fredsøe (1976) in which the bed-load is calculated from the instantaneous Shields parameter.

In *Delft-3D*, details like the deviation of the direction of bed-load transport from the mean bed shear stress cannot be represented (except for the effect of bed slope), and the effect of wave asymmetry can only be handled in a parameterised way.

A2.4.4 Morphology

Both models update the bed continuously throughout a morphological simulation depending on the estimated bed level change rates (dz/dt). The models calculate the sediment transport vectors in the near-bed layer. These are used to compute rates of bed evolution via the sediment balance equation

$$-(1-n)\frac{\partial z}{\partial t} = \frac{\partial Q_x}{\partial x} + \frac{\partial Q_y}{\partial y} \qquad \text{(A2.47)}$$

where z is the bed level and Q_x and Q_y are the sediment transport rates in the near-bed layer.

To improve computational efficiency, in the *Delft-3D* model the bed level change rate is computed at every hydrodynamic time-step, often described as 'On-line'. The DHI approach also provides this option but permits the user to define a time-step factor, such that new values for dz/dt are estimated at every *nth* hydrodynamic time-step. This has the advantage of increasing computational efficiency when the sediment transport rates change at a much slower rate than the hydrodynamic time-step. The new bed levels are obtained from a forward in time differencing scheme of the form

$$z^{new} = z^{old} + \left[\frac{1}{1-n}\frac{\partial z}{\partial t}\Delta t\right] MFAC \qquad \text{(A2.48)}$$

where the bed level change rate is updated at a user-defined interval of Δt and a morphological scaling factor, *MFAC*, can be applied to increase the morphological simulation period. If the bed level change rate calculation interval has been relaxed, then the sediment transport rate calculation interval can also be relaxed to Δt.

To include the contribution from bed load transport to the bed level change rate, both models use a simple up-winding scheme which translates the sediment transport divergences, computed at the cell centres, to the cell faces where the depth is computed.

A2.5 Summary

A2.5.1 Advantages of the *Delft-3D* system

1. The implicit numerical scheme is not restricted by a low Courant number criterion;
2. A *Generalized Lagrangian Mean* (GLM) formulation in which the frame of reference moves with the mass transport (Stokes Drift) of the progressive waves, eliminates ambiguities with respect to the oscillating water surface and return flows;
3. Secondary flows and their gradual development are modelled directly using the GLM approach;

4. The suspended sediment concentration field is simulated using the same grid and numerical schemes. Thus the model automatically includes gradual adaptation of the suspended transport to spatial or temporal variation in the hydrodynamics and effects of the secondary currents;
5. The model includes a description of density effects due to suspended sediments which is not included in *MIKE*.

A2.5.2 Disadvantages of the *Delft-3D* system

1. The curvilinear grid cannot be locally refined in areas of particular interest.
2. In multi-layer applications the computational effort of the GLS approach is still high, relative to using *MIKE-21* coupled to the *STPQ3* model. Horizontal resolution will be sacrificed in order to improve computational efficiently and thus reduce the benefit relative to the *STPQ3* approach.
3. Details of the wave-current boundary layer cannot be simulated because neither the spatial or temporal resolution will allow anything but simple parameterised representations of the processes.
4. The height of the reference level at which the source and sink terms of sediment transport are computed is high relative to the *STPQ3* model. This means that the interface between material in bed-load and material in suspended load will be less well defined.
5. The eddy viscosity and diffusivity due to the fluctuating wave boundary layer is taken to be constant in time. Therefore, there the time variation in the suspended load over a wave period is not taken into account.
6. There is no means of reducing the re-calculation interval of the sediment transport and bed-updating rates.

A2.5.3 Advantages of the *MIKE-21/3* system

1. The unstructured mesh can be easily refined in regions of interest and can also be tailored to fit complex land and open boundaries. The wave model can be run on the same unstructured grid;

2. The finite volume approach in combination with triangular elements is well adapted to modelling flooding and drying as it does not suffer from 'grid blocking' effects;
3. Horizontal turbulence is modelled using the closure scheme of Smagorinsky (1963) where the energy dissipation is resolved as a function of the rate of the strain on the fluid and the horizontal grid spacing;
4. The number of sigma layers used in the hydrodynamic model can be minimised as complex vertical processes are captured more efficiently using the *STPQ3* model;
5. The wave-current boundary is resolved at the temporal scale of a wave period which means that many of the complexities associated with sediment transport can be modelled directly. For example, wave streaming, boundary layer mixing, apparent roughness and mass transport are all resolved by the *STPQ3* model;
6. The morphological updating scheme permits a relaxation between the sediment transport, flow and bed updating.

A2.5.4 Disadvantages of the *MIKE-21/3* system

1. The explicit numerical scheme puts a CFL number criterion on the hydrodynamic time-step which can be restrictive in large models with areas of high resolution;
2. Sediment transport predictions from the *STPQ3* model are based on the magnitude of the depth-integrated current field provided by the hydrodynamic model. Therefore even in 3-D simulations, although the wave-current boundary layer will be highly resolved, the current field used to compute the sediment transport field will have little information related to the seabed. Flow instabilities due to bed perturbations in deep water will not, therefore, be simulated.
3. A similar problem will occur near the free-surface where modifications to the vertical velocity profile induced by wind stresses will not be accommodated by the *STPQ3* model.

Appendix 3: Model Parameters and Calibration/Validation

A3.1 Model Bathymetry

The bathymetry used in the set up of the MIKE-21 model has been derived from a number of different sources collected between 1972 and 1998. These include both Admiralty Fair Sheets and charts from HMHO surveys as well as local survey data from contracted survey companies. The various sources of bathymetric data that have been interpolated onto the numerical mesh are presented in Table A3.1.

Table A3.1. Bathymetry Sources

Bathymetry Samples (contracted survey company, location name)	**Year**	**Area**
UK Dredging, Port Talbot	1998	Severn Estuary
POB, Bristol Deep and King Road	1997	Severn Estuary
ABP, Helwick Bank	1997	Outer Bristol Channel
Andrews Hydrographic, Holme Sands	1995	Inner Bristol Channel
HRW, Nash Bank	1988	Inner Bristol Channel
HRW, Northwick Roadstead and Dun Sands	1994	Severn Estuary
ARC Marine, Barnstaple Bay	1993	Outer Bristol Channel
Andrews Hydr., Middle Ground	1993	Severn Estuary
Admiralty Chart 1076	1991	Outer Bristol Channel
Admiralty Chart 1164	1991	Outer Bristol Channel
Fair Sheets M1535/1 and M1535/2	1989	Central Bristol Channel
Admiralty Chart 1152	1986	Inner Bristol Channel
Admiralty Chart 1166	1985	Severn Estuary

Datum correction has been applied to each data set to ensure that a common horizontal datum (ODN) is used. Interpolating also involved the import and interpolation of more recent data sets in preference to older ones. Older surveys were only used if they covered areas that were insufficiently covered newer data sets. This was because the newer data sets were considered to be more accurate than the older ones.

A3.3 Flow Model Parameters and Calibration

The hydrodynamic model was calibrated over a 2 week period in June 2000 and validated over another 2 week period in July 2002. Model predictions were compared with real velocity and water level measurements from locations around the Bristol Channel. Table A3.2 describes some of the key model input parameters.

Table A3.2. Key feature of the hydrodynamic model setup

Time Period	01/06/2000 – 15/06/2000
Offshore Boundary Condition	KMS global tidal model (Andersen, 2004)
Eddy Viscosity	Smagarinsky Formulation ($c_s = 0.28$)
Bed Resistance	Depth Varying Manning Number

A number of adjustments were made in order to improve the performance of the model. These included changes to the Manning number, M , which controls the drag coefficient, C_F

$$C_F = \frac{g}{(MH^{1/6})^2} \qquad \text{(A3.1)}$$

where H is the total water depth.

Initial runs were conducted using a uniform bed resistance ($1/M = 32$ $m^{1/3}/s$). Theoreticaly the equation for the bed resistance (A3.1) should account for the diminishing effects of bed friction with increasing water depth. However, it has been shown in numerous modelling studies that, in shallow water, the relationship does not fully describe the frictional influence of the bed. In such cases, it has been necessary to increase the value of the Manning number with decreasing water depth. In this study, after using an initial Manning number of 1/32, a spatially varying map of $1/M$ was produced based on the water depth. This is presented in Figure A3.1 and provided better agreement with velocity measurements in the shallow water regions. The map is not related to the physical roughness imposed by sediment, ripples, sand-waves and rocks.

A3.3 Comparison of Water Levels

The flows inside the model are driven by fluctuating water levels defined at the western boundary. The water levels have been extracted from the KMS global tidal model (Andersen, 1995) which includes eight deep-water tidal constituents. The data was extracted at six equally spaced positions. The flow model linearly interpolated the water levels between these positions to define a spatially varying water level boundary condition.

Data available for the comparison of measured and predicted water levels includes tidal gauge measurements from a number of locations throughout the Bristol Channel/Severn Estuary (see Figure A3.1). The phase is well matched during both spring and neap conditions. Water elevations are also repeated well by the model, occasionally missing peak spring levels (see Avonmouth, Figure A3.3 (a)), and over-predicting the low-water mark during both spring and neap period (see Illfracombe Figure A3.3 (b) and Mumbles Figure A3.5)). Computed values of root-mean-square (RMS) also compare favourably (see Table A3.4). With the exception of Avonmouth (RMS diff.=12%), all stations exhibit RMS differences of less than 10 % with Minehead, Mumbles and Porthcawl much less than 5%.

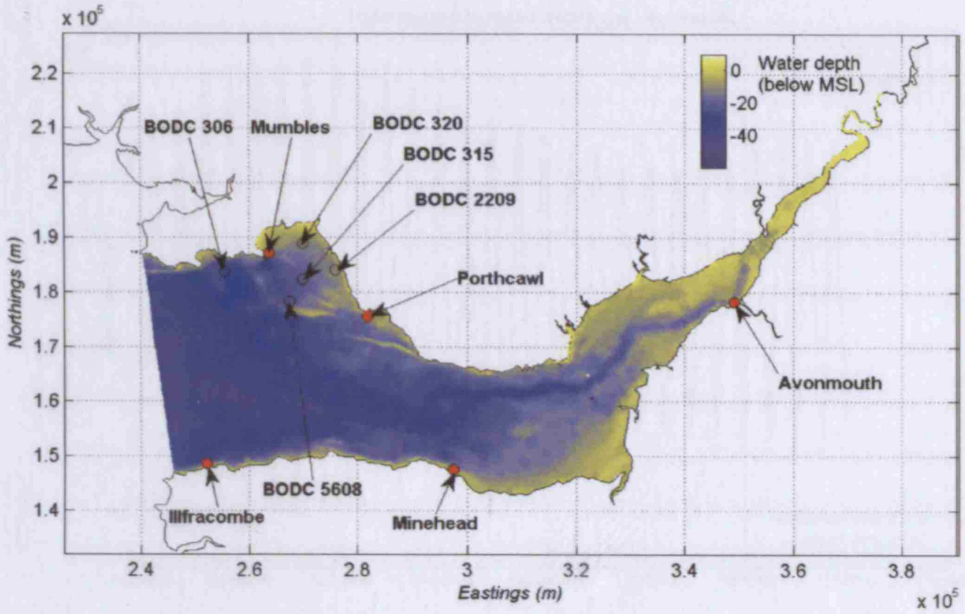

Figure A3.1. Model bathymetry and positions of measuring stations.

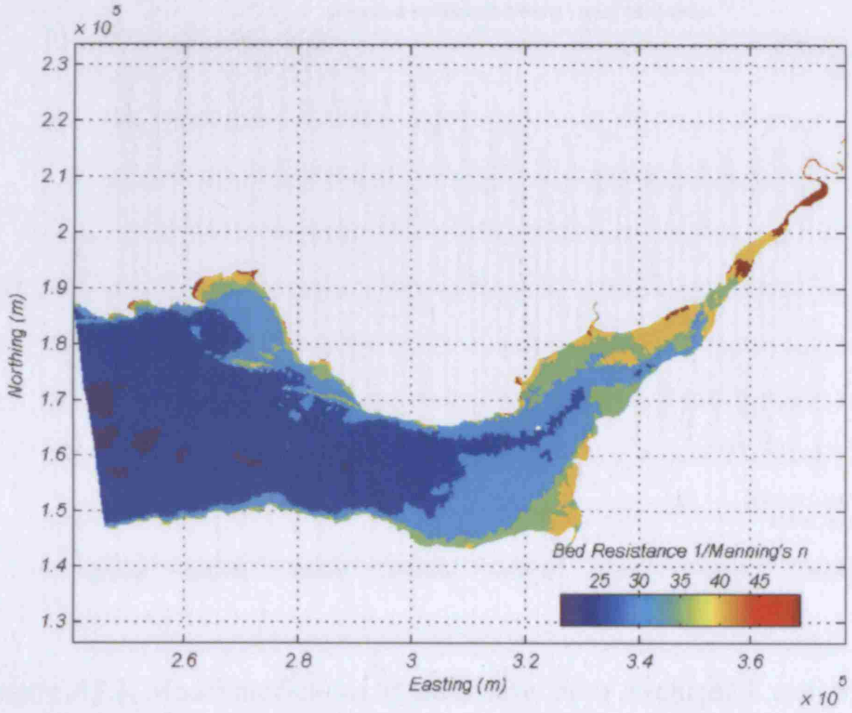

Figure A3.2. Bed resistance map and measurement positions.

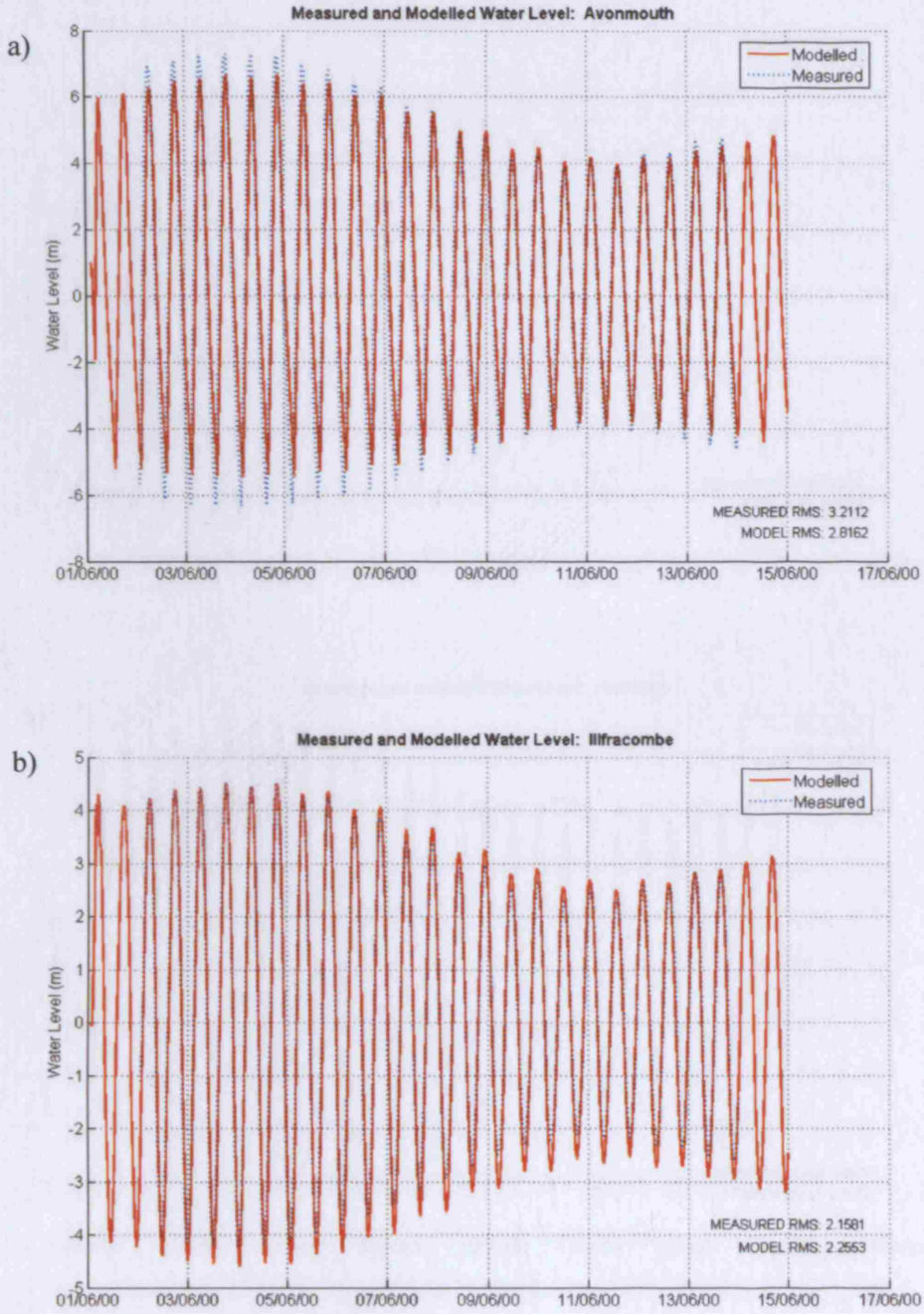

Figure A3.3. Model predictions of water level at a) Avonmouth and; b) Illfracombe compared to measured values.

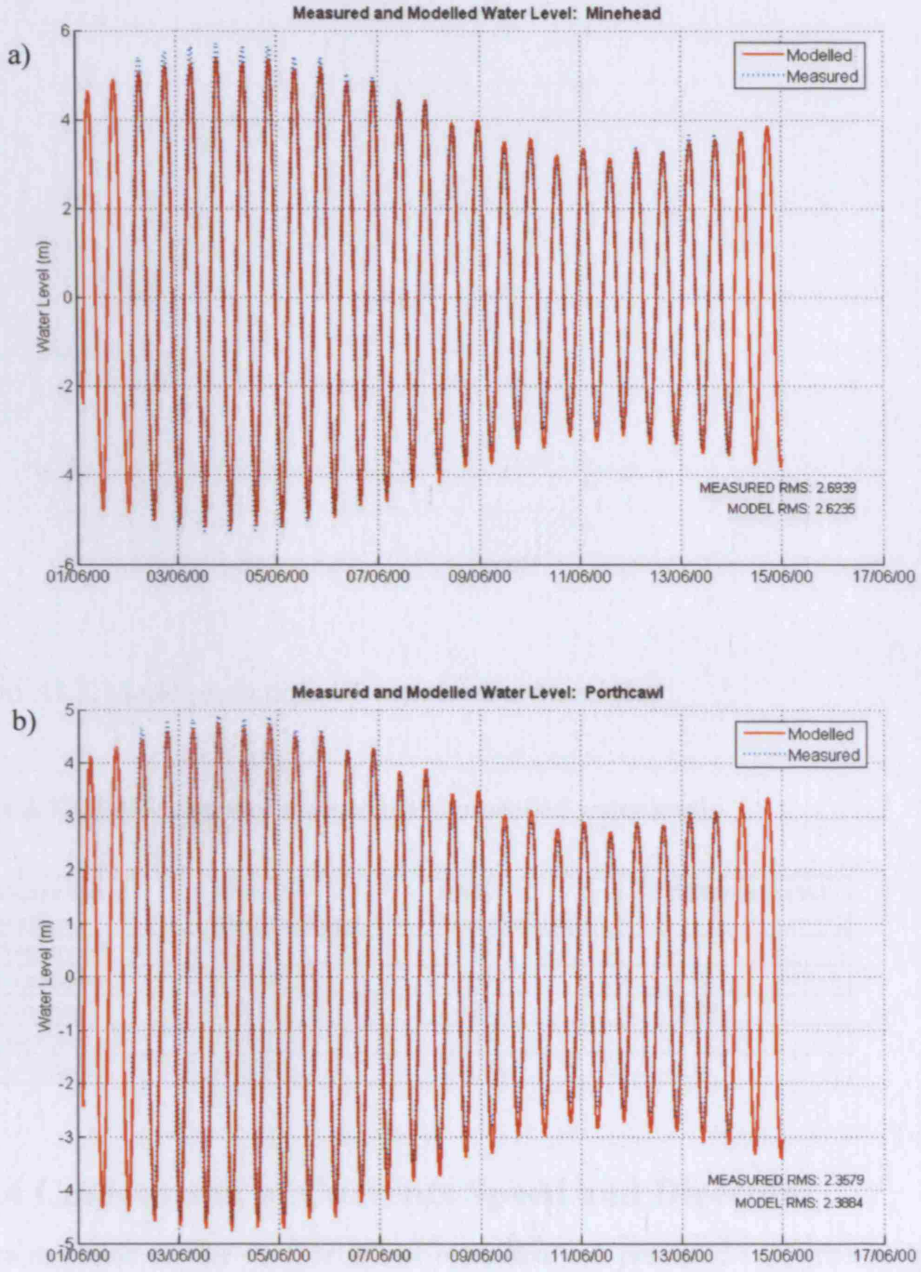

Figure A3.4. Model predictions of water level at a) Minehead and; b) Porthcawl compared to measured values

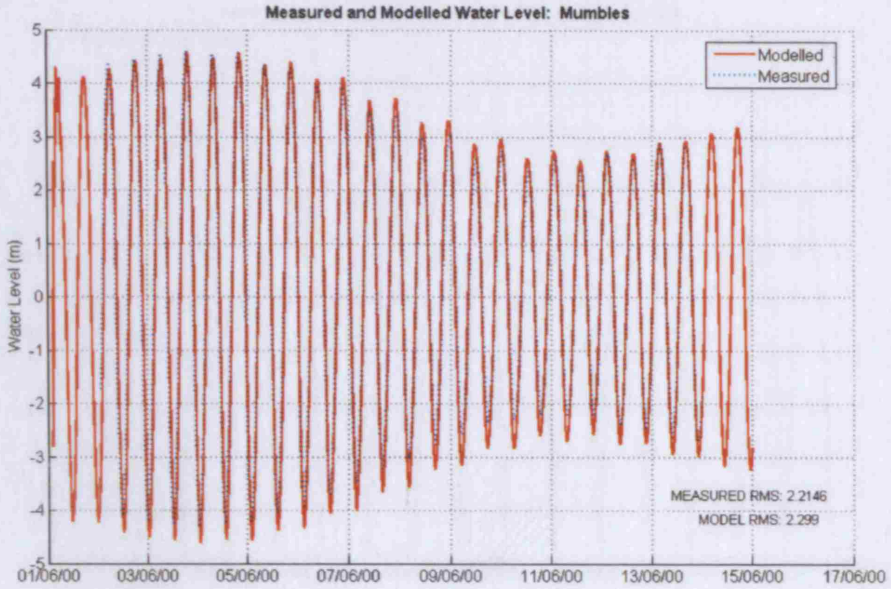

Figure A3.5. Model predictions of water level at Mumbles.

Table A3.3. RMS values of measured and modelled water levels

Water Level Station	RMS Measured (m)	RMS Modelled (m)	Difference (%)
Avonmouth	3.2112	2.8162	-12
Illracombe	2.1581	2.2553	9.72
Minehead	2.6939	2.6255	-2.54
Mumbles	2.2146	2.299	3.81
Porthcawl	2.3579	2.3664	0.36

A3.4 Comparison of Currents Speed and Direction

Data available for the comparison of measured and predicted velocities includes current meter buoys deployed by the BODC (see Figure A3.1). Unfortunately the distribution of the available data is restricted principally to the Swansea Bay area. It is therefore difficult to gauge how the rest of the model is performing in terms of predicted velocities. Comparisons of model predictions and measured values from the Swansea Bay area are presented in Figures A3.6 to A3.15.

a)

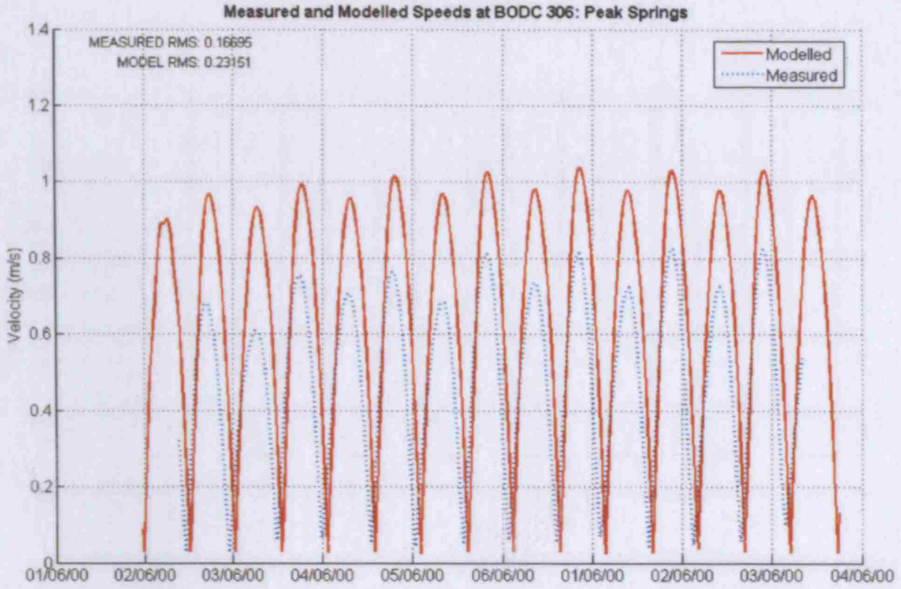

b)

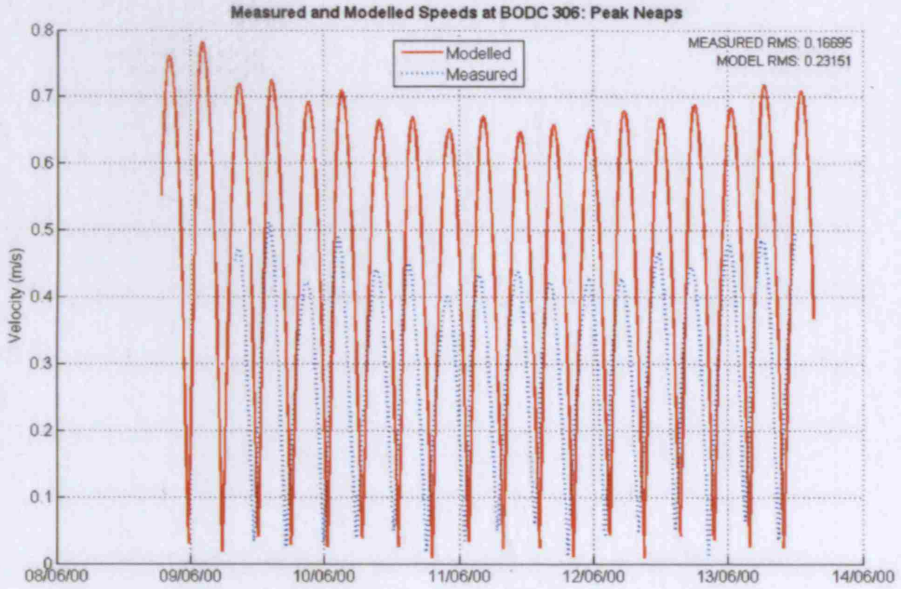

Figure A3.6. Current speed during a) spring and; b) neap conditions at current meter BODC 306

a)

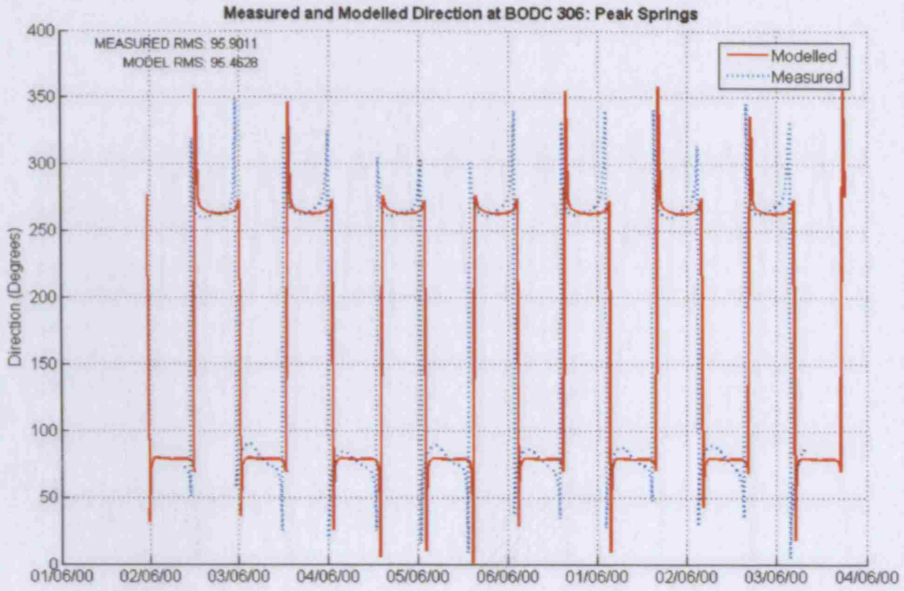

b)

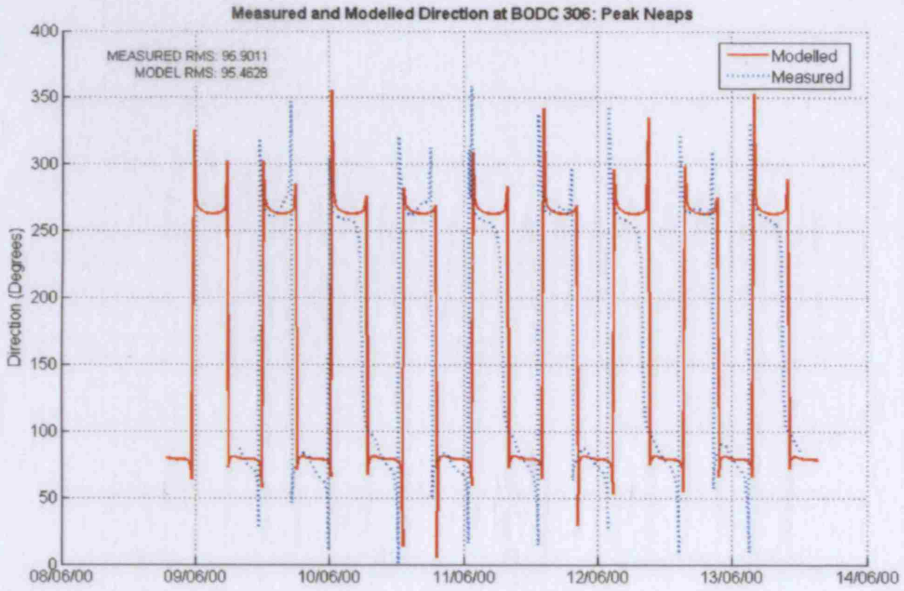

Figure A3.7. Current direction during a) spring and; b) neap conditions at current meter BODC 306

a)

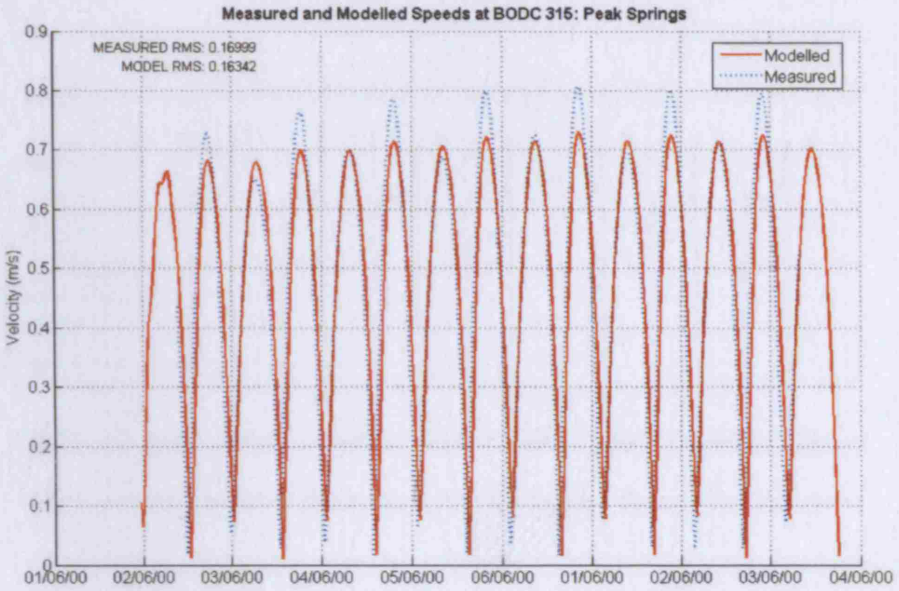

b)

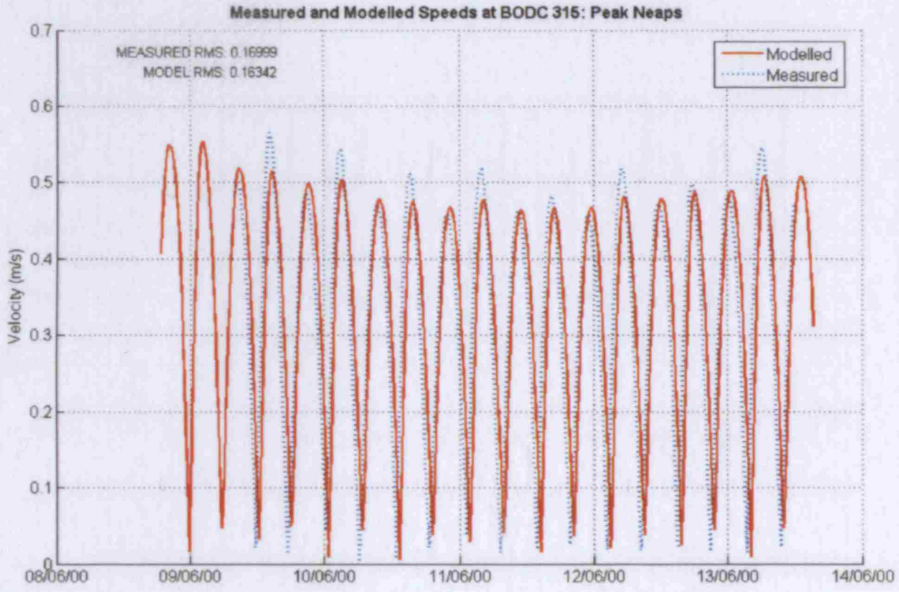

Figure A3.8. Current speed during a) spring and; b) neap conditions at current meter BODC 315.

a)

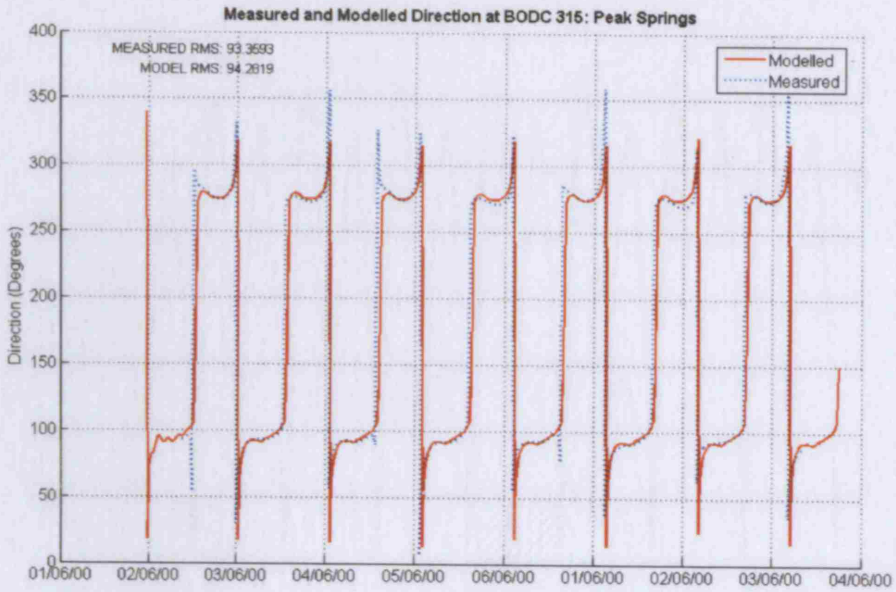

b)

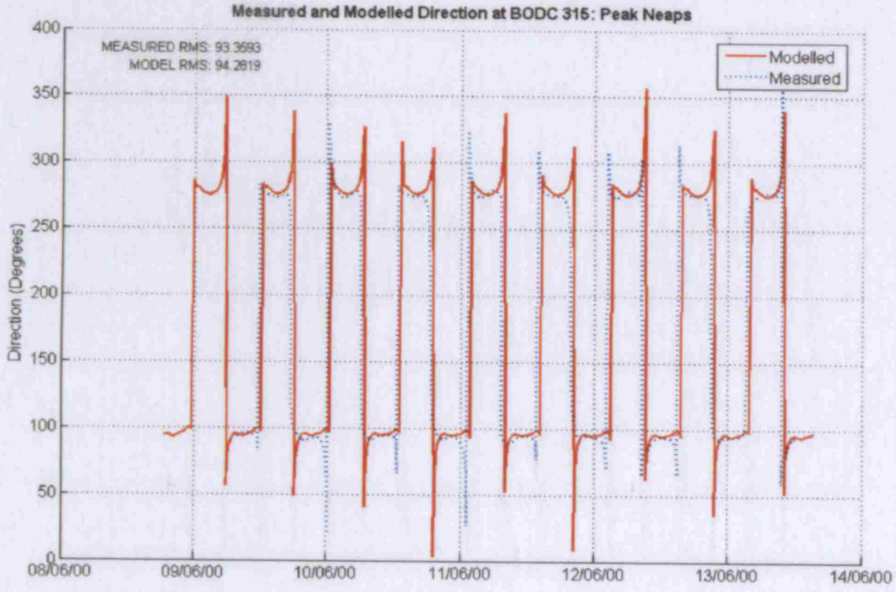

Figure A3.9. Current direction during a) spring and; b) neap conditions at current meter BODC 315.

a)

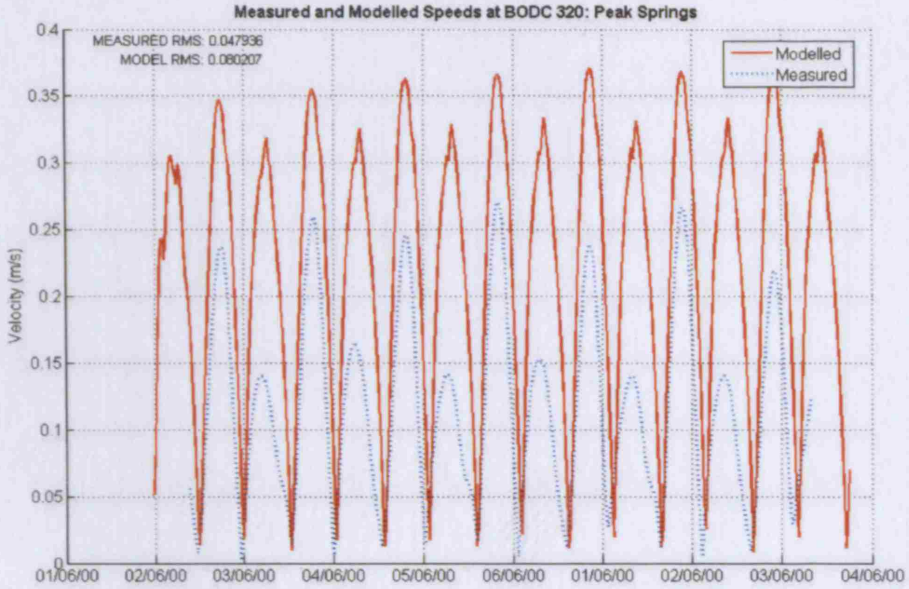

b)

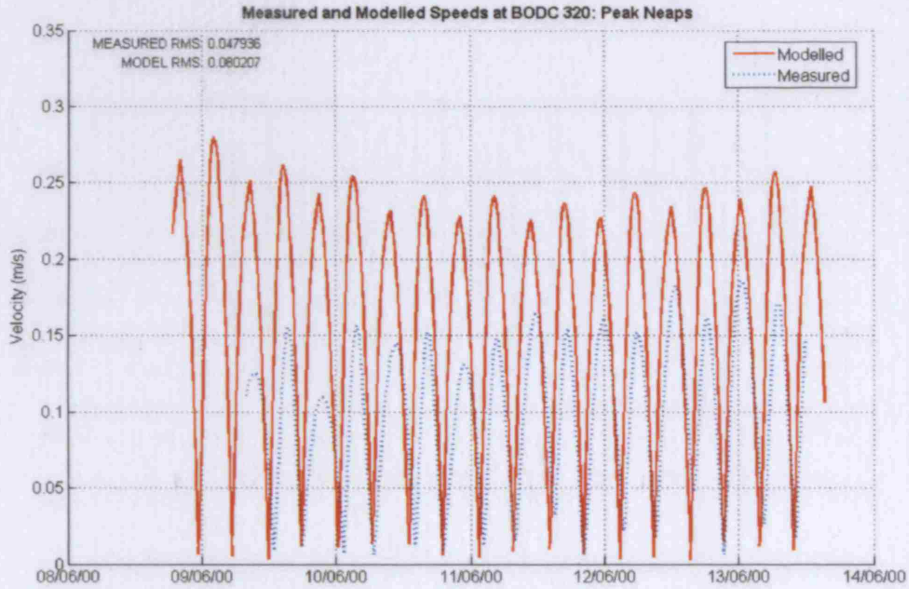

Figure A3.10. Current speed during a) spring and; b) neap conditions at current meter BODC 320.

a)

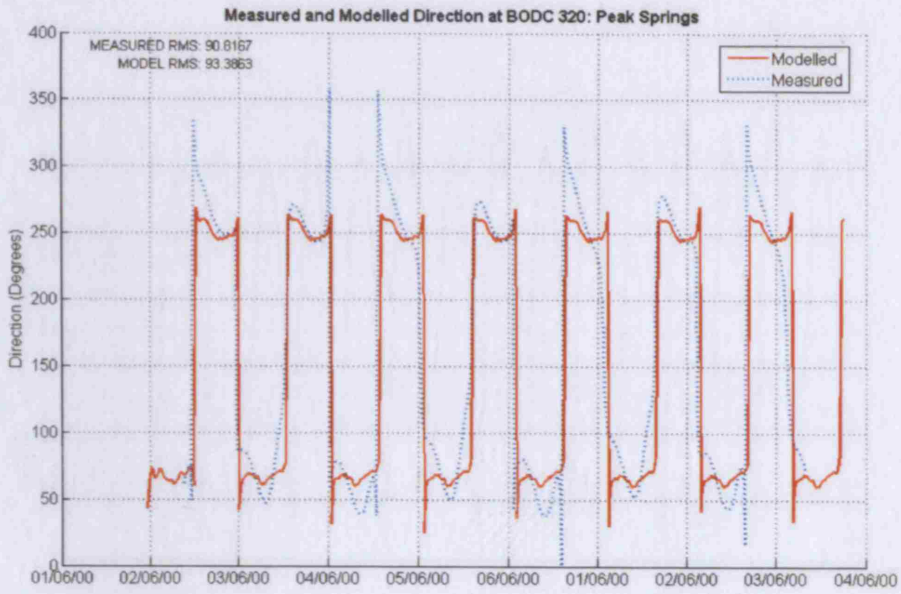

b)

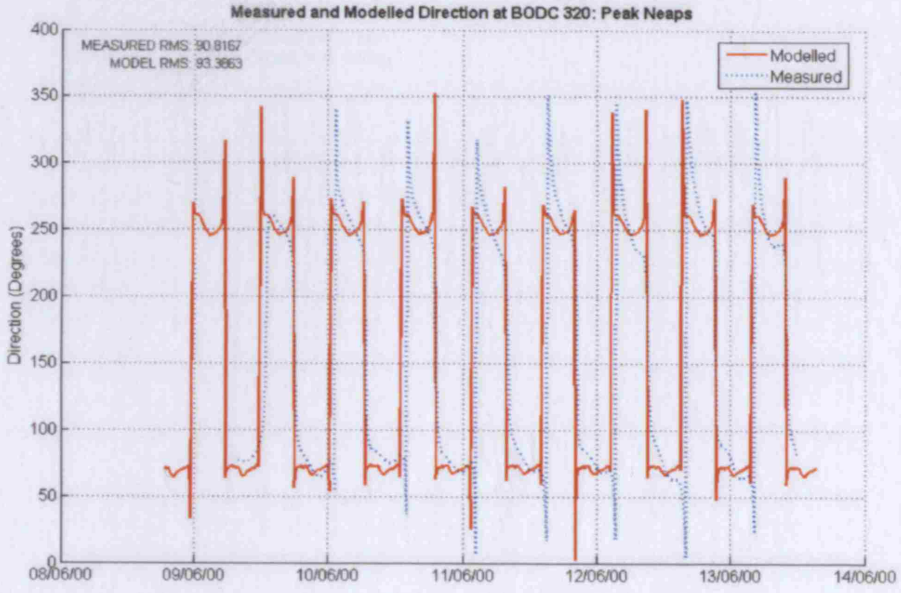

Figure A3.11. Current direction during a) spring and; b) neap conditions at current meter BODC 320

a)

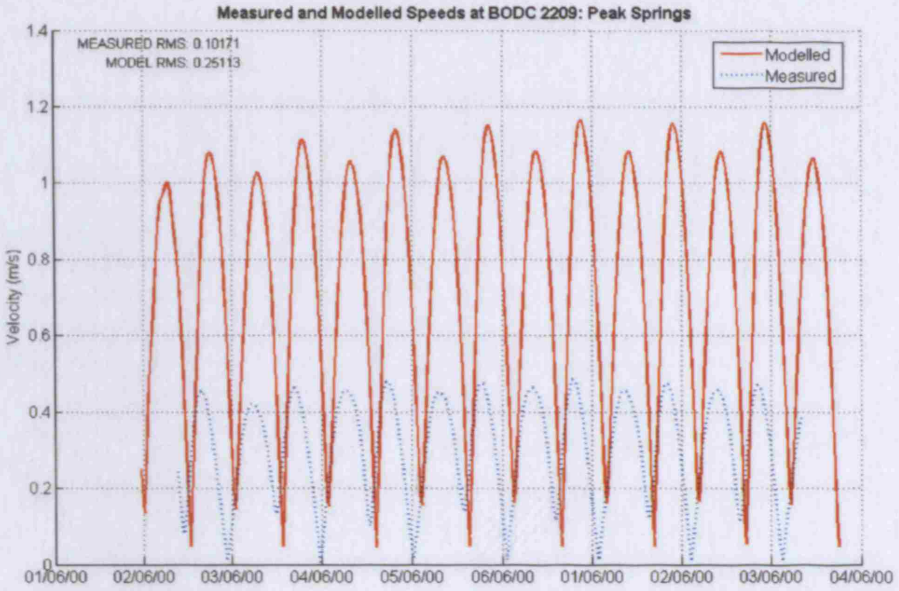

b)

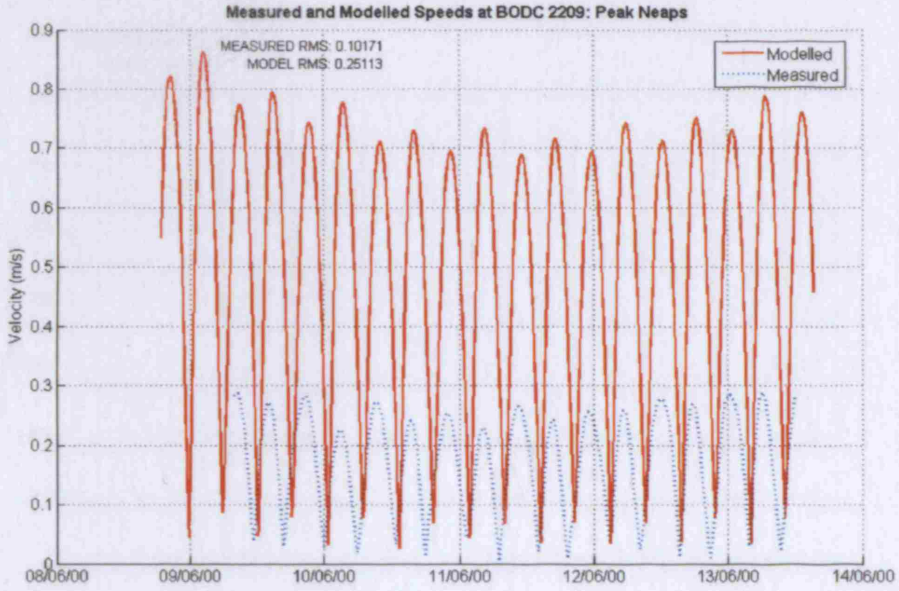

Figure A3.12. Current speed during a) spring and; b) neap conditions at current meter BODC 2209.

a)

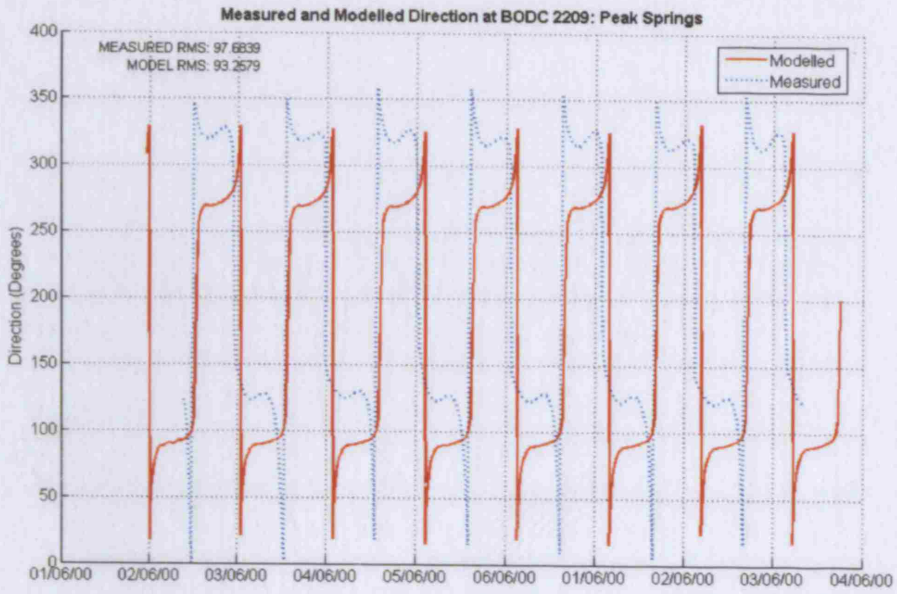

b)

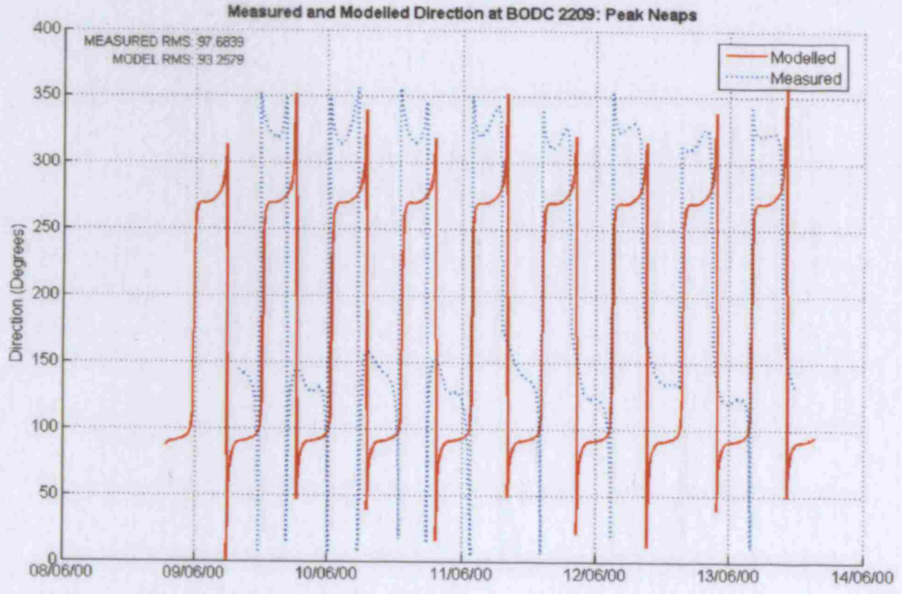

Figure A3.13. Current direction during a) spring and; b) neap conditions at current meter BODC 2209.

a)

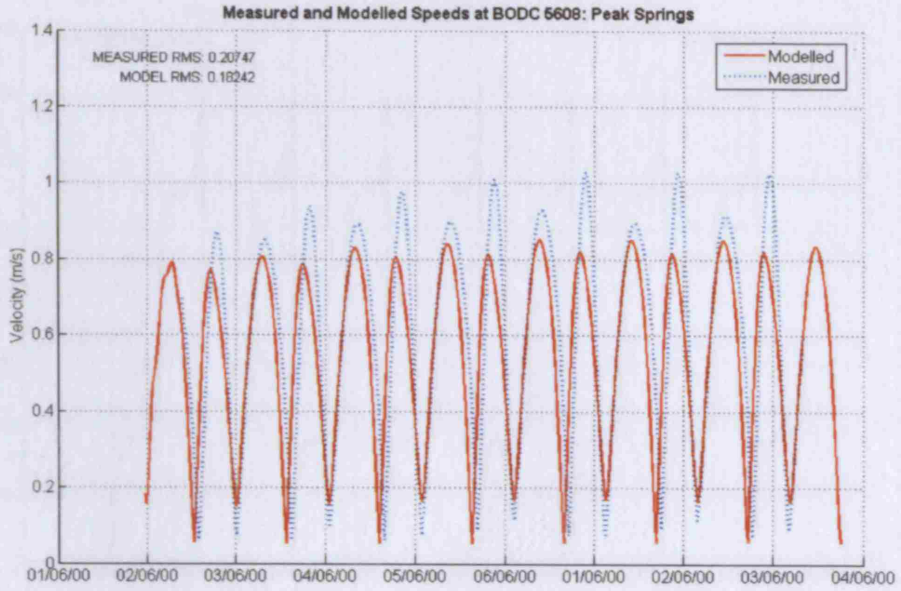

b)

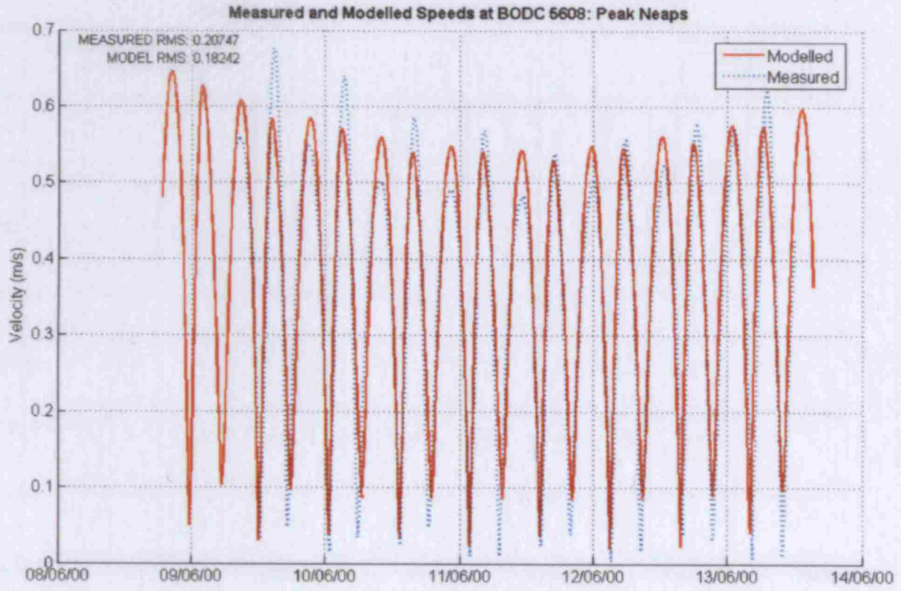

Figure A3.14. Current speed during a) spring and; b) neap conditions at current meter BODC 5608.

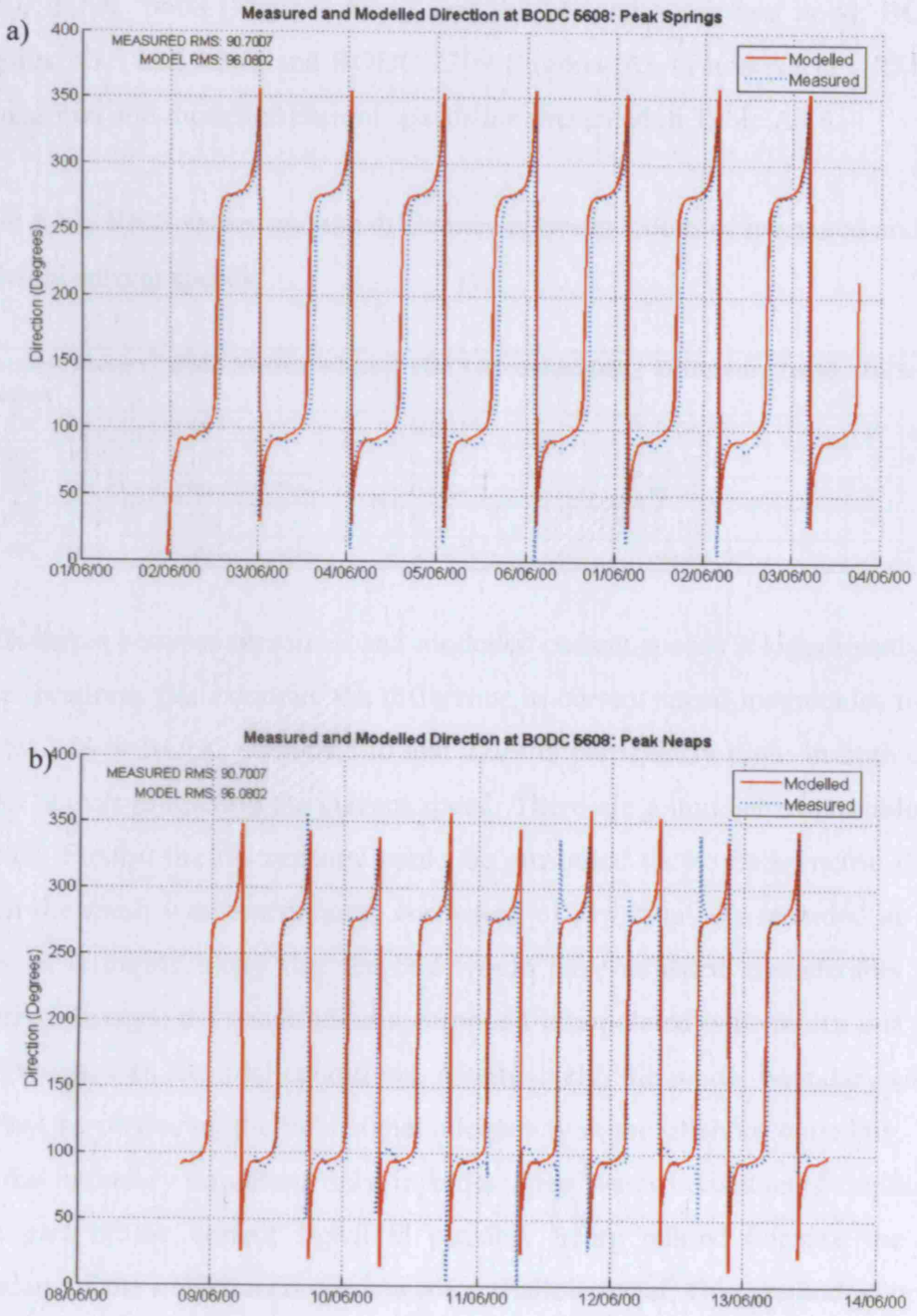

Figure A3.15. Current Direction during a) spring and; b) neap conditions at current meter BODC 5608.

The difference between modelled and predicted phase is consistently low. The calibrated model, therefore, is capturing directional switches and slack water period well. Less good, however, are the differences between modelled and measured

current speeds which in some cases is very good (BODC 315 Figures A3.7 and A3.8), BODC 5608 (Figures A3.13 and A3.14) and some less good: BODC 306 (Figures A3.5 and A3.6) and BODC 2209 (Figures A3.11 and A3.12). RMS values of measured and modelled current speeds are presented in Table A3.4.

Table A3.4. RMS values and the difference between values of measured and modelled current speeds.

Current Meter Station	RMS Measured (m)	RMS Modelled (m)	Difference (m/s)	Difference %
BODC 306	0.167	0.2315	0.0675	29.16
BODC 315	0.167	0.163	-0.004	-2.45
BODC 320	0.05	0.08	0.03	37.5
BODC 2209	0.102	0.25	0.148	59.2
BODC 5608	0.207	0.182	-0.0025	-1.37

Differences between measured and modelled current speeds is significantly large at some locations. For example, the difference in current speed magnitudes of 37.5 % and 59.2 % at BODC stations 320 and 2209 is particularly high. In both cases the model is over-predicting the current speed. There are a number of possible reasons for this. Firstly, the discrepancy could be attributed to the bathymetric data from which the mesh was interpolated, consisting of raw data sets recorded at different times. It is highly likely that the bed would have adjusted considerably between different surveys, the result being a compiled interpolated bathymetry that is not in equilibrium with the tidal conditions. Alternatively, the model boundary conditions may not be producing the tidal signal adequately at the offshore boundary. The fact that the boundary condition only includes deep water constituents implies that a large part of the correct signal is possibly being missed because the western boundary of the model encompasses some shallow water. One method of improving this would be to extend the western boundary much further offshore into deeper water areas, where shallow water constituents have no influence on the tidal signal.

A3.5 Model Validation

Using the improved model setup established from the calibration exercise, the model was run over another 2 week period in July 2002. The performance of the model, gauged by comparison of water levels and currents, was equally as good as

that of the calibrated model (see Tables A3.5 and A3.6). This showed that the model was capable of behaving reliably over any given time period.

Table A3.5. RMS values of measured and modelled water levels.

Water Level Stati	RMS Measured (m)	RMS Modelled (m)	Difference (%)
Avonmouth	2.8162	2.5207	-10.49
Illracombe	1.8387	1.9223	4.55
Minehead	2.3291	2.2827	-1.99
Mumbles	1.8988	1.9698	3.74
Porthcawl	2.0262	2.0579	1.56

Table A3.6. RMS values and the difference between values of measured and modelled current speeds.

Current Meter Station	RMS Measured (m)	RMS Modelled (m)	Difference (m/s)	Difference %
BODC 306	0.157	0.2108	0.0538	25.52
BODC 315	0.1577	0.1490	-0.0087	-5.84
BODC 320	0.0436	0.073	0.0294	40.27
BODC 2209	0.0998	0.229	0.1292	56.42
BODC 5608	0.2013	0.1664	-0.0349	-20.97

A3.5 Spectral Wave Model Calibration / Validation

A3.5.1 Model Parameters

The wave model parameters reflect the expected swell and locally generated wave conditions in the Bristol Channel characterised by a mix of high and low frequency waves, propagating in a variety of directions (see Figs. A3.16 and A3.17). These include locally generated waves (frequencies approach 0.5 Hz) and long period swell waves (frequencies as low as 0.05 Hz). Wave directions can also be highly variable with swell waves propagating predominantly from the west and south west and locally generated waves from a similar direction. The model discretisation, therefore, needs to be suitably robust to accommodate this complex wave climate, incorporating suitable frequency and directional ranges. This study, however, used a 'parametrically' decoupled model (see Appendix 2) which means that the frequency domain is parameterised in terms of a *direction action spectrum* and a mean wave frequency. In the directional space, the discretisation includes a full 360° comprising 24 directional bins. The discretisation and other modelling parameters, that remain

constant throughout the wave calibration and validation phase, are listed in Table A3.8 below.

The calibration exercise consisted of running a number of separate sensitivity tests in which a single input parameter was varied (see Tables A3.7 and A3.8). Simulations included a combination of wave alone and coupled wave-current model runs. Model predictions of significant wave height (H_s), peak wave period (T_{pk}) and zero crossing period (T_z) are compared with data from the UKMO Scarweather directional wave-rider buoy. Figure A3.20 demonstrates that the effect of a coupled air-sea interface is to amplify the peak wave events. The decoupled model run (SW2) predicts peak wave events that are much closer to those of the measured data. Comparisons of peak and mean crossing wave period show very minor differences in predictions.

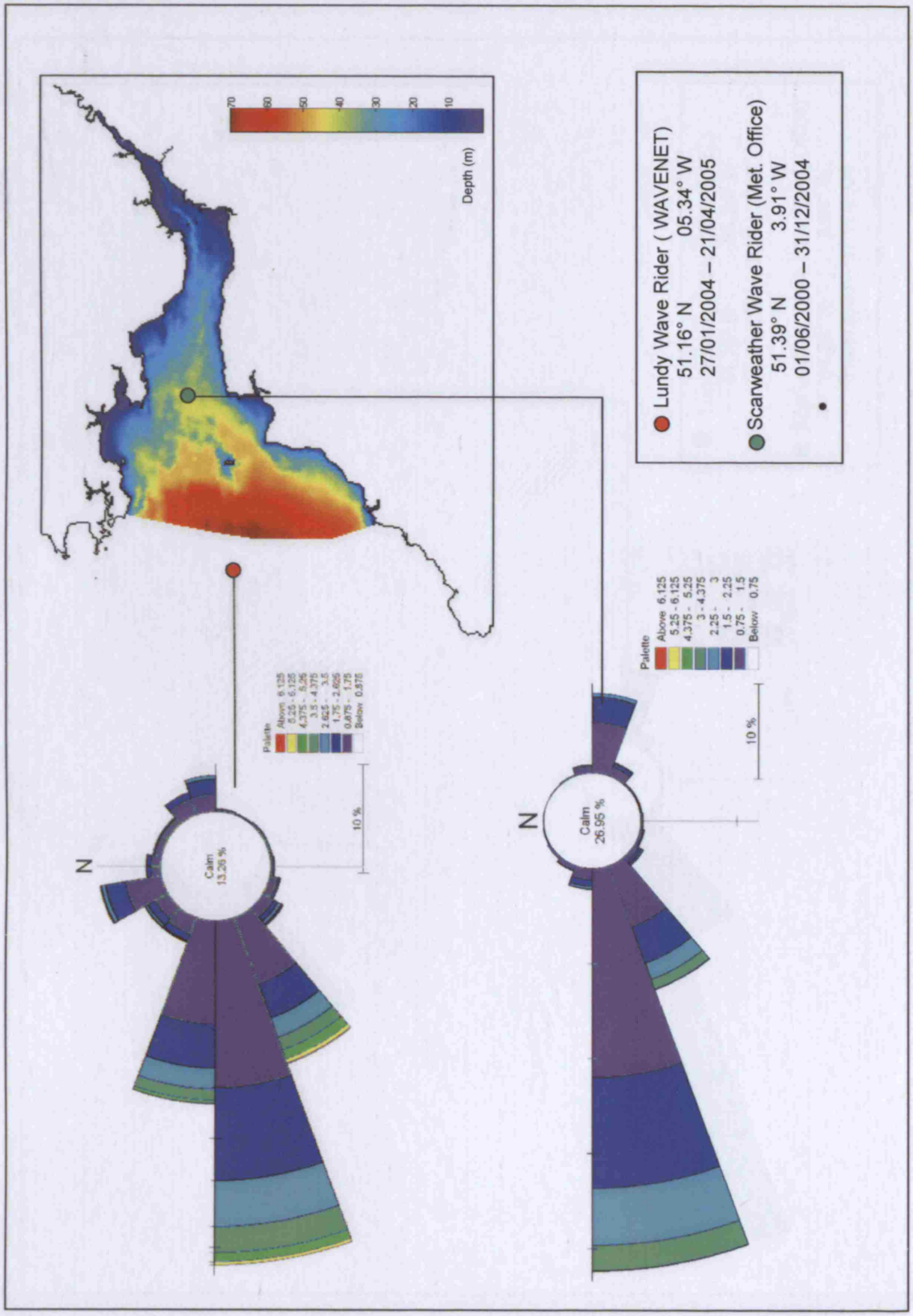

Figure A3.16. Significant Wave Height Roses for Lundy and Scarweather wave rider buoys.

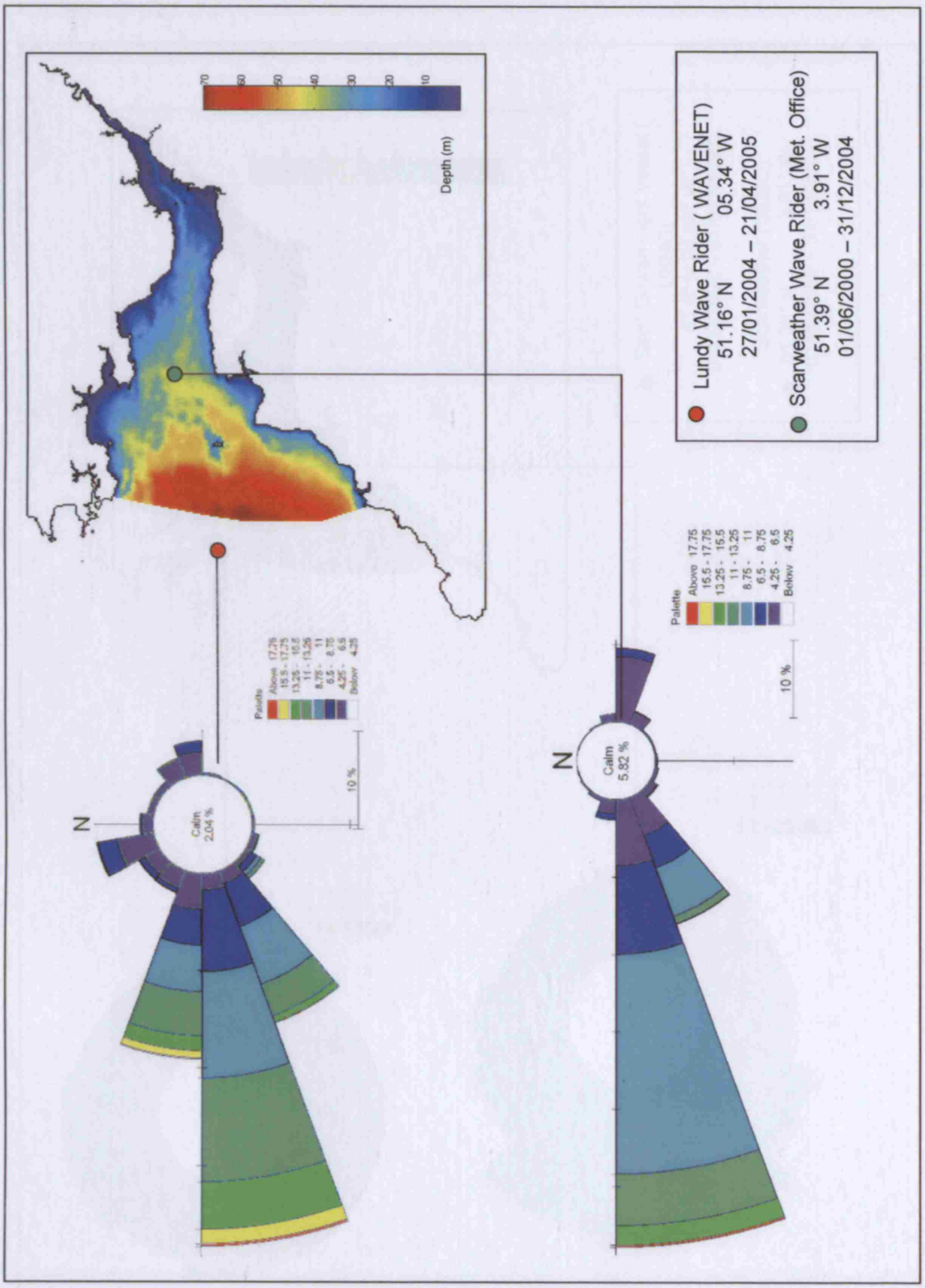

Figure A3.17. Peak Wave Period Roses for Lundy and Scarweather wave rider buoys.

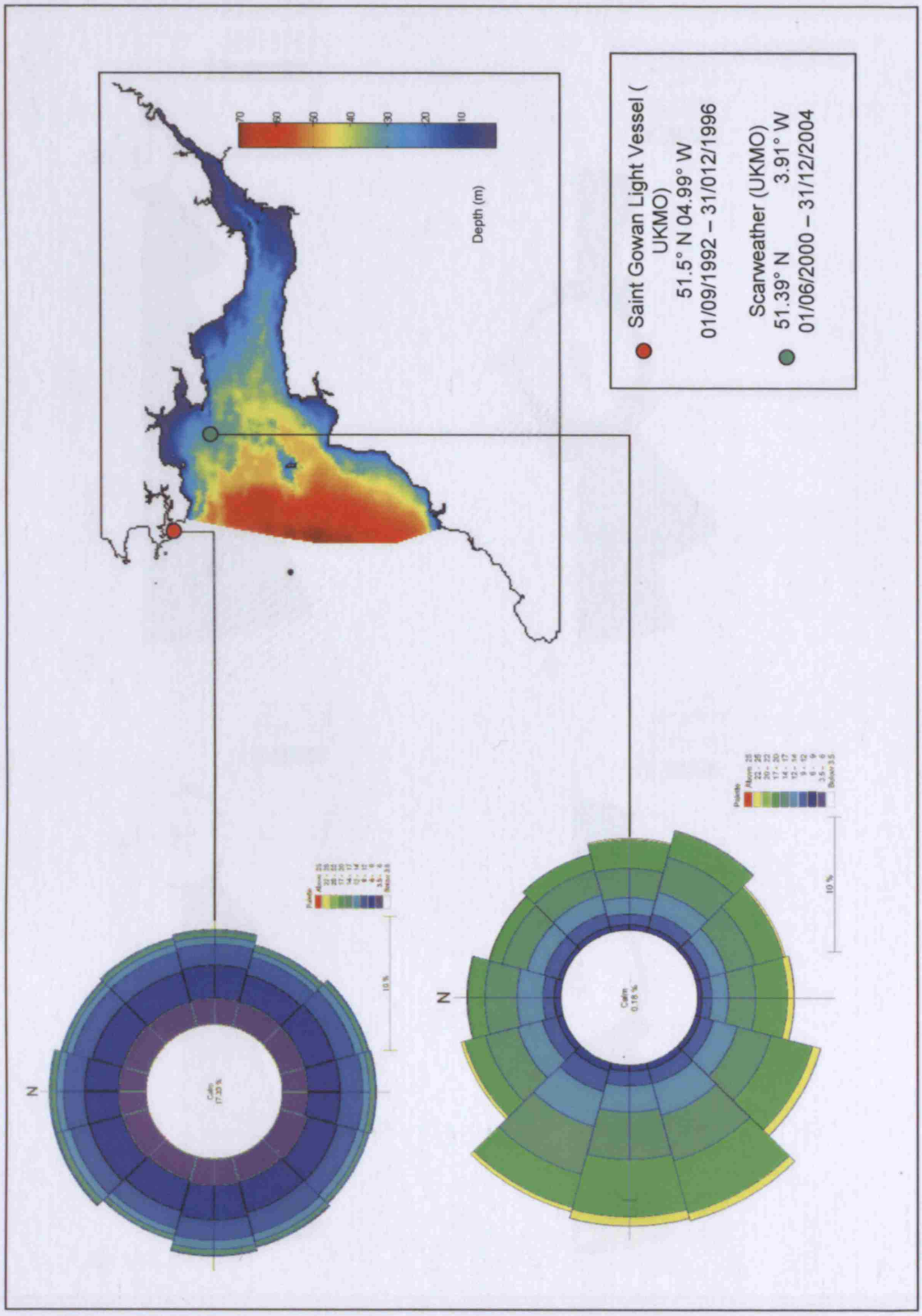

Figure A3.18. Wind Roses for Saint Gowan and Scarweather

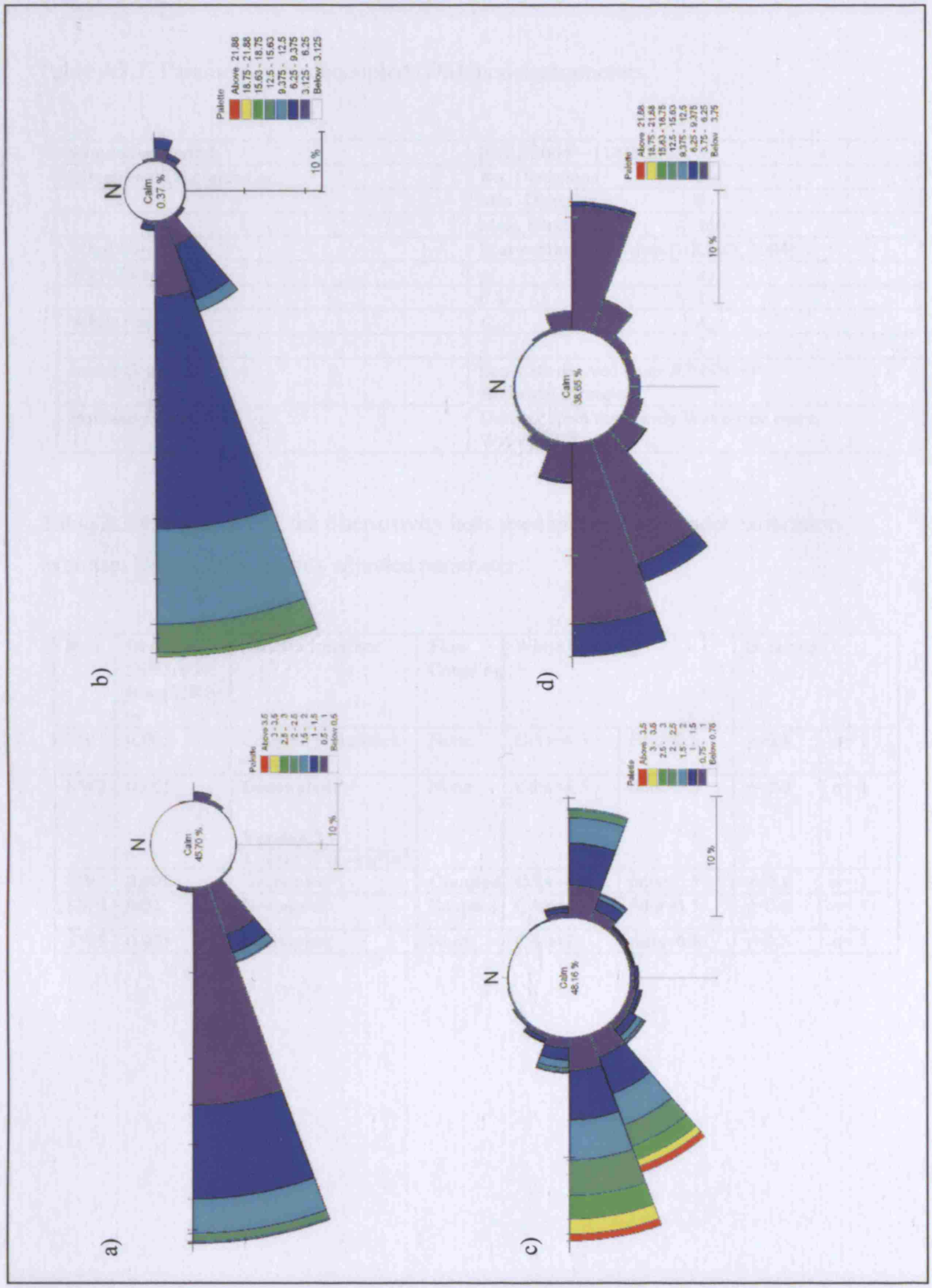

Figure A3.19. Scarweather a) H_s and b) T_z swell components and; c) H_s and d) T_z locally generated Components.

Table A3.7. Parametrically decoupled (DS) model parameters.

Simulation Period	02/02/2004 – 11/02/2004	
Directional Discretisation	No. Directions	24
	Min. Direction	0
	Max. Direction	360
Wind Forcing	Scarweather wind data (UKMO, 2004)	
Wave Breaking	γ_b	α_b
	0.8	1
White Capping	C_{ds}	δ_w
	5	2
Initial Conditions	Sea-state derived from JONSWAP empirical formulae	
Boundary Conditions	Derived from the Lundy Wave-ride buoy. WAVENET	

Table A3.8. Summary of the 6 sensitivity tests used in the wave model calibration exercise. Bold text highlights adjusted parameter.

Run	Bed Res. (Nikarudse Rough. Kn) m	Air-Sea Interface	Flow Coupling	White Capping		Breaking	
SW1	0.005	Coupled (Charnock = 0.01)	None	Cdis=4.5	δdis=0.5	γ=0.8	α= 1
SW2	0.005	**Decoupled:** **Version.2** **A =6*10^{-4} | B =6.6*10^{-3}**	None	Cdis=4.5	δdis=0.5	γ=0.8	α= 1
SW3	0.005	Decoupled	**Coupled**	Cdis=4.5	δdis=0.5	γ=0.8	α= 1
SW4	**0.02**	Decoupled	Coupled	Cdis=4.5	δdis=0.5	γ=0.8	α= 1
SW5	0.005	Decoupled	None	**Cdis=2**	**δdis=0.8**	γ=0.8	α= 1

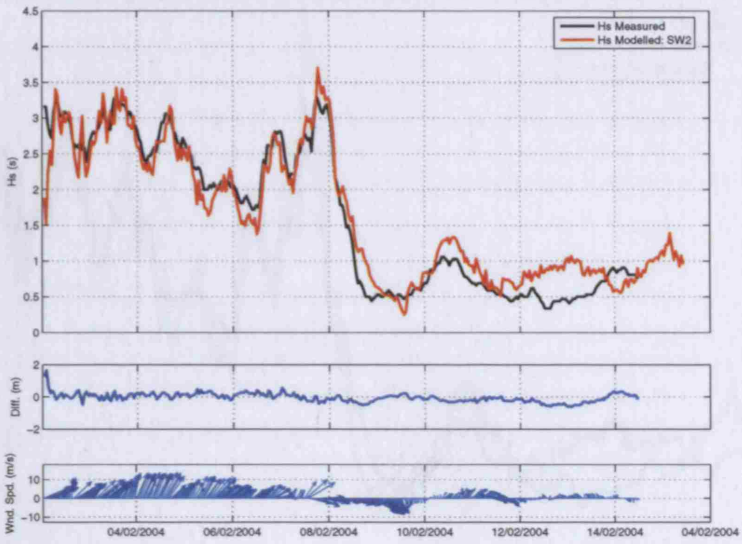

Figure A3.20. Comparison of measured and modelled significant wave height for the simulation 'SW2' comprising of a decoupled air-sea interface. Also plotted are time-series of calculated difference and a wind speed/direction. The coupled air-sea interface runs produced an exaggeration of the peak wave events

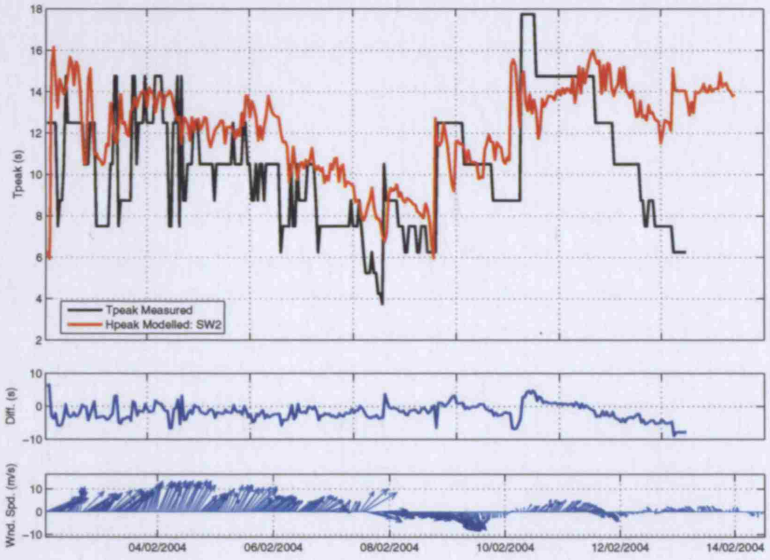

Figure A3.21. Comparison of measured and modelled peak wave period. Also plotted are time-series of calculated difference and a wind speed/direction.

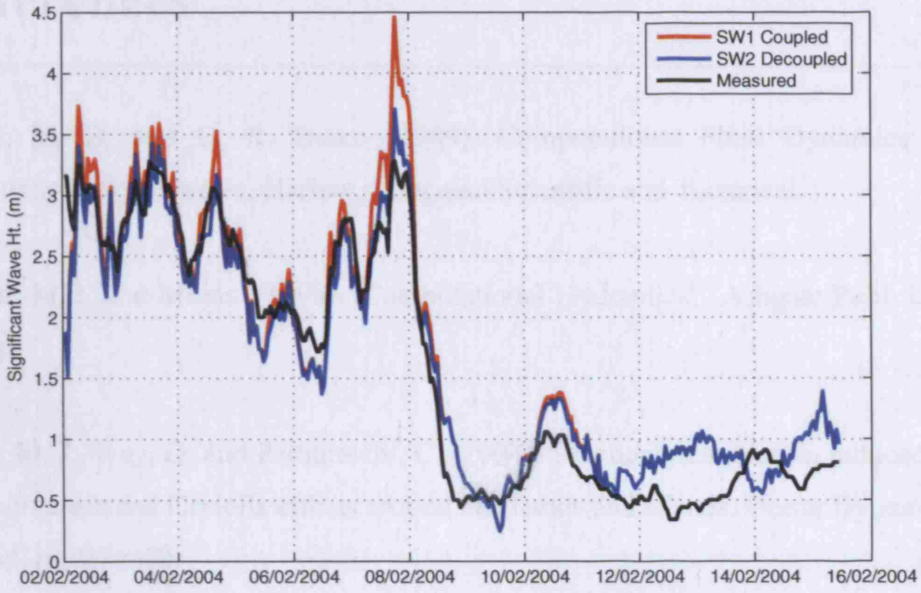

Figure A3.22. Comparison of SW1 (coupled), SW2 (decoupled) and measurements.

References

Abbot, M. B. and D. R. Basco (1989). Computational Fluid Dynamics: an introduction for engineers. Harlow, Longman Scientific and Technical.

Abbott, M.B. and Minns. (1998) "Computational Hydraulics", Ashgate Publ. Ltd., 557 pp.

Alaee, M. J., Ivey, G. and Pattiaratchi, C. (2004). Secondary circulation induced by flow curvature and Coriolis effects around headlands and islands. Ocean Dynamics. Vol. 54, pp. 27 – 38.

Andersen, O. B. (1995). Global Ocean Tides from ERS-1 and TOPEX/POSEIDON Altimetry Journal of Geophysical Research 100(C12), pp. 25249-25259.

Andrews (2005). Nash Bank Seabed Monitoring Survey, Winter, 2003. Andrews survey report ref, 0587/SMB(04).

Bakker W., and T. Van Doorn, (1978) Near bottom velocities in waves with a current. In Proceedings of Sixteenth Coastal Engineering Conference, Hamburg, Germany, ASCE, New York, Vol. 2, pp. 1394-1413.

Bastos, A. C., Collins, M. B. and Kenyon, N. H. (2003) Morphology and internal structure of sand shoals and sandbanks off the Dorset coast, English Channel. Sedimentology 50. pp. 1105-1122.

Bastos, A. C., D. Paphitis and M. B. Collins (2004). Short-Term Dynamics and Maintenance Processes of Headland-Associated Sandbanks: Shambles Bank, English Channel, U.K. Estuarine, Coastal and Shelf Science 59, pp. 22-47.

Battjes, J. A. and J. P. F. M. Janssen (1978). Energy loss and set-up due to breaking of random waves. In Proc. 16th Int. Conf. of Coastal Engineering, Hamburg, Germany, ASCE, New York, Vol. 1, pp. 569-587.

Baumert, H. and G. Radach (1992). Hesteresis of turbulent kinetic energy in non-rotational tidal flows: A model study. Journal of Geophysical Research 97, pp. 3669-3677.

Belderson, R. H. and A. H. Stride (1966). Tidal current fashioning of a basal bed. Marine Geology, Vol. 4, pp. 237-257.

Bellamy, A. G. (1998). The UK marine sand and gravel industry: an application if Quarternary geology. In: Advances in Aggregates and Armourstone Evaluation, Ed. Latham, J. P., Geological Society, London, Engineering Geology Special Publications 13, pp. 33-45.

Berthot, A. and C. Patiaratchi (2005). Maintenance of headland-associated linear sandbanks: modelling the secondary flows and sediment transport. Ocean Dynamics 55(5/6), pp. 526-540.

Berthot, A and C. Pattiaratchi (2006). Mechanisms for the formation of headland-associated linear sandbanks. Continental Shelf Research, Vol. 26, pp. 987-1004.

B.G.S. (1986). Sea Bed Sediments and Quaternary Geology: Bristol Channel Sheet 51N-04W, HMSO, London.

Booij, N., L. H. Holthuijsen and R. C. Ris. (1996). The "SWAN" wave model for shallow water. Proc.25th Int. Conf. on Coastal Engineering, Orlando, FL., ASCE, New York, pp. 668-676.

Britton, R. C. and S. R. Britton (1980). Sedimentary bed forms and linear sandbanks. In: Industrialised Embayments and Their Environmental Problems. Eds. Collins, M. B., Banner, F. T., Tyler, P. A., Wakefield, S. J. & James, A. E. Pergamon, Oxford, pp. 193–213.

Chang, C.H., Wang, J.C. and Y.K. Tung, (1993). Sensitivity and uncertainty analysis of a sediment transport model: a global approach. Stochastic Hydrology and Hydraulics, 7, pp. 299-314.

Chesher, T.J. and Miles, G.V., (1992). The concept of a single representative wave for use in numerical models of long terms sediment transport predictions. Proc. 2nd Int. Conf. on Hydraulic and Environmental Modelling of Coastal, Esuarine and River Waters, Vol. 1. Hydraulic and Environmental Modelling: Coastal Waters. Eds. Falconer RA, Chandler-Wilde SN and Liu SQ.

Cefas, (2002). WAVENET directional wave data from 'Lundy wave-rider buoy', 51.16 N 5.34 W; 27/01/04-21/04/05

Chung, T. J. (2002). Computational Fluid Dynamics. Cambridge, U.K., Cambridge University Press.

Coastal Geophysics (1995). South-east Swansea Geophysical Survey: Unpublished confidential report no. 1767C. Prepared by Coastal Geophysics Ltd. on behalf of UMD Ltd., ARC Marine Ltd., British Dredging Aggregates Ltd.

Collins, M. B. (1983). Supply, distribution and transport of suspended sediment in a macro-tidal environment: Bristol Channel, U.K. Canadian Journal of Aquatic Science 40 (Suppl. L), pp. 44-59.

Collins, M. B. and G. Ferentinos (1984). Residual circulation in the Bristol Channel, as suggested by Woodhead seabed drifter recovery patterns. Oceanol. Acta 7, pp. 33-42.

Cudemo, M. (2003). Interpolation and trend analysis of bathymetric survey data of the Nash Bank. MSc Thesis, Dept. Geographic Information Science, University College London.

Culver, S. J. (1980). Differential two-way transport in the Bristol Channel and Severn Estuary, U.K. Marine Geology 83, pp. 237-252.

Davies, A. M. and H. Gerritsen (1994). An intercomparison of three-dimensional tidal hydrodynamic models of the Irish Sea. Dynamic Meteorology and Oceanography, Vol. 46A(2), pp. 200-221.

Deigaard, R., N. Drønen, J. Fredsøe, J. H. Jensen and M. P. Jørgensen (1999). A morphological stability analysis for a long straight barred coast. Coastal Engineering Vol. 36, pp. 171-195.

Deigaard, R., J. Fredsøe and I. B. Hedegaard (1986). Suspended sediment in the surf zone. Journal of Waterway, Port, Coastal and Ocean Engineering Vol. 112(1), pp. 115-128.

De Vriend, H. J., M. Capobianco, T. Chesher, H. E. De Swart, B. Latteux and M. J. F. Stive (1993). Long-term modelling of coastal morphology. Coastal Engineering, Vol. 31(1-3), pp. 225-269.

De Vriend, H. J. (1991). Mathematical modeling and large-scale coastal behaviour. Journal of Hydraulic Research, Vol. 29(6), pp. 727-753.

DHI (2005). MIKE 21/3 Flow Model FM Hydrodynamic and Transport Module Scientific Documentation. Hørsholme, DHI Group.

Dong, P. and H. Chen (2001). Wave chronology effects on long-term shoreline erosion predictions. Journal of Waterway, Port, Coastal and Ocean Engineering Vol. 127(3), pp. 186-189.

Dong, P. (2005). Coastal Morphodynamics - Conceptual Frameworks. Mathematical Methods for Coastal Engineering., Plymouth, June, 2005.

Dronkers, J. J. (1986). Tidal asymmetry and estuarine morphology. Netherlands Journal of Sea Research, Vol. 20, pp. 117-131.

Duffy, G. P. (2006). Bedform migration and associated sand transport on a banner bank: application of repetitive multibeam surveying and tidal current measurement to the estimation of sediment transport. PhD Thesis. Dept. Geodesy and Geomatics Eng. Univ. New Brunswick, 210 pp.

Dyer, K. R. and D. A. Huntley (1999). The origin, classification and modelling of sand banks and ridges. Continental Shelf Research, Vol. 19, pp. 1285-1330.

Dyer, K.R. (1986), Coastal and Estuarine Sediment Dynamics. Wiley, Chichester, U.K., 342 pp.

Engelund, F. and J. Fredsøe (1976). A Sediment Transport Model for Straight Alluvial Channels. Nordic Hydrology, Vol. 7, pp. 293-306.

Evans, C. D. R. (2006). Sandbanks and offshore river channel: examples of geodiversity from areas of marine aggregate extraction, Report to the Marine Aggregate Levy Fund.

Fenton, J. (1985). A fifth order Stokes theory for steady waves. Journal of Waterway, Port, Coastal and Ocean Engineering, Vol. 111, pp. 216-234.

Fenton, J. (1990). Non-linear wave theories. Wiley, New York.

Fredsøe, J. (1984). The turbulent boundary layer in combined wave-current motion. Journal of Hydraulic Research, Vol. 110(HY8), pp. 1103-1120.

Fredsøe, J., O. H. Andersen and S. Silberg (1985). Distribution of suspended sediment in large waves. Journal of Waterway, Port, Coastal and Ocean Engineering, Vol. 111(6), pp. 1041-1059.

Fredsøe, J. and R. Deigaard (1992). Mechanics of Coastal Sediment Transport, World Scientific, 369 pp.

Gadd, N.R. (1987). Geological setting and Quaternary deposits of the Ottawa region, in Quaternary Geology of the Ottawa Region, Ontario and Québec, Fulton, R.J., (ed.), Geological Survey of Canada, paper no. 86-23.

Gau, S. and M. B. Collins (1995). Water and sediment transport around the Nash Bank, Bristol Channel: Literature Reviews. Report No. SUDO/TEC/95/32

Groeneweg, J. (1999). Wave-current interactions in a generalized Lagrangian mean formulation. Delft, Delft University of Technology. PhD thesis, 135 pp.

Grunnet, N. M. (2004). Morphodynamics of a shoreface nourishment in a barred nearshore zone. PhD Thesis, University of Utrecht, Netherlands Geographical Studies 323, pp. 153.

Harris, J. M. and O. P. Jones (2005). Modelling the Effect of Wave Current Interaction on Morphological Evolution in the Bristol Channel, U.K. Waves 2005. Madrid, Spain, CEDEX.

Harris, P.T. and Collins, M.B. (1985). Bedform distributions and sediment transport paths in the Bristol Channel and Severn Estuary, U.K. Marine Geology, Vol. 62, pp. 153-166.

Harris, P. T. and M. B. Collins (1988). Estimation of annual bed-load flux in a macrotidal estuary: Bristol Channel, U.K. Marine Geology, Vol. 83, pp. 237-252.

Harrison, D. J., Laban, C., Leth, J. O. and Larsen, B. (1998). Sources of sand and gravel on the northern European continental shelf. In: Advances in Aggregates and Armourstone Evaluation, (1998), Ed. J. P. Lathan, Geological Society London, Engineering Geology Special Publications, Vol. 14, pp. 33-45.

Heaps, N. S., (1978), Linearized vertically-integrated equations for residual circulation in coastal seas, Deutsch Hydrog. Zeit., Vol. 5, pp. 147-169.

Heathershaw, A. D. and F. D. C. Hammond (1980). Secondary circulation's near sand banks and in coastal embayments. Deutsche Hydrog. Zeit, Vol. 33(4), pp. 135-151.

Holthuijsen, L. H., N. Booij and T. H. C. Herbers (1989). A Prediction Model for Stationary, Short-Crested Waves in Shallow Water with Ambient Currents. Coastal Engineering, Vol. 13, pp. 23-54.

Houbolt, J. J. H. C. (1968). Recent sediments in the southern bight of the North Sea. Geol. Mijnbouw, Vol. 47, pp. 225-273.

Hudson, J., J.S. Damgaard, N. Dodd, T.J. Chesher and A.J. Cooper (2006). Numerical Approaches for 1D morphodynamic modelling. Coastal Engineering, Vol. 53, Issue 7, pp. 629-630.

Huthnance, J. M. (1982). On one mechanism forming linear sand banks. Estuarine, Coastal and Shelf Science 14, pp. 79-99.

Huthnance, J. M. (1982). On one mechanism forming linear sand banks. Estuarine, Coastal and Shelf Science 14, pp. 79-99.

Idier, D. and D. Astruc (2003). Analytical and numerical modeling of sandbanks dynamics. Journal of Geophysical Research, Vol. 108(C3), pp. 3060.

Jelgersma, S. (1979). Sea-level changes in the North Sea basin. In: Oele, E., Schuttenhelm, R.T.E. and Wiggers, A.J. (eds) The Quaternary history of the North Sea. Acta Universitatis Upsaliensis: Symposium Universitatis Upsaliensis Annum Quingentesimum Celebrantis, Vol. 2, pp. 233-248.

Jones, O. P., J. M. Harris, O. S. Petersen, and R. R. Simons (Submitted for review, July 2006), On wave-induced sediment transport in a macro-tidal sea, Continental Shelf Research.

Jones, O. P., R. R. Simons, E. J. W. Jones and J. M. Harris (2006). The influence of seabed slope and the Coriolis effect on sandbanks near headlands. The Journal of Geophysical Research, Vol. 111(CO3020).

Kalkwijk, J. P. T. and R. Booij (1991). Adaption of secondary flow in near-horizontal flow. Journal of Hydraulic Research, Vol. 24, pp. 19-37.

Kemp, P. and R. R. Simons (1983). The interaction of waves and a turbulent current: waves propagating with the current. Journal of Fluid Mechanics, Vol. 116, pp. 227-250.

Kenyon, N. and B. Cooper (2004). Sand banks, sand transport and offshore windfarms, Unpublished Report, National Oceanographic Centre, Southampton, U.K.

Komen, G. J., L. Cavaleri, M. Doneland, K. Hasselmann, S. Hasselmann and P.A.E.M Janssen. (1994). Dynamics and modelling of ocean waves. Cambridge University Press, U.K, 560 pp.

Lanzoni S. Seminara G. (2002). Long-term evolution and morphodynamic equilibrium of tidal channels. Journal of Geophysical. Research, Vol. 107, C1

Latteux, B. (1987). Transport modelling of particulate matter- methodology of long term simulations of bed evolution, Lab. Nat. d'Hydro. Chaton.

Latteaux, B. (1992). Long-term morphological simulation under tidal current with non-cohesive sediment. MAST G6-M Final Workshop, paper 5.18.

Leont'yev, I. O. (2003), Modeling erosion of sedimentary coasts in the western Russian Arctic. Coastal Engineering, Vol., 47, pp. 413-429.

Lesser, G. R., J. A. Roelvink, J. A. T. M. van Kester and G. S. Stelling (2004). Development and validation of a three-dimensional model. Coastal Engineering, Vol. 51, pp. 883-915.

Longuet-Higgins, M. S. and R. W. Stewart (1964). Radiation stress in water waves; a physical discussion, with applications. Deep Sea Research, Vol. 11, pp. 529-562.

McLaren, P., M. B. Collins, S. Gao and R. I. L. Powys (1993). Sediment dynamics of the Severn Estuary and inner Bristol Channel. Journal of the Geological Society, London, Vol. 150, pp. 589-603.

Murray, J. W. and A. B. Hawkins (1976). Sediment transport in the Severn Estuary during the past 8000-9000 years. Journal of the Geological Society of London, Vol. 132, pp. 385-398.

O'Connor, B. A. (1987). Short and long term changes in estuary capacity. Journal of the Geological Society. Vol. 144(1), pp. 187-195.

O'Connor, B. A., Nicholson. J. and Rayner, R. (1990). Estuary geometry as a function of tidal range. In Proc. 22nd In. Conf. on Coastal Engineering, ASCE, New York, pp. 3050-3062.

Park, M. J. and D. P. Wang (1991). Transient tidal vorticity over a hollow. Tidal Hydrodynamics. B. Parker. New York, John Wiley & Sons, pp. 419-434.

Park, M. J. and D. P. Wang (2000). Tidal vorticity around a coastal promontory. Journal of Oceanography, Vol. 56, pp. 261-273.

Pattiaratchi, C. B. and M. B. Collins (1984). Sediment transport under waves and tidal currents: A case study from the northern Bristol Channel, U.K., Marine Geology, Vol. 56, pp. 27-40.

Pingree, R. D. (1978). The formation of the Shambles sandbank and other banks by tidal stirring of the seas. Journal of Mar. Biol. Assoc. of the U.K., Vol. 58, pp. 211-226.

Pingree, R. D. and L. Maddock (1979). The tidal physics of headland flows and offshore tidal bank formation. Marine Geology, Vol. 32, pp. 269-289.

Rasmussen, E. (2005). The Optimal Choice of Model. Unpublished Report. Hørsholme, DHI Water and Environment.

Rodi, W. (1984). Turbulence models and their application in hydraulics- A state of the art review. Special IAHR Publication

Roelvink J. A. (2006). Coastal morphodynamic evolution techniques. Journal of Coastal Engineering, Vol. 53, pp. 277-287

Ruessink, B.G., Walstra, D.J.R. and Southgate, H.N. (2003). Calibration and verification of a parametric wave model on barred beaches. Coastal Engineering, Vol. 48, pp. 139-149.

Resource Management Association (2003). Nash Bank Seabed Monitoring Survey Summer 2003. Report no. 0587/SBM(02).

Reeve, D. E., Li, B. and Thurston, N. (2001). Eigenfunction analysis of decadal fluctuations in sandbank morphology at Great Yarmouth. Journal of Coastal Research, Vol. 17, No. 2, pp. 371.382.

Robinson, I. S. (1981). Tidal vorticity and residual circulation. Deep Sea Research, Vol. 28A, pp. 195-212.

Rodi, W. (1984). Turbulence models and their application in hydraulics- A state of the art review. Special IAHR Publication.

Roelvink, J. A. and I. Brøker (1993). Cross shore profile models. Coastal Engineering, Vol. 21, pp. 163-191.

Sánchez-Arcilla, A. S. and C. M. Lemos (1990). Surf Zone Hydrodynamics. Ed. CIMNE, Barcelona, Spain, 310 pp.

Signell, R. and W. R. Geyer (1990). Numerical simulation of tidal dispersion around a coastal headland. In: Residual Currents and Long-Term Transport. Ed. R. T. Cheng. New York, Springer-Verlag, pp. 210-222.

Signell, R. and C. K. Harris (2000). Modelling sand bank formation around tidal headlands. In: 6th Int. Conf. in Estuarine and Coastal Modelling, New Orleans, LA, ASCE, pp. 209-222

Signell, R (2006). Personal communication.

Smagorinsky, J. (1963). General circulation experiment with the primitive equations. Monthly Weather Review, Vol. 3(91), pp. 99-164.

Sørensen, O. R., H. Kofoed-Hansen and O. P. Jones (2006). Numerical modelling of wave-current interaction in tidal areas using an unstructured finite volume technique. Proc. 30th Int. Conf. on Coastal Engineering, ASCE, New York.

Sørensen, O. R., H. Kofoed-Hansen, M. Rugbjerg and L. S. Sørenson (2004). A third-generation spectral wave model using an unstructured finite volume technique. Proc. 29th Int. Conf. on Coastal Engineering, ASCE, New York, pp. 894-906.

Southgate, H.N. (1995). The effects of wave chronology on medium and long term coastal morphology. Coastal Engineering, Vol. 25, pp. 251-270.

Stride, A. H. and R. H. Belderson (1990). A reassessment of sand transport in the Bristol Channel and their regional significance. Marine Geology, Vol. 92, pp. 227-236.

Soulsby, R. L., L. Hamm, G. Klopman, D. Myrhaug, R. R. Simons and G. P. Thomas (1993). Wave-current interaction within and outside the bottom boundary layer. Coastal Engineering, Vol. 21, pp 41-69.

Southgate, H. N. (1995). The effects of wave chronology on medium and long term coastal morphology. Coastal Engineering, Vol. 26(3), pp. 251-270.

Taylor, G. I. (1954). The dispersion of matter in turbulent flow through a pipe. Proceedings of the Royal Society of London, Series A 223, pp. 446-468.

Tee, K. T., (1976). Tide-induced residual current, a 2-D nonlinear numerical tidal model, Journal of Marine Research, Vol. 34, pp. 603–628.

Thompson, A., D. Knapman and J. Pethick (2002). Comparative Impact Assessment of Land and Marine Sand and Gravel in South East Wales. Final Report, May 2002. A Report to the Welsh Assembly Government compiled by Symonds Group Ltd.: 184.

UKMO (1997). St. Gowan light vessel percentage frequencies of exceedence.

UKMO (2005) Directional wave-data from the Scarweather wave-rider buoy: 51.39° N 3.91° W; 01/06/2000 – 31/12/2004

Uncles, R. J. (1982). Computed and observed residual currents in the Bristol Channel. Oceanologica Acta, Vol. 5, pp. 11-20.

U.S. Army Coastal Engineering Research Centre (1984). Shore Protection Manual, 4th Edition, U.S. Govt. Printing Office, Washington DC.

Van Ormondt, M., Walstra D.J., van Rijn L.C., Roelvink D., Spanhoff R. (2005). Optimising and understanding shoreface nourishments. Proc. 5th Int. Conf. on Coastal Dynamics, Ed. A. Sanchez-Arcilla, ASCE.

Van Rijn, L. C. (1993). Principles of Sediment Transport in Rivers, Estuaries and Seas Aqua Publications.

SANDPIT (2005). Sand Transport and Morphology of Offshore Sand Mining Pits. Eds. Van Rijn, L.C., Soulsby, R. L., Hoekstra, P. Davies, A. G., Aqua Publications, The Netherlands.

Walstra, D. J. R., J. A. Roelvink and J. Groeneweg (2000). Calculation of wave-driven currents in a 3D mean model. Proc. 27th Int. Conf. on Coastal Engineering, ASCE, New York.

Whitham, G. B. (1965). A general approach to linear and nonlinear dispersive waves using a Lagrangian. Journal of Fluid Mechanics, Vol. 22, pp. 273-283.

Wijnberg, K. M. and Terwindt, J. H. J. (1995). Extracting morphological behaviour from high-resolution, long-term bathymetric surveys along the Holland coast using Eigenfunction analysis. Marine Geology, Vol. 126, pp. 301-330.

WL|Delft-Hydraulics (2001). User Manual Delft 3D-FLOW. Delft.

Zimmerman, J. T. F. (1978). Topographic generation of residual circulation by oscillatory (tidal) currents. Geophys. Astrophys. Fluid Dynamics, Vol. 11, pp. 35-47.

Zyserman, J. A. and J. Fredsøe (1994). Data analysis of bed concentration of suspended sediment. Journal of Hydraulic Engineering, Vol. 120(9), pp. 1021-1042.